MINERAL IDENTIFICATION USING DATA-MINING IN HYPERSPECTRAL INFRARED IMAGERY

Thèse

Bardia Yousefi

Doctorat en génie électrique
Philosophiæ doctor (Ph. D.)

Québec, Canada

MINERAL IDENTIFICATION USING DATA-MINING IN HYPERSPECTRAL INFRARED IMAGERY

Thèse

Bardia Yousefi

Sous la direction de:

Xavier P.V. Maldague, directeur de recherche
Georges Beaudoin, codirecteur de recherche

Résumé

Les applications de l'imagerie infrarouge dans le domaine de la géologie sont principalement des applications hyperspectrales. Elles permettent entre autre l'identification minérale, la cartographie, ainsi que l'estimation de la portée. Le plus souvent, ces acquisitions sont réalisées in-situ soit à l'aide de capteurs aéroportés, soit à l'aide de dispositifs portatifs. La découverte de minéraux indicateurs a permis d'améliorer grandement l'exploration minérale. Ceci est en partie dû à l'utilisation d'instruments portatifs. Dans ce contexte le développement de systèmes automatisés permettrait d'augmenter à la fois la qualité de l'exploration et la précision de la détection des indicateurs.

C'est dans ce cadre que s'inscrit le travail mené dans ce doctorat. Le sujet consistait en l'utilisation de méthodes d'apprentissage automatique appliquées à l'analyse (au traitement) d'images hyperspectrales prises dans les longueurs d'onde infrarouge. L'objectif recherché étant l'identification de grains minéraux de petites tailles utilisés comme indicateurs minéral -ogiques. Une application potentielle de cette recherche serait le développement d'un outil logiciel d'assistance pour l'analyse des échantillons lors de l'exploration minérale.

Les expériences ont été menées en laboratoire dans la gamme relative à l'infrarouge thermique (Long Wave InfraRed, LWIR) de 7.7μm à 11.8 μm. Ces essais ont permis de proposer une méthode pour calculer l'annulation du continuum. La méthode utilisée lors de ces essais utilise la factorisation matricielle non négative (NMF). En utlisant une factorisation du premier ordre on peut déduire le rayonnement de pénétration, lequel peut ensuite être comparé et analysé par rapport à d'autres méthodes plus communes. L'analyse des résultats spectraux en comparaison avec plusieurs bibliothèques existantes de données a permis de mettre en évidence la suppression du continuum. Les expérience ayant menés à ce résultat ont été conduites en utilisant une plaque Infragold ainsi qu'un objectif macro LWIR. L'identification automatique de grains de différents matériaux tels que la pyrope, l'olivine et le quartz a commencé. Lors d'une phase de comparaison entre des approches supervisées et non supervisées, cette dernière s'est montrée plus approprié en raison du comportement indépendant par rapport à l'étape d'entraînement.

Afin de confirmer la qualité de ces résultats quatre expériences ont été menées. Lors d'une première expérience deux algorithmes ont été évalués pour application de regroupements en

utilisant l'approche FCC (False Colour Composite). Cet essai a permis d'observer une vitesse de convergence, jusqu'a vingt fois plus rapide, ainsi qu'une efficacité significativement accrue concernant l'identification en comparaison des résultats de la littérature. Cependant des essais effectués sur des données LWIR ont montré un manque de prédiction de la surface du grain lorsque les grains étaient irréguliers avec présence d'agrégats minéraux. La seconde expérience a consisté, en une analyse quantitaive comparative entre deux bases de données de Ground Truth (GT), nommée rigid-GT et observed-GT (rigide-GT: étiquet manuel de la région, observée-GT:étiquetage manuel les pixels). La précision des résultats était 1.5 fois meilleur lorsque l'on a utlisé la base de données observed-GT que rigid-GT. Pour les deux dernières epxérience, des données venant d'un MEB (Microscope Électronique à Balayage) ainsi que d'un microscopie à fluorescence (μXRF) ont été ajoutées. Ces données ont permis d'introduire des informations relatives tant aux agrégats minéraux qu'à la surface des grains. Les résultats ont été comparés par des techniques d'identification automatique des minéraux, utilisant ArcGIS. Cette dernière a montré une performance prometteuse quand à l'identification automatique et à aussi été utilisée pour la GT de validation. Dans l'ensemble, les quatre méthodes de cette thèse représentent des méthodologies bénéfiques pour l'identification des minéraux. Ces méthodes présentent l'avantage d'être non-destructives, relativement précises et d'avoir un faible coût en temps calcul ce qui pourrait les qualifier pour être utilisée dans des conditions de laboratoire ou sur le terrain.

Abstract

The geological applications of hyperspectral infrared imagery mainly consist in mineral identification, mapping, airborne or portable instruments, and core logging. Finding the mineral indicators offer considerable benefits in terms of mineralogy and mineral exploration which usually involves application of portable instrument and core logging. Moreover, faster and more mechanized systems development increases the precision of identifying mineral indicators and avoid any possible mis-classification. Therefore, the objective of this thesis was to create a tool to using hyperspectral infrared imagery and process the data through image analysis and machine learning methods to identify small size mineral grains used as mineral indicators. This system would be applied for different circumstances to provide an assistant for geological analysis and mineralogy exploration. The experiments were conducted in laboratory conditions in the long-wave infrared ($7.7\mu m$ to $11.8\mu m$ - LWIR), with a LWIR-macro lens (to improve spatial resolution), an Infragold plate, and a heating source. The process began with a method to calculate the continuum removal. The approach is the application of Non-negative Matrix Factorization (NMF) to extract Rank-1 NMF and estimate the down-welling radiance and then compare it with other conventional methods. The results indicate successful suppression of the continuum from the spectra and enable the spectra to be compared with spectral libraries. Afterwards, to have an automated system, supervised and unsupervised approaches have been tested for identification of pyrope, olivine and quartz grains. The results indicated that the unsupervised approach was more suitable due to independent behavior against training stage. Once these results obtained, two algorithms were tested to create False Color Composites (FCC) applying a clustering approach. The results of this comparison indicate significant computational efficiency (more than 20 times faster) and promising performance for mineral identification. Finally, the reliability of the automated LWIR hyperspectral infrared mineral identification has been tested and the difficulty for identification of the irregular grain's surface along with the mineral aggregates has been verified. The results were compared to two different Ground Truth(GT) (i.e. rigid-GT and observed-GT) for quantitative calculation. Observed-GT increased the accuracy up to 1.5 times than rigid-GT. The samples were also examined by Micro X-ray Fluorescence (μXRF) and Scanning Electron Microscope (SEM) in order to retrieve information for the mineral aggregates and the grain's surface (biotite, epidote, goethite, diopside, smithsonite, tourmaline, kyanite, scheelite, pyrope, olivine,

and quartz). The results of μXRF imagery compared with automatic mineral identification techniques, using ArcGIS, and represented a promising performance for automatic identification and have been used for GT validation. In overall, the four methods (i.e. 1.Continuum removal methods; 2. Classification or clustering methods for mineral identification; 3. Two algorithms for clustering of mineral spectra; 4. Reliability verification) in this thesis represent beneficial methodologies to identify minerals. These methods have the advantages to be a non-destructive, relatively accurate and have low computational complexity that might be used to identify and assess mineral grains in the laboratory conditions or in the field.

Contents

List of Tables

List of Figures

Abbreviations

ACE: Adaptive Coherence/Cosine Estimator.

AES: Atomic Emission Spectrometry.

ADMM: Alternating Direction Method of Multipliers.

AISA: Airborne Hyperspectral Imaging Systems.

ALI: Advanced Land Imager.

AMD: Acid Mine Drainage.

AMF: Adaptive Matched Filter.

AMSD: Adaptive Matched Subspace Detector.

ANN: Artificial Neural Networks.

AOTF: Acousto-Optic Tunable Filter.

ASD: Analytical Spectral Device.

ASI: Italian space agency.

ASTER: Advanced Spaceborne Thermal Emission and Reflection Radiometer.

AVIRIS: Airborne Visible / Infrared Imaging Spectrometer.

BB: Blackbody.

BC: Band Combination.

BLU: Bayesian Linear Unmixing.

BRDF: Bidirectional Reflectance Distribution Function.

CASI: Compact Airborne Spectrographic Imager.

CFAR: Constant False Alarm Rate.

CEM: Constrained Energy Minimization.

CLoPF: Crude Low Pass Filter.

CO: Carbon Monoxide.

CO_2: Carbon Dioxide.

CPCs: Compound Parabolic Concentrators.

CR: Continuum Removal.

CRISM: Compact Reconnaissance Imaging Spectrometers for Mars.

CSSP: Clustering Signal Subspace Projection.

CWA: Continuous Wavelet analysis.

DCE: Double Cat's Eye.

DEM: Digital Elevation Models.

DPCA: Directed Principal Component Analysis.

DWT: Discrete Wavelet Transform.

EDAX: Energy Dispersive X-ray Spectroscopy.

ECD: Elliptically Contoured Distributions.

EEA: Endmember Estimation Algorithm.

EELS: Electron Energy-Loss Spectroscopy.

EIAs: Endmember Identification Algorithms.

ELM: Extreme Learning Machine.

EnMAP: Environmental Mapping and Analysis Program.

EO1: Earth Observing-1.

ETM+: Enhanced Thematic Mapper+.

FCC: False Color Composites.

FFT: Fast Fourier Transform.

FD: First Derivative.

Fe: Fayalite.

FPGA: Field-programmable gate array.

FRK: Fixed Rank Kriging.

FIR: Far Infrared.

FIRST-MWE: Ffield-portable Imaging Radiometric Spectrometer Technology Mid-Wave Extended.

FIRST HYPER-CAM: Field-portable Imaging Radiometric Spectrometer Technology-Hyper-Camera imaging spectroradiometer.

FOV: Field Of View.

FRQ-NT: Fonds de Recherche du Québec - Nature et Technologies.

FT-IR: Fourier-Transform Infrared.

FTS: Fourier-Transform Spectrometer.

FWHM: Full Width at Half Maximum.

GA: Genetic Algorithms.

GASMET: Global solutions for Gas Monitoring.

GAMLR: GA-Multiple Linear Regression.

GENE-AH: Geometry-based Estimation for Number of Endmembers- Affine Hull.

GENECH: Geometry-based Estimation for Number of Endmembers- Convex Hull.

GERB : Geostationary Earth Radiation Budget.

HIS: Hyperspectral imaging.

HHT: Hilbert-Huang Transform.

HiRISE: High Resolution Imaging Science Experiment.

HS: Hyperspectral Data.

HSV: Hue-Saturation-Value.

HyspIRI: NASA Hyperspectral Infrared Imagery.

ICA: Independent Component Analysis.

ICP-ES: Inductively coupled plasma-emission spectrometry.

ICP-MS: Inductively coupled plasma-mass spectrometry.

ILDs: Interior Layered Deposits.

IIM: Interference Imaging Spectrometer.

InSAR: Interferometric Synthetic Aperture Radar.

IOCG: Olympic Dam iron Oxide-Copper-Gold.

IPSE: Italian Package for Scientific Experiments.

IRMA: Infrared Microscope Analysis.

IVA: Independence Vector Analysis.

JPL: Jet Propulsion Laboratory.

LIBS: Laser-Induced Breakdown Spectroscopy.

LiDAR: Light Detection and Ranging.

LSU: Linear Spectral Unmixing.

LWIR: Long-Wave Infrared.

M3: Moon Mineralogy Mapper.

MAGI: Mineral and Gas Identifier.

MAP: Maximum A Posteriori-probability.

MCA: Morphological Component Analysis.

MCBC: Maximum Correlation Band Clustering.

MCR-ALS: Multivariate Curve Resolution-Alternating Least Squares.

MESMA: Multiple Endmember Spectral Mixture Analysis.

MF: Matched Filter.

MICA: Material Identification and Characterization Algorithm.

MIR: Mid-Infrared.

MIVIM: Tire 1 - Canadian research chair in Multipolar Infrared Vision.

MLE: Maximum Likelihood Estimates.

MMCA: Multichannel Morphological Component Analysis.

MMD: Maximum-Minimum apparent emissivity Difference.

MNF: Minimum Noise Fraction.

MODIS: Moderate Resolution Imaging Spectroradiometer.

MPLS: Modified Partial Least Squared.

MRSFF: Multi Range Spectral Feature Fitting.

MSS: Multispectral Scanning System.

MOPSO: Multi-Objective Particle Swarm Optimization.

MTMF: Mixture-Tuned Matched-Filtering.

μXRF: Micro X-ray fluorescence.

NASA: National Aeronautics and Space Administration.

NAPC: Noise Adjusted Principal Components.

NEM: Normalized Emissivity Method.

NHI: Neighborhood Homogeneity Index.

NIMS: Near Infrared Mapping Spectrometer.

NIR: Near-Infrared.

NormXCorr or **NoXCorr**: Normalized Cross Correlation.

NMF-GD: Non-Negative Matrix Factorization Gradient-Descent-based multiplicative rules.

NMF-NNLS: Non-Negative Matrix Factorization Non-Negative Least Squares.

NNFCLS: Non-Negativity Fully Constrained Least Square.

NNs: Neural Networks.

NRMSD: Normalized Root Mean Squared Deviation.

OMEGA: Observatoire pour la Minéralogie, l'Eau, les Glaces et l'Activité.

OSP: Orthogonal Subspace Projection.

PC-DFA: Discrimination Function Analysis.

PCA: Principal Component Analysis.

PCC: Pearson's Correlation Coefficient.

PIMA II: Portable Infrared Mineral Analyzer II.

PLMF: Local Matched Filter.

PLS: Partial Least-Squares.

PLSR: Partial Least Squares Regression.

PPI: Pixel Purity Index.

RATIO: Ratio algorithm.

RBD: Relative Absorption Band-Depth.

REE: Rare Earth Elements.

RF: Radio Frequency.

RIM: Regression Intersection Method.

RMSE: Root Mean Squared Error.

RSBR: Reference Spectral Background Removal.

SAM: Spectral Angle Matching.

SASI: Spectrographic Imager.

SCA: Sparse component analysis.

SEM: Scanning Electron Microscope.

SEBASS: Spatially Enhanced Broadband Array Spectrograph System.

SEVIRI: Spinning Enhanced Visible and Infrared Instruments.

SID: Spectral Information Divergence.

SIMBIO-SYS: Spectrometers and Imagers for BepiColombo Integrated Observatory-System.

SIMPLE-Pro: Simplex Estimation by Projection.

SIPS: Spectral Image Processing System.

SMA: Spectral unMixing Analysis.

SML: Supervised Metric Learning.

SNR or **S/N**: Signal-to-Noise Ratio.

SOM: Soil Organic Matter.

SPCA: Sparse Principle Component Analysis.

SPC1: First Sparse Principal Component.

SSPP: Spatial-Spectral PreProcessing.

ST: S-Transform.

STC: Stereo Camera.

stereo: photogrammetric-derived.

SVM: Support Vector Machine.

SVMR: Support Vector Machine Regression.

TASI: Thermal Airborne Spectrographic Imager.

TES: Mars Global Surveyor Thermal Emission Spectrometer.

TES: Temperature and Emissivity Separation.

THEMIS: Mars Odyssey Thermal Emission Imaging System.

THIRSPEC: Field-Portable Thermal Infrared Grating Spectrometer.

TIMS: Thermal Infrared Multispectral Scanner.

TPH: Total Petroleum Hydrocarbons.

TRI-P: Pure Pixel Identification.

TRUST: Thermal Remote sensing Unmixing for Sub-pixel Temperature.

USGS: United States Geological Survey.

UV: Ultraviolet.

VNIR: Visible-Near-Infrared.

VIHI: Visible-Near Infrared Hyperspectral Image.

VIMS: Visual and Infrared Mapping Spectrometer.

VIS: SWIR and Visible.

VisNIR DRS: Visible Near Infrared Diffuse Reflectance Spectroscopy.

XRD: X-Ray Diffraction.

XRF: X-ray Fluorescence.

Acknowledgments

I would like to express my sincere gratitude to Prof. Xavier P. V. Maldague and many thanks for his guidance, supports, his patience, and tolerance. He has driven me forward on my research and was always there for me. I am also enormously thankful to Prof. Georges Beaudoin for his constructive supports and comments. His presence provided a great momentum toward the geological direction, the place where I needed more guidance and support.

I would like to sincerely thank Dr. Clemente Ibarra Castanedo at Department of Electrical and Computer Engineering, Laval University for his continuous support and sharing his valuable experience, and gave me lots of knowledge related to infrared thermography and guided me throughout this project. I am truly appreciate and tremendously grateful to Dr. Annette Schwerdtfeger, from the Department of Electrical and Computer Engineering at Laval University, for all of her efforts, constructive comments, and help.

I appreciate all the efforts and considerations in members of Computer Vision and System Laboratory (CVSL) and Department of Electrical and Computer Engineering, Laval University and their respected professors, management office and staffs for their support throughout my research work, particularly Denis Ouellet who helped me in numerous matters and for his positive energy in everything. I cherish all the moments of my research in Multipolar Infrared Vision - Vision Infrarouge Multipolaire: MIVIM Canada Research Chair-tier 1.

Also I give a big thanks to my colleagues in E4M particularly Émilie Bédard for her mineral grains preparation, experiments arrangement and many other preparations plus providing the reports of my results. I thankfully acknowledge the efforts of my team-members and former colleagues of mine: Saeed Sojasi and Kévin Liaigre at Laval University for their help in different parts of the project. I also acknowledge Dr. Martin Chamberland vice-president at Telops Inc. for his countless help and collaboration.

Last but not least, I would like to thank my family and friends especially my lab-mates (Lei Lei, Mana Eskandary, Hossein Memarian Sharifipour, Julien Fleuret, Patrick Deschênes Labrie, Arman Afrasiyabi, Hai Zhang, Fang Qiang) for putting up with me and constant support, patience and continuous encouragements.

Foreword

This thesis is submitted to the "Faculté des études supérieures et postdoctorales-Université Laval" to fulfill the requirement of the Philosophiae Doctor (Ph.D.) degree in Electrical Engineering.

The presented thesis is consisted of eight chapters along with appendices. The first chapter is an Introduction mentioned after foreword and then literature review in second chapter where it over-viewed the infrared hyperspectral and spectroscopy applications in relevant fields, including hyperspectral infrared spectroscopy for geological and mineralogical approaches, geology-astronomy applications, earth sciences and mineralogy, a very brief reviewing of hyperspectral unmixing techniques and endmember estimation, and portable instrument. Following this chapter, the third chapter highlighted the problems, hypothesis and objectives.

Chapter four to seven are in the form of journal article, several approaches and experiments were conducted in long wave infrared band an approach for spectral preparation and continuum removal (four) and followed by other chapters (five to seven) for different approach of automated mineral identification, includes their results and their discussions accordingly. At the end, the results obtained in the current thesis are concluded, chapter eight presents a general conclusions and provided the perspective of the future of the performed studies.

The first article in the 4th chapter is titled **Continuum removal for ground based LWIR hyperspectral infrared imagery applying non-negative matrix factorization**, was submitted for Applied Optics journal, 2018, Authors: Bardia Yousefi, Saeed Sojasi, Clemente Ibarra Castanedo, Xavier P.V. Maldague, Georges Beaudoin, Martin Chamberland.

The second article presented in the 5th chapter titled **Automatic Mineral Identification using Ground-based Hyperspectral LWIR Infrared Spectral Analysis and Extreme Learning Machine**, Authors: Bardia Yousefi, Saeed Sojasi, Clemente Ibarra Castanedo, Xavier P.V. Maldague, Georges Beaudoin, Martin Chamberland.

The third article in the 6th chapter is titled **Comparative clustering analysis applying K-means rank^1-NMF and FCC on mineral identification in long wave hyperspectral infrared imagery**, Authors: Bardia Yousefi, Saeed Sojasi, Clemente Ibarra Castanedo,

Xavier P.V. Maldague, Georges Beaudoin, Martin Chamberland.

Finally, the fourth article in 7th chapter which is titled **Automated LWIR Hyperspectral Infrared mineral identification reliability** and is submitted for Applied Optics journal, 2018, Authors: Bardia Yousefi, Clemente Ibarra Castanedo, Xavier P.V. Maldague, Georges Beaudoin.

Bardia Yousefi was in charge of designing and implementing the proposed algorithms and a part of data collection for all experiments. He was also responsible for designing and analyzing the statistical calculations of the collected data and preparation of the manuscripts. Prof. Xavier P.V. Maldague and Prof. Georges Beaudoin, research supervisor and co-supervisor, oversaw all steps of this work in which Prof. Georges Beaudoin provided the idea for studies for applications of infrared hyperspectral imagery for mineral indicators and Prof. Xavier P.V. Maldague guided the process. Dr. Clemente Ibarra Castanedo along with Dr. Martin Chamberland designed the experiments in long wave infrared and prepared the hyperspectral camera. Dr. Castanedo also provided the scientific support throughout the project. Émilie Bédard was involved in the preparation of the minerals and designing of our last experiment. Saeed Sojasi and Kévin Liaigre worked for part of the data validating and performing the experiments.

Furthermore, the candidate has presented this research in several different scientific conferences such as International Congress on Thermal Infrared Applications XXXVIII (Thermosense), May 2016, Baltimore, USA; TELOPS Scientific Workshop, September 2016, Baltimore, USA; Quebec-Mines 2016, Quebec city, Canada; the 14th International Workshop on Advanced Infrared Technology and Applications, AITA 2017 and the 2nd Asian Conference on Quantitative InfraRed Thermography (QIRT-Asia 2017), July, 2017, Daejeon, Republic of Korea.

During the period of receiving Ph.D., the candidate co-authored one article in Thermosense 2016:
Saeed Sojasi, B. Yousefi, Clemente Ibarra Castanedo, Georges Beaudoin, Xavier P. V. Maldague, François Huot, Martin Chamberland, titled **Role of discrete wavelet transform in mineral identification using hyperspectral imaging in the long-wave Infrared (7.7 to 11.8 μm) by using SVM classifier**, Thermosense -SPIE 2017, Anaheim, California, United States.

Also our manuscript in QIRT-Asia 2017 was pre-selected for QIRT journal publication titled **Mineral Identification in LWIR Hyperspectral Imagery Applying Sparse Spectral Clustering**. This manuscript's title is modified for QIRT journal to **Mineral Identification**

in **LWIR Hyperspectral Imagery Applying Sparse based Clustering**.

Chapter 1

Introduction

Hyperspectral imagery has recently been considered as one of the important active research area which involves many researchers in different fields. This technique provides a wealth of spectral information and has been successfully applied in various domains such as environmental monitoring, satellite imagery, agriculture and mineralogy. Remote sensing data normally suffers due to low spatial resolution in the hyperspectral sensor. This creates critical problems in the interpretation of hyperspectral data and the overall accuracy of the analysis. But nowadays the instruments used for spectroscopy have been developed to create good opportunities and provide precise measurements in the different infrared wavelength. Thereby giving better spectral and spatial emissivity information from the surface of materials. The automatic/semi-automatic/ non-automatic approaches in the identification of minerals are extensively related to this information. One of the critical elements in hyperspectral mineralogy relates to identifying the endmember which is the best representative for the mineral group. High categorization ability requires an adjustment of the spectral information. However, categorization based on chemical and physical properties themselves provide a reasonable outcome. A hyperspectral image contains detailed information recorded from the reflection of the energy source in the spatial position (in hyperspectral remote sensing the energy source is solar energy, whereas in the laboratory situation it is the heating element). hyperspectral becomes a technique for the identification of various materials according to their spectral fingerprint. However, due to non-uniform radio-metrical conditions in the laboratory and rough spatial resolution and many other factors, most of the pixels are composed of several different ground materials which are known as mixed pixels or mixtures. This influences the image classification and mineral identification performance. However, the extraction of abundance fractions from pure materials, a spectral unmixing known as an endmember [1] within a pixel has been developed as a solution of such mixed-pixel problems. But before going into the identification of minerals, there is an issue which is more concerned with the reflection from the mineral grains that is a radiometric property within visual observation in acquisition. This matter concerns the

---

[1]An endmember in mineralogy is a mineral that is at the extreme end of a mineral series in terms of purity.

current research at the initial steps to retrieve the emissivity of reflection information so as to conduct a comparison among the hyperspectral libraries (i.e. ASTER/JPL (Baldridge et al. 2009)). The information obtained is highly sensitive to certain parameters in the experimental setup such as non-uniformity of thermal exposure, acquisition angles and many similar other parameters. It controlled to minimum the influence and disruption on the data. For the past three decades, spectrometric imaging has been used to provide necessary information in the field of mineralogy and geology (Goetz 2009). The community of hyperspectral remote sensing has developed general datasets which are considered to be reasonably similar to the collection of the spectral libraries in the laboratory or field. The generated hyperspectral data can support the hyperspectral analysis and information extraction through the development of the algorithms. The signature of the natural materials present in such spectral libraries provides opportunities for feature extraction and classification techniques to be applied to imagery and thereby define the spectral endmembers as inputs or ground truths for comparison among the spectra. The number of spectral libraries is increasing and the publicly available libraries are widely used in the applications of hyperspectral image analysis. Direct comparison of the spectra attained from materials and with the spectra available in the libraries is influenced by the disparities of illumination and viewing measurement (Rivard et al. 2008). In this study, a laboratory spectroscopy has been conducted along with computational algorithms to identify the mineral samples automatically. The paradigm follows several pure mineral grains on the specific substrate and spectroscopy processes have then been conducted based on an active thermography scenario which was involved heating an element in front of the hyperspectral camera. Two experiments have been conducted in different resolutions and heating conditions. One of the stages of analysis comprised the emissivity retrieval which is one of the vital steps of the spectral analysis and provided continuum removal similar property to the spectra. The analysis of mineral identification has required a spectral reference which included several analysis such as decomposition and supervised and unsupervised learning algorithms to make the mineral identification automated.

The main objective of the present thesis was to create a tool for using hyperspectral infrared imagery data and process the data through image analysis and machine learning methods to identify small size mineral grains used as mineral indicators. This research has striven to develop a contribution in providing segmentation and automated mineral identification using data-mining and machine learning approaches.

Chapter 2

Literature Review

Hyperspectral infrared imagery is defined as the sensing of reflected, scattered or emitted heat from the targeted surface by any source such as the sun or a heating element, which have electromagnetic or thermal content. Hyperspectral infrared imagery is one of the latest infrared imaging technologies which was created by developments in infrared acquisition in different spectral band and obtained by concatenation of these images. Hyperspectral imaging measures contiguous spectra unlike Multispectral Scanning System (MSS) which measures spaced spectral bands. The signature in the hyperspectral imaging is considered at the molecular level while the photon scattering and absorption and it can be distinguished due to the mineral's characteristics and chemical properties (chemical bond between molecules). The images are combined to form a three-dimensional data cube, where the first two dimensions represent the spatial information (spatial resolution) and the third dimension designates the spectral information (spectral resolution). The spectral range in the hyperspectral sensors is dependent on the characteristics of the sensor and most of the time spectral and spectral resolution have a relationship between each-other, increasing in one of them decreases the other one.

Hyperspectral imagery has been considerably developed during the recent decades and its applications with infrared thermography have been the subject of several studies in different fields (Goetz, 2009). This variety provides remarkable researches and contributions in different areas (i.e. geology/mineralogy, remote sensing, optics, infrared and thermography, computer science, and optimizations).

Mineralogy has been an intriguing subject in geology from the very beginning (Borie, 1965; Adams, 1975; Farmer, 1974; Hunt, 1977; Nash and Conel, 1974; Gamble, 1972; Kinsey, 1977; Preissler and Loercher, 1995), and has been carried out through manual categorization of minerals by the experts or using an automated system (later). Even after the development of spectroscopy instruments (Herrmann and Onkelinx, 1984; Siegbahn and Axel, 1966), the process of mineral recognition has been done by manual spectral categorization. After the development of computer-aided applications for mineral identification, many automated /semi-automated techniques were developed (i.g. Kruse, 1996a, 2012; Kruse et al., 1993a). The

hyperspectral mineral identification process is based on comparison of a Region Of Interest (ROI) spectra in the mineral hyperspectral image with a targeted spectrum available from the Advanced Space-borne Thermal Emission and Reflection Radiometer (ASTER)/Jet Propulsion Laboratory (JPL) (Baldridge et al., 2009) or the United States Geologic Survey (USGS) (Clark et al., 2007) mineral libraries, or mineral sample's spectra that are known (e.g. Yousefi et al., 2016a).

The application of hyperspectral imagery in remote sensing is also very common and involves the identification or analysis of possible mines (Zabcic et al., 2014; Koch et al., 2017) or particular targets (Zhang et al., 2014; Jin et al., 2009; Chang et al., 2000), drill core analysis (Speta et al., 2013), urban area development (Kotthaus et al., 2014) and different types of mapping (Cui et al., 2015; Xiaojia et al., 2010) or even the hyperspectral image from other planets in order to identify particular minerals or the existence of life (Ehlmann et al., 2011; Capaccioni et al., 2001; Gou et al., 2015; Smith et al., 2013). In contrast to the wide diversity of hyperspectral imagery's applications, the basic technique for hyperspectral mineral identification follows only one principle which involves finding the difference between the targeted and reference spectra. Consequently the hyperspectral mineral identification research is divided into several categories:

- The approaches based on the geological and mineralogical points of view;

- Endmember Estimation Algorithm (EEA) methods which use the estimation of the endmember as the reference spectrum and then carry out a hyperspectral unmixing process which gives a recognition profile of the mineral spectra.

- Mineral mapping methods which usually involve finding the targeted mineral reference spectrum and then applying the spectral comparison methods to segment the hyperspectral images. Here, the application of hyperspectral imaging for mineral identification is briefly reviewed. The research in this field is vast and a review requires the categorization in terms of similarity of the applications, techniques or wavelengths.

2.1   Infrared spectroscopic and hyperspectral imagery

Infrared spectroscopic and hyperspectral imagery follow developments in infrared, optical and instrumental methods (Herrmann and Onkelinx, 1984; Siegbahn and Axel, 1966). In this section the hyperspectral analysis regarding the geology/mineralogical techniques are briefly reviewed.

2.1.1   Spectroscopy

Spectroscopy is defined as the analysis and study of light as a function of wavelength. Light is normally reflected, emitted or scattered from a gas, liquid, or solid. A summary of mineral spectroscopy and its principle applied to a variety of materials is briefly discussed in this

section (Adams, 1975; Farmer, 1974; Clark and Roush, 1984; Clark et al., 1990; Gaffey et al., 1993; Hunt, 1977, 1982; Salisbury, 1993).

2.1.2 Scattering and Absorption

When a mineral is exposed to photons, some photons enter into the mineral, some pass through the grain, a few are absorbed, and some are reflected from the surfaces of the grains. The reflectance or refraction of photons through a particle from the surface of the grain is called scattered photons. Scattered photons may encounter another grain's surface or be scattered away from the surface so they might be detected by the instrument and to be measured. There are certain photons which originate from the surface and are referred emission. Normally all of the surfaces which have a natural origin emit photons when they are above absolute zero temperature. This emission is subject to the physical laws of refraction, reflection, and absorption. Absorption of the photons in minerals depends on several conditions. The variation in absorption level and its dependence on wavelength can provide the information on mineral chemical properties by the light which is emitted and reflected.

2.1.3 Spectroscopy terms

Spectrometry [1] is derived from spectro-photometry and the wavelength function and has been used to measure photons for years. The capability of a spectrometer is described by four parameters:

i) Spectral sampling;

ii) Spectral bandwidth;

iii) Signal-to-Noise Ratio (SNR);

iv) Spectral range which is important to cover sufficient analytic spectral absorptions as a solution for the desired problem.

There are normally lower spectral details and resolution systems between the remote sensing and laboratory spectrometry. Sampling conducted at greater than 25 nm quickly leads to a loss of the absorption of the minerals. The Near Infrared Mapping Spectrometer (NIMS) and the Visual and Infrared Mapping Spectrometer (VIMS) systems measure out to 5 μm, and consequently the absorption bands can be seen (the band-pass profile shape is also important). Every channel of a spectrometer ideally refuses all light apart from the desired particular narrow wavelength range; however due to optical influences, light may occasionally leak in from beyond the band-pass (e.g. insufficient blocking filters, or spreading inside the optical system). The Gaussian profile is the most common band-pass in spectrometry (Hagen et al., 2007; Guo, 2011). The optical system aberrations usually smear for a profile close to the Gaussian shape while the designs of specific spectrometers are theoretically well-defined in band-pass profiles.

---

[1] "Imaging spectroscopy has many names in the remote sensing community, including imaging spectrometry, hyperspectral, and ultraspectral imaging" from the USGS library (Clark et al., 2007).

The band-pass width is usually defined as the wavelength width at 50% of the function response level named as Full Width at Half Maximum (FWHM) (Weisstein, 2017). The distance between the wavelengths of the spectral band-pass profile for every spectrometer channel is considered as the spectral sampling which is often confused with band-pass. According to the Nyquist theorem, the maximum of the information obtained from the sampling in one-half the FWHM, in the spectrometers are designed with a ratio of half-Nyquist (Grenander, 1959; Mishali and Eldar, 2010) amount. The precision of recording in the spectrometer and the SNR (Johnson, 2006) are important factors in solving the particular problem depending on the detector sensitivity, intensity of light reflected or emitted from the surface, and the spectral bandwidth (Swayze, 1997).

2.1.4   Imaging Spectroscopy

The specific chemical bonds in materials of all types and forms such as solid, liquid and gas, are related to the emittance and reflectance spectroscopy of natural surfaces. The spectrometers or hyper-cameras are used for application in the laboratories, as in the case of our research, or for applications in the field, in aircraft (looking downwards or upwards), or in satellites and remote sensing. Spectroscopy is a sensitive method to analyze the amorphous and crystalline materials which considers the advantage of such a method over diagnostic methods such as X-ray diffraction (Borie, 1965; Gamble, 1972). It also can be used in different distance ranges. For example here we use it under laboratory conditions, while it can also be used in the observation of the Earth or even to look up at other planets. The disadvantage of spectroscopy is its sensitivity to small changes in the chemical content and structure of materials. The change in material composition regularly shifts the position and shape of the absorption spectral bands. The vast variety of chemical characteristics is met in the real world and spectral signatures can sometimes be unintelligible or quite complex. These changes increase the variation and knowledge in spectral features and the causes of their shift. The previous drawback becomes into a very substantial advantage, providing more details on chemical properties in the natural environment. Following the development of detectors and computer technology, spectroscopy entered into a new field of research and facilitated spectral analysis (Goetz et al., 1985; Vane et al., 1993; Green, 1992; Mustard and Sunshine, 1999; Kruse, 1999). The spatial positions in imaging spectroscopy represent the spectra related to that spatial information that can be used to provide a recognizable image which can be a rock of any mineral in the laboratory, or in field applications involving aircrafts, satellites, spacecrafts or Earth-based telescopes. By analyzing the spectral features and specifications in the chemical bonds of the materials, the researchers can generate the map representing the properties of the materials.

2.2 Hyperspectral technology in astronomy

2.2.1 Lunar hyperspectral research

Hyperspectral research has been used for space geological research for a several years (Goetz, 2009). Here, a brief summary of such research is presented (see Table 2.1 - for a review summary). A synthetic powder mixture of ilmenite, plagioclase, and pyroxene constituting the major material phase for the lunar surface materials has been presented by Nash and Conel, 1974. Some parameters such as band depth, albedo [2], and blue to red ratios versus the composition of the mixture reveal that each mineral phase concentration in the mixture influences the spectrum reflectance. Two major effects of principle mixing are: the persistence concentration proportionality of the 1μm band of pyroxene and the depth versus darkening which is inconsistent from opaque Ilmenite. The results show the ability to determine the crystalline phase ratio in a material from the spectra telescopically obtained from lunar or other planet surfaces. Hyperspectral research was also conducted on Saturn through Phoebe spectroscopy imaging resulting from the Cassini-Huygens spacecraft on 11 June 2004. The results revealed the presence of organics, ferrous-iron-bearing minerals, trapped CO_2, bound water, probable phyllosilicates, nitriles and cyanide compounds which are the most compositionally diverse objects ever observed (Clark et al., 2005). A lunar mineralogical research has been conducted for mineral mapping of the lunar surface for abundance of olivine, plagioclase, and clinopyroxene. The wavelength covered was $480-960nm$ for Interference Imaging Spectrometer (IIM) of Chang'E-1 with 32 bands and applying the modified Multiple Endmember Spectral Mixture Analysis (MESMA) (Shuai et al., 2013). Moreover, a smooth surface inferred from the Digital Elevation Models (DEM) for the impact melt flows and ponds, and Moon Mineralogy Mapper (M3) study and the Lunar Prospector data from Gamma Ray Spectrometer instrument has been conducted by Wöhler et al., 2014.

---

[2]Albedo is defined as the ratio of light reflected by a planet or satellite to that received by it.
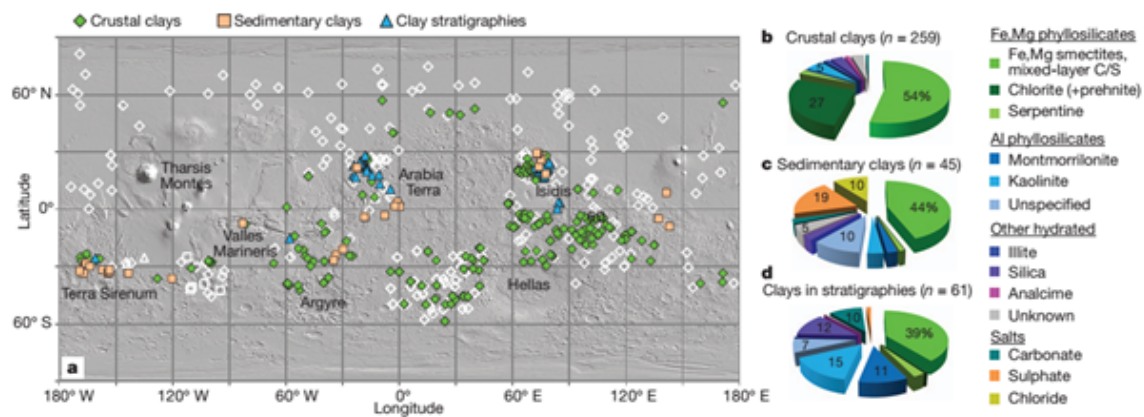
Figure 2.1: The distribution of Clay mineral on Mars. This map was generated by the geologist and surveyed for the clay mineral presence with respect to by geological setting (Figure is taken from Ehlmann et al., 2011).

2.2.2   Hyperspectral research in Mars

The observation of clay minerals shows the long duration of the interaction between the water and rock for over 3.7 billion years which was more recently discovered on Mars's Noachian terrains (Amos, 2012; Tanaka, 1986; Carr and Head, 2010; Mustard et al., 2008). They have basically used spectroscopic images, a Compact Reconnaissance Imaging Spectrometer for Mars (CRISM) and the Observatoire pour la Minéralogie, l'Eau, les Glaces et l'Activité (on Mars Express (OMEGA) visible/near-infrared orbital imaging spectrometers (Mustard et al., 2008). The images were taken by spectrometers on-board the Mars Reconnaissance and Mars Express Orbiter spacecraft, respectively. They have shown thousands of outcrops with clay minerals from the planet's southern highlands (Mustard et al., 2008) and northern lowlands (Ehlmann et al., 2011; Mustard et al., 2008; Carter et al., 2010) (Figure 2.1).

Infrared Microscope Analysis (IRMA) involves hyperspectral imaging spectrometers which can quantitatively characterize the mineral and the microphysical structure in Martian rocks and soils as a part of the sampling mechanism. This type of spectrometer has $38 \sim tm$ in the 0.8-5 lxm infrared spectral range spatial resolution. The Italian Space Agency (ASI) selected the experiment as an Italian framework to participate in NASA's surveyor program. The ill-fated Mars 2001 in a mission called Mars sample return [3], IRMA and IPSE [4] details information regarding Martian material obtained. It includes the microphysical texture and characteristics of the grains and mineralogical composition with no accuracy of 1% and a very high SNR. The information provided the physical and chemical assessment of environmental conditions on the surface of Mars (Capaccioni et al., 2001). Also mineral identification on the Gale crater on Mars using near infrared spectral data from CRISM on board the Mars Reconnaissance Orbiter (MRO) with enhancement in its spectral resolution provided information on a spatial and time scale. The identification for mineral classes at the Martian Gale region was conducted by analysis of the features using SAM which gave the identity of some minerals such as jarosite, northupite, smectite, chlorites, and kaolinite (Xue and Jin, 2013). Thermal-infrared and near-infrared spectroscopy was used to verify the degree of relativity for bulk SiO_2 (less diversity) and crystallinity abundance on Martian surfaces having hydrated silica, including non-crystalline (hydrated glass) to weakly crystalline (opal) to crystalline (quartz) having a silica deposit (Smith et al., 2013). An analysis of Interior Layered Deposits (ILDs) was conducted using the instruments on board the Mars Odyssey, NASA's Mars Global Surveyor, ESA's Mars Express spacecraft and Mars Reconnaissance Orbiter for Iani Chaos involving topographic and visible-infrared hyperspectral datasets. Data from HRSC and CRISM (with infrared (1.0-4.0μm) and visible/NIR (0.36-1.07μm) detectors) suggests kieserite and gypsum (minerals such as jarosite and alunite) are present in most of the deposits on the surface of Mars (Sefton-Nash et al., 2012). The Mars Global Surveyor Thermal Emission Spectrometer

---

[3]No Mars sample return mission has taken place yet. So far there have been Mars Exploration Rover missions to prepare for a Mars sample return mission.

[4]the Italian Package for Scientific Experiments (IPSE).

Spectroscopy and Hyperspectral imagery for astronomy

Paper	System Used	Application	Location (if available)
Goetz et al. (2009)	Hyperspectral research	space geological research for decades	
Nash & Conel (1974)		synthetic powder mixture of Ilmenite, plagioclase, and pyroxene that are, major material phase types virtually for the lunar surface materials	Moon
Clark et al. (2005)	Phoebe spectroscopy imaging	organics, ferrous-iron-bearing minerals, trapped CO_2, bound water, probable phyllosilicates, nitriles and cyanide compounds mapping	Saturn
Ehlmann et al. (2011)	A review	distribution of Clay mineral	Mars
Mars's Noachian terrains : Amos (2012), Tanaka (1986), Carr (2010), Mustard et al. (2008)	Spectroscopic images, Compact Reconnaissance Imaging Spectrometer for Mars (CRISM) and Observatoire pour la Minéralogie, l'Eau, les Glaces et l'Activité (on Mars Express (OMEGA) visible/near-infrared orbital imaging spectrometers	observation of Clay minerals	Mars
Ehlmann et al. (2011) , **Carter** et al. (2010), **Mustard** et al. (2008)	The Mars Reconnaissance Orbiter CRISM instrument visible/near-infrared orbital imaging spectrometers	clay minerals	northern lowlands, southern highlands, Mars
Bannon (2009)	Spatial and spectral information combination	chemical content of the materials	
Capaccioni et al. (2001)	Infrared Microscope Analysis (IRMA) is hyperspectral imaging spectrometers	characterize the mineral and the microphysical structure soil analysis	Mars
Shuai et al. (2013)	480–960 nm for Interference Imaging Spectrometer (IIM) of Chang'E-1 with 32 bands and applying the modified Multiple Endmember Spectral Mixture Analysis (MESMA)	mineral mapping for abundance of olivine, plagioclase, and clinopyroxene	Moon
Wohler et al. (2014)	Gamma Ray Spectrometer	Moon Mineralogy Mapper (M3) study	Moon
Clark et al. (2005)	Phoebe spectroscopy	ferrous-iron-bearing minerals, trapped CO_2, bound water, probable phyllosilicates, nitriles and cyanide compounds mapping	Saturn
Zambon et al. (2014)	Visible and Infrared (VIR) spectrometer	Mineral mapping	
van Ruitenbeek et al. (2014)	hyperspectral OMEGA imagery	mapping	Mars
Smith et al. (2013)	Thermal-infrared and near-infrared spectroscopy	verify the degree of relativity for bulk SiO_2 (less diversity) and crystallinity abundance of Martian surfaces having hydrated silica	Mars
Sefton-Nash et al. (2012)	HRSC and CRISM (contains infrared (1.0–4.0 µm) and visible/NIR (0.36–1.07µm) detectors)	Mineral mapping Kieserite, gypsum, jarosite and alunite	Mars
Viviano et al. (2013)	visible/near-infrared wavelength range	detection of phyllosilicates	Mars
Gou et al. (2015)	HiRISE images	Martian mineral analysis	
Fischer & Pieters (1994)	combination of near-infrared and visible spectroscopy	lunar soils Iron	Moon
Sgavett et al. (2007)	Stereo Camera (STC) with visible-near infrared and panchromatic filters plus a Visible-Near Infrared Hyperspectral Image (VIHI) with 400-2000 nm spectral range	geologic investigation	surface of Mercury
Xue et al. (2013)	near infrared spectral data from CRISM	mineral identification minerals such as jarosite, northupite, smectite, chlorites, and kaolinite	Mars

Table 2.1: A brief summary of spectroscopy and hyperspectral imagery for astronomy applications.

(TES) was used to analyze data from the Mars Odyssey Thermal Emission Imaging System (THEMIS) for the detection of phyllosilicates in the visible/near-infrared wavelength range and simultaneously investigate the effects of spatial resolution (Viviano and Moersch, 2013). The resolution of 100-m/pixel provided by THEMIS considerably enhanced the phyllosilicate detection likelihood. Martian mineral analysis derived from the Multiple Endmember Spectral Mixture Analysis (MESMA) indicated that the mineral abundance attained from HiRISE images and Mawrth Vallis: Al phyllosilicates and Fe/Mg phyllosilicates was conducted by (Gou et al., 2015). CRISM determines Martian surface reflectance spectra in the visible to near infrared (0.36-3.92μm) which showed that Al phyllosilicates such as hydrated silica, montmorillonite and kaolinite as well as Fe/Mg phyllosilicates like saponite, nontronite and serpentine are found on the light-toned outcrops.

A study in hyperspectral OMEGA imagery of Mars reports that the wavelength position of deepest absorption features mapping ranges between 2.1 and 2.4mm for mineral exploration diversity (van Ruitenbeek et al., 2014). The mentioned range of absorption features provides useful mineralogical information. A combination of near-infrared and visible spectroscopy for Iron concentration of lunar soils was studied by (Fischer and Pieters, 1994).

2.2.3 Hyperspectral research for other geological-astronomical applications

A Stereo Camera (STC) with visible-near infrared and panchromatic filters plus a Visible-Near Infrared Hyperspectral Image (VIHI) with 400-2000nm spectral range integrated into spectrometers and imagers for BepiColombo Integrated Observatory-System (SIMBIO-SYS) were used for a geological investigation on the surface of Mercury. Two sensors were used to evaluate the feasibility of determining the diagnostic spectroscopic features of rock for the formation of minerals and discriminating among different lithotypes considering the additional noise. For STC and S/N 1/4200, the low reflectance of the rock's surface can cause the band ratios to partly overlap. VIHI and S/N 1/4100 performed well to define the spectral features with the band depth of 0.1 reflectance unit. The band position shift gives less than 0.03 atoms/formula unit of spectrally active phases (Sgavetti et al., 2007). The Visible and Infrared (VIR) spectrometer on-board Dawn for mineralogical analysis of Vesta's surface [5]. They have used some spectral parameters such as band depths, band centers, and Band Area Ratio (BAR) for the pyroxene bands at $\sim$0.9 and $\sim$1.9μm. They have found that the band depths are related to the abundance of absorbing minerals and/or opaque materials; and it has positive correlation with albedo (Zambon et al., 2014).

2.3 Spectroscopy and Hyperspectral imagery for Earth Sciences and Mineralogy

2.3.1 Environmental analysis

Analysis of groundwater, soil, gas samplers and organic contamination is carried out Raman spectroscopy (Graves and Gardiner, 1989), infrared spectrometry and Laser-Induced Fluorescence (Kinsey, 1977). Using the situ near-infrared spectroscopy, the water types speciation in haplogranitic melts and glasses was determined by (Nowak and Behrens, 1995) and wildfires airborne infrared (Worden et al., 1997). An air monitoring system using Fourier-Transform Infrared (FT-IR) open-path for volcanic fumaroles gases monitoring was presented by (Chaffin et al., 1995). The infrared spectrometer includes an infrared field source and a $1 - mm$ 2

---

[5]Vesta means a giant object in asteroid belt, NASA's Dawn spacecraft mission in 2012.

Hg-Cd-telluride detector which was cooled down with liquid N_2. The monitoring techniques include passive and active techniques that analyze HC and SO_2 in volcanic plume gases. Gas monitoring using diode-laser-based NIR was described by (Martin and Fehér, 1996). This spectrometer was used to analyze the waste or atmospheric gases. The measurements can be made by applying extractive measurement and situ techniques and this research study provides information on the design details and sensitivity of the spectrometer.

Spectroscopy and Hyperspectral imagery for Earth Sciences and Mineralogy

Paper	System Used	Application	Location (if available)
Graves & Gardiner (1989)	Raman spectroscopy	Groundwater, soil, gas samplers and organic contamination analysis	
Kinsey (1977)	Infrared spectrometry and Laser-Induced Fluorescence (LIF)	Applications of the laser to various aspects of chemistry, physics, and biology	
Nowak & Behrens (1995)	Near-infrared spectroscopy	The water types speciation in haplogranitic melts and glasses	Nowak and Behrans
Worden et al. (1997)	Airborne infrared	Wildfires airborne infrared Worden and coworkers	
Chaffin et al. (1995)	Fourier-Transform Infrared (FT-IR) open-path	Volcanic fumaroles gases monitoring	
Martin & Feher (1996)	Diode-laser-based Near-Infrared (NIR)	The infrared spectrometer includes an infrared field source and a 1-mm 2 Hg-Cd-telluride detector that cooled down with liquid N2.	
Watson et al. (1996)	Free-flying hot-air balloons for carrying on the FT-IR spectrometers, multispectral imaging spectrometers, far- and mid-IR cameras, radiometers, forward-looking IR cameras, plus a variety of other sensors	Environmental analyzes	
Thompson & Reynolds (1978), Uden (1992)	Atomic Emission Spectrometry (AES) and FT-IR spectrometry	Chemical effluents detection, finding the contamination of Hg, stack testing, the various pollutants atmospheric concentration situ vertical profiling and multisite air quality monitoring	
Hammaker et al. (1995)	Remote FT-IR for monitoring	Atmospheric volatile organic compounds	
Griffin (1996)	Far-infrared spectroscopy	Study of planetary and extraterrestrial or terrestrial atmospheres	
Zwicker (1996)	Remote sensing FT-IR spectrometry	Forestry studies	North Carolina
Malley et al. (1996)	NIR	Quantitative and rapid assessment from Precambrian shiled lakes	Precambrian shiled lakes
Howell (1995)	NIR visible spectroscopy	Characterizing the composition of asteroid in the surface mineralogy	
Miller et al. (1995)	FT-IR spectroscopy	Characterize interfacial water species in situ at mineralogy hydrophobic surfaces.	
Camy-Peyret et al. (1995)	Remote sensing forms via balloon-borne	Analyze the atmosphere	
Blake et al. (1996)	Mid-infrared magnetic rotation spectrometer	Atmospheric free radicals assessment	
Yang (1994)	Short-wave infrared spectrometry	Oil and gas resources	
Gao et al. (1995)	An infrared micro-spectroscopy	Rapid identification of gemstones	
Franca et al. (1995)	Multispectral camera	Recording the biomass burning	West Africa
Fischer & Pieters (1994)	Near-infrared and visible spectroscopy	Iron concentration and exposure levels of lunar soils	
Riaza et al. (2001)	Hyperspectral imagery and spectral behaviour image processing	The textural and mineralogical processes associated with geo-morphological in the various granitic facies, mapping , estimation of spatial erosion controls and soil studies	laboratory condition
Meteosat-8 (2007)	Geostationary Earth Radiation Budget (GERB) and Spinning Enhanced Visible and Infrared Instruments (SEVIRI), Meteosat-8	Aerosols detection and radiative effect estimation at spatial and high temporal resolution which set in the Meteosat-8	Meteosat-8
MODIS (2017)	longwave and shortwave fluxes, thermal infrared SEVIRI channels Moderate Resolution Imaging Spectroradiometer (MODIS)	Saharan dust outbreaks multiple-linear regression, dust aerosol detection and estimation of the optical depth at 0.55 µm.	Sahara from Terra and Aqua platforms
Brindley, HE and Russell (2006)	Shortwave in the sun-glint and during the night	Dust detection	
Applegarth et al. (2006)	High-resolution remote sensing corresponds to airborne mid-infrared multispectral imagery and Thermal Infrared Multispectral Scanner (TIMS)	Particle size which are utilized as a geomorphic tool in arid regions	
Elliott et al. (2007)	GA-Multiple Linear Regression (GAMLR), FT-IR	Soil analysis	
van der Meijde et al. (2013)	Thermal and short wave infrared	Hydrocarbons detection, Soil analysis	
Hecker et al. (2010)	Infrared techniques (0.7–25 µm)	Identification of feldspar group minerals	
Soto-Càmara et al. (2012)	near infrared spectroscopy- NIR (1100-2500 nm) and VISbNIR (400-2500 nm)	Fungicide treatment detection for wheat samples Modified Partial Least Squared (MPLS)	
Reath and Ramsey (2013)	Shortwave linfrared (SWIR), Thermal Infrared (TIR), and Visible Near Infrared (VNIR) remote sensing concerning more focus on TIR (8-12 µm)	Linear mixing behavior of TIR emission mapping	
Wang et al. (2014)	Near-infrared band	Mineral identification Noise elimination approaches based on the altered mineral absorption peak.	
Gillespie et al. (2015)		potential prediction quality biomass	
Xiaojia et al. (2010)	EO-1 Hyperion	Spectral Angle Matching (SAM) for classification of Hyperspectral Remote Sensing (HRS) Altered mineral mapping	the east Kunlun of Qinghai-Tibet plateau
Fan et al. (2011)	hyperspectral imaging in 1.0 –2.50 µm wavelength range	Hydrated silicate and hydroxylated mineral identification	
Pendock et al. (2012)		Image processing method	
Speta et al. (2013)	shortwave infrared	See through the thin bitumen at the surface of oil sands	
Zhang et al. (2014)	Airborne Visible/Infrared Imaging Spectrometer image	Hyperspectral target, fabric and vehicle detection	
Li et al. (2014)	Hyperspectral imagery	Target detection technique in forest area for finding the Ding-Ma gold deposit	Zhenan
Zhao et al (2014)		Identification of minerals and physical surface properties	
Cui et al. (2015)	hyperspectral infrared imagery-thermal infrared remote sensing (8–12 µm) (TIR) Thermal Airborne Spectrographic Imager (TASI)	Mineral mapping and image analysis. The targeted minerals were quartz, diopside/hedenbergite, calcite, microcline and hornblende	
Fieldspec-spectroradiometers (2017)	an ASD portable spectrometer (0.4–2.5 µm) using Thermo/Nicolet Nexus 6700 FTIR spectrometer	Mineral mapping	Nevada
Calvin et al. (2015)	Thermo/Nicolet Nexus 6700 FTIR spectrometer	Mineral GIS databases maps targeted minerals such as Sinter, tufa, travertine, argillic	
Feng et al. (2013)	long-wave (3–14 µm) spectral sensing from airborne SEBASS imagery	Find lichens effects on mineral analysis	
Beiranvand & Hashim (2015)	land imager and thermal infrared sensor Landsat-8 data for 2&4bands (VNIR), 6&7 bands of SWIR, 10th band for thermal infrared.	Hydrothermal alteration mapping	Sar Cheshmeh copper mining district, Urumieh-Dokhtar volcanic belt, south-eastern Iran
Ross et al. (2013)	Short-Wave Infrared (SWIR) and Visible (VIS) infrared wavelengths (0.3–2.5 µm)	Identification of minerals	Sao Paulo, Brazil.
Chudnovsky et al. (2011)	shortwave infra-red (2080-2380 nm) wavelengths	Dust-laden flows (Saharan dust storm) clay minerals (include illite-moscovite, Fe-rich nontronite, and kaolinite)	
Rogge et al. (2014)	AISA airborne hyperspectral imagery by spaceborne EnMAP scene (30 m spatial resolution)	investigating lithologic maps	subarctic region (Nunavik, Canada)

Table 2.2: A breif summary of spectroscopy and hyperspectral imagery for earth sciences and mineralogy application.

Watson and his co-workers used free-flying hot-air balloons to carry FT-IR spectrometer instrumentation, multispectral imaging spectrometers, far- and mid-IR cameras, radiometers, forward-looking IR cameras, plus a variety of other sensors, for environmental analyzes (Watson et al., 1996). Their experiments used Atomic Emission Spectrometry (AES) (Thompson and Reynolds, 1978; Uden, 1992) and FT-IR spectrometry which could provide chemical effluent detection, determine the contamination of Hg, conduct stack testing, use atmospheric concentration situ vertical profiling to identify various pollutants and conduct multisite air quality monitoring. A remote FT-IR was used to monitor the atmospheric volatile organic compounds and the results were described by (Hammaker, 1995). Griffin, 1996 continued the study of planetary and extraterrestrial or terrestrial atmospheres by applying far-infrared spectroscopy. Zwicker used the remote sensing FT-IR spectrometry for forestry studies in North Carolina (Zwicker, 1996). NIR was used by Malley et al. for quantitative and rapid assessment from Precambrian Shiled lake (Malley et al., 1996). A NIR visible spectroscopy technology used in balloon-borne remote sensing forms to analyze the atmosphere (Camy-Peyret et al., 1995). A mid-infrared magnetic rotation spectrometer was used for Atmospheric free radical assessment by (Blake et al., 1996). SWIR spectrosmetry airborne has been used to study oil and gas resources by Bailin (1994). Gao and his team showed that infrared micro-spectroscopy can be used for rapid identification of gemstones (Gao et al., 1995). Ricardo et al. (1995) chose multispectral instrumentation to record the biomass burning in West Africa. The partial least square regression of near infrared spectroscopy for the prediction of the quality indices of biomass pellet mixes was measured by Gillespie et al. (2015). The identification of the gross calorific and moisture levels was of excellent and good accuracy, whereas the carbon and ash levels were estimated to be fair and good, respectively. Consequently, the potential prediction of the quality of biomass [6] pellets indices have been shown by (Gillespie et al., 2015).

The mapping and different evaluations of variation density for vegetation where covers the land. Near infrared spectroscopy for fungicide treatment detection for wheat samples has been performed by using NIR (1100-2500 nm) and VISbNIR (400-2500 nm). The study involved the analysis of different mathematical pre-treatments for signals such as derivatives and scatter correction to enhance discrimination accuracy using Modified Partial Least Squared (MPLS) (Soto-Cámara et al., 2012).

2.3.2 Analysis of soil

The chemical and physical processes are used to assess a loose material mixture of the rocks from soil in terms of textural variation and mineralogical perspective using spectral behavior image processing in laboratory conditions. The help provided by hyperspectral imagery for these purposes vitally rely on hyperspectral information. The maps obtained can provide information on mineralogical and lithologies and this contributes to the estimation of spatial

---

[6] "A diverse range of biomass was used including wood, Miscanthusand herbaceous energy grasses" from (Gillespie et al., 2015).

erosion controls and other relevant information regarding soil studies (Riaza et al., 2001). The Geostationary Earth Radiation Budget (GERB) and a combination of the Spinning Enhanced Visible and Infrared Instruments (SEVIRI) was used for aerosol detection and radiative effect estimation at spatial and high temporal resolution, installed in Meteosat-8 (Meteosat-8, 9 July 2007). The records showed the misidentification of Saharan dust outbreaks that can bias the longwave and shortwave fluxes. An algorithm employs multiple-linear regression from selected thermal infrared SEVIRI channels for dust aerosol detection and an estimation of the optical depth at 0.55 μm. The test performance and results were compared to the Moderate Resolution Imaging Spectroradiometer (MODIS)(MODIS, 2017) observation obtained from Terra and Aqua platforms. The detection and identification using the algorithm is approximately 60-70 % of these points depending on the dust model employed. The capability of dust detection was also tested by using shortwave in the sun-glint and during the night (Brindley and Russell, 2006). The differences between geomorphic and slopes backing two different desert piedmont types gave a proxy indicator in the type of landform at the mountain base. An airborne mid-infrared multispectral imagery and a Thermal Infrared Multispectral Scanner (TIMS) showed the slope's mantle and the particle size which are used as a geomorphic tool in arid regions (Applegarth and Stefanov, 2006).

The investigation of soil as a complex environmental medium and the determination of its organic and biological characteristics was conducted using FT-IR. The data was first subjected to Principal Component Analysis (PCA) and Discrimination Function Analysis (PC-DFA) and Genetic Algorithms (GAs) to determine important discriminatory variables in the model. The algorithm distinguishes between reclaimed soils of differing age, and GA-Multiple Linear Regression (GAMLR) analysis has shown that the recovery of disturbed soils which may not be complete for a period of 50 years. Secondly, it offers a possible well-organized method to screen complex changes in soil (Elliott et al., 2007). Hydrocarbon detection, indirectly or directly, in remote sensing has been achieved by the detection of hydrocarbons in soil through laboratory sample spectral analysis utilizing thermal and short wave infrared regions. Spectral analysis reveals the hydrocarbon development absorption features as the soil becomes increasingly more contaminated (van der Meijde et al., 2013). SWIR and Visible (VIS) infrared wavelengths (0.3-2.5μm) was used to determine soil mineralogy together with ASTER to map mineral components of soils in a part of the state of São Paulo, Brazil. 42 soil samples have been collected and the spectral data which is relevant was extracted using a FieldSpec FR spectrometer. Their spectral signatures were analyzed on ASTER SWIR (AST5-9: 1.60-2.43μm) and VNIR (AST1-4: 0.52-0.86μm) reference spectra to achieve the mapping of minerals such as kaolinite, gibbsite, and montmorillonite and the distinction between iron-poor and iron-rich soils (Vicente and de Souza Filho, 2011). Analyzing of the longest division of SWIR (2080-2380 nm) wavelengths was conducted for dust-laden flows (Saharan dust storm) and the results show the possibly of clay minerals (include illite-moscovite, Fe-rich nontronite, and kaolinite) used as tracers for atmospheric dust monitoring even above bright areas (Chudnovsky et al.,

2011).

2.3.3 Mineralogical and Mineral exploration applications

The potential of Thermal Infrared Remote sensing (TIR) (8-12 μm) for the purposes of geological remote sensing has been successfully demonstrated for planetary and terrestrial geological studies involving the mapping of surface materials. The study describes how the new generation of commercial hyperspectral infrared sensors, known as Thermal Airborne Spectrographic Imagers (TASI), is used for mineral mapping and image analysis. For that aim, a combination of methods such as the ratio algorithm (RATIO), the Maximum-Minimum apparent emissivity Difference (MMD), and the Normalized Emissivity Method (NEM) have been used in the multispectral data to verify emissivity retrieval suitability for TASI hyperspectral data. Calcite, hornblende, microcline, quartz, and diopside/hedenbergite have been mapped by emissivity images. The spectroscopy and X-ray powder diffraction was used for the identification of minerals, and it appeared that both the combined temperature emissivity and atmospheric correction methods were suitable for TASI images. Carbonate skarnization was found by the spatial diopside extent and the information indicated the suitability of TASI for deposit and prospect scale exploration (Cui et al., 2015).

The data attained from NIR visible spectroscopy has been used to characterize the mineral composition the surface of asteroid by (Howell, 1995). Miller et al., 1995 used FT-IR spectroscopy in situ on mineralogy hydrophobic surfaces. The ability of infrared spectroscopy to detect different types of feldspar has been investigated and appears that the detection of feldspar is limited to around 5% and the plagioclase composition is mostly $\pm$ 4% anorthite component and IR-spectroscopy cannot detect Zonation or certain different generations of feldspars (Hecker et al., 2010). A geothermal exploration and major-rock mineral classification approach involving analysis using SWIR, TIR, and VNIR remote sensing with afocus on TIR (8-12 μm) has been presented by Reath and Ramsey (2013). The mapping was carried out to study the linear mixing behavior of TIR emission. To investigate the distribution of active geothermal surfaces and mineral composition, a Spatially Enhanced Broadband Array Spectrograph System (SEBASS)sensor collected 128 wavelength channels having $\sim 1m$ spatial resolution and provided hyperspectral TIR data. The identification of rare minerals is associated with geothermal areas. Such methods are referred to as Mineral and Gas Identifier (MAGI) airborne sensors. "indicator minerals" have been used in order to understand the influence of the ground and surface of water and the ultimate location of the new geothermal targets (Reath and Ramsey, 2013). The improvement of the accuracy level of mineral identification has been investigated by Wang and his team through considering the noise elimination approaches based on the altered mineral absorption peak. Their method is based on optimizing the position of the altered mineral absorption peak to increase the average accuracy rate

to 17.7% (Wang et al., 2014).

The application of Spectral Angle Matching (SAM) for the classification of the Hyperspectral Remote Sensing (HRS) technology for the purpose of automatic mineral identification and information retrieval was used for the ZhongYang mountain in the east Kunlun of the Qinghai-Tibet plateau, where altered mineral mapping areas used EO-1 Hyperion HRS image data. The hydrated silicate and hydroxylated mineral identification using hyperspectral imaging in the 1.0 to 2.50 μm wavelength range considers molecular variation. The analysis of hydrated and/or hydroxylated minerals using the spectral library of common silicate minerals involving the absorption features at ~ 1.40, ~ 1.91 and 2.20 - 2.40 μm wavelengths was presented by Fan et al. (2011). It was shown in their work that the identification of hydrated silicate and hydroxylated minerals cannot be based on these absorption features only but the integration of environment and geology in situ is vital (Fan et al., 2011). Pendock et al. (2012) presented an image processing method to handle the problem of multiple core trays and the separation from the rock material which is robust and insensitive to rotation and contamination of tray material (Pendock et al., 2012).

The evaluation of different transformation methods, for instance Fast Fourier Transform (FFT), First Derivative (FD), Discrete Wavelet Transform (DWT), S-Transform (ST) and Hilbert-Huang Transform (HHT) in spectral unmixing was investigated. A similarity evaluation was carried out using Pearson's Correlation Coefficient (PCC), t-test based approach, spectral similarity scores and Root Mean Squared Error (RMSE) estimated using SAM. It revealed that SAM and RMSE have relatively reasonable efficiency (Singh et al., 2012a). Speta et al. (2013) presented an analysis of spectral imagery in the SWIR through the thin bitumen at the surface of oil sands (Speta et al., 2013). Zhang et al. (2014) presented a Supervised Metric Learning (SML) algorithm for the detection of hyperspectral targets, vehicle detection, in Airborne Visible/Infrared Imaging Spectrometer images. In this approach, targeted pixels are in the positive space and the background pixels are pushed to the negative space (mathematical space). The algorithm initially maximizes the distance between negative and positive samples through an objective function of supervised distance maximization. The similarity propagation constraint of SML links the target pixels with positive samples and links the background to negative samples. It rejects false alarms for the detection of the target. At the end, the imposition of a manifold smoothness regularization to positive samples preserves a local geometry (Zhang et al., 2014).

A target detection technique to identify Ding-Ma gold deposits in Zhenan was described by Li et al. (2014). Some hyperspectral techniques were used, such as Constrained Energy Minimization (CEM), SAM, Orthogonal Subspace Projection (OSP), Adaptive Matched Filter

(AMF), Adaptive Coherence/Cosine Estimator (ACE), and Elliptically Contoured Distributions (ECD) (Li et al., 2014). Absorption depth quantitative analysis of minerals for the identification of minerals and physical surface properties was conducted by Zhao et al (2014) to extract the absorption features and band range containing absorption factors. A Continuum Removal (CR) was used along with a new feature called Reference Spectral Background Removal (RSBR). It eliminates the effects of unwanted contribution factors and gives some basic absorption feature parameters such as absorption width, absorption depth, and absorption center which provide more accurate absorption (Zhao et al., 2015). Thermal properties have been used as surface indicators of geothermal resources as well as for mineral characterization in Nevada. Validation of spectral information was performed using an ASD portable spectrometer (ASD, 2017) (0.4-2.5μm) and a Thermo/Nicolet Nexus 6700 FTIR spectrometer. Another research study has been carried out to determine the effect of lichens on mineral identification in long-wave (3-14 μm) spectral sensing using airborne SEBASS imagery. In this research study the ability to identify the lichen's effects on mineral analysis due to the lichen's organic compounds is focused on the reflectance in a particular wavelength band (3.41, 6.58, 8.13μm) (Feng et al., 2013a). An identification of altered rocks, lithological units and vegetation in the Urumieh-Dokhtar volcanic belt in south-eastern Iran using Landsat-8 (Landsat-8, 2017) operational land imager and thermal infrared sensor data was performed by (Pour and Hashim, 2015b).

In another study, visible/near infrared spectrometry was employed with energy-dispersive, volumetric magnetic susceptibility, and density using gamma-ray attenuation as well as X-ray and fluorescence spectrometry for the identification of minerals (Ross et al., 2013).

An approach has been presented for atmospheric correction and converting radiance-at-sensor to ground reflectance and correction of spectroscopic mis-identification of minerals in ASTER VNIR / SWIR reflectance using SWIR Compact Airborne Spectrographic Imager (CASI). The atmospheric correction using ASTER data has been completed and the mineral identification was achieved more quickly using the reflectance factor to the atmospheric-corrected ASTER L1B data (Jing et al., 2014). A spatial distribution of the alteration minerals in the Kap Simpson complex was conducted by analyzing of the HyMap airborne hyperspectral data. ASTER VNIR-SWIR data enabled the detection of jarosite, Al-OH, and ferric oxides. But, due to ASTER moderate spectral and spatial resolution imagery in the data, ASTER data is appropriate merely for the reconnaissance level mineral study (Bedini, 2011). An approach for the estimation of the surface pH feasibility on airborne hyperspectral (HS) data (HyMap) basis on the Sokolov lignite mine was presented by Kopackova (2014). Very low pH($\leq$3.0) minerals such as jarosite, pyrite, or lignite were the diagnostic. goethite by itself was characterized as almost neutral or lower pH ($\geq$6.5). However, jarosite in association with goethite showed a lower pH (3.0-6.5). A Multi-Range Spectral Feature Fitting (MRSFF) was used for the pH indicator map in the HS dataset and it was sensitive enough to identify the differences and a regression model was provided in the pH model. Another study covered the

surface pH characteristics using Hyperspectral airborne imagery for mineralogy of pyrite mine tailing and is described by Zabcic et al., 2014. They have used HyMap in 126 spectral bands covering the 0.45-2.48 μm infrared (Kopačková, 2014). A Mineral mapping in the Maherabad area, in eastern Iran was carried out using HyMap remote sensing data. Minimum Noise Fraction (MNF) transform was coupled with a Pixel Purity Index (PPI). This was used on HyMap images for the extraction of the alteration mineral endmembers which included montmorillonite, kaolinite, calcite, sericite (muscovite/illite), epidote, goethite, and chlorite. Also a virtual verification was attained by USGS spectral library (Molan et al., 2014). Hyperion Earth Observing-1 (EO1) and Advanced Land Imager (ALI) data for hydrothermal alteration and lithological mapping was conducted using Hyperion images with ALI covering the Meiduk and Sar Cheshmeh porphyry copper mining districts, is south-east Iran. Phyllic, propylitic alteration zones and advanced argillic were associated with porphyry copper mineralization (Pour and Hashim, 2015a). Another study for the investigation of lithologic maps in a sub-arctic region (Nunavik, Canada) involving the use of AISA airborne hyperspectral imagery of a spaceborne EnMAP scene (30 m spatial resolution). The extraction of Spatial Spectral Endmembers was achieved for the Environmental Mapping and Analysis Program (EnMAP) and Hyperspectral Sensor Surveying (AISA) data. The results of their research indicated that AISA data were more suitable as compared with EnMAP (Rogge et al., 2014). The spatial and spectral information combined some details and created a suitable opportunity for quick analysis to discover the chemical content of the materials. The research conducted for identification of diamonds has indicated that diamonds form in ultrahigh-pressure rocks in the Italian western Alps. Raman micro-spectroscopy has confirmed the presence of 42 diamond inclusions (Frezzotti et al., 2011).

2.4 Hyperspectral unmixing techniques

The linear unmixing technique supposes that pixels in endmember spectra are in convex combinations, and consequently the identification of the endmember is required for unmixing processes. Linear spectral mixtures in the thermal infrared are used with the pure pixels emissivity and its thermal information using the temperature and emissivity separation (TES) algorithm. Then abundance and the sub-pixel temperature estimation is applied which is referred to as Thermal Remote sensing Unmixing for Sub-pixel Temperature (TRUST) in urban area research (Cubero-Castan et al., 2015). An implementation of hyperspectral unmixing on GPU and mutli-code processors has been conducted by Bernabé et al. (2013) to decrease the computational load for the process. Their full processes were divided into three different stages: Endmember estimation, automated identification, and fractional abundance fraction for every endmember. For testing, they have used an Airborne Visible / Infrared Imaging Spectrometer (AVIRIS) data set (BernabÃ©é et al., 2013). An implementation of the HySime Algorithm on FPGA to determine the numbers of endmember in hyperspectral

data was carried out by Gonzalez et al. (2015).

2.4.1 Application of decomposition analysis for spectral unmixing

A Spectral unMixing Analysis (SMA) approach was performed in remote sensing images. Several unmixing methods such as Bayesian Linear Unmixing (BLU) and VCA were shown as alternative analysis methods such as least square fitting, PCA, Independent Component Analysis (ICA) on the Electron Energy-Loss Spectroscopy (EELS) data. The results show that BLU leads to a more significant outcome as compared with other VCA (Dobigeon and Brun, 2012). Another SMA approach on Earth Observer 1 (EO-1) satellite for Visible (VIS) to SWIR for Iron age copper mining in ASTER imagery used PCA for the unmixing (Savage et al., 2012). An additional approach involved AVIRIS data and developed new Spatial-Spectral Pre-Processing (SSPP), Endmember Identification Algorithms (EIAs) for endmember identification and spectral unmixing of remotely sensed hyperspectral images. They have compared their proposed algorithm with well known algorithms such as N-FINDR, OSP, VCA, MVSA, and SISAL. Then they have added SPP, RBSPP, and SSPP to each algorithm (Martin and Plaza, 2012). Some endmember and SMA methods tried to develop robust endmember extraction and SMA techniques in hyperspectral imaging such as the combination of Support Vector Machine (SVM) classification with MNF, PCA and ICA (Dópido et al., 2011). Notice that MNF had a relatively better response. Real-Time Endmember Extraction was computationally efficient for orthogonal subspace projection and N-FINDR (Remon et al., 2011). This method was called HEEA and was tested along with IEA, OSP, SGA, SMACC, and SSEE automatic endmember extraction methods (Li and Zhang, 2011). A novel unsupervised SPP module which is basically a region-based EEA approach was proposed by Martin and Plaza (2011). PCA and SAM in the supervised classification with the hyperspectral tools such as Pixel Purity Index (PPI), MNF, and nD-visualizer has been studied by Rajendran et al. (2013). For the mineral reference ASTER was used to provide the hydrothermal mineralization (silicification, listwaenites, talc alteration and serpentinization) zones (Rajendran et al., 2013). Mapping using a geological and the geochemical approach with PCA and ICA was presented by Yang & Cheng (2015) for the geochemical dataset in Pinghe, Fujian, Southern China (Yang and Cheng, 2015). Also ICA has been used for the transformation on ETM images of southern Masule, Iran (Gholami et al., 2012). Geological Mapping by ASTER SWIR and lithological discrimination data in Udaipur area of Rajasthan, India was achieved by applying Band Combination (BC) to component based approaches e.g. ICA over PCA and MNF transform. The research targeted some metals such as copper, lead and zinc, micas and marbles rocks using the same technology and unmixing (Kumar et al., 2015). One study addressed the mineral identification of kaolinite-montmorillonite, sericite-illite, and chlorite-calcite-epidote mapping using Spectral Information Divergence (SID), spectral angle Mapper (SAM), PCA methods, and Directed Principal Component Analysis (DPCA) and employing the ASTER

SWIR data (Khaleghi et al., 2014). For the extraction of the spectral information, four types of algorithms were used on ASTER data:

(i) Principal PCA, MNF; (ii) SAM, Matched-Filtering (MF), and Mixture-Tuned Matched-Filtering (MTMF), (iii) Linear Spectral Unmixing (LSU) and Constrained Energy Minimization (CEM), (iv) Relative Absorption BandDepth (RBD) (Pour and Hashim, 2012a).

The performance of PCA, MNF, SAM, LSU, MF and MTMF methods and band ratio was tested for the identification of hydrothermally altered rocks, lithological units and quartz rich igneous rocks for copper and gold minerals (Pour and Hashim, 2012b). A research study on Multivariate Curve Resolution-Alternating Least Squares (MCR-ALS) application in AVIRIS was carried out by Zhang & Tauler (2013). This involves an EEA method for the extraction of the spectral signature of the pure constituents from spectroscopic imaging fields such as VCA and MVSA. The USGS library has been used for mineral identification comparison (Molan et al., 2014). A comparative study was performed for three types of estimators (ENVI-SVD, QP, Bayesian maximum a posteriori probability (MAP) estimator) on two different Observatoire pour la Minéralogie, l' Eau, les Glaces et l' Activité (OMEGA) hyperspectral data sets to perform mineral and ice detection on large hyperspectral datasets. OMEGA employs three special detectors, with, an average of 21 nm spectral resolution in the range of 2.65 to $5:2\mu$m (LWIR), 7.5 nm spectral resolution in the $0:35$-$1:05\mu$m wavelength range (VNIR) and 14 nm spectral resolution between 0.94 and $2:70\mu$m (SWIR). The results indicate that, the computational complexity of MAPs was much lower (Themelis et al., 2012b). A combination of the SWIR, VNIR, and TIR for the 8-12μm wavelength range was used for the identification of rare mineral assemblages associated with geothermally-active areas using SEBASS airborne sensors with SEM and XRD analysis (Reath and Ramsey, 2013).

2.4.2 A brief on data fusion approaches for spectral unmixing

Kruse and coworkers conducted the following mineral identification: (i) in VNIR they have analyzed in minerals such as goethite, hematite, and jarosite; (ii) in the SWIR they have identified micas, clays, sulfates, and carbonates, and in the long wave infrared (LWIR) carbonates and silicates were identified (Kruse, 2012). AST-07XT and RefL1b were also employed as two new crosstalk-corrections of ASTER SWIR. Research regarding geological information and exploration of epithermal gold and porphyry copper in the semi-arid and arid regions on ASTER data for SWIR was conducted by BeiranvandPour (2012). The determination of relations between derived landforms and mineralogy has been analyzed using hyperspectral imagery in combination with complimentary datasets for example Light Detection and Ranging (LiDAR), Interferometric Synthetic Aperture Radar (InSAR), or photogrammetric-derived (stereo) and Digital Elevation Models (DEMs) (Kruse, 2012). Another structural mapping of the mineralized zones has been proposed by BeiranvandPour et al. (2013) employing Hyperion and Phased Array type L-band Synthetic Aperture Radar (PALSAR), Landsat Enhanced

Thematic Mapper+ (ETM+) data (Pour et al., 2013).

A mineral mapping to determine the clay, mica and carbonate mineral distributions and their abundances has been investigated using Material Identification and Characterization Algorithm (MICA) for spectral dominant identification and the results were joined with ASTER data applying multinomial logistic regression to distribute the mineral maps. Results showed a high correlation for calcite and mica, and a medium correlation for smectite and kaolinite (Mulder et al., 2013). The hyperspectral data for the identification of kaolinite and smectite and alteration mineral assemblages range from silicic to argillic to zeolite-type and were obtained using a SVM algorithm on ASTER data (Brandmeier et al., 2013). Ayerdi & Grana presented non-linear unmixing using Extreme Learning Machine (ELM) regression ensembles that do not require endmember identification since it is implicit in the non-linear transformation. This method was employed on vegetation type recognition research (Ayerdi and Graña, 2016).

2.5   Endmember estimation

Spectral unmixing is frequently employed in the exploitation of hyperspectral data, and uses the spectral signature as an important feature that is usually calculated for each pixel of data. Here, endmember is defined as spectral pure constituent spectra. Abundances is defined as a set of correspondent fractions that shows the proportion of every endmember in the mixture which reveals a major role in the identification of the minerals. Automatic endmember identification considers the presence of at least one pure spectral signature for the minerals and over the last years, quite a few algorithms were developed in this area. Martin et al. (2011) presented an investigation in the spatial information for endmember searching without an assumption for the presence of pure pixels in data. They have used a spatial preprocessing technique which does not require modification for the subsequent endmember. The identification process is based on a minimum volume enclosing algorithm. It reveals the benefit of spatial information to guide the identification process of the endmember (Martin et al., 2011). Ambikapathi et al. (2011) proposed two pure-pixel based endmember extraction algorithm named the p norm based pure pixel identification (TRI-P) algorithm and the simplex estimation by projection (SIMPLE-Pro) algorithm. These algorithms were theoretically proved under the assumption of pure pixels and they never need any initialization.

Jimenez et al. (2012) presented a new open source system for inter-comparing and evaluation of spectral unmixing, called HyperMix. The created tool can perform the inter-comparison of the algorithms for abundance estimation and endmember extraction (Jiménez et al., 2012). The research was continued by developing the EEAs concerning the hyperspectral linear mixing model and geometrical approach for endmember estimation and Geometry-based Estimation for Number of Endmembers- Affine Hull (GENE-AH) algorithm and Convex Hull (GENE-CH) algorithm were proposed. These algorithms follow the fact that all the observed pixel

vectors lie under the endmember signatures in affine hull and convex hull. Neyman-Pearson hypothesis testing has been used for both the algorithms as well as the TRI-P algorithm. The algorithm was tested on the real AVIRIS hyperspectral data obtained over the Cuprite mining site in Nevada.

The conventional endmember extraction and unmixing procedures in hyperspectral remote sensing involved certain uncertainties. An algorithm that uses Pearson's Correlation Coefficient (PCC) and Crude Low Pass Filter (CLoPF) was used to identify the endmember spectra from spectral library. A Non-Negativity Fully Constrained Least Square (NNFCLS) optimization approach was applied to determine the identified end-members and fractional abundances. The method is similar to that of the GENE algorithms tested by SAM and Normalized Root Mean Squared Deviation (NRMSD) and computational timing efficiency. The appropriateness of identified candidates for the approach was also examined(Singh et al., 2012b). In the hyperspectral remote sensing image, SNR often reduces due to processing on the images. The sensor normally receives the radiance which has instrumental noise and atmospheric effects. The noise related to instrument includes shot (photon) noise, quantization noise and thermal (Johnson) noise. Quantization noise and thermal (Johnson) noise are modeled as Gaussian additive noise which is independent from the signal. Shot noise is also modeled as additive noise and its variance is dependent on the level of the signal (Kerekes and Baum, 2003; Landgrebe and Malaret, 1986; Acito et al., 2011a; Qian and Ye, 2013). The additive Gaussian noise which is from the atmospheric effects is compensated and the noise is assumed to have spatial identical distribution and be spectrally uncorrelated. The hyperspectral imaging systems might also induce some artifacts referred to as pattern noise. Modeling and estimation of the noise in hyperspectral images is an active research area in remote sensing (Kerekes and Baum, 2003; Acito et al., 2011a; Curran and Dungan, 1989; Bioucas-Dias and Nascimento, 2008; Gao et al., 2008; Acito et al., 2011b; Xu et al., 2013). There are some methods which focus more on noise modeling or minimization, such as MNF (Green et al., 1988) or Noise Adjusted Principal Components (NAPC) transformation (Lee et al., 1990), in an effort to try to reduce the hyperspectral image noise.

2.5.1 Component Analysis for finding Endmember

Signal processing depends on the characteristics of signal components and thus the process is frequently called X-CA (X-Component Analysis). For example, if the independency among the components is assumed, there will be ICA or if the assumption is linearly dependent on the components, the analysis is PCA. Sparse component analysis (SCA) assumes that the observed signal is comprised of sparse components which are linearly mixed. Moreover, it assumes that there are different levels of sparsity for the components i.e. either intrinsically sparse or sparse in some sparsifying dictionary or basis. This finding has many applications like Blind Source Separation (BSS) and signal restoration (Model and Zibulevsky, 2006; Gribonval

and Lesage, 2006), dimensional reduction (Zhou and Tao, 2013), and image super-resolution (Gao et al., 2012). A method which is more similar to SCA is Morphological Component Analysis (MCA) (Starck et al., 2005) which seeks the morphological difference among the components and was developed for multivariate signals (multichannel MCA (MMCA) (Bobin et al., 2005). MCA and BSS gives GMCA (Bobin et al., 2007) and for hyperspectral data it is called hyperGMCA (Moudden and Bobin, 2011)). The X-CA method been used for a variety of conditions and purposes. In the same applications a combination of the X-CAs is used to cope with potentioal drawbacks and this provides a powerful alternative and very useful tool. For example, PCA is an orthogonal projection based on the variance of the signal and is broadly used for dimension reduction and data processing in various fields and particularly in hyperspectral image analysis (Kaewpijit et al., 2002; Du and Fowler, 2008). But this method has a drawback in high dimensional applications in that linear combinations of all variables appear in PCs which reduces SNR.

The smoothed PCA involves the application of a smoothing regularization for data functioning (Ulfarsson and Solo, 2006; Silverman et al., 1996; Ramsay, 2006) or a more recent method automatically attempts to zero out noisy variables considering the penalty terms. For example, the zero leading is performed by lasso exploiting (called SCOTLASS) (Tibshirani, 1996). There are some other methods for this purpose, such as the optimization regularization frame-work (Johnstone and Lu, 2009) and Elastic Net regularizer (Zou and Hastie, 2005). Moreover, ASPCA is an algorithm which provides SPCA (Zou and Hastie, 2005) for cases involving the comparison between the number of variables and observations. For that, a suitable basis is used for the projection of the signal and then a data subset is chosen based on the number of largest variances. Afterwards, a classical PCA is applied while the calculated eigenvectors are filtered out by the hard thresholding function. The smoothed PCA and classical PCA were outperformed by ASPCA. ICA is also broadly employed in BSS, whereas one of its drawback involves the fact that several components have linear dependency. Consequently, an ICA extension which is called Independence Vector Analysis (IVA) (Kim et al., 2006) is proposed where the multivariate signal is observed (vectorized signal).

2.6 Infrared Spectroscopy in different band range

Application of a portable infrared spectroscopy instrument was initially reported by Takacs and coworkers to analyze wheat (Takacs et al., 1996) and then, a real time gas analyzer (GASMET) proposed by Ahonen et al., 1996, which was a portable FT-IR for industrial hygiene situations. The application of this technology have being widely expanded till today. Here, the infrared spectroscopic analysis categorized by different band range (NIR and VNIR, SWIR, MWIR, LWIR and TIR, and Other types of spectroscopy) also table 2.3 presents a brief summary of portable instrument infrared spectroscopy.

2.6.1 NIR and VNIR

A portable instrument in the form of an Airborne Visible/Infrared Imaging Spectrometer (AVIRIS) from the Kelso Dunes and Granite Mountain areas of southern California was used for the extraction of atmospheric effects, surface-reflectance, and identification of the spectral relationship of composition and mineralogy (Sun et al., 2001). This study used an adaptation of Crippen's âregression intersection method" (RIM) to determine the homogeneity and spatial relationship in rugged terrain. The AVIRIS airborne instrument and hyperspectral data analysis have also been used for a study which took place in an area near Alto Paraíso de Goías. The analysis involved mineral identification including mixtures of primary and secondary minerals which can be identified in the image based on spectral signatures of the pixels. The mineral identification was confirmed by laboratory Scanning Electron Microscope (SEM) analysis of the soil samples (Crósta and de Souza Filho, 2017). This is similar to another diffuse reflectance near-infrared (350-2500 nm) spectroscopy for petroleum-contaminated soils using PLS (Okparanma et al., 2014). An evaluation of NIR spectroscopy on soil as a tool for case definition in agricultural and environmental applications at sub-Saharan Africa was presented by Awiti et al., 2008. Soil research was more developed by Wang et al. (2015), while principal component regression was used in (VIS/NIR) diffuse reflectance (FT-IR) spectroscopy to estimate the soil contents (i.e. pH of soil and OM, K, N, and P elements)(Wang et al., 2015). This research was continued by O'Rourke et al. (2016) using VNIR spectroscopy and X-ray fluorescence (XRF) spectrometers and the previous method was modified through application of model averaging procedures to combine the model outcomes (O'Rourke et al., 2016).

Figure 2.2: Photograph showing measurements carried out with the PIMA II field spectrometer (taken from: Kruse, 1996a).

The location of contaminated areas and the mapping of the natural oil seepages or accidental leaks was proposed using infrared hyperspectral remote sensing tools (HyspIRI; Hyperion; EnMap) and multispectral (WordView-3) sensors, wavelet transform and analyzing of the soil (Scafutto et al., 2016) (Figure 2.4). Wang et al. (2017) presented a determination of Rare Earth Elements (REE) in soil using VNIR spectroscopy (350 to 2500 nm) involving Inductively coupled plasma-emission spectrometry (ICP-ES), ICA-mass spectrometry (ICP-MS), 130 soil samples near REE mines, and Partial Least Squares Regression (PLSR). This resulted in distinction of REE in soil spectra, for Nd at 798 nm, unlike 400-1000 nm spectral range (for Sm, Nd, Pr, La, and total light REE (ΣLa-Eu excluding Pm)) (Wang et al., 2017). Soil Organic Matter (SOM) estimation has been carried out through portable spectroscopy and Support Vector Machine Regression (SVMR) to evaluate the Brown-Forest Areas of the Shandong Peninsula, China, and good results were obtained for five sensitive wavelengths (2267 nm, 1996 nm, 1007 nm, 991 nm, and 917 nm) (Lulu et al., 2017). A graphic user interface software for field spectroscopy with sub-nanometer spectral resolution was presented by Meroni and Colombo (2009). Another mineral mapping comparison was proposed with AVIRIS and airborne hyperspectral data using National Aeronautics and Space Administration Earth Observing 1 Hyperion sensor (EO-1 Hyperion) in the 0.4 - 2.5 μm wavelength range and involved the following minerals for mapping: alunite, epidote, chlorite, hydrothermal silica, carbonates, buddingtonite, zeolite, muscovite, and kaolinite (Kruse et al., 2003). Mineral mapping of Regolith Materials and Landforms using hyperspectral visible-near infrared imagery from the Olary Domain in South Australia was presented by Lau et al., 2003, using PIMA II and MTMF (Mixture Tuned Matched Filtering) processing techniques in ENVI. Stenberg et al. (2010) proposed VNIR spectroscopy of soil analysis, focusing on soil attributes: i.e. texture, Soil Organic Matter (SOM), heavy metals, pH, minerals, water, and nutrients (Stenberg et al., 2010). Ground-based NIR spectroscopy for the detection of molecules, conditions, and compositions of exoplanet atmospheres (such as carbon monoxide (CO), carbon dioxide (CO2), Water (H2O), and methane (CH4)) was presented by Swain et al., 2010. Another application of PIMA II for hydrothermal mineral alteration (devoted to the octahedral Al content and the abundance of white mica (sericite)) at Hellyer, Tasmania was proposed by Yang et al., 2011. A handheld Raman spectrometer with near infrared (785 nm) was used for mineralogical field examinations which involved plenty of minerals (e.g. Aragonite, Smithsonite, Titanite) (Jehlička et al., 2011). An active volcano surveillance using infrared imagery was proposed by Spampinato et al., 2011. VNIR (400 - 1200 nm) hyperspectral imagery was used for mineralogy and ferric Iron crystal field absorption (at around 900nm). This imagery was also used for mineral indicators to study the proportion of goethite in crushed rock mixtures (Murphy et al., 2014). A soil contamination (total petroleum hydrocarbons (TPH)) investigation was reported by Douglas et al. (2018) which used an analytical spectral device (ASD) spectrophotometer (350-2500 nm) in diffuse reflectance mode, PLSR, and Random forest regression (Douglas et al., 2018). A research study based on using NIR and XRF to determine

the mineral elements in artichokes was proposed by Mir-Marqués et al.(2016) (Mir-Marqués et al., 2016). Koch et al. (2017) presented an investigation of 419 samples of mine tailings in South Africa using PXRF spectrometry and visible near infrared diffuse reflectance spectroscopy (VisNIR DRS). Then, XRD, Energy Dispersive X-ray Spectroscopy (EDAX) coupled with Scanning Electron Microscopy (SEM) were used to confirm the tailings mineralogy and revealed relatively satisfactory calibrations to PXRF analysis along with VisNIR DRS models of prediction (Koch et al., 2017). FT-IR spectroscopy was used to study for fourteen samples of tourmaline from the Real Museo Mineralogico of Federico II University at Naples along with several methods and allowed the classification and identification of the following tourmalines: tsilaisite, rossmanite, dravites, elbaites, uvites, and schorl (Mercurio et al., 2018).

Portable Instrument Infrared Spectroscopy

Paper	System Used	Application	Location (if available)
Goodacre et al. (1996)	Machine learning based approach using FT-IR spectroscopy	Identify and analyze of Streptococcus and Enterococcus species in 18 hospitals	
Blakeney et al. (1996)	Portable infrared spectroscopy	For determination of leaf nitrogen	
Rivard et al. (1994)	Field-Portable Thermal Infrared Grating Spectrometer (THIRSPEC) for 7.9-11.3μm (LWIR)	Soil	
Rivard et al. (1994)	FT-IR	Determine the spectral emissivity of natural geological samples	
Preissler & Loercher (1995)	Visible and Near Infrared and in short wave infrared	Soil properties and parameters for reflectance spectra	
Ahonen et al. (1996)	Portable FT-IR	Real time gas analyzer (GASMET)	
Wilks (1996)	FI-IR portable instrument	C-H stretch band of oils (fats)	
	PIMA II – 1.3 - 2.5 μm wavelengths	Drill core at 1*cm*	
Egevskaya (1997)	Double Cat's Eye (DCE)	Interferometer uses a movable beam-splitter and two spherical mirrors created the higher resolution against motion and lower sensitivity in misalignment	Institute of Semiconductor Physics and the Russian Academy of Sciences
Blakeney et al. (1996)	Portable infrared spectroscopy	Leaf nitrogen determination	
Alexay et al. (1996)	Patent	Compound Parabolic Concentrators (CPCs)	
Crosta et al. (2017)	AVIRIS	Soil	near Alto Paraíso de Goiás
Sun et al. (2001)	SWIR-PIMA	Finding alteration zones associated with the Elura zinc-lead-silver deposit	Elura Mine, Cobar, Australia
Yang et al. (2001)	SWIR-PIMA	Hydrothermal alterations	Broadlands-Ohaaki geothermal field, New Zealand
Kruse et al. (2002)	SWIR, AVIRIS and EO-1 Hyperion	Geologic application (minerals mapped), zeolites, buddingtonite, chlorite, alunite, dolomite, muscovite, calcite, hydrothermal silica, montmorillonite, and dickite.	northern Grapevine Mountains (NGM) site (located at the extreme north end of Death Valley, CAN).
Cudahy & Barry (2002)	Hyperion hyperspectral VNIR-SWIR satellite imagery	Mapping of amphibole, chlorite-epidote, pyrophyllite, white mica (with Tschermak substitution variations)	Panorama, Pilbara Block, Western Australia
Hubbard et al. (2003)	0.4-2.4 μm visible and shortwave infrared ASTER, Advanced Land Imager (ALI), Hyperion	Mineral alteration mapping	area in the Central Andes between Volcan Socompa and Salar de Llullaillaco
Kruse et al. (2003)	0.4–2.5 μm range with 242 spectral bands AVIRIS an EO-1 Hyperion	Mineral mapping comparison	Nevada, Death Valley, California
Lau et al. (2003)	PIMA II and MTMF (Mixture Tuned Matched Filtering) processing technique in ENVI. hyperspectral visible-near infrared imagery	Mineral mapping: Kaolinite and smectite (montmorillonite)	Olary Domain, South Australia
Vaughan and Calvin (2004)	High spatial resolution (~2m) hyperspectral VNIR/SWIR and TIR images airborne spectrometers HyperSpecTIR and SEBASS	Mineral resource exploration; Hydrothermal alteration; acid mine drainage	The Comstock mining district, around Virginia City, Nevada
Montero et al. (2005)	Visible to short-wave infrared range of light (0.35–2.5 μm)	Acid mine drainage (AMD), Characterization of waste rock	Penn Mine in the Foothills massive sulfide belt of the Sierra Nevada
Piccinini et al. (2006)	FT-IR micro-spectroscopy used for	Mapping of H_2O and CO_2 in volcanic minerals	SINBAD beamline, Frascati, Italy
Kruse and Perry (2006)	Commercial off-the-shelf (COTS) atmospheric correction software		
Hecker (2008)	Ground-spectra PIMA II, HyMap, and USGS	Endmember of minerals (illite, alunite, kaolinite)	
Meroni and Colombo (2009)	Graphic user interface software	Field spectroscopy with subnanometer spectral resolution	
Stenberg et al. (2010)	VNIR spectroscopy	Soil and more concentration on soil attributes (*i.e.* texture, Soil Organic Matter (SOM), heavy metals, pH, minerals, water, and nutrients	
Swin et al. (2010)	Ground-based NIR spectroscopy	Detection of molecules, conditions, and compositions of exoplanet atmospheres (such as carbon monoxide (CO), carbon dioxide (CO_2), Water (H_2O), and methane (CH_4))	
Yang et al. (2011)	PIMA II	Hydrothermal mineral alteration (more focus on the octahedral Al content and the abundance of white mica (sericite)), Hellyer massive sulfide	Hellyer, Tasmania
Jehlicka et al. (2011)	Handheld Raman spectrometer with near infrared (785 nm)	Mineralogical field examinations Aragonite, Kutnahorite, Ankerite, Hydromagnesite, Artinite, Strontianite, Smithsonite, Witherite, Alstonite, Cerussite, Muscovite, Titanite, Zircon, Spessantine, Grossular	Albertov (Prague, Czech Republic), Vlastejovice quarry, Plesovice quarry, Zernez, Switzerland, Chiavenna, Italy, St. Leonhard im Pitztal
Khanmohammadi et al. (2012)	MIR and NIR	Characterization of petroleum products	
Vitek et al. (2012)	Raman spectrometer equipped with 1064 nm laser excitation	Geological, forensic, and geobiological analysis which includes inorganic and organic minerals	
Tappert et al. (2012)	Near and Mid wave infrared reflectance spectroscopy	Mineral chemistry via degrees of hydrothermal alteration (phengite-bearing rocks, high and low phengite)	Olympic Dam iron oxide–copper–gold (IOCG) deposit, South Australia
Soriano-Disla et al. (2013)	Reflectance mid-infrared FT-IR spectroscopy	Chemical element estimation totally 4130 soils sampling along with X-ray fluorescence (XRF) using partial least-squares (PLS) regression models	the GEMAS European soil sampling program
Okparanma et al. (2014)	Diffuse reflectance near-infrared (350-2500 nm) spectroscopy	Petroleum-contaminated soils using PLS	
Kotthaus et al. (2014)	FT-IR spectroscopy, LWIR	Derivation of urban materials	London Urban Micromet
Murphy et al. (2014)	VNIR (400–1200 nm) hyperspectral imagery	Mineralogy and ferric Iron crystal field absorption	
Eisele et al. (2015)	Thermal infrared and LWIR (8-14 μm) in FT-IR spectroscopy	Soil characteristics quantify and detect semi-arid soil properties	
Murphy et al. (2015)	SWIR (1002-355nm) hyperspectral imagery	Mineralogy and ferric Iron crystal field absorption	
Greenberger et al. (2015)	Visible/shortwave infrared imaging spectroscopy	Detection Of Organic-Rich Oil Shales	Green River Formation, Utah, USA
Awitti et al. (2015)	NIR spectroscopy	Soil propoerties	sub-Saharan Africa
Wang et al. (2015)	Principal component regression in (VIS/NIR) diffuse reflectance (FT-IR) spectroscopy	Soil contents (i.e. pH of soil and OM, K, N, , and P elements)	
O'Rourke et al. (2016)	VNIR spectroscopy and X-ray fluorescence (XRF) spectrometers	Soil properties model averaging procedures	
Black et al. (2016)	Airborne hyperspectral thermal data	Map Anchorage Island, Antarctica	Anchorage Island, Antarctica
Scafutto et al. (2016)	Infrared hyperspectral imaging HyspIRI; Hyperion; EnMap	Soil Mineral characterization substrates impregnated by crude oils	
Liu et al. (2016)	LIBS	Soil Toxic metal contamination-review	
Mir-Marqués et al. (2016)	NIR and XRF	Determining the mineral elements in artichokes: magnesium, zinc, potassium, calcium, manganese and iron in artichoke samples	Spanish areas (Benicarló, Valencia and Murcia)
Calvin and Pace (2016)	Field portable spectoradiometer	Wide range of phyllosilicate minerals (hydroxides, calcite, iron oxides, opal, zeolites, and variety of phyllosilicates) identification	
Govil (2016)	SWIR spectroscopy and Hyperion data (for regolith mapping)	Hydrothermal alteration minerals clay minerals (i.e. montmorillonite and illite along with the dolomite, goethite, hornblende, clinochlore, epidote, and muscovite)	Himalaya
Salehi et al. (2017)	SWIR spectroscopy	Affect of lichen in the signature of mineral (mica)	
Shin et al. (2017)	SWIR spectroscopy	relationship between the moisture content and beach sand minerals Calcite-Quartz-Alkali Feldspar-Plagioclase and Quartz–Alkali Feldspar–Plagioclase	
Wang et al. (2017)	VNIR spectroscopy (350 to 2500 nm)	Determination of Rare Earth Elements (REE) in soil	
Koch et al. (2017)	PXRF spectrometry, VisNIR DRS, XRD, EDAX coupled with SEM	Tailings mineralogy	mine tailing in South Africa
Lulu et al. (2017)	Portable spectroscopy	Soil Organic Matter (SOM) estimation	Brown-Forest Areas of the Shandong Peninsula, China
Feng et al. (2018)	Airborne hyperspectral VNIR-SWIR, LWIR	Lithological mapping three ultramafic units (pyroxenite, peridotite, dunite) shown in SWIR and LWIR and a significant differences are observed for quartz-rich sediments in the SWIR	
Douglas et al. (2018)	Spectrophotometer (350–2500 nm) in diffuse reflectance mode	Soil contamination	
Mercurio et al. (2018)	FT-IR spectroscopy	Classify and identify following tourmalines: tsilaisite, rossmanite, dravites, elbaites, uvites, and schorl	Real Museo Mineralogico of Federico II University at Naples

29

2.6.2 SWIR

A system called the Portable Infrared Mineral Analyzer II (PIMA II) is a field spectrometer which is used to measure the reflectance spectra from the split drill core at 1cm (Figure 2.3). This spectrometer is used in 1.3 - 2.5 mum wavelengths. Both wavelengths, the along-core and cross-core, have 600 spectral channels for the spectrometer image. This analytical technique was developed for hyperspectral data analysis for field and laboratory experiments (Kruse, 1996a; Boardman, 1989). Another application of the portable infrared spectroscopy for leaf nitrogen determination is proposed by Blakeney et al., 1996. A comparison of AVIRIS and EO-1 Hyperion covering the 0.4 to 2.5 μm spectral range was proposed by Kruse et al., 2002a,b, for geological application (minerals mapping- Figure 2.4). Using Hyperion on the validation sitesm, several minerals such as zeolites, buddingtonite, chlorite, alunite, dolomite, muscovite, calcite, hydrothermal silica, montmorillonite, and dickite were identified. Sun et al. (2001) used a SWIR PIMA in the Elura Mine, Cobar, Australia and identified white mica, chlorite and carbinats in a hydrothermal region and the results were found to be consistent with the mineralogical data from XRD and XRF analysis. The limitation of the alteration zones was found to be at 80m distance around the ore bodies (Sun et al., 2001). A very similar approach was performed by Yang et al. (2001) for hydrothermal alterations in the Broadlands-Ohaaki geothermal field, New Zealand, and three major alteration zones were found: a lower illite-chlorite, a middle illite, and an upper smectite (Yang et al., 2001a) and spectral mapping of white micas with compositional variation (Yang et al., 2001b). An airborne hyperspectral HyMap imagery in the VNIR-SWIR band was conducted for mineralogical purposes including mapping of amphibole, chlorite-epidote, pyrophyllite, white mica (with Tschermak substitution variations) (Cudahy and Barry, 2002). A comparison on the mineral alteration mapping in the 0.4 - 2.4 μm visible and shortwave infrared for three different spectral resources (i.e. ASTER, Advanced Land Imager (ALI), Hyperion) was presented by Hubbard et al., 2003. A visible to short-wave infrared range of light (0.35 - 2.5 μm) was used for the characterization of waste rock (Acid Mine Drainage (AMD)), at Penn Mine in the Foothills massive sulfide belt of the Sierra Nevada (Brimhall et al., 2005). A FT-IR micro-spectroscopy was used to map H_2O and CO_2 in volcanic minerals at the SINBAD beamline, Frascati, Italy (LR46). Moreover, the mineral identification using a hyperspectral infrared system in the 0.4 - 2.5 μm (VNIR/SWIR) spectral range has been conducted and involved ASTER multispectral data (Kruse and Perry, 2007). A spectral matching algorithm (i.e. SAM) was used for the classification of airborne and portable infrared instrument (ground spectra) data mapping applying the USGS standard library (Hecker et al., 2008). This research was more focused on the endmembers of minerals (illite, alunite, and kaolinite) but it also involved the comparison of the spectra; data for PIMA II, HyMap, and USGS were included which make this study more innovative.

Murphy et al. (2014) used Gaussian processes to estimate the wavelength position of the ferric Iron crystal Field Feature in SWIR (1002-1355nm) and used X-ray diffraction (XRD) analysis to determine the proportions of geothite and hemitite (Murphy et al., 2015). A rapid
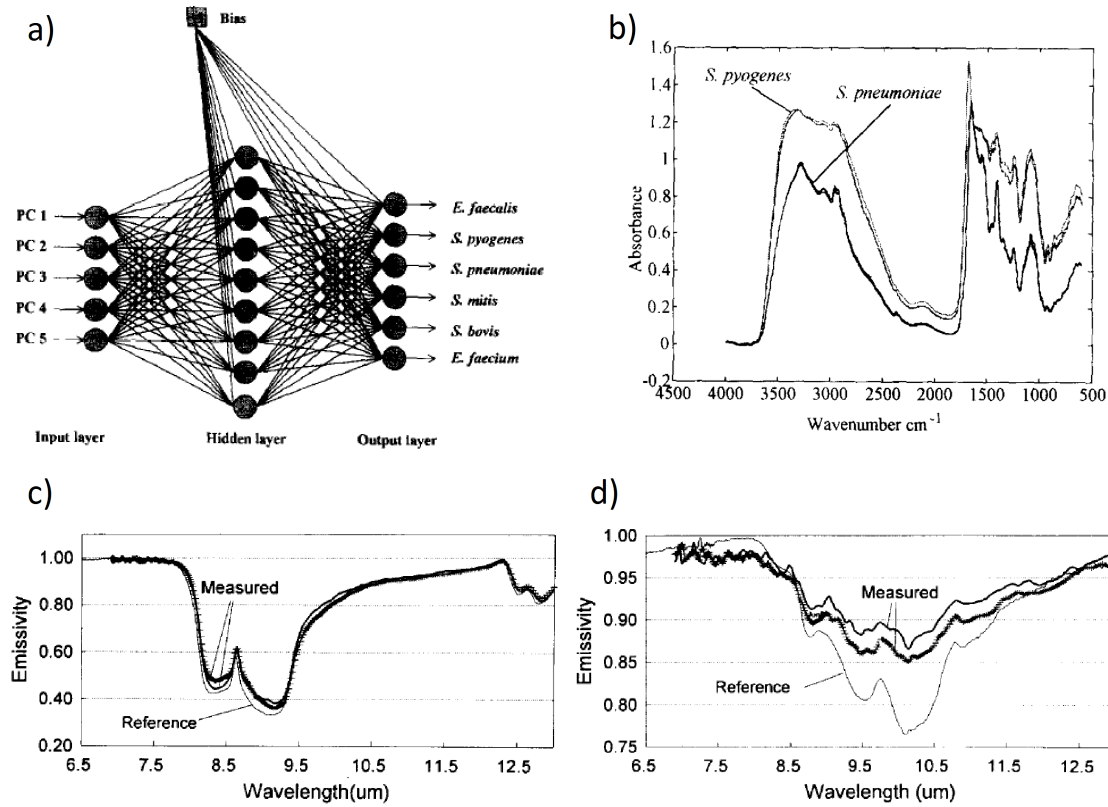
Figure 2.3: The scheme of a Neural Networks consisting of five inputs (five scores of principal components) and six outputs (each one corresponds to four streptococci and two enterococci) with fully interconnected architectures is shown in (**a**)). The reflectance-absorbance spectra of Strrprococcus pneumoniae 18 and Streptococcus pyogenes 7 are shown using FT-IT spectroscopy (**b**)). (Graph **b**) is adopted from Goodacre et al., 1996). The emissivity spectra of gabbro and quartzite using the technique of Rivard et al. (1995) are shown in **c**) and **d**), respectively.

hydrothermal alteration of minerals on drill core and chips was presented using a field portable spectoradiometer to identify a wide range of phyllosilicate minerals (hydroxides, calcite, iron oxides, opal, zeolites, and variety of phyllosilicates) (Calvin and Pace, 2016).

Hydrothermal alteration minerals using SWIR spectroscopy and Hyperion data (for regolith mapping) in the Himalayas was conducted which revealed the presence of clay minerals (i.e. montmorillonite and illite along with the dolomite, goethite, hornblende, clinochlore, epidote, and muscovite) (Govil, 2016). SWIR spectroscopy for modeling and wavelength displacements was used for rock forming minerals covered by lichens, which have effects on SWIR band range (Salehi et al., 2017). The mica group minerals show strong spectral signatures around 2200nm and 2340-2350nm which are not affected when these minerals were encrusted by 30% lichen, but when covered with a greater amount of lichen, there were shifts toward the shorter wavelengths (Salehi et al., 2017). A regression modeling of the relationship between the moisture content of beach sand minerals (i.e. average grain size, sand mineralogy, and band selection) in SWIR reflectance using a hand-held spectrometer (3-6 nm spectral resolution) was proposed by Shin et al. (2017). The mineral components were comprised of Calcite-Quartz-Alkali Feldspar-Plagioclase and Quartz-Alkali Feldspar-Plagioclase (Shin et al., 2017). The results revealed that three ultramafic units (pyroxenite, peridotite, dunite) were shown in SWIR and LWIR and significant differences was observed for quartz-rich sediments in the SWIR.

2.6.3 MWIR

A diffuse reflectance mid-infrared FT-IR spectroscopy for chemical element estimation was used for soil analysis (involving a total of 4130 soil samples from the GEMAS European soil sampling program) along with X-ray fluorescence (XRF) using partial least-squares (PLS) regression models (Soriano-Disla et al., 2013). A soil contamination research including a wide range of organic compounds and synthetic/natural metallic and minerals has been reviewed in terms of cost-efficiency and sampling design along with VNIR, mid and PXRF field spectroscopy (Horta et al., 2015). The chemistry of minerals using near and mid wave infrared reflectance spectroscopy was investigated by Tappert et al. (2012) (Tappert et al., 2013) at the Olympic Dam iron oxide-copper-gold (IOCG) deposit in South Australia.

2.6.4 LWIR and TIR

Previously a Field-Portable Thermal Infrared Grating Spectrometer (THIRSPEC) for 7.9-11.3μm (LWIR) was proposed by Rivard et al., 1994. These authors proposed a laboratory technique to determine the spectral emissivity of natural geological samples using FT-IR which did not require sample temperature control (Rivard et al., 1994). Preissler & Loercher (1995) proposed an extraction of soil properties and parameters for reflectance spectra (Preissler and Loercher, 1995). Their research included the relationship between the reflectance spectra and the chemical and physical properties of soil such as color, texture, organic material content, and mineral composition.

A development in the internal structure of FT-IR patented by Alexay et al. (1996) for using Compound Parabolic Concentrators (CPCs) which the reflectance returned through the CPC and beam splitter and afterward a stationary filter and discrete detector array (Alexay et al.,

1996). During a laboratory-based work using thermal infrared and LWIR (8-14μm) in FT-IR spectroscopy, soil characteristics have been analyzed and applied to quantify and detect semi-arid soil properties (Eisele et al., 2015). Vaughan and Calvin (2004) proposed a high spatial resolution ($\sim 2m$) for hyperspectral VNIR/SWIR and TIR images in the Comstock mining district in Virginia City in Nevada for mineral alteration using airborne spectrometers Hyper-SpecTIR and SEBASS (Vaughan and Calvin, 2004). An application of FT-IR spectroscopy in airborne and urban materials using Long Wave Infrared (LWIR) was proposed by Kotthaus et al. (2014). Their study includes VNIR and SWIR spectra as well (Kotthaus et al., 2014). An introduction to NASA Hyperspectral Infrared Imagery (HyspIRI) which was comprised of VSWIR (380-2500 nm spectral range) and LWIR (4-13μm) and more was used for ecosystem applications (Lee et al., 2015). Black et al. (2016) used the airborne hyperspectral thermal data to map Anchorage Island, Antarctica (mapping Granodiorite (Gd), two-feldspar-pink granite and medium crystalline diorite) and also used image processing techniques, linear unmixing, endmember extraction, segmentation and classification in the process (Black et al., 2016). Airborne Hyperspectral Imaging Systems (AISA), SWIR, SEBASS, and LWIR were used for geological mapping using Continuous Wavelet analysis (CWA) to enhance several parameters of images (e.g. radiometric quality, residual errors minimization in ISAC radiometric correction and estimation of targeted temperature for LWIR, and improving the calibration) and create a platform for SWIR and LWIR data combination (Feng et al., 2017).
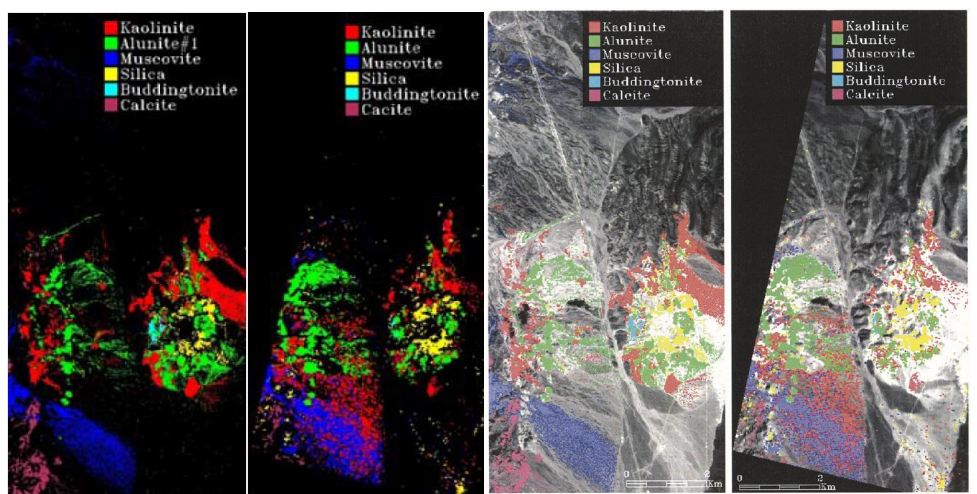
False color mineral mapping using AVIRIS (left image) and Hyperion (right image) (image adopted from Kruse et al. (2002))

MTMF mineral maps applying AVIRIS data (left image) and Hyperion data (right image) false color pixels to depict the spectrally predominant mineral (more than 10% concentration). (image adopted from Kruse et al. (2002))
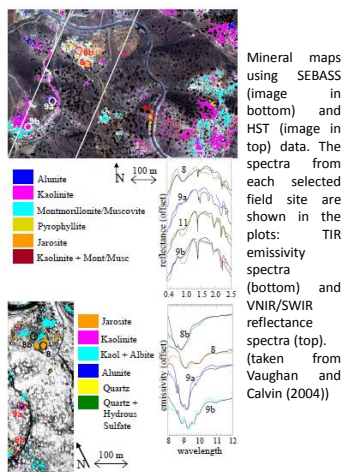
Mineral maps using SEBASS (image in bottom) and HST (image in top) data. The spectra from each selected field site are shown in the plots: TIR emissivity spectra (bottom) and VNIR/SWIR reflectance spectra (top). (taken from Vaughan and Calvin (2004))
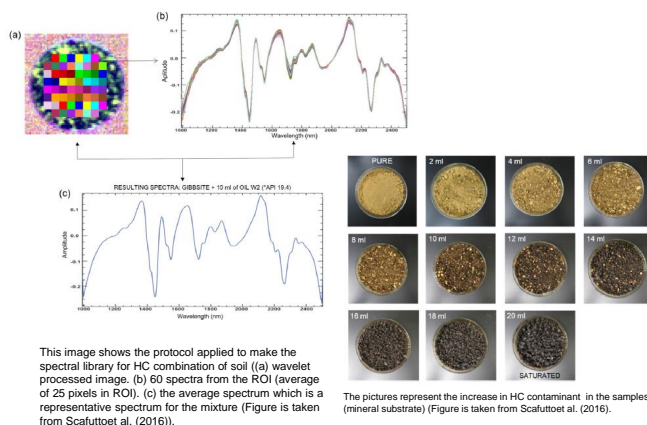
This image shows the protocol applied to make the spectral library for HC combination of soil ((a) wavelet processed image. (b) 60 spectra from the ROI (average of 25 pixels in ROI). (c) the average spectrum which is a representative spectrum for the mixture (Figure is taken from Scafuttoet al. (2016)).

The pictures represent the increase in HC contaminant in the samples (mineral substrate) (Figure is taken from Scafuttoet al. (2016).

Figure 2.4: Several research works on mineral mapping which were taken from (Scafutto et al., 2016; Kruse et al., 2002b; Vaughan and Calvin, 2004).

2.6.5 Other types of spectroscopy

Egevskaya, from the Institute of Semiconductor Physics and the Russian Academy of Sciences, (1997) proposed a portable FT-IR spectrometer based on the Double Cat's Eye (DCE) interferometer which uses a movable beam-splitter and two spherical mirrors creating a higher resolution against motion and lower sensitivity in misalignment (Egevskaya, 1997). An actual machine learning based approach using FT-IR spectroscopy and Artificial Neural Networks (ANN) and PCA to identify and analyze of Streptococcus and Enterococcus species in 18 hospitals (Goodacre et al., 1996) (Figure 2.2.a-b). The application of infrared spectroscopy was performed in a modern way which involved back-propagation algorithm with the scores of principal components of spectra for the FT-IR spectra strains recognition. A portable Raman spectrometer equipped with 1064 nm laser excitation was used for geological, forensic, and geobiological analysis which includes inorganic and organic minerals (Vítek et al., 2012). A Laser-Induced Breakdown Spectroscopy (LIBS) technique used for terrestrial mineral rocks was reviewed by Senesi, 2014. The adsorption tube method was compared in four factories using organic solvent mixtures using modified classical least-squares lineshape fitting using CALCMET^{TM} software (CALCMET, 2017) to identify and quantify the compounds.

2.6.6 Review papers in spectroscopic analysis

An in-depth review concerning the applications of portable infrared spectroscopy has been published (Workman Jr, 1999). Another review summarized toxic metal contamination (agriculture applications) which involved soil analysis using LIBS was presented by Peng et al., 2016. NIR spectroscopy for monitoring the soil contamination was reviewed by Cozzolino (2016) (Cozzolino, 2016). The estimation of the bidirectional reflectance distribution function (BRDF) from directional reflectance measurements was also reviewed by Meroni & Colombo, (2009). Twenty years of development in field spectroscopy and reflectance factor calculation has been reviewed by Milton et al. (2009). The applications of infrared spectroscopy and chemometric for the characterization of petroleum products was reviewed by Khanmohammadi et al. (2012) (Khanmohammadi et al., 2012). A geological remote sensing application is reviewed by Bishop et al. (2018) (Bishop et al., 2018) which involved many applications of airborne infrared spectroscopy.

2.7 summary

In view of the above mentioned research studies, the variety of the parameters for applications of hyperspectral infrared imagery in the form of portable instruments is significant in terms of mineral identification and utilization of the system on a small grain scale (indicator minerals). Numerous research studies have used hyperspectral infrared imagery and particularly mineral mapping large-sized mineral samples located at a significant distance from the infrared cameras (Feng et al., 2017; Mercurio et al., 2018; Lee et al., 2015; Black et al., 2016; Mir-Marqués et al.,

2016; Calvin and Pace, 2016; Scafutto et al., 2016; Kruse et al., 2002b; Vaughan and Calvin, 2004). However, the proposed applications of this research are limited for LWIR hyperspectral infrared imagery for small grains. Therefore, the identification of these small grains could lead to the identification of new mines or the abundance of a particular mineral presence which would not only provide a great benefit in terms of mineralogy but could also demonstrate that the system can be considerably beneficial and can represent an efficient computer-aided identification which can be used to assist geologists and mineralogy experts in the field or laboratory conditions.

Chapter 3

Issue, hypothesis and objectives

3.1 Problem Statement

The identification of minerals is challenging in the field of geology and mineralogy. The problem of mineral identification initially relates to geological research and is usually conducted by geologists. The manual process is time consuming, but also requires specially trained geologists. Poor identification can cause mis-classification of the minerals. The recent technological advancements in hyperspectral infrared technology have led to extensive investigations involving by hyperspectral portable instruments for the identification of minerals, giving rise of many research studies, and the development of many methods developed to perform the identification process. However, the identification of small grains has not received much attention and one of the reasons might be due to the a new level of challenges which involve different research perspectives such as mineralogy and chemical composition of the minerals, thermography and infrared analysis, spectral analysis, and data-mining. Small grain identification through the hyperspectral camera requires higher spatial resolution. Conducting hyperspectral infrared acquisitions in laboratory conditions involves a detailed investigation on a small scale to confirm the accurate identification. The collected geological samples require detailed analysis to identify the targeted mineral, which can then be also used for system validation. Furthermore, an automated mineral identification system which creates reasonable results mainly depends on the pre- spectral analysis. Without research development in this field, the process of small grain mineral identification would remain a geological and manual identification problem which is a time-consuming process and involves a high level of disparity due to fatigue or any other method for this specific application.

3.2   Objectives

The main objective of this research is to create a tool to use hyperspectral infrared imagery data and process the data through image analysis and machine learning methods to identify small size mineral grains. This research targets the analysis and development of the current existing techniques for spectral comparison and mineral identification. The research objective involves the development of hyperspectral techniques through data-mining approaches and their use for the identification purposes. The development and modification focuses on laboratory applications and can be generalized for any other type of spectroscopy or hyperspectral infrared bands. The objectives of this project can be summarized as follow:

1) Preparing grains and making a setup to take hyperspectral infrared images;

2) Retrieving the spectra obtained by acquisitions (Continuum Removal);

3) Using data-mining approaches to automatize the mineral identification process;

4) Create corresponding Ground Truth sets to validate and benchmark the automated approaches.

3.3   Hypothesis

Hyperspectral infrared imagery has the potential of being a useful tool to identify the small mineral grains through spectral data assessment. This system can be developed to automatically perform the process through the application of automated/semi-automated or supervised/unsupervised data analysis. This involves pre-processing spectral analysis to create viable spectral data and spectral comparison analysis between Advanced Space-borne Thermal Emission and Reflection Radiometer (ASTER) mineral library at NASA Jet Propulsion Laboratory (JPL) (Baldridge et al. 2009) or United States Geological Survey (USGS) spectral library (Clark et al. 2007) and targeted spectra within the region of interests. The aforementioned techniques may be useful to study the impact of hyperspectral infrared imagery and data-mining analysis on small grain identification which can be validated by using a ground truth data-set. A brief summary of proposed hypothesis is presented as below:

- Hyperspectral infrared imagery is a useful tool to identify the small mineral grains;

- Pre-processing spectral analysis create a possibility to use spectral comparison analysis;

- Supervised and Unsupervised learning approaches can make the process automatized;

- Other analysis such as (X-ray) can be a potential method to make a ground truth sets.

3.4 Scope and Significance of Study

The scope of the study is defined by the replacement of geologist/mineralogy manual work into an automated/semi-automated segmentation system having hyperspectral images as its input. The mineral identification by the developed methods can eliminate some of the disparities which occur during mineral identification and alleviate the computational complexity.

The mentioned research subject can contribute in various research topics and has applications which principally can involve many fields such as: thermography, data-mining, pattern recognition, and hyperspectral infrared image analysis. However, the major definition lies under geological/mineralogy sciences and it also includes applied science. There is basically an interconnection among the above mentioned fields in geological applications related to mineral identification.

3.5 Methodology

The proposed system follows the segmentation of mineral regions in the hyperspectral infrared images obtained by our experiments. There are two categories of mineral grains used in our tests, unmixed grain samples (pure samples [1]) and mixed grains samples, which are used in training and testing stages, respectively, while supervised learning methods used. The methods used for the system follow the hypothesis and objective of this research and mentioned as follows:

- Data retrieval (for continuum removal);
- Evaluation of the supervised/unsupervised approaches for identification;
- Sensitivity check for automated approaches;
- Verification and reliability;

---

[1]This type of sample has only one mineral type and purity does not imply the purity on a chemical or geological composition level.

Step 1 (Chapter 4)	**Data retrieval** (Continuum Removal)	**Contribution:** New method of continuum removal by twice image acquisitions
Step 2 (Chapter 5)	**Mineral Identification** (Supervised/unsupervised approaches)	**Contribution:** Comparison analysis of Classification and clustering Generating spectral reference by Low rank Sparse PCA
Step 3 (Chapter 6)	**Clustering sterategies**	**Contribution:** Comparison analysis of two clustering algorithms
Step 4 (Chapter 7)	**Reliability check**	**Contribution:** New way to assess the accuracy an reliability verification

Table 3.1: The flowchart of the proposed method is shown.

The automated methods are basically divided into two main categories: supervised approaches which need training and testing stages and labeling the data; and unsupervised learning approaches that involve direct grouping of the spectra into the different categories. It is expected that spectral references (such as ASTER/JPL or USGS mineral libraries) will be used in both of the cases for segmentation or validation of the methods.

Chapter 4

Continuum removal for ground based LWIR hyperspectral infrared imagery applying non-negative matrix factorization

4.1 Résumé

L'élimination du continuum est une étape essentielle dans le processus d'analyse d'images hyperspectrales qui permet d'utiliser les données pour toutes les applications et nécessite généralement certaines approximations ou hypothèses à effectuer. Une de ces approximations est liée au calcul des spectres de la température de corps noir de l'arrière plan. Nous présentons ici une nouvelle méthode pour calculer le processus d'élimination du continuum qui élimine ce calcul pour l'imagerie infrarouge hyperspectrale au sol en appliquant deux ensembles d'acquisition avant et après l'utilisation de la source de chauffage. L'approche décrit une expérience en laboratoire avec les ondes infrarouges longues (de $7.7\mu m$ à 11.8 μm), avec une lentille LWIR-macro, une plaque Infragold et une source de chauffage. Pour calculer l'élimination du continuum, l'approche applique la factorisation matricielle non négative (NMF) pour extraire le NMF de rang 1 et estimer le rayonnement de downwelling, puis compare le résultat avec d'autres méthodes conventionnelles. Pour obtenir le NMF de rang 1, on utilise des algorithmes d'optimisation basés sur la descente de gradient (GD) et des moindres carrés non négatifs (NNLS). L'analyse comparative est réalisée avec un bruit additionnel de $1 - 10\%$ pour tous les algorithmes utilisant Spectral Angle Mapper (SAM) et la Normal Correliation Corrélation (NCC). Les résultats indiquent une performance relativement prometteuse en utilisant NMF-GD (moyenne de 72.5% pourcentage de similarité en utilisant NCC) et NMF-NNLS (moyenne de 77.6% de similitude en utilisant la NCC).

General Explanation

Although the process of mineral identification is highly depended on the comparison of spectra between the minerals and references from spectral libraries, a major issue in terms of having the comparable spectral data is always challenge the process. To alleviate such matter, here a method for Continuum Removal (CR) process is proposed for Long Wave Infrared (LWIR) which modified a previously mentioned approach Balick et al. (2009) and employs two times hyperspectral acquisitions, with and without the heating source. In addition, Non-Negative Matrix Factorization (NMF) is also deployed to robustness of down-welling spectra.

The results of this study were partially presented at the poster session of the International Congress on Thermal Infrared Applications XXXVIII (Thermosense), May 2016, Baltimore, USA.

Contributing authors:

Bardia Yousefi (Ph.D. candidate): a part of the experiment planning, data collection, data analysis, designing and implementing the algorithm. Moreover, testing their accuracy and robustness throughout the process and writing the manuscript.

Saeed Sojasi: assisting the experiment planning, data collection, mineral preparation.

Clemente Ibarra Castanedo: the experiment planning, data collection, mineral preparation, revision and correction of the manuscript.

Xavier P.V. Maldague and **Georges Beaudoin**: (The main research director and co-director, respectively): supervision, revision and correction of the manuscript.

Martin Chamberland: Providing the LWIR hyperspectral camera, experiment planning, data collection, guidance for improvement of down-welling calculation, providing comments for manuscript.

Other contributors:
Annette Schwerdtfeger (research officer): manuscript preparation.

Continuum removal for ground based LWIR hyperspectral infrared imagery applying non-negative matrix factorization

Bardia Yousefi[1], Saeed Sojasi[1], Clemente Ibarra Castanedo[1], Xavier P.V. Maldague[1], Georges Beaudoin[2], Martin Chamberland[3]

[1] *Computer Vision and System Laboratory, Department of Electrical and Computer Engineering, Laval University, 1065, av. de la Médecine, Quebec, QC, Canada*

[2] *Department of Geology and Geological Engineering, Laval University, 1065, av. de la Médecine, Quebec, QC, Canada*

[3] *Telops, Inc., 100-2600 St-Jean-Baptiste Ave, Quebec City, QC, G2E 6J5, Canada*

Corresponding author: bardia.yousefi.1@ulaval.ca

4.2 Abstract

Continuum removal is vital in hyperspectral image analysis. It enables data to be used for any application and usually requires approximations or assumptions to be made. One of these approximations is related to the calculation of the spectra of the backgroundâs blackbody temperature. Here, we present a new method to calculate the continuum removal process. The proposed method eliminates the calculation for ground-based hyperspectral infrared imagery by applying two acquisition sets before and after using the heating source. The approach involves a laboratory experiment on a long-wave infrared (7.7μm to 11.8μm - LWIR), with a LWIR-macro lens, an Infragold plate and a heating source. To calculate the continuum removal process, the approach applies non-negative matrix factorization (NMF) to extract Rank-1 NMF, estimate the downwelling radiance and compare it with that of other conventional methods. NMF uses gradient-descent-based multiplicative rules (GD) and non-negative least squares (NNLS) optimization algorithms to obtain Rank-1 NMF. A comparative analysis is performed with 1%20% additive noise for all algorithms by using the spectral angle mapper and normalized cross correlation (NCC). Results reveal the promising performance of NMF-GD (average of 72.5% similarity percentage using NCC) and NMF-NNLS (average of 77.6% similarity percentage using NCC).

Keywords: Long-wave infrared hyperspectral imaging; Continuum removal; spectral comparison method; Ground based hyperspectral imagery; Mineral identification.

4.3 Introduction

Hyperspectral infrared imagery has been used in remote sensing and airborne imaging in the past three decades. Apart from optical and thermographic equipment improvements, the process and data mining developments in this field have also displayed remarkable growth and have been adopted in various applications, such as target detection (Nasrabadi, 2014; Mayer et al., 2003), aviation (Wang et al., 2016), spectral unmixing (Eismann and Hardie, 2004) and geology (Kruse, 1996b; Yajima et al., 2004; Davis, 2001; Hirsch and Agassi, 2010). An important element in successful data analysis is proper spectral information retrieval, that is, continuum removal (CR), at the beginning of the analysis. A continuum in hyperspectral infrared imagery is mainly caused by solar energy or the heating source. Many methods have been developed to retrieve spectra and perform CR. These methods were proposed for remote sensing, airborne-type data analysis (Thulin et al., 2004; Sanches et al., 2014), endmember-based algorithms (Filippi and Jensen, 2007) and retrieval of emissivity and downwelling radiation by using the spectral radiance of rocks (Balick et al., 2009b). The process for ground-based hyperspectral imagery (Kruse, 1996b; Yajima et al., 2004; Sun and Khan, 2016; Krupnik et al., 2016) is similar but involves close-range acquisitions. It has been extensively used in different applications, including quality control in chemical reactions (Aksenova et al.; Ghasemzadeh-Barvarz et al., 2013), raw material sorting in the tobacco industry (Garcia-Allende et al., 2008), investigation of anomalies in target detection (Heinz et al., 2010), checking of exhaust from diesel-fuelled turbine technologies (Bradley et al., 2010) and geology (Balick et al., 2009b). Active-thermography ground-based close-range imagery allows for the use of a heating source in the place of any other source (e.g. solar energy in airborne or remote sensing applications). The process of hyperspectral analysis is similar in long- and close-range hyperspectral imagery, but the use of a heating source usually allows for increased control on the experiment (Yousefi et al., 2016b). One of the early studies on determining sample emissivity was conducted by Salisbury et al. (1991) (Salisbury and Vergo, 1991), who estimated the reflectance and transmittance spectra of 78 minerals in mid-wavelength infrared. The authors calculated the effect of different particle size ranges and the scattering effect. Thermal infrared for remote sensing and Kirchhoff's law were investigated for directional hemispherical reflectance and directional emittance measurements of rock and soil in a laboratory (Salisbury et al., 1994). Korb et al. (1996) calculated the radiance (downwelling) and emissivity for a Fourier transform in-

frared spectroradiometer (FTIR) for 3-5 μm and 8-14 μm atmospheric windows (Hecker et al., 2010), followed by the development of the μFTIR system (Reath and Ramsey, 2013) and laboratory technique for measurement and calibration (Ruff et al., 1997) and for the emissivity and reflectance of soil (Sobrino et al., 2009). Gomez et al. (2008) also presented a partial least-squares regression (PLSR) method for clay and calcium carbonate content estimation at visible and near-infrared (VNIR, 400-1200 nm) and shortwave infrared (SWIR, 1200-2500 nm) for airborne hyperspectral measurements (Gomez et al., 2008). Malenovsky et al. (2013) proposed a neural network-based CR for spruce leaf chlorophyll content estimation (Malenovskỳ et al., 2013). The continuum-removed absorption features used for predicting in situ pasture quality adopted the standard first derivative reflectance (FDR), band depth (BD) and band depth ratio (BDR) in airborne imaging spectrometers (Mutanga et al., 2004). Moreover, a continuum removal analysis was performed in a previous study to estimate foliage nitrogen concentration in HYMAP sensor data by using modified partial-least squares (MPLS) (Huang et al., 2004b). Balick et al. (2009) (Balick et al., 2009a) presented an emissivity retrieval method using field-portable imaging radiometric spectrometer technology mid-wave extended (FIRST-MWE) and calculated atmospheric downwelling spectral radiance. The research involved a similar continuum removal method although the calculation was for non-ground based spectroscopy.

The proposed approach modifies the Balick method (Balick et al., 2009a) by eliminating its dependency on the blackbody spectra at surface temperature. Our approach involves a series of experiments conducted using a Telops Long Wave Infrared (LWIR) hyperspectral camera in close range for small mineral grains. Moreover, the approach proposes another modification for CR calculation by applying first-rank NMF instead of the previously used spectral averaging or random selection of spectra, thus increasing efficiency. The remainder of the paper is organized as follows. Section 2 provides information about the hyperspectral infrared camera and targeted minerals. Section 3 presents the methodology and explains how continuum removal and segmentation are performed. Section 4 describes the experimental and simulation results. A short discussion is presented in Section 5, and the conclusions and directions for future work are provided in Section 6.

Table 4.1: A brief review of the characteristics of the minerals investigated in this study.

Minerals	Chemical formula	Short Description
Biotite	$K(Mg,Fe)_{2-3}Al_{1-2}Si_{2-3}O_{10}(OH,F)_2$	substantial group of dark mica minerals.
Diopside	$MgCaSi_2O_6$	Forms complete solid solution series with hedenbergite ($FeCaSi2O_6$) and augite, and partial solid solutions with orthopyroxene and pigeonite.
Epidote	$Ca_2(Al_2,Fe)(SiO_4)(Si_2O_7)O(OH)$	silicate mineral.
Tourmaline	$((Na, Ca)(Mg,Li,Al,Fe^{2+})_3Al_6(BO_3)_3Si_6O_{18}(OH)_4)$	boron silicate minerals compounded with element such as Al, Fe, Mg, Na, Li or K.
Olivine	$(Mg^{+2}, Fe^{+2})_2 SiO_4$	
Pyrope	$Mg_3 Al_2 (SiO_4)_3$	garnet group minerals.
Quartz	SiO_2	the most abundant mineral in the Earth's crust.

Grains of olivine & quartz
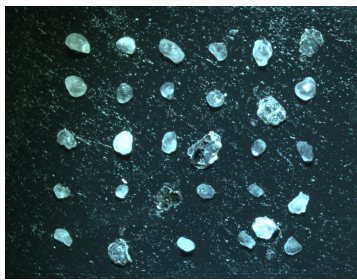
Grains of biotite & quartz

Sample of olivine & quartz

Infragold plate and grains sample

Radiation Source

Display and Acquisition

13 cm

~25cm

Hyperspectral Infrared Camera

Control

Scheme of the experimental setup

Heating Source hyperspectral infrared camera

Infragold plate
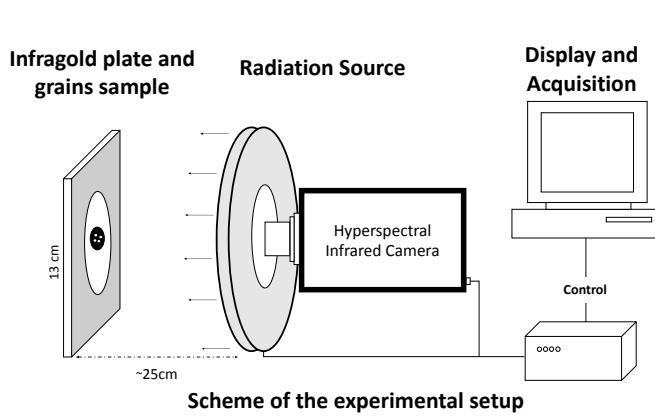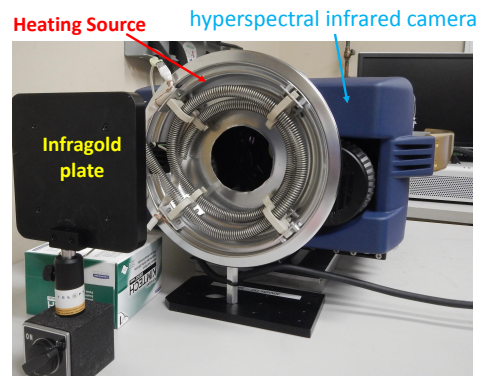
Experimental setup

Figure 4.1: The experimental setup is shown along with the binocular image of the samples and the scheme of the experimental setup.

4.4 Data

4.4.1 Sensor

The sensor used to make the measurements was a lightweight FIRST hyper-camera imaging spectroradiometer (HYPER-CAM LW) (Telops, 2016) operating in the long-wave infrared (LWIR) band (from 7.7 to $11.8\mu m$). The sensor has a Stirling-cooled indium antimonide (InSb) focal plane array (FPA) that contains 320×256 pixels. It has a spectral resolution of 0.25 cm^{-1}. The spectral resolution of the spectrometer, 6 $cm^{-1}(\sim 0.0119\mu m$ at $7.7\mu m$ and $\sim 0 : 0465\mu m$ at 11.8 μm), provided 88 spectral bands. The spatial extent of the scene was windowed to a small field of view (FOV) to increase the temporal resolution. The spectra were measured using a Fourier transform spectrometer (FTS), and the hyper-camera measured a complete spectrum for every pixel using an LW macro 50 $\times10^4\mu m$ lens providing an instantaneous FOV of 0.35 mrad (Kruse, 1996a). Measurements were performed from a distance of 35 cm, which provided a pixel footprint of 0.1 $\times10^4\mu m$. Figure 4.1 presents the experimental setup and binocular images of the samples. A heating source was placed in front of the samples (active thermography [1]) and provided heating energy during the experiment. Image acquisition was continued after turning off the heating source to achieve a gradual cooling effect (several minutes). For optimal results, the grains were attached to adhesive carbon-based tape, and an Infragold plate was placed on the background. Its reflectance assisted in removing the continuum from the spectrum. The images were obtained perpendicular to the mineral grains under uniform heating by the source.

4.4.2 Grain samples and reference panels

The problem of spatial resolution was not an issue because a magnification lens was used for the FOV of the sensor. Figure 4.1 shows a photograph of the minerals obtained with a binocular microscope and the scheme of the experimental setup. Seven mineral grains (biotite, diopside, epidote, tourmaline, pyrope, olivine and quartz) are presented in Table 4.1, which provides a brief review of the minerals and their chemical formulas. A square InfraGold plate (Labsphere, North Sutton, NH, USA) (r19) was placed in the scene of the grains as a reference

---

[1]Active thermography occurs once an energy source creates thermal contrast for the specimens and background (Maldague, 2001). An example of active thermography was provided in (Zhang et al., 2016b).
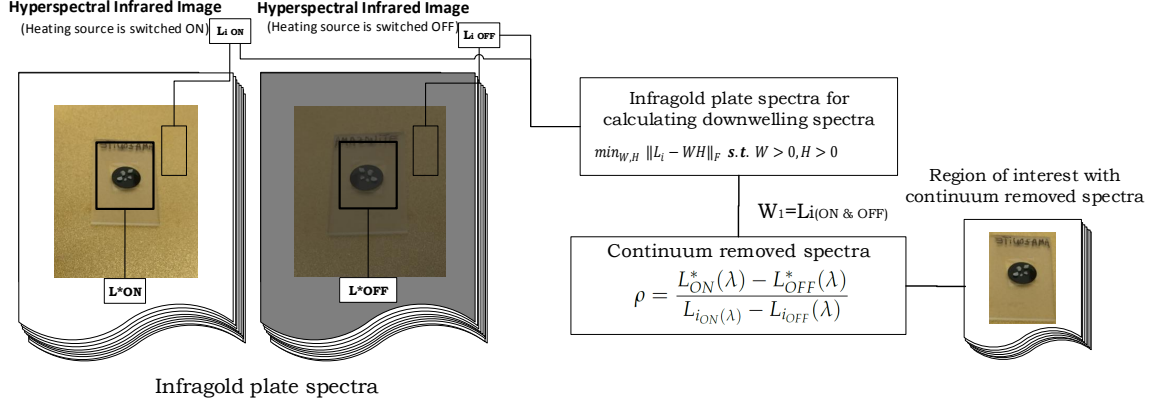
Figure 4.2: Flowchart which shows the proposed approach for the estimation of the downwelling radiance among all the possible points. In the figure, $W_1 = L_{i(ON\&OFF)}$ represents the spectral of Infragold with and without the heating source.

panel. According to the information provided by the manufacturer, the panel has a reflectivity of $92\% - 96\%$ for $10^4 \mu m$ to $16 \times 10^4 \mu m$ wavelength radiation. For the range of the FIRST camera, the spectral reflectance is approximately between 96% and 97% by DuraflectÂ® coatings of 0.94-0.96 (r19). The emissivity of the panel is very low, which makes it insensitive to temperature. The panel was placed in a perpendicular position in front of the hyperspectral camera.

4.5 ANALYSIS

Here, the proposed method is presented by downwelling radiance calculation, continuum removal and Infragold and thermal image analyses using $Rank^1$ NMF (Figure 4.2 presents the flowchart of proposed approach).

4.5.1 Downwelling radiance calculation

Following the protocols for accurate determination of sample emissivity (Hecker et al., 2010; Reath and Ramsey, 2013; Ruff et al., 1997; Resnick et al., 1999) and considering the modification of Balick et al. (2009) (Balick et al., 2009a) while noting that the distance between the samples and camera is short, the downwelling spectral radiance ($L_i(\lambda)$) in the atmospheric environment was calculated with the equation

$$L_i(\lambda) = \frac{L^*(\lambda) - \varepsilon BB(\lambda, T_s)}{\rho} \tag{4.1}$$

where L^* is the measured spectral radiance of the panel and $BB(\lambda, T_s)$ is the spectra of the blackbody at a surface temperature of T_s. ε and ρ are the emissivity and reflectivity of the panel, respectively (Balick et al., 2009a). In ideal conditions, the surface temperature of the panel and the measured temperature are similar. Considering that the specimen has a very low transmission of infrared energy (~ 0), then according to Kirchhoff's law (Kirchhoff, 1860; Salisbury et al., 1994), $1 = \varepsilon + \rho$. Thus, the aforementioned equation can be rewritten based on the measured spectral radiance.

$$L^*(\lambda) = \varepsilon BB(\lambda, T_s) + (1 - \varepsilon)L_i(\lambda) \tag{4.2}$$

The measured spectral radiance is a parameter that is related to the emissivity of the panel and blackbody spectral radiance.

4.5.2 Continuum removal

To calculate the reflectance spectrum that contains no continuum, the measured spectral radiance of the specimen was divided by the entire spectrum radiated from the heating source (Fig. 4.3). The InfraGold plate was used to estimate the total radiance from the source (or downwelling radiance L_i) because it ideally reflects $\sim 100\%$ of the input radiance. Given that these experiments strive to calculate the ground spectra and control of the heat source is
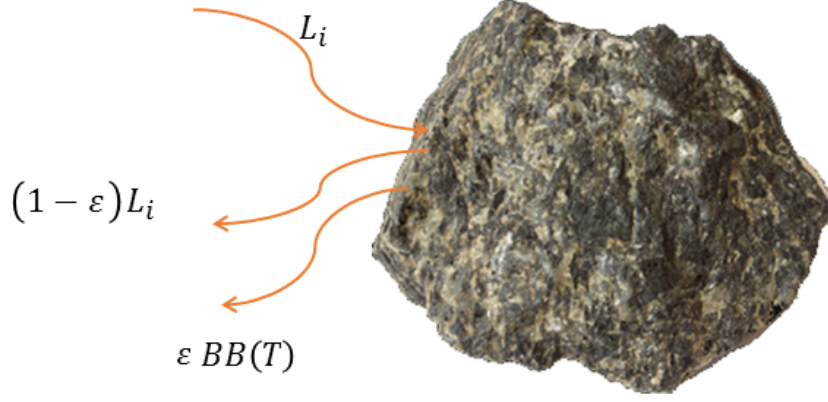
Figure 4.3: The spectral radiance from the source and its reflection from the mineral grain is shown.

possible, we performed image acquisition twice: once while the heating source was switched on and once while the heating source was switched off (4.7). Then, we obtained

$$
\begin{cases}
L_{ON}^*(\lambda) = \varepsilon BB(\lambda, T_s) + (1 - \varepsilon)L_{i_{ON}}(\lambda) \\
L_{OFF}^*(\lambda) = \varepsilon BB(\lambda, T_s) + (1 - \varepsilon)L_{i_{OFF}}(\lambda)
\end{cases}
\tag{4.3}
$$

Considering that the temperature of the blackbody with or without heating is the same, if we subtract the two previous equations from each other, then we will have

$$
L_{ON}^*(\lambda) - L_{OFF}^*(\lambda) =
$$

$$
\varepsilon BB(\lambda, T_s) - \varepsilon BB(\lambda, T_s) + (1 - \varepsilon)L_{i_{ON}}(\lambda) - (1 - \varepsilon)L_{i_{OFF}}(\lambda)
\tag{4.4}
$$

In Equation (4), the blackbody spectral radiance of the panel at the surface temperature, $BB(\lambda, T_s)$, and the emissivity of the plate, ε, have the same value when the heating source is in the circuit or out of the experiment. Thus, the return radiance amount from the mineral grain is given by

$$L_{ON}^*(\lambda) - L_{OFF}^*(\lambda) = (1 - \varepsilon)(L_{i_{ON}}(\lambda) - L_{i_{OFF}}(\lambda)) \tag{4.5}$$

The reflectivity spectra of a factor that is independent of the blackbody spectral radiance were then calculated, and we obtained

$$\rho = \frac{L_{ON}^*(\lambda) - L_{OFF}^*(\lambda)}{L_{i_{ON}}^p(\lambda) - L_{i_{OFF}}^p(\lambda)} \tag{4.6}$$

This equation has reflectivity spectral radiance whose continuum is already suppressed. Equation (6) represents the continuum removal for our ground-based spectra that is solely dependent on the measured spectral radiance from the surface of mineral grains and the Infragold plate. In the equation, $L_{i_{ON}}(\lambda)$ and $(L_{i_{OFF}}(\lambda)$ are converted to $L_{i_{ON}}^p(\lambda)$ and $L_{i_{OFF}}^p(\lambda)$ to emphasis the pixel-scale dependency of the downwelling spectral radiance.

4.5.3 Infragold and thermal image analysis using Rank-1 NMF

Following Equation (6), the spectral radiance of the Infragold plate is needed to calculate the downwelling spectral radiance L_i (for L_{iON} and L_{iOFF}). Since the Infragold plate reflects the entire radiance, we calculated a representative spectral radiance to include in Equation (6). To measure the spectral radiance, some pixel spectra in Infragold were manually selected and used to calculate downwelling radiance. Multifarious techniques, such as random selection and spectra averaging, are often adopted to achieve this purpose, but these techniques are attenuated when faced with noise or incorrect selection of the Infragold region. Random selection of downwelling spectral radiance is not an appropriate means of determining the spectra because this method may select the wrong spectrum. By contrast, spectral averaging is a more reasonable means to estimate the spectra, but it is theoretically insensitive to non-homogeneous spectral grouping. For example, if the selected region of the Infragold plate extends beyond the plate itself, the averaging might be influenced by the spectral radiance of other regions. Several other approaches, such as eigen decomposition methods, improve spectrum selection (Golub and Van Loan, 2012; Franklin, 2012). For example, principal component analysis (PCA) (Pearson, 1901; Jolliffe, 1986) is a popular method that can select the principal component spectrum of a selected region, but having negative values in its calculation leads to
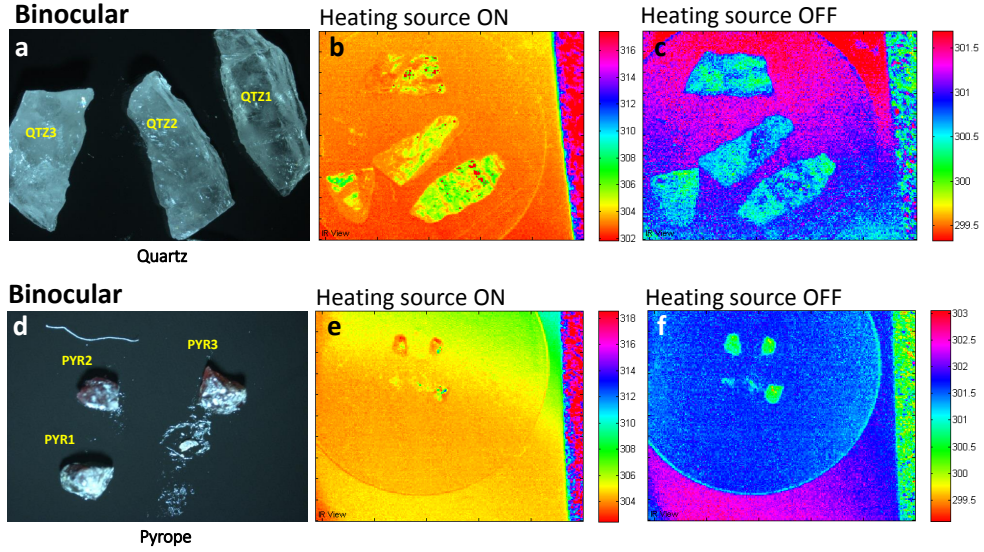
Figure 4.4: The IR-images were taken before (left-side thermal images in each mineral(**c**,**f**)) and after (right-side thermal images in each mineral (**b**,**e**)) heating the mineral grains. The binocular images from the grains are also shown on left side of each example (**a**,**d**).

an uncertainty in its application in choosing the best representation of reconstructed spectra (first basis vector). This problem is solved by different modifications (such as (Panagakis et al., 2010)) or non-negative matrix factorization (NMF) (Sra and Dhillon, 2006; Ding, 2005; Lee and Seung, 1999).

The approach presented in this study calculates the aforementioned radiance (particularly for a non-uniform heating source) by applying NMF. NMF is a factor analysis method that provides an unsupervised linear representation of the data similar to PCA. However, by using non-negative coefficients in the calculation of eigenvalues, the issue with PCA is solved. NMF produces the basis from data representations and can be formulated using the following optimization problem (Ding et al., 2005).

$$min_{W,H}\|L_i - WH\|_F \quad s.t. \ \ W \geq 0, H \geq 0 \tag{4.7}$$

L_i refers to all possible points of spectral radiance in the Infragold plate while the heating source is switched on and off, with the assumption that the measured T in our data consists of N non-negative scalar variables.

$$L_{N \times M} \approx W_{N \times T} H_{T \times M} \tag{4.8}$$

W is an $N \times T$ matrix that includes the basis vectors w_i as its columns. Every measured vector is shown by the same basis vectors. W has N basis vectors and can be represented by "building blocks" of the data having T-dimension. H denotes the coefficient matrix and explains the level of power for every building block, where ℓ_i is a measurement vector. H includes the coefficient vector h_t corresponding to the measurement vector ℓ_t, which produces a linear data representation obtained from data factorization. In general, M is the number of observations in matrix L_i. W contains the basis vectors that are needed to determine the best representative of spectral radiance and is even used for clustering (Lee and Seung, 1999).

$$L_{N \times M} = \begin{bmatrix} \ell_{i\,1,1} & \ell_{i\,1,2} & ... & \ell_{i\,1,m} \\ \ell_{i\,2,1} & \ell_{i\,2,2} & ... & \ell_{i\,2,m} \\ . & & & . \\ . & & & . \\ . & & & . \\ \ell_{i\,n,1} & \ell_{i\,n,2} & ... & \ell_{i\,n,m} \end{bmatrix} \tag{4.9}$$

$$W_{N \times T} = \begin{bmatrix} w_{i\,1,1} & w_{i\,1,2} & ... & w_{i\,1,t} \\ w_{i\,2,1} & w_{i\,2,2} & ... & w_{i\,2,t} \\ . & & & . \\ . & & & . \\ w_{i\,n,1} & w_{i\,n,2} & ... & w_{i\,n,t} \end{bmatrix} \tag{4.10}$$

In the equation, $[\ell_{i\,1,1}, \ell_{i\,2,1}, ..., \ell_{i\,n,1}]^T$ shows the first pixel spectrum selected from the Infragold plate that has $W^1 = [w_{i\,1,1}, w_{i\,2,1}, ..., w_{i\,n,1}]^T$ basis vectors corresponding to it. $T = 1$ is a very particular case because the optimal solution is given by SVD, and performing successive minimization by H with fixed W and vice versa is not needed. This case is used for the extraction of the best spectral representative of the Infragold plate (downwelling spectrum), W^1. NMF performs as a clustering method to group the spectra in different categories (similar to (Lee and Seung, 1999)), whereas Rank-1 NMF does not allow further grouping because it limits the clustering to abundant spectra existing in the input data (ROI mainly consists of the Infragold region). NMF is still considered a linear method for non-negative approximation (standard NMF can be calculated by two optimization algorithms: gradient-descent-based multiplicative rules (GD) and non-negative least squares (NNLS)) (Lee and Seung, 1999; Panagakis et al., 2010; Cho and Choi, 2005). NNLS is a constrained form of the least-squares problem and applies a similar minimization strategy for the minimization of NMF, considering the non-negative constraints to control the coefficients. NMF is applied by NNLS to Equation (7), given a matrix W and vectorized matrix L_i. The goal is to solve the Euclidean norm problem and ultimately perform the mentioned minimization (Chen and Plemmons, 2010). NMF through GD converts the minimization problem to a first-order iterative optimization algorithm. It finds the local minimum by applying gradient calculation and its direction towards the minimization through steps proportional to the negative gradient from the current point. If Equation (7) is represented by $G(w)$ and w_n represents the current observation point, then the minimization w_{n+1} should be selected based on $w_{n+1} = w_n - \gamma G(w_n)$, where γ is the step size and $G(w_n) \geq G(w_{n+1})$ (Kiwiel, 2001).
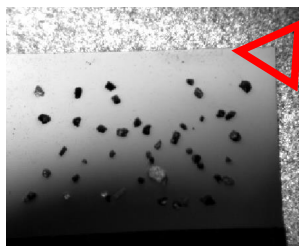
Infragold ROI region selected in hyperspectral image
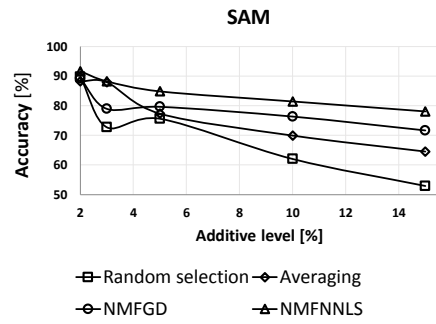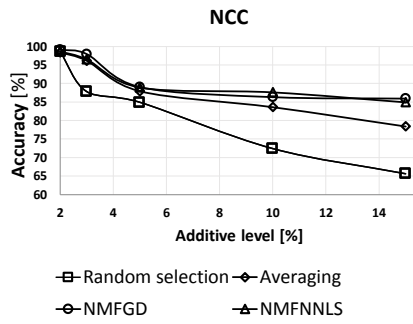
Figure 4.5: The similarity percentage of spectra while Infragold region wrongly selected based on the mis-selection percentage is also mentioned.

Table 4.2: The computational time (CPU time) is shown for each part of the method for around 1000 pixels of Infragold plate.

Mineral	Computational Complexity			
	Averaging	NMFGD	NMFNNLS	Random
Biotite	0.2	0.79	1.18	0.28
Diopside	0.18	0.68	1.31	0.28
Epidote	0.18	0.98	1.33	0.26
Tourmaline	0.18	0.62	1.32	0.26
Pyrope	0.16	0.60	1.21	0.23
Olivine	0.17	0.76	1.11	0.23
Quartz	0.19	0.79	1.12	0.24

Table 4.3: The similarity percentage of the continuum removed approach in comparison with the reference spectra from the ASTER/JPL spectral library is measured. Also the robustness of the approach is shown applying additive noise.

Mineral	Noise	Method (%)							
		NCC				SAM			
		Average	NMFGD	NMFNNLS	Random selection	Average	NMFGD	NMFNNLS	Random selection
Biotite	0%	90.3	89.9	86.8	90.1	72.3	71.9	69.9	72.2
	1%	93.1	92.9	89.9	90.2	78.9	78.8	76.5	73.5
	2%	89.3	89.3	85.2	75.1	70.9	70.9	68.3	51.2
	5%	92.9	91.7	89.4	21.4	78.7	76.9	75.9	<1
	10%	89.2	78.5	83.2	6.3	70.9	59.2	64.7	<1
	20%	74.1	66.4	76.3	<1	62.2	49.8	59.8	<1
Diopside	0%	72.2	72.8	74.3	71.8	57.5	58.3	60.8	56.9
	1%	71.4	71.2	74.2	69.7	57.9	57.6	62.6	57.1
	2%	71.8	72.5	75.4	64.5	57.8	58.6	62.7	49.4
	5%	71.7	70.4	73.6	16.8	57.7	57.1	60.8	<1
	10%	71.5	56.2	71.5	<1	57.7	40.9	59.01	<1
	20%	68.4	51.1	69.2	<1	56.8	38.5	57.4	<1
Epidote	0%	84.4	82.1	84.8	84.6	66.1	62.8	68.4	66.4
	1%	85.3	85.7	87.7	82.8	63.5	63.9	67.2	61.6
	2%	82.8	82.9	86.8	79.9	64.1	64.3	69.8	61.7
	5%	84.3	84.7	83.9	4.8	65.9	65.5	67.2	<1
	10%	79.8	57.9	81.1	<1	62.7	39.7	63.9	<1
	20%	76.2	44.1	77.02	<1	61.4	28.02	61.8	<1
Tourmaline	0%	52.6	51.9	53.4	52.1	38.5	33.2	32.9	32.9
	1%	47.5	47.8	50.4	46.5	36.9	37.2	40.1	35.4
	2%	47.4	48.1	51.1	43.2	36.9	37.4	39.7	35.2
	5%	46.5	45.9	47.1	7.6	35.1	34.6	35.2	<1
	10%	50.8	29.6	55.9	9.6	30.3	26.8	34.1	<1
	20%	45.7	12.1	52.8	<1	28.01	22.9	31.2	<1
Pyrope	0%	93.5	94.1	75.4	93.5	44.9	46.1	28.4	44.5
	1%	93.9	93.9	86.6	88.4	54.8	56.1	41.5	51.8
	2%	92.7	93.4	85.9	75.2	55.8	56.5	43.1	48.3
	5%	92.2	93.3	87.5	4.1	62.3	63.7	53.1	<1
	10%	92.9	55.9	84.2	<1	56.2	33.3	45.1	<1
	20%	87.01	32.2	81.2	<1	52.2	28.2	42.1	<1
Olivine	0%	84.9	84.9	80.8	84.7	64.9	64.6	56.8	64.5
	1%	86.4	86.1	85.5	86.1	66.7	66.01	64.2	66.4
	2%	87.6	88.2	87.2	75.5	68.3	69.1	65.7	53.9
	5%	86.1	82.1	81.1	16.01	65.9	61.7	58.3	<1
	10%	86.1	28.1	81.1	<1	65.8	51.4	59.2	<1
	20%	80.9	21.5	80.4	<1	61.2	47.5	57.9	<1
Quartz	0%	73.6	75.2	82.3	75.3	62.2	62.8	65	62.5
	1%	70.4	69.6	80.7	66.5	61.9	61.7	65.9	58.7
	2%	73.5	75.5	80.3	64.1	62.1	62.9	63.3	53.7
	5%	68.6	63.4	77.1	11.6	63.7	57.5	66.8	<1
	10%	69.7	50.5	73.3	11.8	61.5	38.8	60.3	<1
	20%	64.2	47.9	70.6	5.8	57.3	28.1	57.8	<1
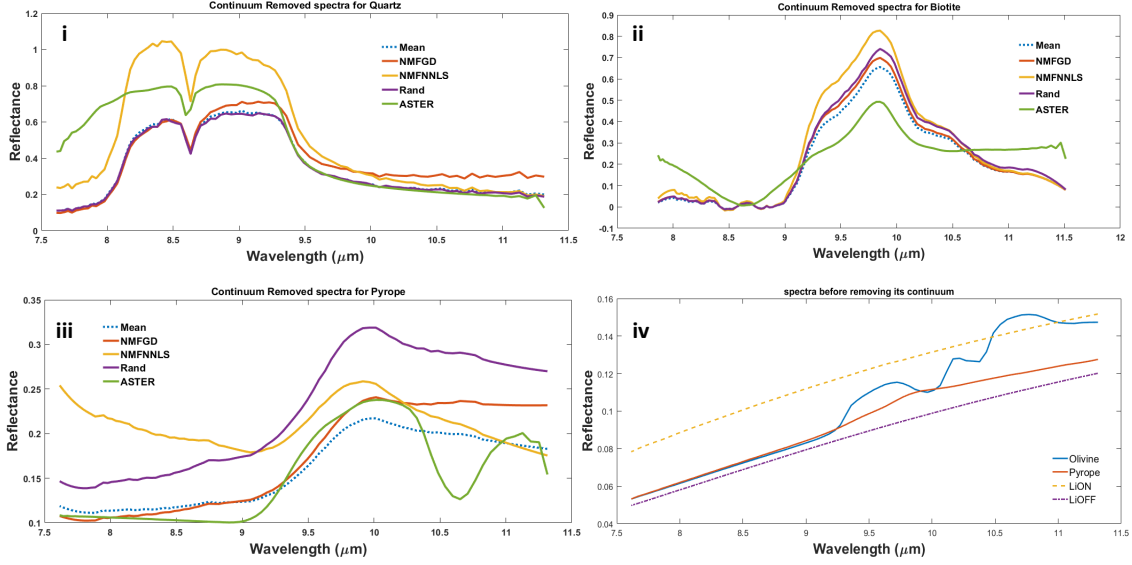
Figure 4.6: Some examples of the continuum removed spectra of pyrope, and quartz in the 7.7 μm to 11.8μm wavelength range are shown. The plot diagrams in each mineral depicts the spectra for the Infragold plate and some spectra from the surface of the mineral while the heating source is On and Off. Spectral radiance corresponding to the Infragold plate and three minerals space (quartz, biotite, and pyrope) are also shown in **i,ii,iii**. The spectral of radiance the Infragold panel and spectral of Olivine before continuum removal process are shown (**iv**). The downwelling radiance is calculated by subtracting these two spectra. The downwelling spectra of the other minerals are shown using this subtraction and presented with the reference spectra of the targeted mineral from the ASTER library.

4.5.4 Spectral comparison methods

Spectral angle mapper (SAM) is a method based on the physical property of a spectrum. It provides features for discrimination among spectra through an error generated by the angle difference between two vectors (target spectrum and its reference). SAM is used for n-dimensional geometrical space and determines the dissimilarity between the unknown spectrum t and the reference spectrum r by using the equation (Kruse et al., 1993a)

$$\alpha = \cos^{-1} \left[\frac{\sum_{i=1}^{n} t_i r_i}{\left[\sum_{i=1}^{n} t_i^2\right]^{1/2} \left[\sum_{i=1}^{n} r_i^2\right]^{1/2}} \right] \tag{4.11}$$

where n is the number of bands. For each pixel spectrum selected in the hyperspectral image cube, the spectral angle reference spectrum calculates an error. The radian values regarding every corresponding pixel at the output of SAM represent the difference in the spectral vector direction from that of the reference.

Normalized cross correlation (NCC) is a method to determine the correlation between two spectral data. NCC uses two types of entry: the data and their reference. It uses a formula for r through substitution-estimation of the covariances and variances based on a sample in the formula. If the dataset presented by $\{x_1, ...x_n\}$ includes n values and $\{y_1, ...y_n\}$ presents another dataset having n values, then the formula for r is

$$NCC = \frac{1}{n} \Sigma \frac{1}{\sigma_{f_{Data}} \sigma_{r_{Ref}}} (f_{Data} r_{Ref}). \tag{4.12}$$

where n is the number of pixel spectrum in f_{Data} and r_{Ref} (f_{Data} and r_{Ref} are normalized) and $\sigma_{f_{Data}}$ and r_{Ref} are standard deviations of f (data) and r (reference spectra) sets, respectively.

4.6 Results

A selected set of the spectra from the targeted minerals is given in Figure 4.6 along with the calculation of downwelling spectral radiance for the selected minerals. The proposed approach presented two novelties, namely, spectral (radiometric) information and statistical analysis. The computational analysis of hyperspectral data from both perspectives are presented here. The continuum-removed spectra using random selection, averaging, NMF-GD and NMF-NNLS for downwelling radiance are shown in Figures 4.6 i-iv. To compare the different radiance calculated by different methods, all radiance spectra are presented on the

same graphs. For a more quantitative assessment of the spectra obtained by each method, a reference spectral library was used, and the difference between targeted and reference spectra was calculated. The Advanced Space-borne Thermal Emission and Reflection Radiometer (ASTER) (Baldridge et al., 2009) library contains the spectra of nearly 2000 types of soils, rocks, minerals, snow, water and artificial minerals. Several of these spectra cover the wavelengths measured in this study (0.4-14 μm). The spectral data for each mineral cover visible, near-IR, mid-IR and thermal-IR wavelengths.

The difference between targeted and reference spectra was obtained using NCC and SAM. The main difficulties were related to using two different spectral resolutions in the calculation, which was performed by downsampling the high spectral resolution to a low resolution. Thus, NCC and SAM were applied to the four continuum-removed spectra obtained (spectral averaging, NMF-GD, NMF-NNLS and random selection). The computation results are presented in Figure 5 and Table 4.3 in percentages that express the quantitative similarity of these spectra with the reference spectra for additive noise and mis-selection of the Infragold plate, respectively. The level of similarity was reduced by adding noise for all of the methods, but random selection of spectra showed the highest sensitivity against noise compared with the three other methods. At a high level of noise, NMF showed a robust behavior (with the exception of pyrope and olivine). At a low level of additive noise, NMF-NNLS showed considerably higher robustness in the presence of noise for diopside, epidote, tourmaline and quartz, whereas in the pyrope case, NMF-GD showed higher robustness compared with the other methods. This result is due to the minimal dependency of NNLS on the amplitude of spectra in the calculation compared with the other methods involving NMF-GD, averaging and random selection of spectra (Figure 4.6). The signal-to-noise Ratio (SNR) was calculated for this approach by following the formulation

$$SNR = \frac{\mu_S}{\sigma_N} \tag{4.13}$$

where μ_S and σ_N are the average of the signal in the ROI region in the hyperspectral image and the standard deviation of noise, respectively (Figure 7 shows the graph of SNR when the additive noise level increases). Spectral averaging showed higher similarity with the reference spectra for biotite and olivine because of the higher reflectance of these minerals compared with the other minerals (Table 4.3). In general, SAM produced a lower similarity percentage

compared with NCC, but the similarity trend was nearly the same. Figure 5 shows the similarity percentage when the Infragold ROI includes other parts of the hyperspectral image (this region was added by additive pixel-spectral percentage). The results presented in Figure 5 reveal the higher robustness of averaging compared with random selection and the higher similarity measure for NMF compared with the two other methods (with the exception of 3% where the similarity of averaging is higher than that of NMF-GD).

Table 4.4: Comparative accuracy of the proposed approach is shown with PLSR.

Average NCC	Comparative accuracy				
	PLSR	Random selection	Averaging	NMFGD	NMFNNLS
Biotite	63.2	90.1	90.3	89.9	86.8
Diopside	61.2	71.8	72.2	72.8	74.3
Epidote	68.8	84.6	84.4	82.1	84.8
Tourmaline	44.7	52.6	51.9	53.4	52.1
Pyrope	90.1	93.5	93.5	94.1	75.4
Olivine	69.6	84.7	84.9	84.9	80.8
Quartz	70.7	75.3	73.6	75.2	82.3

The computation complexity (in seconds) of these calculations is presented in Table 4.2. NMF-GD and NMF-NNLS calculations proceeded for 1000 and 200 iterations, respectively. The computation of these algorithms was about 20 times more demanding than that of the algorithms for random and average selection of radiance. NMF-NNLS showed a higher computational complexity than NMF-GD, thus indicating the difference between a first-order iterative optimization algorithm and a constrained version of the least-squares problem, which is equivalent to a quadratic programming problem (Franc et al., 2005). The average accuracy of the proposed approach was compared with that of previous methods (PLSR) (Gomez et al., 2008; Huang et al., 2004b), as shown in Table 4.4. For each method, continuum removal was calculated and compared using NCC to its corresponding spectra in ASTER/JPL. To calculate the continuum removal using PLSR, the spectral radiance with heating source was used to estimate the continuum. The results of the comparison indicated that the proposed approach (using spectral radiance without a heating source) has a high average accuracy in suppressing the spectral continuum from spectra (ACC) is: $ACC_{NMFGD} = 78.9\%, ACC_{NMFNNLS} = 76.7\%, ACC_{Averaging} = 78.6\%, ACC_{Random} = 78.8\%, ACC_{PLSR} = 66.9\%$) (Yousefi, 2018).
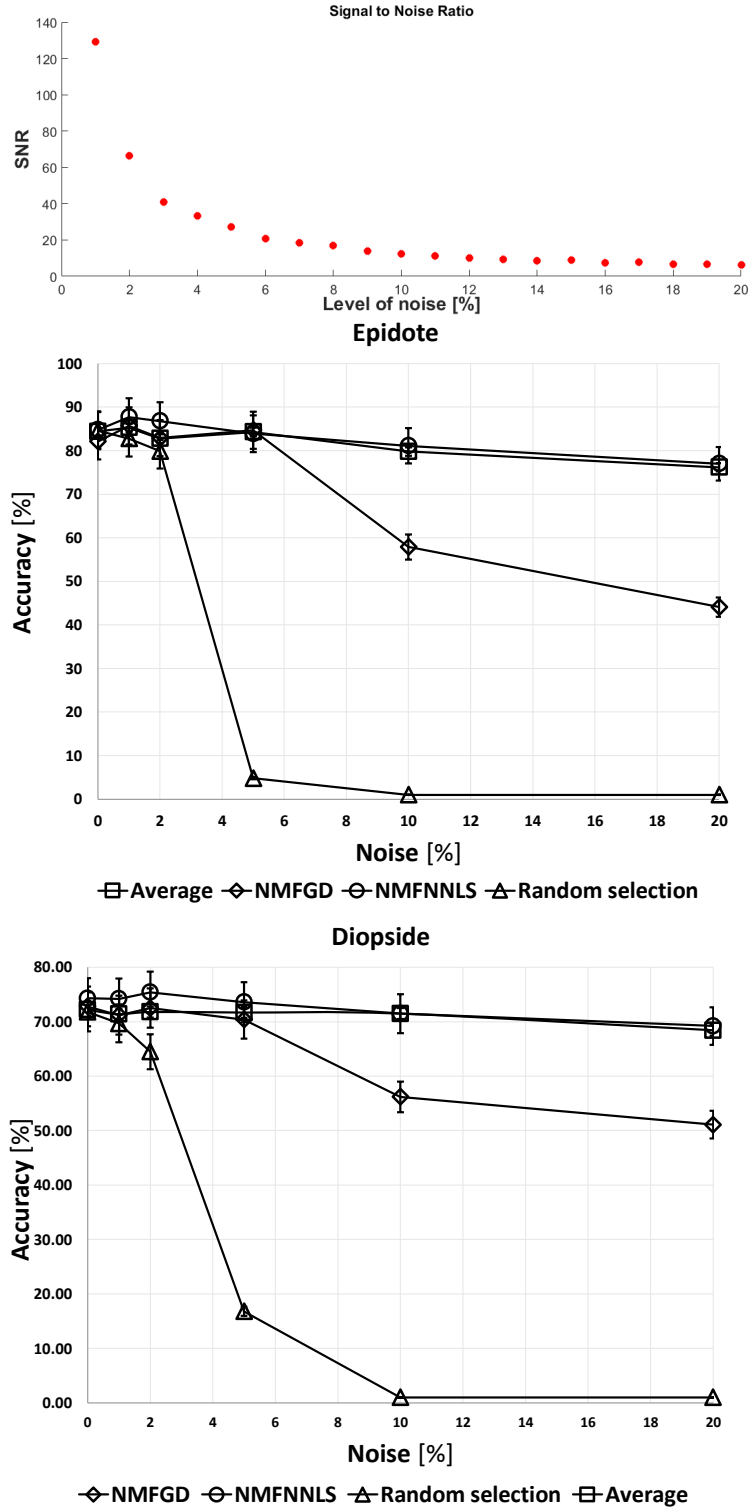
Figure 4.7: Signal to noise ratio along with similarity level of continuum removed to ASTER/JPL spectral library are shown.

4.7   Discussion

The presented approach proposes a new modification of the continuum removal technique for ground-based hyperspectral imagery. The method facilitates the calculation of continuum removal for hyperspectral image acquisitions with and without a heating source. This feature alleviates the difficulty of the process by suppressing the blackbody temperature on the panelâs surface. An experiment was conducted within the $7.7\mu m$ to $11.8\mu m$ LWIR wavelength range using a FIRST FTIR LW hyperspectral camera of Telops. Another novelty of this approach is related to applying NMF analysis to downwelling radiance. The proposed algorithm uses Rank-1 NMF to determine the downwelling radiance and ensures the best basis radiance selection. The application of NMF in comparison with other linear Eigen decomposition methods (e.g. PCA (Jolliffe, 1986)) showed better basis representative calculation due to non-negative coefficients in the process (Ding, 2005). Negative coefficients indicate the relationships among some of the bases that occurs in eigen decomposition approaches, such as PCA. In addition, Rank-1 NMF represents the basis corresponding to the heat matrix in the factorization process, which is a guarantee for obtaining a better representative of the input data (downwelling radiance set) (Lee and Seung, 1999). The standard NMF optimized by GD and NNLS algorithms were tested for the evaluation of the performance of Rank-1 NMF calculation from downwelling radiance through each of these algorithms. These results were in agreement with those obtained using the averaging and random selection of spectra. The use of random spectrum selection from the Infragold panels provided a sensitive radiance that did not reliably denote the downwelling radiance. Furthermore, incorrect selection of the Infragold panel (in the image) for spectrum calculation is another potential source of error that may influence the calculation. The application of NMF provided a solution and led to enhanced robustness in the presence of such complications.

The comparison of continuum-removed radiance with ASTER spectra as a reference through NCC provided an estimate of the similarity level. The results indicated that continuum-removed radiance was highly consistent with the reference spectra. The NNLS algorithm showed higher similarity compared with the GD algorithm. This result indicates the difference between a constrained least-squares algorithm (in NNLS) and local minimum calculation in the GD algorithm, which resulted in a better response of NNLS to amplitude variations compared with the GD algorithm. However, the computational complexity of the GD calculation was

lower than that of NNLS.

4.8 Conclusions

The approach proposed is a modification of the continuum removal process of spectral radiance for ground-based spectroscopy. It alleviates the calculation of the blackbody temperature on the panelâs surface by conducting the acquisition before and after heating the samples. The calculation was verified by using data generated from an experiment conducted within the $7.7\mu m$ to $11.8\mu m$ LWIR wavelength range using a FIRST FTIR LW hyperspectral camera of Telops. Subsequent calculations of continuum removal were also modified by an estimation of the downwelling spectral radiance using NMF optimized by GD and NNLS. The result was then compared with the results obtained using spectral averaging and random selection of spectra in the presence of $1\% - 20\%$ additive noise. The similarity percentage of the continuum-removed spectra with each method was compared with the spectra of the minerals from the ASTER spectral library by using SAM and NCC. The method was also subjected to $2\% - 15\%$ wrong pixel spectrum selection of Infragold, and its similarity percentage was measured by SAM and NCC. The results showed a higher similarity value when NMF is used compared with the situation when the other approaches are utilized. In general, NMF-NNLS showed more robustness to noise in comparison with NMF-GD, averaging and random selection. The computation complexity of the proposed algorithms may be affected by other possible artifacts (e.g. inaccurate selection of reference radiance spectra). A cross-validation method to determine the number of iterations involved when applying NNLS and GD can be a subject for future work. Moreover, NMF can be employed with semi- optimized NMF using multiplicative rules, NNLS or non-negative quadratic programing rules, which may improve the NMF calculation and its possible sensitivity to spectral radiance calculation.

Canadian research chair in Multipolar Infrared Vision (MIVIM) and the Chaire de recherche industrielle CRSNG- Agnico-Eagle en exploration minérale.

Chapter 5

Automatic Mineral Identification using Ground-based Hyperspectral LWIR Infrared Spectral Analysis and Extreme Learning Machine

5.1 Résumé

Les développements de la technologie hyperspectrale dans différentes applications sont connus dans de nombreux domaines, en particulier dans la télédétection, l'imagerie aérienne, l'identification des minéraux et l'exploitation des carottes. Le système d' identification automatique des minéraux fournit une aide considérable en géologie pour identifier les minéraux. Ici, l'approche proposée consiste en un système automatisé pour l'identification minérale (c'est-à-dire, pyrope, olivine, quartz) dans la spectroscopie du sol par ondes infrarouges longues (7.7 μm à 11.8 μm - LWIR). Des méthodes de comparaison spectrale telles que Spectral Angle Mapper (SAM), Spectral Information Divergence (SID), NCC (Normalized Cross Correlation) ont été utilisées pour extraire les caractéristiques sous forme d'images composite de fausses couleurs. L'analyse des composantes de principe clairsemées (SPCA) est utilisée pour extraire la référence spectrale pour l'utilisation de telles techniques et montre une grande similarité avec la bibliothèque spectrale ASTER (JPL / NASA). Une machine ELM (Extreme Learning Machine) utilisée pour la prise de décision donne une précision de classification allant jusqu'à 76.69% en utilisant un noyau polynomial basé sur SAM pour le mélange de pyrope et 70.95% en utilisant un noyau sigmoide ELM pour le mélange d'olivine. Cette précision est légèrement inférieure à celle de la classification, ce qui donne une précision de 84.91% (NCC) pour le pyrope et de 69.9%

(SAM) pour l'identification de l'olivine. Cependant, la classification supervisée dépend de maniére significative du nombre d'échantillons d' entraînement et est considérablement plus difficile par rapport à la classification en raison des limites d' étiquetage et d' entraînement. De plus, les résultats indiquent une similarité considérable entre les spectres de calcul SPC1 et les spectres de la bibliothèque spectrale ASTER.

General Explanation

An automated system for mineral identification in long-wave infrared (LWIR) ground-based spectroscopy is proposed in this chapter. Several spectral comparison methods have been applied to create false colors composite. The similarity between the ASTER (JPL/NASA) spectral library and the spectra from Sparse Principle Component Analysis (SPCA) for each mineral is tested. But the main contribution of this article is testing a supervised learning method for decision making and compared it with unsupervised learning algorithm. For that, a kernel Extreme Learning Machine (ELM) used for classification and its results have been compared to clustering. We concluded that the supervised classification significantly depends on the number of training samples and is considerably more difficult as compared to clustering due to the nature of supervised learning process.

The results of this study were partially presented at the poster session of the International Congress on Thermal Infrared Applications XXXVIII (Thermosense), May 2016, Baltimore, USA.

Contributing authors:

Bardia Yousefi (Ph.D. candidate): a part of the experiment planning, data collection, data analysis, designing and implementing the algorithm. Moreover, testing their accuracy and robustness throughout the process and writing the manuscript.

Saeed Sojasi: assisting the experiment planning, data collection, mineral preparation.

Clemente Ibarra Castanedo: the experiment planning, data collection, mineral preparation, revision and correction of the manuscript.

Xavier P.V. Maldague and **Georges Beaudoin**: (The main research director and co-director, respectively): supervision, revision and correction of the manuscript.

Martin Chamberland: Providing the LWIR hyperspectral camera, experiment planning, data collection, guidance for improvement of down-welling calculation, providing comments for manuscript.

Other contributors:
Annette Schwerdtfeger (research officer): manuscript preparation.

Automatic Mineral Identification using Ground-based Hyperspectral LWIR Infrared Spectral Analysis and Extreme Learning Machine

Bardia Yousefi[1], Saeed Sojasi[1], Clemente Ibarra Castanedo[1], Xavier P.V. Maldague[1], Georges Beaudoin[2], Martin Chamberland[3]

[1] *Computer Vision and System Laboratory, Department of Electrical and Computer Engineering, Laval University, 1065, av. de la Médecine, Quebec, QC, Canada*

[2] *Department of Geology and Geological Engineering, Laval University, 1065, av. de la Médecine, Quebec, QC, Canada*

[3] *Telops, Inc., 100-2600 St-Jean-Baptiste Ave, Quebec City, QC, G2E 6J5, Canada*

Corresponding author: bardia.yousefi.1@ulaval.ca

5.2 Abstract

The developments in hyperspectral technology in different applications are known in many fields particularly in remote sensing, airborne imagery, mineral identification and core logging. The automatic mineral identification system provides considerable assistance in geology to identify mineral automatically. Here, the proposed approach addresses an automated system for mineral (i.e. pyrope, olivine, quartz) identification in the long-wave infrared (7.7μm to 11.8μm - LWIR) ground-based spectroscopy. Spectral comparison methods such as Spectral Angle Mapper (SAM), Spectral Information Divergence (SID), Normalized Cross Correlation (NCC) have been used to extract the features in the form of false colors composite. Sparse Principle Component Analysis (SPCA) is used to extract the spectral reference for using such techniques and show high similarity with the ASTER (JPL/NASA) spectral library. A kernel Extreme Learning Machine (ELM) used for decision making yields classification accuracy up to 76.69% using SAM based polynomial kernel ELM for pyrope mixture, and 70.95% using SAM based sigmoid kernel ELM for olivine mixture. This accuracy is slightly lower as compared to clustering which yields an accuracy of 84.91% (NCC) for pyrope and 69.9% (SAM) for olivine identification. However, the supervised classification significantly depends on the number of training samples and is considerably more difficult as compared to clustering due to labeling and training limitations. Moreover, the results indicate considerable similarity between the spectra from SPC1 calculation and the spectra from the ASTER spectral library.

Keywords: Thermal image analysis, Hyperspectral infrared image analysis, Mineral identification, Sparse principle component analysis, Extreme learning machine.

5.3 Introduction

Technological developments in different wavelength bands in spectroscopy have created interesting opportunities, providing spectral and spatial information from the surface of materials. The automatic/semi-automatic/non-automatic approaches in mineral identification extensively depend on this information. The proposed approach is to develop a ground-based spectroscopy system for automatic mineral identification using Extreme Learning Machine(ELM). It uses spectral comparison technique for creating the false color composite and the spectral reference calculated by applying Sparse Principal Component Analysis (SPCA) and selecting the first sparse principal component(SPC1) of the spectra from mineral's sample. Spectrometric imagery gives information which can be exclusively used in geology and mineralogy field (Goetz, 2009; Van der Meer et al., 2012). Several spectral databases (e.g. ASTER (Baldridge et al., 2009)), have been widely used as reference for spectral analysis and contain a collection of the spectral libraries including sample in laboratory or field conditions. The signature of the natural materials in such spectral libraries provides opportunities for data-mining techniques to be applied to imagery. The spectra from these libraries can serve as reference or ground truth to enable comparison among the spectra. Recent hyperspectral methods focus on spectral techniques; for estimation of abundance of quartz and clays in oil sand (Entezari et al., 2017) or identifying minerals for mapping (Feng et al., 2013b). These methods typically compare the targeted spectra in the hyperspectral images to the spectra of the minerals in libraries (Cloutis (Cloutis, 1996) and Plaza et al. (Plaza et al., 2009)). There are many spectral comparison approaches developed and applied for spectral analysis such as SAM and NCC, which more commonly used (Baldridge et al., 2009). Moreover, for better spectral representation, several features which are dealing with wavelength position and the spectral absorption have been developed.

The objective of this study concerns a ground-based mineral identification deploying supervised and unsupervised approach similar to airborne imagery (Murphy et al., 2014; Deng et al., 2014; Wan et al., 2017) and core logging (Salisbury et al., 1994; Korb et al., 1996; Hook and Kahle, 1996). The absorption information (signature) and the wavelength position are depend on the mineral composition and change based on geochemical information which leads to mineral identification (Crowley et al., 2003; Morris et al., 1985; Scheinost et al., 1999). The local and global minima or maxima (extrema) in different wavelengths lead to distinguishing the

minerals and this method is becoming a commodity for mineral identification (e.g. effect of lichen in mineral identification (Feng et al., 2013b)).

Short Wave Infrared (SWIR) band range is relatively confined (Feng et al., 2017; Clark et al., 1990; Murphy, 1995) comparing to other band such as visible and near infrared (VNIR) and Long Wave Infrared (LWIR). This matter creates level of difficulties for precise determination of extrema and comparative analysis (Murphy et al., 2014). Selection of the spectral representative for identification of the pure minerals may involve prior knowledge of physical (roughness, particle size, etc) and chemical properties of the material, its surface and illumination geometry of measurement (i.e. background continuum, particular albedo, and absorption features) (Clarke, 1999; Clark and Roush, 1984). This involves some research in order to minimize such effects (Clarke, 1999; Clark et al., 2003). Contain approaches have a more suitable shape of the known continuum spectra and attempt to fit either locally or entirely in linear or curved baseline approaches (Clarke, 1999; Sunshine and Pieters, 1993). Spectral comparison methods such as SAM, spectral feature fitting (SFF, (Clark and Swayze, 1995) and Tetracorder (Clark et al., 2003)) can be applied after continuum removal. The data is sensitive to a variety of factors including the non-uniform thermal property and background reflection of the minerals, angle of acquisition, and several other parameters, whereas continuum removal provides a correction to the spectra and prepares the spectra for comparison. This minimizes the influence of such parameters on the data by removing the continuum from the spectrum. In this study, the experiments involve to study a set of pure and mixed mineral grains and active thermography which involves placing a heating source in front of the hyperspectral camera to illuminate the samples. Continuum removal uses Non-negative Factor Analysis (NMF) to find the best spectral representative from down-welling radiation. The analysis of mineral identification uses SPCA to find the spectra reference and compared with the ASTER spectral library (Baldridge et al., 2009). After, spectral comparison techniques use these references and creates the false colors and ultimately segmentation of the mineral grains is conducted. The proposed approach uses hyperspectral imaging in the wavelength range of 7.7 μm to 11.8 μm (Long Wave Infrared-LWIR) for certain mineral grains, in laboratory conditions using a FTIR hyperspectral camera equipped with a magnifying lens to improve spatial resolution. The remainder of the paper is organized as follows. In Section 2, we introduce the methodology and explains, how the continuum removal and segmentation processes are performed. Section 3 describes the experimental and simulation results. We discuss the challenges and advantages
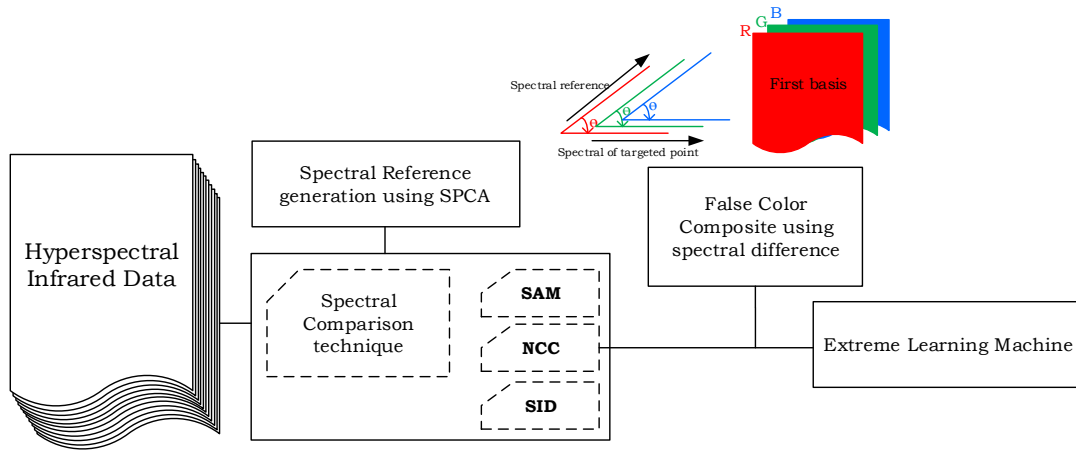
Figure 5.1: The scheme of the proposed algorithm.

of the approach in Section 4. Finally, we conclude and describe future work in Section 5.

5.4 Method

Here, an automated mineral identification for ground-based spectroscopy has been challenged through application of supervised (Extreme Learning Machine-ELM) and unsupervised approaches (clustering). But before that to have the classification attributes, several spectral comparison techniques used (i.e. SAM, SID, and NCC). To apply spectral comparison techniques, spectral references are requires that the proposed method deployed Sparse Principal Component Analysis (SPCA) to extract the spectral references from single mineral samples and even compared them with ASTER spectral library.

5.4.1 Spectral Comparison techniques

textitSpectral Angle Mapper (SAM) technique calculates angle between the reference and targeted spectra as an error between them (Kruse et al., 1993a, 1992) which represents their physical composition property and uses the $n - D$ angle to match the targeted spectra to reference spectra. The spectral references for using SAM usually involve using the spectral libraries whereas the proposed approach modified it by extracting it directly from the spectra of pure samples (such as those presented here). The amount of the error generated by SAM represents the significant difference between the mineral compositions (Kruse et al., 1993a).

Spectral information divergence (SID)

SID is another spectral comparison techniques. $x = (x_1, x_2, \ldots x_L)^T$ represents the pixel-spectra, X_l component, in hyperspectral data cube and considered to be a probability distribution aim to estimate the correlation between the spectra (targeted and reference spectra). $y = (y_1, y_2, \ldots y_L)^T$ is additional pixel vector that has the probability distribution of $q = \{q_l\}_l^L = 1$ and $q_j = \frac{y_j}{\sum_{l=1}^{L}} y_l$ and compose SID through following formula:

$$SID(x, y) = D(x||y) + D(y||x) \tag{5.1}$$

where $p = \{p_l\}_{l=1}^{L}$ is the desired probability vector from the x and $p_j = \frac{x_j}{\sum_{l=1}^{L} x_l}$, and $D(x||y) = \sum_{l=1}^{L} p_l \log(\frac{p_l}{q_l})$. The $D(y||x) = \sum_{l=1}^{L} q_l \log(\frac{p_l}{q_l})$ is the relative entropy or a directed divergence (cross entropy) of x and y through Kullack-Leibler function (Chang, 1999.

Normalized Cross Correlation (NCC)

NCC involves a simple correlation comparison between the spectral. The images should first be normalized due to many factors such as the image brightness variation, exposure conditions,

and lighting caused by the mineral grains non-uniform shape. This is performed through division of the mean by standard deviation subtraction. NCC provides a correlation number as a valuable information showing the spectral difference between the reference spectrum (similar SAM the reference spectra calculated by the spectral of pure samples) and the targeted spectrum. This method has been used for template matching and image analysis (Zou et al., 2006).

SPCA to extract spectral reference

PCA is a linear transformation that can be presented by $S = XL$ (L is an orthonormal basis matrix and X is a mean-zero data matrix) which maximizes the projected data (S) variance (even hybrid methods such as Two-dimensional principal component analysis(2DPCA)(Huang et al., 2016) are still linear). Principle components (PCs) are extracted from the vectors in X and are the compact representation of the basis vectors while $K < p$. This is not the first time that sparse computation is used in spectral analysis (Iordache et al., 2012, 2014; Themelis et al., 2012a). However, their research was related to unmixing and endmember analysis in hyperspectral remote sensing imagery which is different from the perspectives of this paper. The regularization terms imposed for mathematically solving the sparse unmixing in three types of methods such as convex relaxation methods (Iordache et al., 2012, 2014), greedy algorithms (Iordache et al., 2011), and sparse Bayesian methods (Themelis et al., 2012a) but here we use it for extraction of spectral reference through using the first basis attained by SPCA calculation. The replacement of the non-smooth l_0 with l_1 or l_p norm imposes the well-defined optimization problems to a tractable solution (Tropp and Wright, 2010) in the convex relaxation methods: e.g. the alternating direction method of multipliers (ADMM) method (Afonso et al., 2011; Mei et al., 2015). The l_0 regularization problem in the greedy algorithm is solved by an iterative identification of potential endmembers from the spectral library until the advent of best reconstruction in the mixed pixel (Tropp and Wright, 2010).

SPCA involves additional regularization parameters which maximizes the uncorrelated PCs variance and converts PCA into the nonlinear transformation (Zou et al., 2006; Sjöstrand et al., 2012). The SPCA elastic-net has a relaxation l_2 and l_1-penalty terms as it is shown in the following formulation:

$$\{\hat{\zeta}_k, \hat{\gamma}_k\} = argmin_{\zeta_k} \|X - X\gamma_k\zeta_k^T\|_F^2 + \delta\|\gamma_k\|_2^2 + \lambda\|\gamma_k\|_1,$$

s. t. $A_k^T A_k = I.$ (5.2)

where X_{ζ_k} is the response vector, $\hat{\gamma}_k = (X^T X + \delta I)^{-1} X^T X_{\zeta_k}$, and $\hat{\zeta}_k = argmin_{\zeta_k} \|X - X\gamma_k \zeta_k^T\|_F^2 \text{s.t.} \zeta_k^T \zeta_k = 1, \zeta_k^T A_{(k-1)} = 0$. In the case where the l_2 regularization parameter δ is changing, the second term of the equation above would be influenced (the γ_k approximation can be done by a soft-thresholding rule (Zou et al., 2006). The SPCA deployed to unmixed sampled spectra to extract the spectral references (one example of quartz is shown in Figure 5.2). Since the experiment involves two types of grain samples: the group that they do not have any aggregation with other minerals (called "pure samples") and other samples that several grain types mixed with other grains (e.g. quartz). By applying the SPCA to the spectra of pure samples, we excerpt the spectra which one can deploy as spectral reference in the application of spectral comparison techniques (as the classification attributes). For example once the SAM is used, the spectral angle between the first SPC in the basis matrix (called SPC1), and every other pixel-spectra in the image cube are calculated and it provides the attributes that been used in classification step.

5.4.2   Segmentation

Segmentation is essential to identify the minerals and it can be done by simple approaches such as spectral information segmentation and implying discrimination ratio (threshold) or applying the more sophisticated techniques such as Extreme Learning Machine (ELM) or K-means clustering. This section briefly reviews the methods employed for segmentation.

Extreme Learning Machine (ELM)

 Artificial Neural Networks (ANN) can estimate a difficult nonlinear mappings from the input sample. A Single Layer Feed-forward Network (SLFNs) structural design called Extreme Learning Machine (ELM) proposed by Huang et al. (Huang et al., 2004a) which solved the initiation problem in the case of using gradient descent application. This reduces the computational complexity for training and enhances learning performance compare to conventional approaches and its capability for nonlinear kernel and activation functions (Rajesh and Prakash, 2011).

Clustering

To cluster hyperspectral image cubes obtained from the experiments in an unsupervised way, a Hue-Saturation-Value (HSV) based K-means clustering has been used. It categorizes the false

colors created to different groups where these groups labels as different mineral using spectral comparison techniques. In general, false color composites are obtained from putting parts of wavelength in different color group (around the wavelengths of 1150 μm = red; 960 μm = green; 1060 μm = blue) but we got them through spectral comparison techniques by putting different values of spectral comparison attributes into the color (for example SAM_{pyrope} = red, $SAM_{olivine}$ = green, and SAM_{quartz} = blue).

5.5   Results

The proposed approach is based on statistical analysis and computer simulations on the hyper-spectral data. The properties of the data-set, the acquisition properties, and the experimental setup are described.
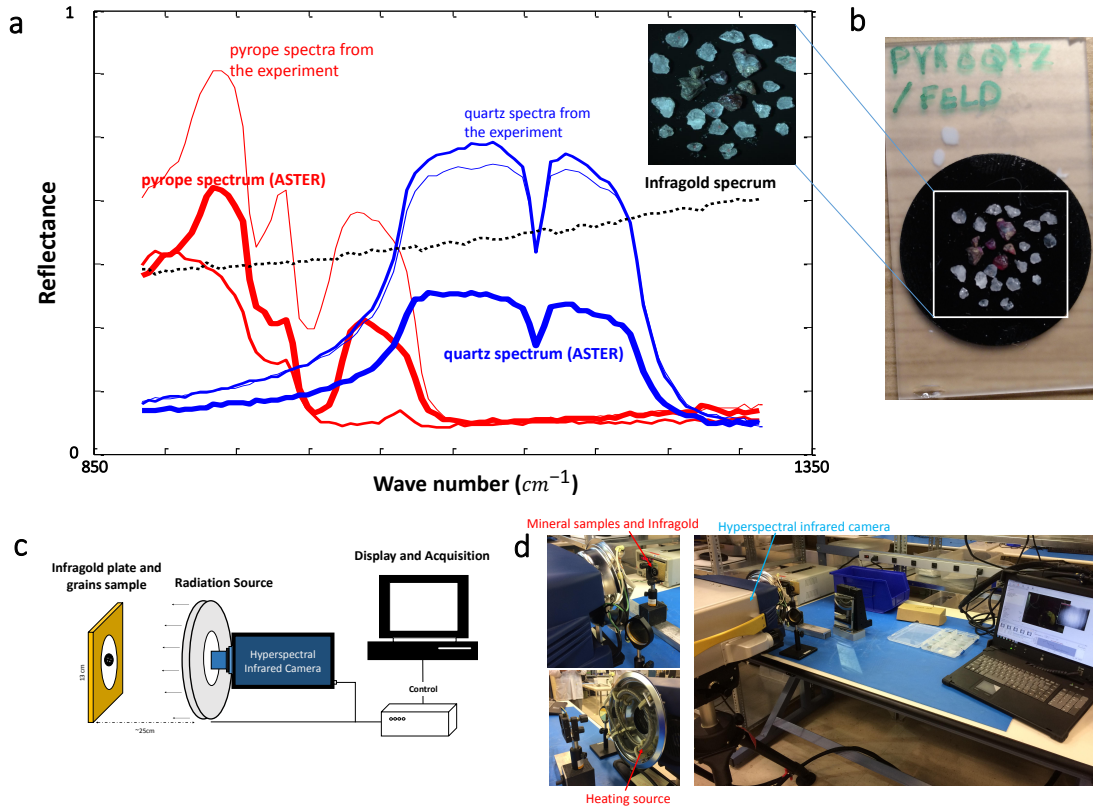
Figure 5.2: Experimental setup and spectra of minerals are shown in the figure. Upper image represents the spectra of the minerals used in the experiment (pyrope and quarts mixed sample) along with spectra from ASTER spectral library (**a,b**). Lower left hand-side image is the scheme of experimental setup (**c**) along with three pictures taken from the conducted experiment (**d**).

5.5.1 Mineral Grains and LWIR spectroscopy

Since the field of view (FOV) of the sensor was small and the grains were between 0.6 mm to 2.0 mm, a special lens was used for higher spatial resolution (which is described in next section). The mineral samples were divided into groups of mixed and pure samples and three minerals which have distinguishable spectra in LWIR (i.e. Olivine $(Mg^{+2}, Fe^{+2})_2 SiO_4$, Pyrope $Mg_3 Al_2 (SiO_4)_3$, and Quartz SiO_2 (Mindat, 2012). Figure 5.2.a-b show the spectra of mineral and one example of mixed samples. The image acquisition in this paper were conducted while the heating source were turned on and off (for performing the continuum removal (Kirchhoff, 1860), and for both conditions, the spatial resolution is 200×256 and 87 spectral channels were recorded. The sensor used to make the measurements was a lightweight Hyper-Camera imaging spectroradiometer (HYPER-CAM LW) (Ding, 2005 operating in the long-wave infrared (LWIR) band (from 7.7 to 11.8 μm). It has spatial resolution of 320×256 LWIR PV-MCT focal plane array detector and having spectral resolution up to $0.22 \mu m$. The spectra is obtained using a Fourier-Transform Spectrometer (FTS) and the Hyper-camera measures complete spectrum for every pixel and having an instantaneous FOV of 0.35 mrad (Ding, 2005). A Long-Wave LW Macro lens provides a pixel footprint of 0.1 mm with working distance of 30 cm (Figure 5.2.b). A heating source was located in front of the samples for providing the active thermographical conditions in the experiment (Figure 5.2.c). However, the image acquisition was continued after turning off the heating source. The grains were attached to adhesive carbon-based tape during the experiment and were placed on an infra-gold plate. The hyperspectral images were taken perpendicularly having the spectral resolution of 6 cm^{-1} ($\sim 0.0119 \mu m$ at $7.7 \mu m$ and $\sim 0.0465 \mu m$ at 11.8 μm) in 87 spectral bands. Since an infragold was placed in the background, its reflectance assisted in removing the continuum from the spectrum (Kirchhoff, 1860).

5.5.2 Results

The results of the proposed approach are presented in this section and it is divided by two stages. First, the results of the application of SPC1 from the pure samples versus ASTER spectral library as the reference spectra in spectral comparison techniques is shown and then the results of using two different learning system are analyzed.

5.5.3   ASTER spectral library and the result of SPCA as reference spectra

The Advanced Space-borne Thermal Emission and Reflection Radiometer (ASTER) imaging program at NASA (Baldridge et al., 2009) comprises compilations of spectral information from the Jet Propulsion Laboratory, Johns Hopkins University, and the United States Geological Survey. The library contains the spectra of nearly 2000 types of soils, rocks, minerals, snow, water and artificial minerals. Several of these spectra cover the wavelengths measured in this study (0.4 to 14 μm). The spectral data for each mineral covers the visible, near-IR, Mid-IR and thermal-IR wavelengths. To apply the spectral comparison techniques, the spectral reference has a key role in the calculations. In general, the ASTER spectral library is used as a reference spectrum for each minerals. Here, the possibility of using SPCA as spectral reference was analyzed through generating the spectral references from pure mineral grains. PCA itself can give a reasonable representation of the statistical information but SPCA provides more robust data facing noise (Iordache et al., 2011, 2012, 2014; Tropp and Wright, 2010; Afonso et al., 2011; Mei et al., 2015; Zou et al., 2006; Sjöstrand et al., 2012). The first sparse principal component (SPC1) extracted from the basis matrix (sparse calculated eigenvector matrix) having the spectra of pure samples as their input and since the abundance spectra of pure samples are usually belong to one mineral, the extracted spectra (SPC1) are also belong to same mineral and used as reference spectra. This matter confirmed by comparing the ASTER spectra to SPC1 spectra which showed identical similarity (Table 5.1) and used SAM and NCC [1]. To calculate the reference spectra using SPCA, a pixel spectra set of pure sample minerals is used as a training set with no overlap to the testing set (testing sets contain pyrope-quartz or olivine-quartz grains- mixed samples).

---

[1]This calculation is just a score of difference and it is different from using spectral comparison for generation classification attributes or false colors images.

Table 5.1: Comparison among the SPC1 spectral references and ASTER mineral spectra using SAM and NCC (percentage of the similarity).

Spectral Comparison Technique	Quartz	Quartz Similarity (%)	Olivine	Olivine Similarity (%)	Pyrope	Pyrope Similarity (%)
SAM	0.4830	51.70	0.2698	73.02	0.2330	76.70
NCC	0.6055	60.55	0.9336	93.36	0.9520	95.20

Table 5.2: Accuracy of ELM for mineral identification.

Minerals		Spatial resolution of RoI	Accuracy of Classification (%)							
			ELM							
			Linear kernel		Polynomial kernel		RBF		Sigmoid	
			SAM	NCC	SAM	NCC	SAM	NCC	SAM	NCC
background	Pyrope	160*161	99.8	98.9	99.9	99.4	99.9	99.1	99.9	99.1
	Olivine	157*139	94.1	98.4	97.2	99.9	95.5	99.9	92.5	98.8
Non-background	Pyrope	160*161	97.7	10	99.1	43.35	98.95	10	98.95	10
	Olivine	157*139	94.8	87.95	97.7	99.55	96.3	99.05	93.55	93.65

5.5.4 Segmentation performance

Results of spectral comparison techniques

The performance of the spectral comparison techniques are presented in this section. Applying SAM and NCC showed higher performance as compare to SID due to direct calculation of the difference between the targeted and referenced spectra. These algorithms calculate the difference between the reference and targeted spectra and this difference is given in the form of an error (in the case of SAM), correlation similarity (in the case of NCC), and cross entropy (in the case of SID). Topological similarities among the mineral's spectra create more suffice performance for SAM and NCC due to their dependency to the shape of the spectra as compared to SID that estimate the difference entropy based on statistical information. Moreover, applying spectral comparison techniques showed good improvement in generating the false colors which led to better identification of the minerals using clustering (Figure 5.4). The main reason behind this improvement is elimination of unrelated part of the spectrum which decrease inconsistently between the target and reference spectra. The comparison took place for each pixel spectrum and it provides the amount of the spectral difference for targeted pixel-spectrum and continued by looping over all the spectral pixels in the hyperspectral cube. Consequently, the spectral variation provides a map which represents the similarity of the spectra to targeted spectra, a false color map. These metrics are the input for the segmentation section in the approach and used as classification attributes or directly false color images for to be grouped in different sets.

Table 5.3: Computational load for ELM classification is shown.

Minerals	Spatial resolution of RoI	Spectral comparison techniques		Computational Cost (time in second)							
				ELM							
				Linear kernel		Polynomial kernel		RBF		Sigmoid	
				Training Time	Testing Time	Training Time	Testing Time	Training Time	Testing Time	Training Time	Testing Time
Pyrope		SAM	21.16	63.10	0.61	71.91	7.67	65.68	4.06	126.07	3.08
	160*161	NCC	27.74	59.83	0.68	73.68	7.67	64.95	4.15	119.55	3.02
Olivine		SAM	20.64	55.63	0.61	66.16	6.98	61.99	3.93	107.09	2.71
	157*139	NCC	26.89	54.61	0.64	64.18	7.07	57.65	3.76	110.41	3.02
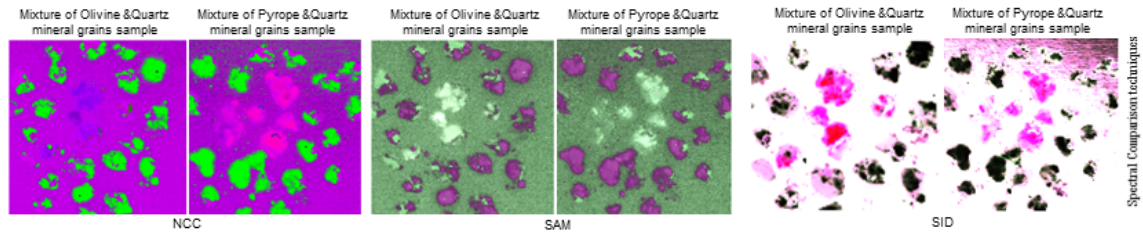
Figure 5.3: The results of spectral comparison analysis (SAM, SID, and NCC) are revealed by false colors in the figure.
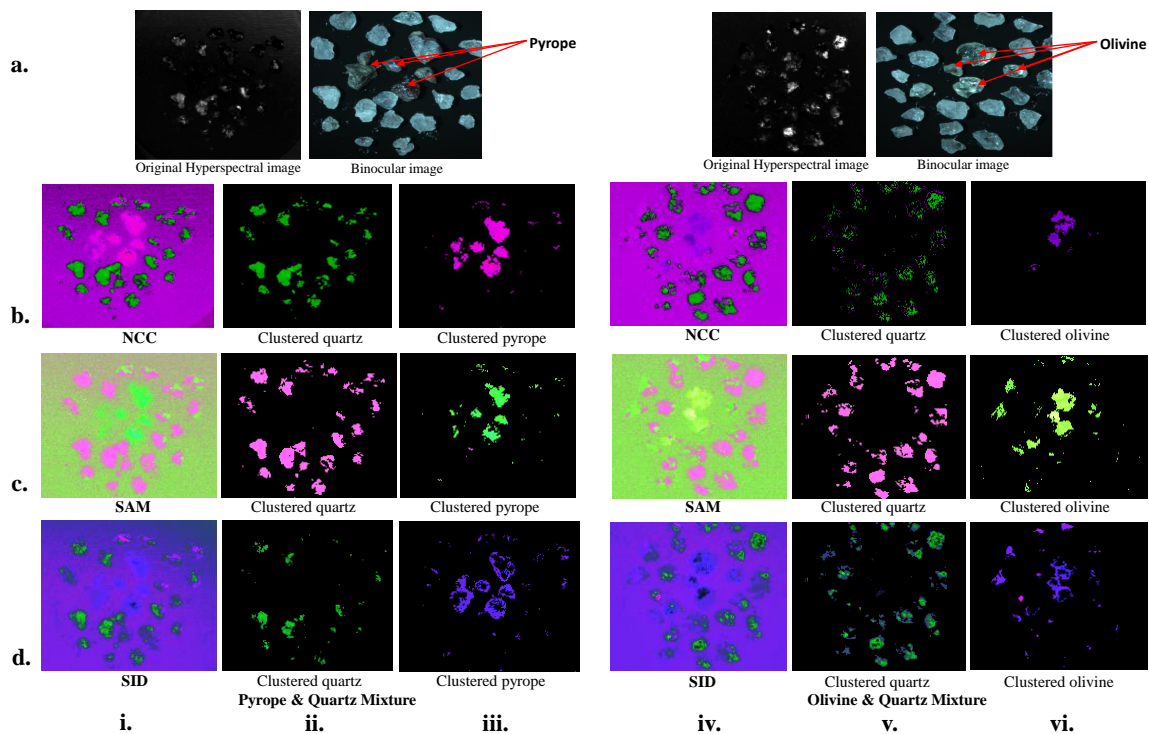
Figure 5.4: The results of the clustering by SAM (**a.**), NCC (**b.**), and SID (**c.**). The mineral grains have been automatically detected through their false colors. **a.** and **b.** show the hyperspectral and binocular images from olivine and pyrope, respectively. Columns **i.** and **iv.** show the false colors results using the spectral comparison techniques. Columns **ii.**, **iii.**, **v.**, and **vi.** depict the clustering results for each minerals and every spectral methods.

Results of ELM and clustering

Identification of the minerals took place in different settings involving supervised/unsupervised approaches. For the supervised approach, there is a training set randomly selected from pixels of mineral grains. In contrast, the unsupervised approach does not require a training stage, but the selection of the clusters needs to be interference of training information (labeled data). Before explaining the performance of segmentation, analyzing the performance of spectral comparison techniques is vital as the segmentation depends on it. Spectral comparison techniques provided the classification attributes and false colors images which facilitated the performing the classification and clustering segmentation of mineral grains in the hyperspectral images, respectively. Here the results of different segmentation methods to identify minerals are shown. Two techniques were tested ELM and k-means clustering. Three different minerals have different signatures in the LWIR band plus the spectra correspond to the sample's background. Consequently, there are four different classes, including the background, that were explored in the hyperspectral images for the presence of alternative classification/clustering methods.

Automated mineral identification using ELM classification followed training and testing scenario. The classification with ELM (with Linear, Polynomial, Radial Based Function(RBF), and Sigmoid kernels)(Huang et al., 2004a; Rajesh and Prakash, 2011; Huang et al., 2006; Ruff et al., 1997) was directly related to the training stage. Training and testing are done based on NCC and SAM feature's values as the attributes separately calculated for each mineral. The number of observations for every spectral analysis and mineral is different due to extra enhancing filtering performed to eliminate inconsistency in the training and testing data. Tables 5.2,5.3 show the accuracy and computational load for ELM classification.

The unsupervised segmentation of the mineral was performed by HSV color based K-means clustering approach. The entire processes of clustering were executed knowing the number of interested clusters and the relevant data to select the particular cluster afterward. The result of HSV based K-mean clustering is shown in Figure 5.5. Given accuracy of the clustering techniques in Tables 5.4 is directly related to accuracy of segmentation using clustering and global accuracy of the approaches can be calculated by multiplying the accuracy of each step by the segmentation results. Table 5.5 shows the computational complexity of false color generation and applying the clustering for mixed sample sets.

Table 5.4: Accuracy of the HSV based clustering for three different samples.

MAM	HSV-based clustering	Quartz (%)	Pyrope (%)	Olivine (%)	Total accuracy (%)
NCC	**Accuracy of mineral detection**	77.95	94.59	85.39	85.98
	Misclassification	22.06	5.41	14.61	14.02
SAM	**Accuracy of mineral detection**	75.82	91.40	99.75	88.99
	Misclassification	29.56	29.34	4.03	20.98
SID	**Accuracy of mineral detection**	68.52	72.01	92.19	77.57
	Misclassification	31.48	27.99	7.81	22.43

Table 5.5: Computational complexity of the false color generation and clustering approach.

Computational Cost (time in second)				
Minerals	**Spatial Resolution**	**NCC**	**SAM**	**SID**
Mixture of Pyrope & Quartz	144*152	362.3	325.4	354.2
Mixture of Olivine & Quartz	157*139	497.7	331.3	368.6

The entire computational process has been done with a PC (Intel Core 2Quad CPU, Q6600, 2.40GHz, RAM 8.00GB, 64 bit Operating System) and data analysis has been conducted using MATLAB programming language. In order to apply these techniques, a MATLAB hyperspectral image index analysis toolbox (Isaac, 2015) was used. Figure 5.5 depicts the segmentation results through clustering. Due to the similarity between first SPCA (SPC1) and ASTER (see table 5.1), either the SPC1 or the ASTER library data can be used as the reference spectrum. Table 5.1 represents an estimation of the spectral similarity among the spectra in percentage. It indicates the sensitivity of the spectral comparison methods which used for spectral comparison calculation.

Accuracy of the classification

The proposed approach provided accuracy based on counting the correct detected pixels of hyperspectral images. For that, a ground truth was required to compare the results of system in order to obtain quantitative assessment. Ground truth was made by rigid manual labeling the images for different types of minerals. This labeled image is verified using Micro X-ray fluorescence (μXRF) images from the samples and ArcGIS to map them with the labeled images or with results of automatic detection (Figure 5.6). Local accuracy (ACC) is calculated by:

$$ACC(\%) = \frac{Correct\ detected\ pixels}{Total\ pixels\ of\ mineral} * 100 \qquad (5.3)$$

It is noticeable that the location of the detected pixels is vital to identify the mineral grains. The total accuracy of both methods is calculated while the total accuracy of each method multiplies to the sensitivity percentage of spectral comparison techniques (table 5.1) which might decrease the current accuracy. But the accuracy here does not indicate the reliability of the system because the main objective is to identify the grains and pixel calculation performed as a comparison criterion and even two or three pixels in the grains provide satisfactory outcome for the system (as these pixels represent the grain's content).

olivine grains

pyrope grains

olivine grains

olivine grain

olivine & quartz

pyrope & quartz

Binocular images of the grains

pyrope & quartz sample

olivine & quartz sample

olivine grain

pyrope grain

µXRF images of the grains
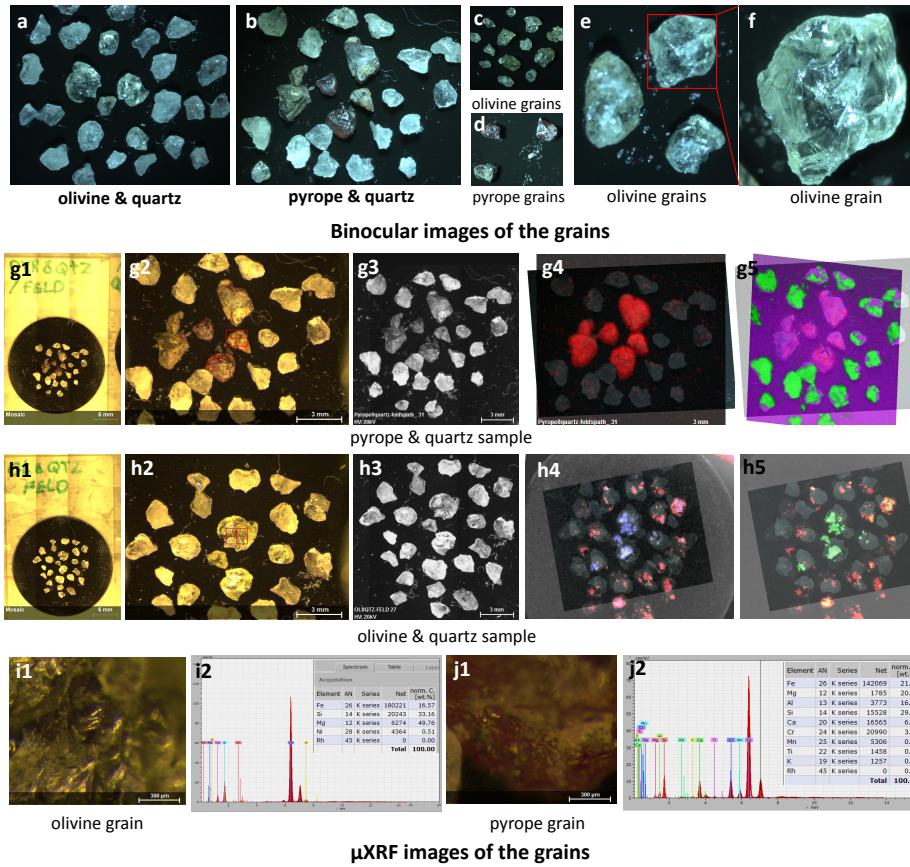
Figure 5.5: The binocular images from the grains of pyrope, olivine, and mixed with quartz grains are shown. Also the $/mu$XRF image of the samples are also shown in the image to verify the ground truth images and labeling. (**g1-g3** and **h1-h3** depict the images of pyrope-quartz and olivine-quartz samples using Micro X-ray fluorescence (μXRF), respectively. **i1,i2**,**j1,j2** show a point in the grains of olivine and pyrope, respectively.

5.6 Discussion

The main objective of this research was to identify the minerals automatically. For this purpose, we used the statistical and spectral information in the form of applying hyperspectral comparison analysis. Segmentation and mineral identification in the hyperspectral images underlined a set of feature combinations using such information. This study has shown the application of hyperspectral infrared imagery in the 7.7-11.8 μm wavelength range for mineral identification through supervised/unsupervised categorization techniques. The presented approach challenged two different types of segmentation involving classification (using SAM and NCC) and clustering (using SAM, SID, and NCC). As the classification is a supervised approach, it suffers from dependency on the number of training samples in training stage. Misclassifications are ultimately inevitable because of small size of the grains and consequently lack of proper training in the system. Moreover, the nature of the classification approach unequivocally creates two stages data-processing which is considered as an inauspicious shortcoming which debilitates supervised system versus unsupervised system (particularly for this application). In addition, application of the supervised procedure (e.g. ELM) might create too much sensitivity against acquisition's parameters such as experimental setup, background, or special temperature of heating source. This might be attributed by specific values of weights in the training matrix (in the case of using ELM or any other neural networks). On the contrary, the clustering leads a direct grouping of the spectral data and is more simple and propitious to be used for such applications. It does not have training stage which considerably decreases the pre-processing analysis and labeling costs but also more robust against acquisition parameters.

The contributions of the proposed approach applying for two major points of view, i.e. geological and spectral analysis perspective. In geology, the presented method increased the perspective of mineral identification from remote sensing, airborne imagery, and core logging to the small mineral grains which includes the analysis for estimation of spectral radiation (continuum removal) and identification computations. There are some related works included hyperspectral mineral identification in core logging (i.e. (Salisbury et al., 1994; Korb et al., 1996; Hook and Kahle, 1996)) which have more similarity to this research which is more in terms of close range (distance between target and hyperspectral camera) experimental condition but their complex mineral aggregate and the shape of the mineral targets are comparatively different. The second point of the contribution is related to major comparison between

two methods for automation of mineral identification and spectral analysis which scrutinizingly compared ELM and clustering approaches for the same sample sets.

5.7   Conclusions

The presented approach involved an experiment in the hyperspectral imagery in the 7.7μm to 11.8μm LWIR wavelength range conducted using a FTIR hyperspectral camera. The objective was automatic identification of the minerals (pyrope, olivine, and quartz). For that, spectral comparison methods such as SAM, SID, and NCC, have been used to extract the features in the form of false colors. Spectral references provided by the statistical information using SPCA which extracted the SPC1 from the pure sample grains. These spectral references have shown identical similarity compared to ASTER (JPL/NASA) spectral library. For final decision making, two approaches were investigated ELM and HSV based K-means clustering to identify the mineral grains in a supervised/unsupervised manner (respectively) and the results indicated promising accuracy. Comparison can cautiously be made by keeping the study limitations in mind as such the non-homogeneous surface of mineral grains that creates the radiometric variation as changing parameters within the test. The supervised classification accuracy reached up to 76.69% using SAM based polynomial kernel ELM for pyrope mixture and 70.95% using SAM based sigmoid kernel ELM for olivine mixture as overall hyperspectral image classification accuracy. The classification accuracy was slightly lower as compared to clustering which indicates an accuracy of 84.91% (NCC) for pyrope and 69.9% (SAM) for olivine identification by adding the sensitivity percentage into the accuracy calculations. The supervised classification showed significant dependency on the number of training samples and considerably more difficult as compared to clustering. The results of SID showed lower efficiency as compared to SAM and NCC. In future work, more analysis to increase the performance of automatic identification of the mineral grains is required.

Chapter 6

Comparative clustering analysis applying K-means rank^1-NMF and FCC on mineral identification in long wave hyperspectral infrared imagery

6.1   Résumé

Les applications géologiques de l'imagerie infrarouge hyperspectrale consistent principalement en l'identification de minéraux à l'aide d'images de télédétection, d'instruments aéroportés ou portatifs et de diagraphie. Les méthodes de classification montrent une influence considérable sur de nombreux algorithmes développés récemment. La stratégie de regroupement des spectres dans l'imagerie hyperspectrale modifie la capacité de performance des algorithmes et joue un rôle important dans le processus d' identification. Ici, nous abordons une analyse par clustering pour la cartographie minérale dans les spectres au sol et nous comparons deux algorithmes. Le premier algorithme utilise des techniques de comparaison spectrale pour tous les spectres de pixels et crée les images composites RGB de fausses couleurs (FCC). Ensuite, un regroupement K-means basé sur la couleur regroupe les régions. Cet algorithme s'appelle FCC-K-means. Cependant, le second algorithme regroupe tous les spectres de pixels pour regrouper directement les spectres. Ensuite, le premier rang de factorisation matricielle non négative (NMF) extrait le représentant de chaque groupe et compare les résultats avec la bibliothèque spectrale de JPL/NASA par des techniques de comparaison spectrale. Ces techniques donnent les valeurs de comparaison sous forme de caractéristiques qui se convertissent en résultats par

RGB-FCC. L'algorithme s'appelle K-means rank [1] -NMF. Les résultats de l'algorithme K-means rank [1] -NMF indiquent une efficacité de calcul significative (plus de 20 fois plus rapide que l'approche précédente) et une performance prometteuse pour l'identification minérale ayant une précision moyenne de 52.5% et 57.1% pour FCC-K -means et K-means-rank [1] algorithmes NMF (en utilisant Spectral Angle Mapper (SAM)), respectivement. En outre, plusieurs techniques de comparaison spectrale sont également utilisées, telles que le détecteur AMSD (Adaptive Matched Subspace Detector), l'algorithme de projection orthogonale de sous-espace, l' analyse PCA (Principal Component Analysis), le filtre local assorti (SAM) et la corrélation croisée normalisée pour les deux algorithmes. La plupart d' entre eux montrent une gamme de précision similaire. Cependant, SAM et NCC sont préférés en raison de leur simplicité. La caméra hyperspectrale que nous avons utilisée pour notre acquisition au sol (conditions de laboratoire) fonctionne dans le spectre d'ondes infrarouges longues (LWIR, 7.7-11.8 μm) et nos algorithmes tentent d' identifier onze grains minéraux différents (biotite, diopside, épidote, goethite, kyanite, scheelite, smithsonite, tourmaline, pyrope, olivine et quartz).

General Explanation

Since it is already shown in the previous chapter that clustering (unsupervised) methods are more suitable for spectral categorization, here two different algorithms involve clustering have been proposed to groups the spectra and ultimately mineral identification. The first algorithm creates FCC using spectral comparison techniques and then group these color categorizes into the different mineral composition. The second algorithm, used direct clustering for spectra and then used spectral comparison methods to create FCC and ultimately identified the minerals. The algorithms strive to identify eleven different mineral grains (biotite, diopside, epidote, goethite, kyanite, scheelite, smithsonite, tourmaline, pyrope, olivine, and quartz) and performed in the Long Wave Infrared (LWIR, 7.7-11.8 μm). We concluded based on the results that the second algorithm has about twenty times faster performance than the first algorithm having relatively similar accuracy.

The results of this study were partially presented at TELOPS Scientific Workshop, September 2016, Baltimore, USA; Quebec-Mines 2016, Quebec city, Canada.

Contributing authors:

Bardia Yousefi (Ph.D. candidate): a part of the experiment planning, data collection, data analysis, designing and implementing the algorithm. Moreover, testing their accuracy and robustness throughout the process and writing the manuscript.

Saeed Sojasi: assisting the experiment planning, data collection, mineral preparation.

Clemente Ibarra Castanedo: the experiment planning, data collection, mineral preparation, revision and correction of the manuscript.

Xavier P.V. Maldague and **Georges Beaudoin**: (The main research director and co-director, respectively): supervision, revision and correction of the manuscript.

Martin Chamberland: Providing the LWIR hyperspectral camera, experiment planning, data collection, guidance for improvement of down-welling calculation, providing comments for manuscript.

Other contributors:
Annette Schwerdtfeger (research officer): manuscript preparation.

Comparative clustering analysis applying K-means rank[1]-NMF and FCC on mineral identification in long wave hyperspectral infrared imagery

Bardia Yousefi[1], Saeed Sojasi[1], Clemente Ibarra Castanedo[1], Xavier P.V. Maldague[1], Georges Beaudoin[2], Martin Chamberland[3]

[1] *Computer Vision and System Laboratory, Department of Electrical and Computer Engineering, Laval University, 1065, av. de la Médecine, Quebec, QC, Canada*

[2] *Department of Geology and Geological Engineering, Laval University, 1065, av. de la Médecine, Quebec, QC, Canada*

[3] *Telops, Inc., 100-2600 St-Jean-Baptiste Ave, Quebec City, QC, G2E 6J5, Canada*

Corresponding author: bardia.yousefi.1@ulaval.ca

6.2 Abstract

The geological applications of hyperspectral infrared imagery mainly consist in mineral identification using remote sensing imagery, airborne or portable instruments, and core logging. Clustering methods show considerable influence on many recent developed algorithms. The strategy to cluster the spectra in the hyperspectral imagery changes the performance ability of the algorithms and plays an important role in identification process. Here, The hyperspectral camera was used for ground-based acquisition (laboratory conditions) worked in the Long Wave Infrared (LWIR, 7.7-11.8 µm) and our algorithms strive to identify eleven different mineral grains (biotite, diopside, epidote, goethite, kyanite, scheelite, smithsonite, tourmaline, pyrope, olivine, and quartz). we address an analysis on clustering for mineral mapping in ground based spectra and compare two algorithms. The first algorithm uses spectral comparison techniques for all the pixel-spectra and creates the RGB false color composites (FCC). Then a color based K-means clustering groups the regions. This algorithm will be called FCC-K-means. However, the second algorithm clusters all the pixel-spectra to directly group the spectra. Then the rank-one of Non-negative Matrix Factorization (NMF) extracts the representative of each cluster and compares results with the spectral library of JPL/NASA through spectral comparison techniques. These techniques give the comparison values as features which convert into RGB-FCC as the results. The algorithm will be called K-means rank[1]-NMF. The results of the K-means-rank[1]-NMF algorithm indicate significant computational efficiency (more than 20 times faster than previous approach) and promising performance for mineral identification having 52.5% and 57.1% average accuracies for FCC-K-means and K-means-rank[1] NMF algorithms (using Spectral angle mapper (SAM)), respectively. Furthermore, several spectral comparison techniques are used also such as Adaptive Matched Subspace Detec-

tor (AMSD), Orthogonal subspace projection (OSP) algorithm, Principal Component Analysis (PCA),
Local Matched Filter (PLMF), SAM, and Normalized Cross Correlation (NCC) for both algorithms
and most of them show a similar accuracy range. However SAM and NCC are preferred due to their
simplicity.

Keywords: Long-wave infrared hyperspectral imaging, Mineral identification, clustering of
hyperspectral data, spectral comparison method.

6.3   Introduction

Hyperspectral infrared imagery provides the spectral and spatial information from the material's surface and has many applications in different fields particularly in geology (Kruse, 1996a; geotechnos, 2004; Yajima et al., 2004; HUZIKAWA et al., 2001; Davis, 2001). From several past decades (Goetz, 2009), the spectral analysis technology has showed considerable interest in airborne (Zhang et al., 2014; Van der Meer et al., 2012; Boardman et al., 1995; Herrmann et al., 2001; Clark et al., 2003; Goetz, 2009), portable instruments and core logging (Kruse, 1996a; geotechnos, 2004). The need for an automatic system to analyze of hyperspectral imagery led to many investigations in the field of datamining (i.e. a Spectral Image Processing System (SIPS) (Kruse et al., 1993a), expert system for mineral mapping in (Kruse et al., 1993b) or many other similar examples (Boardman, 1989, 1991; CSES, 4; Gillespie et al., 1986, 1987)). Applying classification methods (e.g. support vector machine (SVM) (Tuia and Camps-Valls, 2011; Dópido et al., 2012; Pompilio et al., 2014; Izquierdo-Verdiguier et al., 2014; Khodadadzadeh et al., 2014a; De Boissieu et al., 2017; Shao et al., 2014) or neural networks (Zhang et al., 2016c; Yousefi et al., 2016a; Chen et al., 2013) are expensive due to the nature of supervised learning which involves the system to have a training step and hence separate samples for training. The training's quality plays important role in the process in terms of training number and labeling samples (Ma et al., 2016; Persello and Bruzzone, 2014; Shao et al., 2014; Dópido et al., 2013). Semi-supervised approaches alleviate the problem of supervised approaches by decreasing the training with labeled samples (Su et al., 2011; Ma et al., 2016; Chabane et al., 2017; Persello and Bruzzone, 2014; Shao et al., 2014; Dópido et al., 2013; Zhang et al., 2016c; Khodadadzadeh et al., 2014b). On the other hand, clustering approaches do not need training to ultimately label samples, by techniques such as K-means clustering (Funk et al., 2001; Zhong et al., 2006; Paoli et al., 2009; Su et al., 2011; Zhang et al., 2016a;

Pompilio et al., 2014), Fuzzy C-means (Bilgin et al., 2008; Li et al., 2013b; Ghamisi et al., 2015; Kowkabi et al., 2017; Ghaffarian and Ghaffarian, 2014), and other types of clustering (Chang et al., 2011; Tuia and Camps-Valls, 2011; Chabane et al., 2017). However, clustering scheme is important in terms of computation requirement and similarity measurements. Here, the strategy to use clustering is investigated for ground-based spectra (laboratory conditions) to identify the minerals for portable instrument applications. We present in this paper a brief overview of the application of the hyperspectral imagery for the purpose of portable instruments with more concentration of its applications in geology. One very good example of using hyperspectral thermal infrared (TIR) for core logging was presented by Kruse in 1994 and was called Portable Infrared Mineral Analyzer II (PIMA II) it was in fact a Short Wave Infrared spectrometer (SWIR - 1.3 - 2.5 $/mum$). It used Spectral Angle Mapper (SAM) for split drill core at the size of 1 cm intervals in both the cross- and along- core directions (Kruse, 1996a). Two other comparable approaches were presented by Yajima et al. (2004) for POSAM (Portable Spectroradiometer for Mineral identification) which has been developed by the Metal Mining Agency of Japan (former organization of JOGMEC (geotechnos, 2004) in 1993 (Yajima et al., 2004; HUZIKAWA et al., 2001) and Coulter et al. (2007) that reviewed the airborne hyperspectral system from visible infrared spectroscopy (Davis, 2001). Hecker et al. (2008) analyzed the influence of reference spectra on classification of minerals (i.e. kaolinite) using SAM, and used synthetic images of three mineral endmembers to try to classify them applying reference libraries derived from ground spectra (portable infrared analyzer), USGS (United States Geologic Survey) and airborne imagery, this led to increase in classification's accuracy. Moreover, Hecker et al. (2008) used some preprocessing methods to suppress the influence of different referencing sources such as two types of continuum removal (hull subtraction, hull quotient), and a combination thereof (Hecker et al., 2008). The classification of this approach was efficient but it was more a matching process between the targeted and reference spectra rather than relying on any type of clustering or machine learning approaches. The similarity of this approach is due to the ground based spectra and the matching algorithm used in the method. The matching algorithms are not the only methods used as feature extraction and Continuous Wavelet Analysis (CWA) is one of the feature extraction algorithm. CWA is known to increase the processing time during the identification process in spectral imagery. Bruce Li (2001) used wavelet analysis into hyperspectral data (Bruce and Li, 2001) and was followed by Rivard et al. (2008) to create a better representation of

spectral libraries and to minimize the viewing and illumination measurement disparities (Rivard et al., 2008). Moreover, the estimation of oil sands was done applying Gaussian singlets and derivative of Gaussian wavelets (Rivard et al., 2010). The CWA used for hyperspectral longwave infrared (3-14 μm) for rock encrusting lichens using airborne SEBASS (spatially enhanced broadband array spectrograph system, Aerospace Corp.) imagery where performed based on finding the display peaks in reflectance (maximum reflectance) in the mineral's spectra (Feng et al., 2013b). These approaches increased the level of processing whereas they do not transform the process into an automatic identification system. Another research effort on portable instrument which functions for shortwave infrared (SWIR) and visible near-infrared (VNIR) wavelength was proposed for spectropolarimetric imaging. This system was based on acousto-optic tunable filter (AOTF) technology for desert soils analysis is presented by Grupta (2014). The wavelength band covered 450-800nm and 1000-1600nm and enabled a tuned optical wavelength and Radio Frequency (RF) (for piezoelectric transducer of AOTFs) along with the spectral band (Gupta, 2014).

The unsupervised classification (clustering) methods are countlessly used in hyperspectral field. Clustering also employed for various purposes such as improving matched filter (Funk et al., 2001; Dópido et al., 2012), mixed agriculture and forestry application (Jia and Richards, 2002), anomaly finding in target detection (Chang and Chiang, 2002), endmember identification (Martin and Plaza, 2012), urban area (Zhong et al., 2006; Tuia and Camps-Valls, 2011; Tarabalka et al., 2012; Bajorski, 2012; Li et al., 2013b; Izquierdo-Verdiguier et al., 2014; Ghamisi et al., 2015) for Airborne Visible/Infrared Imaging Spectrometer (AVIRIS) data. A semisupervised band clustering on AVIRIS Indian pines (Su et al., 2011) with Non-Negative Least Squares (NNLS) used for endmember estimation in Hyperion and AVIRIS data (Canham et al., 2011) (which was more superivised classification approach). A color based clustering used for mapping Kaolinite presented by Tyo et al. (2003) (Tyo et al., 2003). A GustafsonâKessel clustering and fuzzy clustering (Bilgin et al., 2008) with Multi-Objective Particle Swarm Optimization (MOPSO) framework was used for AVIRIS and ROSIS sensor data (Paoli et al., 2009). Clustering Signal Subspace Projection (CSSP) and Maximum Correlation Band Clustering (MCBC) were employed based on PCA for AVIRIS data (Chang et al., 2011). A Neighborhood Homogeneity Index (NHI) for spectralâspatial clustering (Li et al., 2013a) and a Spectral Angle Mapper (SAM) based clustering were used employing of k-means, CLUES, and SVM analysis for AVIRIS (Pompilio et al., 2014). Most of these applications
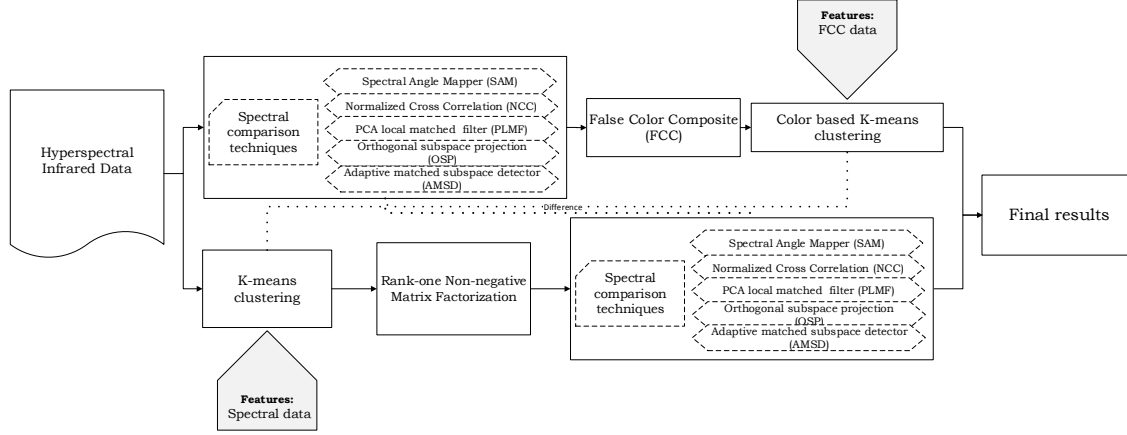
Figure 6.1: The block-diagram of proposed approach is shown here.

provide hybrid approaches employed in various applications rather than specifically analyze the strategy and hierarchy of clustering in their proposed method.

The applications of spectral comparison techniques such as SAM (Kruse, 1996a; Hecker et al., 2008) or matched filter (Funk et al., 2001; Dópido et al., 2012; Padma and Sanjeevi, 2014) and many others could be combined with machine learning approaches (Funk et al., 2001; Dópido et al., 2012; Pompilio et al., 2014; Padma and Sanjeevi, 2014) to increase their performance. Another way is to combine them with other preprocessing approaches such as Continuous Wavelet Analysis (CWA) (Bruce and Li, 2001; Rivard et al., 2008, 2010; Feng et al., 2013b; Scafutto et al., 2016; Feng et al., 2017) in order to increase the performance and efficiency of decision making processes (and deployed in to supervised or unsupervised ways (Dópido et al., 2012; Pompilio et al., 2014; Padma and Sanjeevi, 2014; Scafutto et al., 2016)). A Dynamic Self-Organizing Maps (DSOM) and Fuzzy ART algorithms combination approach has been present for Sonar images segmentation (Chabane et al., 2017) for ocean research and mineral mapping based on blind spectral unmixing method based on sparse component analysis (BSUSCA) (Zhong et al., 2016) and are considered more advanced approaches in terms of datamining analysis.

Application of RGB false color composites (FCC) with wavelet transform used for noise and continuum separation combined with PCA was employed for natural oil seepages identification of the concentration due to the effects that oil in the soil causes on the spectral signatures of vegetation (Scafutto et al., 2016). The last approach has similarity with our approach in terms of using RGB-FCC in the mapping.

The main contributions of this paper lie in: (1) the application of hyperspectral analysis in laboratory conditions using the spectra obtained from portable instrument; (2) the comparative analysis on RGB-FCC and colored based k-means clustering versus rank-one Non-negative Matrix Factorization (NMF) based k-means clustering; (3) The analysis of three different spectral comparison techniques combined with both these algorithms to assess the performance of each one for mineral identification. Figure 6.1 depicts the block-diagram of each algorithm to illustrate the comparison between the two.

The rest of this paper is organized as follows. In the next section (Section 2), the methodology of the approach will be briefly described with different spectral comparison approaches and the two algorithms will be presented. The experimental and computational results, as well as the discussion are presented afterward in Sections 3 and 4, respectively. Conclusion section (Section 5) finally states that the automatic mineral identification in LWIR through the K-means-rank[1] NMF algorithm has lower computational complexity but considerable accuracy as compared to the FCC-K-means algorithm and that fulfills the objectives of this research.
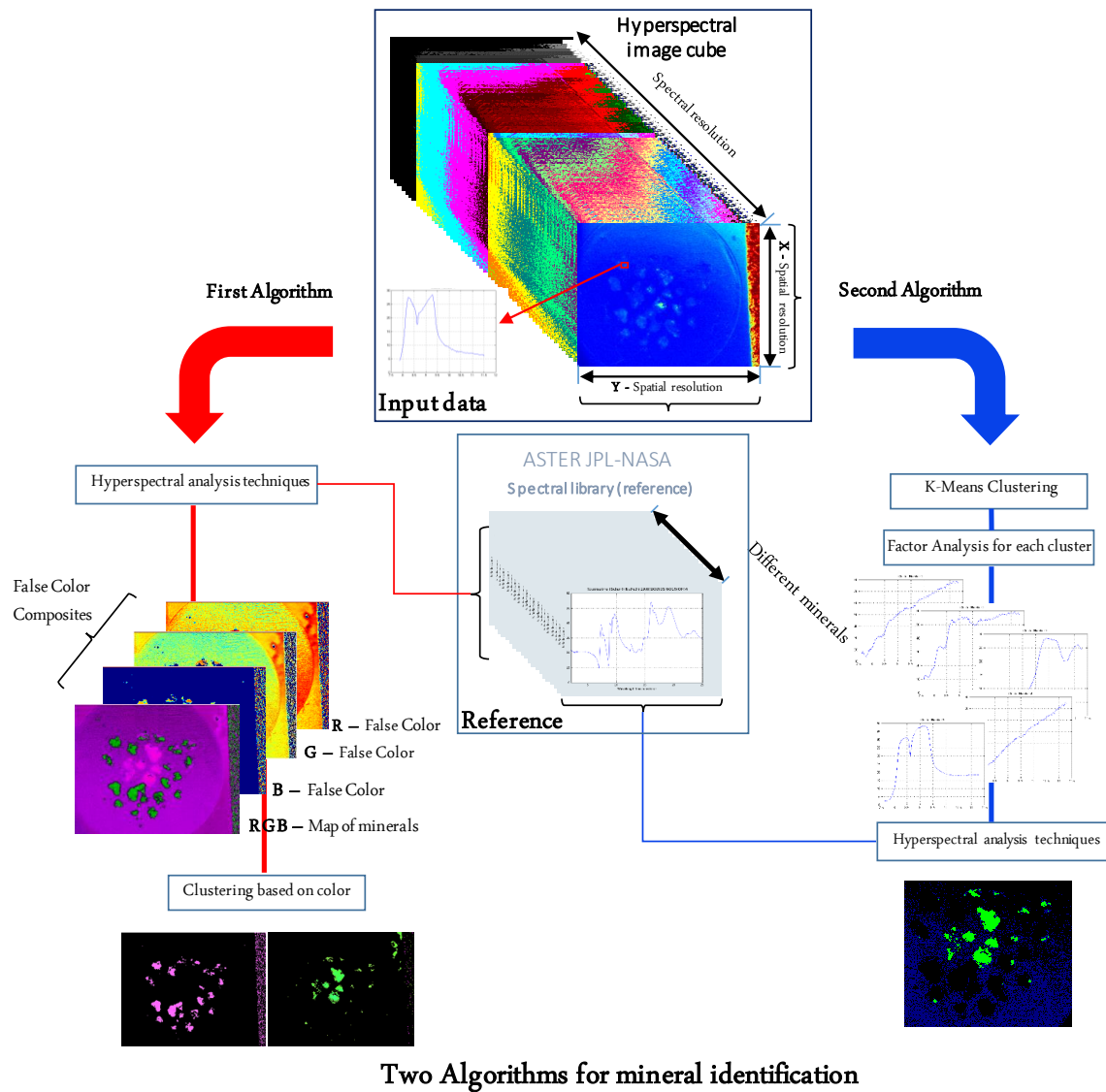
Figure 6.2: The scheme of the proposed approach. Two strategies applied in this system are shown by different pathways in the flowchart.

6.4 Methods

The methodology is summarized by comparing two algorithms for the identification of minerals. Both of them involve spectral comparison techniques and clustering approaches. They both compare the targeted minerals spectra to the ASTER-JPL NASA spectral library (as reference spectra). The difference between these two algorithms is when clustering is applied (Figure 6.2). Here, a brief summary of the spectral techniques used for both algorithms is provided.

6.4.1 Spectral comparison techniques

Matched Filter

Matched Filter(MF) is a technique used for spectral mapping between the targeted and reference spectra. Particularly, MF applies the maximization of the targeted spectrum responses that theoretically suppresses the cluttered background (Turin, 1976). One of the forms of the MF is that it normalizes every component in the space of Principal Component Analysis (PCA), applying the maximum between the global and local eigenvalue in the pixels. The MF algorithm regularization normalizes every component of the PCA space through local and global covariance eigenvalue linear combination. Also, two other forms of this combination were involved by summation of the local and global $MF = \sum_i \frac{T_i^T y_i}{\lambda_{local},\lambda_{Global}}$ or average of the local eigenvalue $MF = \sum_i \frac{T_i^T y_i}{avg(\lambda_{local})}$. The condition of regularization effects on the matched filter is named regularized matched filter (RMF) (Caefer et al., 2008).

Orthogonal subspace projection (OSP) algorithm

Orthogonal Subspace Projection (OSP) considers as the first design, a method for projection of an orthogonal subspace to eliminate the non-target response, and then a matched filter is used to match the designed target from the data. OSP is a method that applies a structured subspace model to describe spectral variability (Sanches et al., 2014; Balick et al., 2009a). The original OSP is described as $T_{OSP}(x) = d^T P_U^\perp x$. This form of OSP is appropriate for the purpose of classification, but is not suitable regarding spectral unmixing and abundance map estimation. Thus another form of OSP has been introduced which is a scaled version of the OSP classifier and can estimate an abundance map. Let $P_U^\perp = I_{L \times L} - UU^*$ being the projector of orthogonal subspace, x is the pixel spectrum, and d is the target spectrum. U is

the spectra matrix for non-target, $U^* = (U^T U)^{-1} U^T$ is the pseudo-inverse of U, and L is the bands number. OSP needs the spectra matrix of non-targeted area (region in the image) and the spectral signatures of the non-targeted can directly be extracted through the endmember from the hyperspectral image (Sanches et al., 2014; Balick et al., 2009a).

Adaptive matched subspace detector (AMSD) algorithm

Based on the assumption of a linear mixing model for a pixel and its endmembers and their abundance, the endmembers are representative of materials spectrally present in the HIS. Thus, the mathematical concept follows:

$$x = Ea, a_i \geq 0 \forall i, \sum_{i=1}^{M} a_i = 1 \tag{6.1}$$

where M is the image number of endmembers, E is an $L \times M$ matrix and its columns signify the ith endmember, a is an $M \times 1$ vector where the ith entry reveals the abundance value a_i, and x is the vector of current pixel spectral signature $L \times 1$. It is assumed that the linear mixing model also involves the abundance values with two constraints: sum-to-one and non-negativity. Considering the interaction of the spectra within a pixel (or the region in this study), a hypotheses set can be made to discriminate those pixels holding targeted pixels that entirely include background spectra. The hypotheses are

$$H_0 : x = Ba_b + n \tag{6.2}$$

$$H_1 : x = Ta_t + Ba_b + n \tag{6.3}$$

where T is an interested endmembers matrix of the target, B is a matrix representing those endmembers that are considered as background, n is considered zeromean, white Gaussian noise with variance $\sigma^2 a_b$ are the abundances of those endmembers, x is the pixel under test, and are the targets abundances. The AMSD algorithm uses the GLRT as a statistical test (Garcia-Allende et al., 2008); but, the sum-to-one constraints and non-negativity on the abundance estimation is not satisfied. So the AMSD leads to a solution of a closed-form approach having the advantages of Constant False Alarm Rate (CFAR) property. Since the AMSD algorithm follows GLRT, the first stage is the calculation of the unknown parameters through Maximum Likelihood Estimates (MLE) employing log-likelihood and solving every unknown parameter that gives the abundance estimation of MLE $\hat{a}_b = (B^T B)^{-1} B^T x$ and the noise variance

estimation of MLE $\sigma^2 = \frac{1}{L}(x - B\hat{a}_b)^T(x - B\hat{a}_b)$. The GLRT then considers the ratio of the hypothesis functions:

$$\frac{f_1}{f_0} \Rightarrow \frac{x^T(I - B(B^TB)^{-1}B^T)x}{x^T(I - E(E^TE)^{-1}E^T)x} = \frac{X^TP_B^\perp x}{X^TP_Z^\perp x} \tag{6.4}$$

As B and E are associated, it is not easy to identify this detection statistic distribution; consequently, a new detection statistic is used

$$D_{AMSD} = \frac{X^T(P_B^\perp - P_Z^\perp)x}{X^TP_Z^\perp x} \tag{6.5}$$

This provides independency to the denominator and numerator. Moreover, it does not depend on the estimation of the variance and abundance under the null hypothesis so the detection possesses the property of CFAR (Garcia-Allende et al., 2008; Manolakis et al., 2001).

6.4.2 Clustering and Proposed Algorithms

Clustering is a term used for unsupervised learning approach (unlike classification which is a supervised learning approach), to discriminate the spectra for the mineral identification in hyperspectral imagery. A clustering method provides a fast performance and reduces the typical difficulties of supervised approaches such as training and labeling that particularly occur when the number of mineral samples are limited (Yousefi et al., 2016a). The proposed approach applies the K-means clustering approach for both algorithms. However, the FCC-K-means algorithm used HSV (Sra and Dhillon, 2006)(color) based K-means to cluster the RGB-FCC and the K-means-rank[1] NMF algorithm directly applies the K-means to group the spectra. FCC-K-means and K-means-rank[1] NMF algorithms are presented in Tables 6.1,6.2, respectively. The spectral comparison techniques used in these two algorithms are referred to as $M_j(x, y)$ and it changes for comparison assessment in both algorithms following different technique used for comparison assessment.

6.4.3 Mineral Grains and Experimental set up

The experiment was conducted in a laboratory environment with a lightweight Hyper-Camera imaging spectroradiometer (HYPER-CAM LW) (Telops, 2016) operating in the long-wave infrared (LWIR) band (from 7.7 to 11.8 μm). It has spatial resolution of 320 $\times$ 256 with a LWIR PV-MCT focal plane array detector and has a spectral resolution of $4cm^{-1}$ which gives

Table 6.1: The FCC-K-means algorithm works by applying the clustering of false colors.

FCC-Kmeans ALGORITHM

Given   Input data $\mathbf{I(x,y,z)} \in \mathbf{R}^{N \times M \times Z}$ is a continuum removed spectral data where $\mathbf{I(x,y)} \in \mathbf{R}^{N \times M}$ is the spatial dimension for RoI and its unit is pixels, $\mathbf{z}$ is the spectral resolution.

Step 1   Calculation of the spectral comparison techniques:

$$\mathbf{M}_j\,(x,y) = \mathbf{ST}_j(I(x,y), \Phi_i)$$

$\mathbf{ST}_j$ is represents the spectral techniques and j reveals the number of techniques exploited (e.g. $\mathbf{j = 1} \rightarrow \mathbf{M}_1 = \mathbf{NCC}$). $\Phi_i \in \mathbf{R}^z$ denotes the reference spectra (i.e. ASTER/JPL) and i is the number of spectra corresponds to number of targeted minerals.

Step 2   FCC, Ψ_{RGB}, generation is dependent on the amount of $\mathbf{M}_j$ (for every j). Three lowest $\mathbf{M}_j$ create$(\mathbf{R,G,B})$ applying thresholding criterion. The output will be, Ψ_{RGB}, an image where the materials have been marked by different color.

Step 3   Let Ψ_{HSV} a representation of FCC in HSV color system, $\Psi_{HSV}(x, y, 3) = \Psi_{RGB}(x, y, 3)$. K-means method Clusters $\Psi_{HSV}(p, 3)$, $p \in \mathbb{R}^{N \times M}$ into k categories.

$$J_k = \sum_{k=1}^{K} \sum_{i=1}^{3} \left\| \Psi_{HSV_i} - \bar{\Psi}_k \right\|_2^2$$

Output J_k represents the targeted mineral grains clustered from other minerals by different color.

---

the spectra from 868 to 1270 cm^{-1}. The individual spectra are gathered using the Fourier-Transform Infrared Spectrometer (FT-IR) for every pixel with an instantaneous field-of-view of 0.35 mrad (Telops, 2016). There is a heating source between the hyperspectral camera and the grain samples (Figure 6.2 depicts the experimental setup), to closely and uniformly radiate the samples. Having the heating source located to the side of the sample and camera enables to radiate the heat more uniformly. There are eight mineral grains targeted to be automatically identified using the spectral analysis. Figure 6.5 shows the spectra from mineral grains used in the experiments together with the spectra from ASTER JPL-NASA spectral library to demonstrate the qualitative similarity among experimental and reference spectra. A brief description of targeted minerals is presented in Table 6.1.

Table 6.2: The K-means-rank[1] NMF algorithm for direct spectral clustering.

Kmeans-Rank[1]NMF ALGORITHM

Given   Input data $\mathbf{I(x,y,z)} \in R^{N \times M \times Z}$ is a continuum removed spectral data where $\mathbf{I(x,y)} \in R^{N \times M}$ is the spatial dimension for RoI and its unit is pixels, $\mathbf{z}$ is the spectral resolution.

Step 1   Clustering $X(p,z)$, $p \in \mathbb{R}^{N \times M}$ into k categories. The clustering is based on the spectral difference among the clusters ($0 \leq J \leq k$).

$$J_k = \sum_{k=1}^{K} \sum_{C(i)=k} \|X_i - \overline{X}_k\|_2^2$$

Step 2 h_1^q is the rank one NMF ($i=1$) of each cluster C_i^q after clustering application.

$$\forall\, q \,|\, 1 < q < k\,, \quad C_i^q = W \times h_i\,, \quad i = 1 \Rightarrow h_1^q, q = 1, ..., k$$

Step 3   Calculation of the spectral comparison techniques:

$$\mathbf{M}_j(x,y) = ST_j(h_1^q, \Phi_i)$$

ST_j is represents the spectral techniques and j reveals the number of techniques exploited (e.g. $\mathbf{j = 1} \rightarrow \mathbf{M_1 = NCC}$). $\Phi_i \in R^z$ denotes the reference spectra (i.e. ASTER/JPL) and i is the number of spectra corresponds to number of targeted minerals.

Output   FCC, Ψ_{RGB}, generation is dependent on the amount of $\mathbf{M}_j$ (for every j). By thresholding, three lowest $\mathbf{M}_j$ create(R, G, B). The output will be, Ψ_{RGB}, an image where the materials have been marked by different color.

InfraGold plate

Carbon surface
Grains sample

Lense aperture in heating source
Heating source

Hyper-Cam's aperture + Macro lense
Hyper-Cam (MWIR)

Hyper-Cam (MWIR)

Hyper-Cam's aperture
+ Macro lense

Heating source

InfraGold plate

Experimental setup
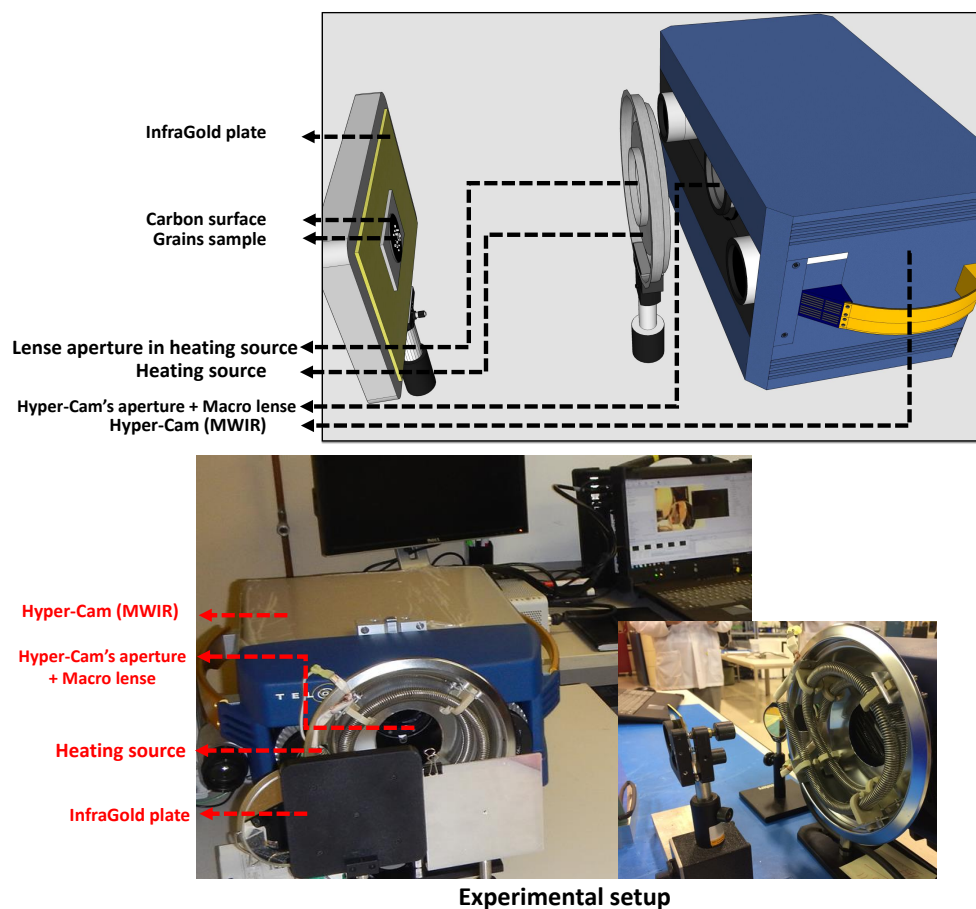
Figure 6.3: Experimental setup and mineral grains are shown in the figure. The experiments in the $7.7\mu m$ to $11.8\mu m$ wavelength took place twice with the heating source is turned on and switched off to calculate the continuum removed spectra (Mayer et al., 2003). The image shows the experimental setup which depicts the location of the hyper-camera, heating source, infragold plate, and mineral grains in the experiment.
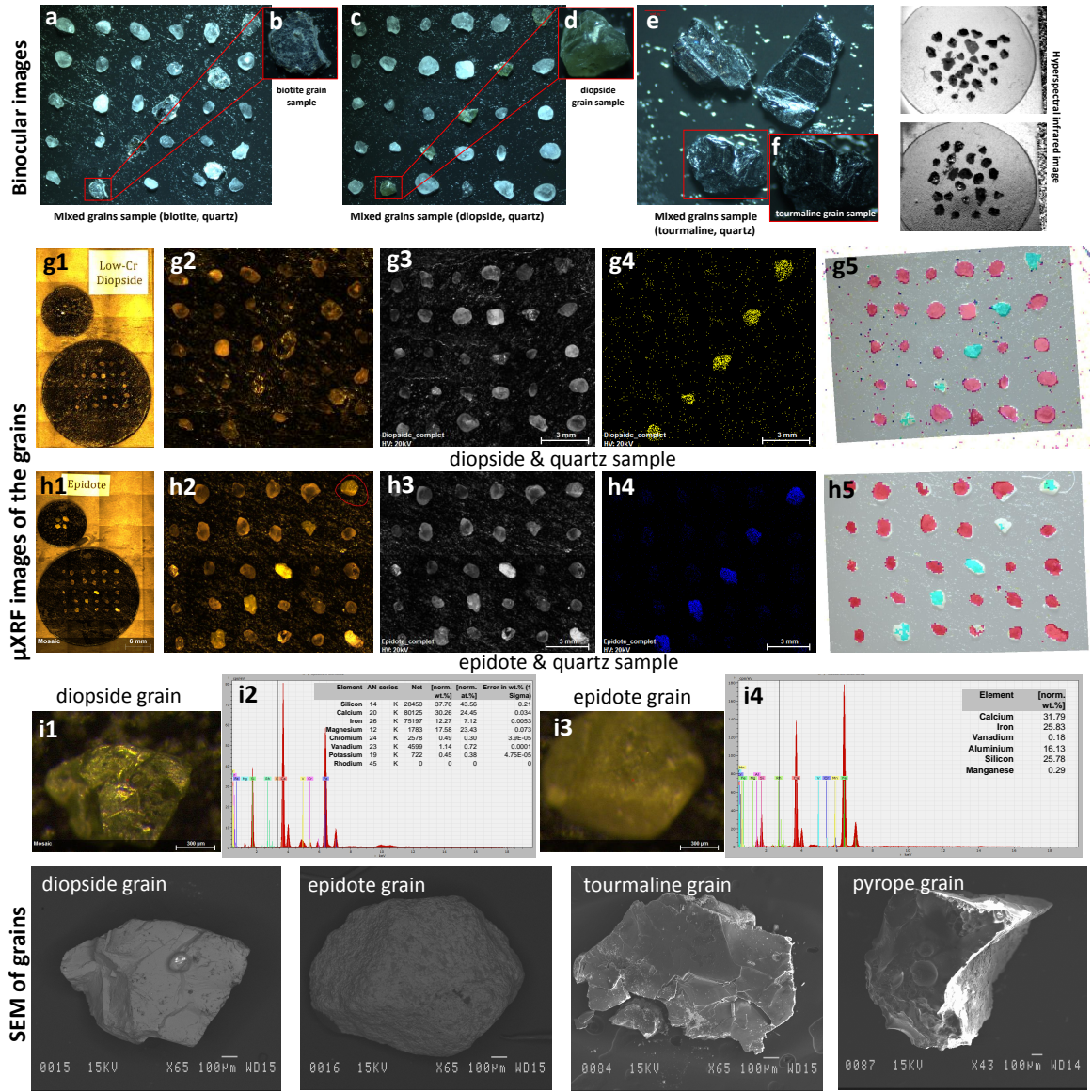
Figure 6.4: Some example binocular images from the grains of biotite **a,b**, diopside **c,d**, tourmaline **e,f** and mixed with quartz grains are shown. Also the /muXRF image of the samples are also shown in the image to verify the ground truth images and labeling. (**g1-g3** and **h1-h3** depict the images of diopside-quartz and epidote-quartz samples using Micro X-ray fluorescence (μXRF), respectively. The presence of magnesium and aluminum elements in dipodise and epidote are shown in **g4** and **h4**, respectively. **i1,i2,j1,j2** show a point in the grains of diopside and epidote. Moreover, the lower raw in the figure shows SEM images of diopside, epidote, tourmaline, pyrope to indicate surface of these grains.

Table 6.3: Characteristic of minerals studied by LWIR.

Minerals	Chemical formula
Biotite	$K(Mg,Fe)_{2-3}Al_{1-2}Si_{2-3}O_{10}(OH,F)_2$
Diopside	$MgCaSi_2O_6$
Epidote	$Ca_2(Al_2,Fe)(SiO_4)(Si_2O_7)O(OH)$
Goethite	$(FeO(OH))$
Kyanite	Al_2SiO_5
Scheelite	$CaWO_4$
Smithsonite	$(ZnCO_3)$
Tourmaline	$((Na, Ca)(Mg,Li,Al,Fe^{2+})_3Al_6(BO_3)_3Si_6O_{18}(OH)_4)$
Olivine	$(Mg^{+2}, Fe^{+2})_2 SiO_4$
Pyrope	$Mg_3 Al_2 (SiO_4)_3$
Quartz	SiO_2

6.4.4 Properties of Hyperspectral Image

The image acquisitions have been performed while the minerals were attached to a carbon substrate (shown in Figure 6.4) and had an infragold plate in the background. The infragold plate reflects all the radiation and is used to calculate the overal radiation's amount for Continuum Removal (CR)(Mayer et al., 2003). The experiment was performed while the heating source was first on and then off. It is required to perform CR and avoid calculation of black-body's temperature (Mayer et al., 2003). The size of hyperspectral images is 180×300 pixels in the spatial resolution and 122 channels of spectral resolution.

Mineral identification using hyperspectral technology depends on spectral comparison techniques and mineral spectral signature. The spectra for some of these minerals (e.g. figure 6.6) are represented by maximum or minimum in particular wavelength (it is called signature).

Such a signature is used to identify the minerals. The location and types of these particular features within the wavelength band play an important role in the identification's accuracy. The minerals for this research have reasonable signatures in the 7.7-11.8 μm band. Smithsonite, scheelite and goethite have more similar spectra to each other in terms of spectral shape (location of extrema). This causes a problem for identification of the minerals once they are combined in a mixture form as their spectral features would be similar. In this example only scheelite has a maximum peak before 11.8 μm and it makes scheelite detectable. In contrast, goethite and smithsonite have a peak after 11.8 μm band (not in the range of our hyper-camera) and this makes them undetectable for both algorithms (geothite example in Figure 6.6) with the used system.

6.4.5 Accuracy of the proposed approach

The accuracy of the algorithms are based on counting the correct detected pixels in the hyperspectral images (Tables 6.2, 6.4). For that, a ground truth is used following the rigid manual labeling of the known location of the mineral grains in the samples and verified by the results of μ X-ray fluorescence (μXRF (Figure 6.4). The number of ground truth pixels in each cases are also mentioned for all the samples with spatial resolution of ROI. For every case of mineral mixture, the targeted mineral grains are mixed with quartz grains, hence for each mixed samples accuracy is estimated through the accuracy of discrimination between these two types of grains. Two types of error are shown by false positive that represents wrong mineral identification and false negative that reveals misidentification of the mineral grains and both are calculated in each cases. Total accuracy of each algorithm is calculated by subtraction of the correct identification and two errors for every samples.

$$Total\ accuracy = ACC(\%) - (FN(\%) - FP(\%)) \tag{6.6}$$

where local accuracy (ACC) is calculated by:

$$ACC(\%) = \frac{Correct\ detected\ pixels}{Total\ pixels\ of\ mineral} * 100 \tag{6.7}$$

Let FN being the false negative error and estimates using below mentioned formulas:

$$FN(\%) = \frac{Total\ pixels\ of\ mineral - Correct\ detected\ pixels}{Total\ pixels\ of\ mineral} * 100 \tag{6.8}$$

The False Positive (FP) error is the wrongly classified pixels and calculates by:

$$FP(\%) = \frac{Wrong\ classified\ pixels}{Total\ pixels\ of\ image} * 100 \tag{6.9}$$

6.5 Results

6.5.1 The results of spectral comparison techniques

The results are shown for the FCC-K-means proposed algorithm using the RGB-FCC (Figures 6.5, 6.6). This provides a better visualization of the spectral differences among the minerals by placing each mineral target as a certain weight amount in colors. FCC provides a good difference criterion which can be easily discriminated by a clustering approach (the results of the FCC-K-means algorithm is shown in Figure 6.5). Some of the spectral techniques applied to the images are not necessarily for spectral comparison approaches such as NCC or SAM. However, these techniques have been used to investigate the strength of the method with respect to the extraction of spectral differences. In order to apply these techniques, a MATLAB hyperspectral image index analysis toolbox (Isaac, 2015) was used. The quantitative results of the FCC-K-means algorithm is shown in table 6.2.

6.5.2 Results of the two algorithms

The results of the spectral comparison technique were presented in the previous section, in this section the K-means clustering results are shown in figures 6.5 and 6.6. This includes the clustering approach for both algorithms. The results of the FCC-K-means strategy are presented in comparison to the second method of hyperspectral unmixing. As aforementioned, applying the clustering in a different hierarchy with spectral analysis techniques creates two approaches which have two similar outcomes. Figure 6.5 shows the performance of the color based clustering approach for the algorithms. Besides the computational load which is considered as significantly different between these methods (table 6.3), clustering after using spectral analysis (in the FCC-K-means algorithm), is considered as a more sensitive algorithm and this is caused by the dependency of the clustering to the generated color (RGB-FCC). A low performance in spectral comparison techniques creates misclassification in the algorithm, for instance: diopside applying NCC has lower performance than SAM and it created more false negatives after clustering (Table 6.2). However, the sensitivity of the K-means-rank[1] NMF algorithm lies under the application of clustering techniques. The same example of diopside which has more false negatives because of clustering poor performance (Table 6.2). Sometimes due to the spectral curve which does not have significant extrema in the band of the hyperspectral information, the clustering method cannot discriminate the clusters from each other

(i.e. in the case of goethite and smithsonite minerals). In such a situation, increasing the number in the clustering initialization partially solves the problem. Even though this solves the problem in the clustering, the clusters selected as different categories might have similar content materials. This is corrected by the application of the spectral comparison techniques which categorize all these similar grouping in one category. However, in the case of similar mineral spectra or unspecified spectral exterma in mineral, the problem remains unsolved.
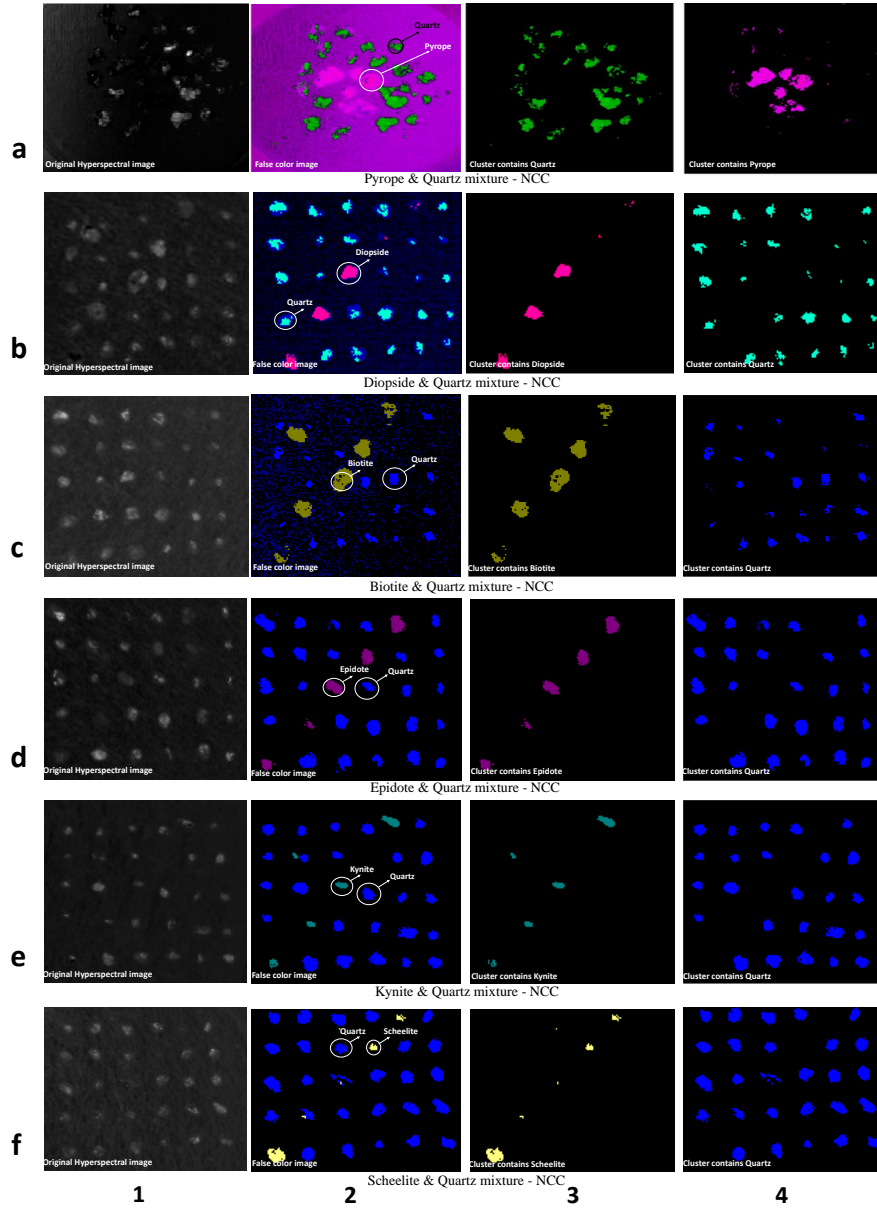
Figure 6.5: Figure shows the qualitative presentation of mineral grains segmentation after applying the clustering using FCC-K-means algorithm. The left hand-side column shows the hyperspectral image, the second left column presents FCC images using NCC (it can be any other spectral comparison techniques) before applying the clustering, and two right hand-side columns show the results of segmented grains.
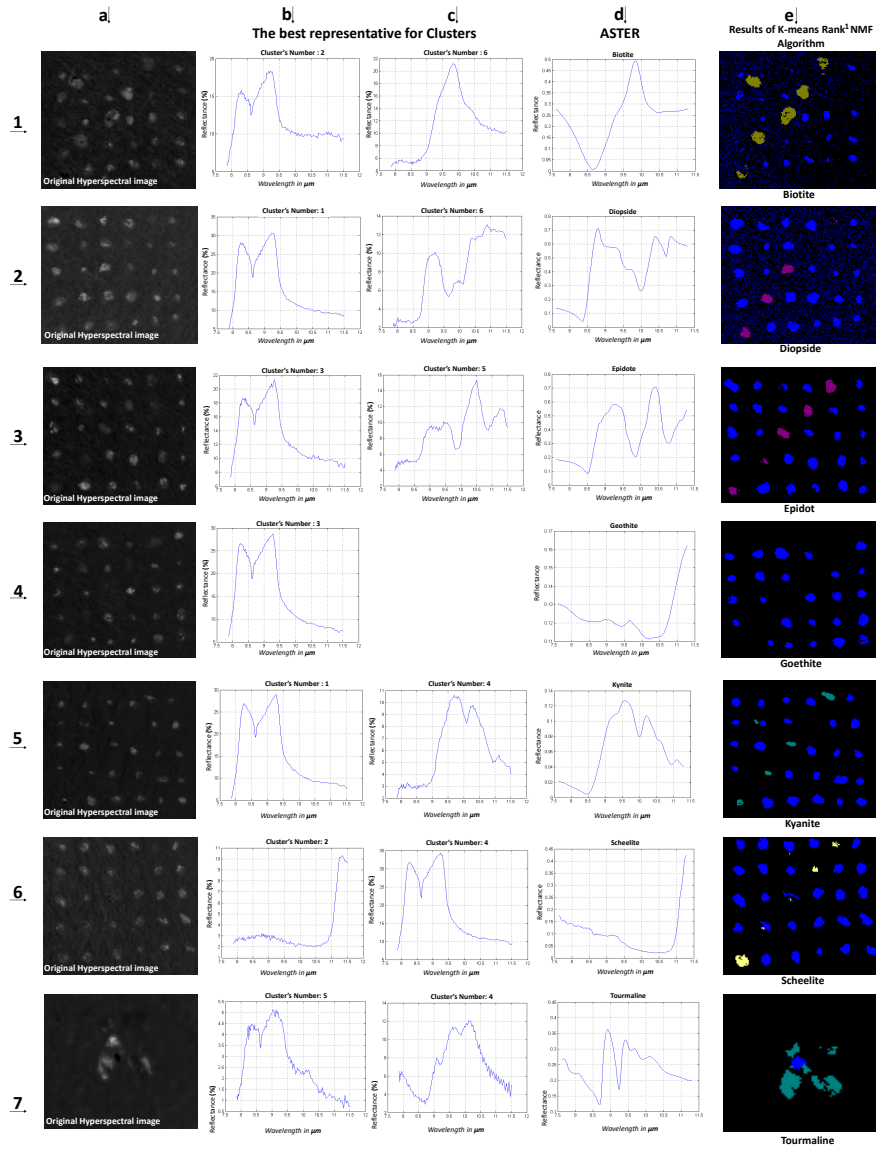
Figure 6.6: Some examples of K-means rank[1] NMF algorithm results are shown in the figure. Column **a** shows the original hyperspectral images of minerals. Columns **b, c** represent the rank one NMF of K-means clustering on spectra and **d** are the mineral signatures from JPL-ASTER spectral library in 7.7-11.8 μm. FCC results of the algorithm using SAM are shown in column **e**. In each mixed sample minerals, two different mineral signatures are present because the targeted grains are mixed with quartz grains. In **4.c**, there is no signature shown for geothite because the clustering was not able to detect the signatures of goethite.
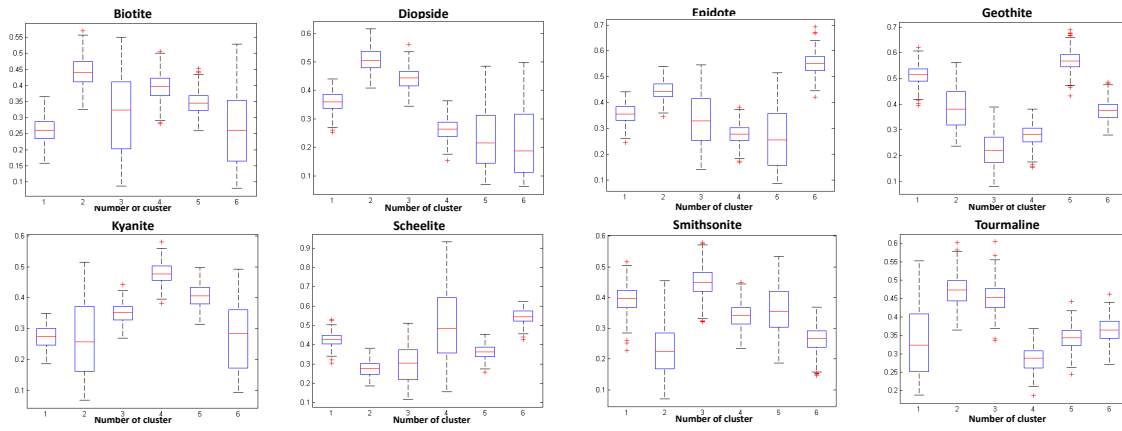
Figure 6.7: The box plot of the spectral angle (SAM) between the spectra in every cluster and their first rank NMF for every mineral segmentation using the K-means rank^1 NMF algorithm (Similarity per cluster by spectral angle difference). The Whisker and box plots are representing the similarity between the best representation of each cluster using NMF and the entire spectra of the cluster itself (to show the NMF functioning). The higher the median line in the whisker plot is, the more it shows the numbers of spectral similarity in the clusters. In general, the bigger box and Whisker plots represent the higher variation of similarity between the best representative spectrum in every mineral and spectra of the cluster.

Table 6.4. The quantitative accuracy of the two algorithms.

Accuracy

Mineral	Spatial resolution	Rigid GT		First Algorithm		Second Algorithm	
				NCC	SAM	NCC	SAM
		Mineral	Quartz	Acc (%)	Acc (%)	Acc (%)	Acc (%)
Biotite	123*138	496	885	52.45	68.79	78.58	78.58
Diopside	126*143	299	888	40.21	71.59	70.17	59.906
Epidote	123*148	260	890	48.64	70.54	81.66	81.66
Geothite	118*141	235	718	33.76	64.36	55.94	55.94
Kyanite	123*144	88	659	37.44	69.54	81.48	81.48
Scheelite	123*158	168	1006	48.69	56.51	84.87	59.29
Smithsonite	119*160	402	1117	28.39	47.24	50.91	67.15
Tourmaline	58*80	122	14	75.81	49.73	57.77	68.08
Pyrope	159*159	259	1654	<1	8.67	61.07	11.63
Olivine	172*142	435	2649	6.53	18.49	<1	7.028

Table 6.5. The computational complexity of two algorithms.

Minerals	Spatial resolution of RoI	NCC	SAM	OSP	AMSD	MF	PLMF	RMF sum	RMF meanLocal	RMF meanGlobalLocal	Spatial resolution of RoI	NCC	SAM	OSP	AMSD	MF	PLMF	RMF sum	RMF meanLocal	RMF meanGlobalLocal
												First Algorithm (FCC-K-means)								Second Algorithm (K-means-Rank[1]NMF)	
Biotite	131*143	310.39	273.74	808.21	865.07	609.35	376.20	376.36	383.67	377.87	123*141	15.25	15.23	15.63	15.69	15.36	15.20	15.19	15.20	15.63
Diopside	128*145	288.62	254.89	717.27	792.97	619.64	421.45	447.48	405.89	380.92	124*125	14.78	14.76	15.23	15.02	14.89	14.74	14.73	14.74	15.23
Epidote	125*157	332.82	320.90	863.70	907.06	608.15	433.59	440.40	459.21	468.72	125*157	22.12	22.11	22.49	23.1	22.23	22.08	22.08	22.08	22.49
Geothite	124*144	298.09	261.75	751.28	794.36	545.00	374.33	374.12	381.94	376.25	120*149	21.72	21.69	22.06	23.18	21.81	21.67	21.67	21.69	22.07
Kyanite	129*144	304.68	264.29	609.55	657.05	609.36	487.18	664.28	394.87	386.91	126*147	24.34	24.33	24.74	24.89	24.46	24.31	24.31	24.31	24.74
Scheelite	136*172	514.34	462.17	834.13	886.73	846.71	582.24	621.27	658.24	634.79	125*160	22.99	22.96	23.36	23.92	23.07	22.95	22.95	22.94	23.36
Smithsonite	120*163	384.92	293.94	783.89	826.86	641.74	409.60	411.54	417.70	410.70	119*160	22.37	22.35	22.89	23.51	22.51	22.35	22.35	22.34	22.88
Tourmaline	50*55	211.01	205.60	269.15	289.13	252.78	213.70	213.57	214.16	213.51	56*62	7.79	7.78	8.12	8.83	7.89	7.75	7.75	7.75	8.12
Pyrope	144*152	362.38	325.40	674.05	693.06	652.95	349.78	346.04	356..81	347.67	159*170	18.75	18.73	19.14	19.94	18.83	18.70	18.70	18.70	19.14
Olivine	157*139	497.70	331.28	1.0067e+03	841.98	627.43	7.8214e+03	369.47	356.42	1.2252e+03	159*173	22.14	22.11	22.58	23.27	22.21	22.07	22.07	22.06	22.58

Applying these algorithms provides an opportunity to compare them through the mineral identification task and resulting computational load. The FCC-K-means algorithm seems heavier in computation time when compared to K-means-rank[1] NMF algorithm due to the application of the spectral analysis for each spectrum. Furthermore, the K-means-rank[1] NMF algorithm clusters all the spectra which results in heavy computations as well. Table 6.2 presents the accuracy of both algorithms and Table 6.3 indicates the computational load for each algorithm with different spectral analysis. Averaging and factor analysis can provide better outcome, particularly the factor analysis provides more statistical information for the selection of the spectral representative in the algorithm. We applied NMF to select a spectral representative for each cluster. Figures 6.6 and 6.7 show some examples of NMF results and box-plots for different categories of minerals and present the qualitative and quantitative representation for the application of such techniques, respectively. Higher number of initialization for the clustering allows a re-selection of the same spectral mineral in two or more different categories. This difficulty can also be solved in the latter hierarchy by applying spectral analysis, which means that these analysis select the same mineral categories for these selections.

Table 6.2 represents the accuracy of both algorithms for comparison purposes. It is noticeable that the location of the detected pixels is vital to identify the mineral grains. In other words, we would like to have correctly detected pixels located on the surface of mineral grains and even one or two pixels detected on the surface of minerals indicate the grain content and ultimately could yield to an accurate identification (grain-based identification). We also provide pixel-based accuracy percentages (at Tables 6.4 or 6.2). For example kyanite and scheelite have been detected with a very limited number of pixels but very accurate because these pixels are in the grain's surface. In terms of spectral comparison technique accuracy of the algorithms, the SAM and NCC provided better accuracy as compared to OSA and AMSD that required the background spectra in their calculations. Matching filter (PLMF) did not succeed detecting the minerals and was omitted from the accuracy calculations. Table 6.4 shows the accuracy of spectral comparison techniques using the K-means-rank[1] NMF algorithm. The accuracy of biotite & quartz, epidote & quartz, geothite & quartz, and kyanite & quartz are the same for NCC and SAM and this indicates the dependency of the K-means-rank[1] NMF algorithm to the clustering. This is also shown in Table 6.2 for the K-means-rank[1] NMF algorithm. However, the accuracy of NCC and SAM in the FCC-K-means algorithm is not similar and indicates that the identification process in the FCC-K-means algorithm depends more on the performance of the spectral comparison techniques than on clustering.

6.6   Discussion

6.6.1   Automatic identification process

Mineral identification has been studied and researched for several decades and most of these approaches have been categorized under the hyperspectral remote sensing, airborne, portable instruments (Lee and Seung, 1999), and core logging (Ding et al., 2005) applications. The proposed research addressed the application of hyperspectral infrared in the LWIR (7.7-11.8 μm) for the purpose of automated mineral identification applying two algorithms which involved un-supervised segmentation and spectral comparison techniques. It has been previously shown that clustering techniques are more suitable for categorizing the minerals as compared to classification (supervised) approaches. This is because of not having enough data to properly train the classifier and expensive labeling (Yousefi et al., 2016a; Mayer et al., 2003). Applying spectral comparison techniques and clustering approaches gave the opportunity to identify the

Table 6.6. The quantitative accuracy for spectral comparison techniques in the second algorithm.

Minerals mixture	NCC (%)			SAM (%)			OSP (%)			AMSD (%)		
	ACC	FN	FP	ACC	FN	FP	ACC	FN	FP	ACC	FN	FP
Biotite & Quartz	96.81	14.85	3.37	96.81	14.85	3.37	55.43	34.94	0.84	77.52	11.93	4.11
Diopside & Quartz	87.02	13.67	3.18	82.42	4.33	18.18	80.57	52.61	1.87	71.25	26.05	1.08
Epidote& Quartz	92.01	6.99	3.36	92.01	6.99	3.36	97.14	34.38	7.12	79.49	21.59	4.83
Geothite & Quartz	80.86	21.77	3.15	80.86	21.77	3.15	79.01	55.36	1.25	67.39	17.66	1.92
Kyanite & Quartz	90.86	5.66	3.72	90.86	5.66	3.72	71.84	24.30	1.39	86.29	6.01	7.04
Scheelite & Quartz	96.60	7.58	4.19	81.24	2.30	19.64	95.76	30.19	1.43	90.25	8.49	2.51
Smithsonite & Quartz	78.72	23.96	0	93.96	21.50	5.31	69.85	37.07	1.44	66.37	31.96	0.98
Tourmaline& Quartz	73.76	12.96	4.31	86.28	15.16	3.03	75.32	22.55	2.26	86.24	21.56	2.36
Pyrope & Quartz	72.13	4.28	6.78	81.74	0.68	69.43	86.83	12.54	2.07	51.08	6.65	5.17
Olivine & Quartz	62.69	60.83	1.42	84.78	5.85	71.90	83.96	5.57	3.64	73.17	10.67	8.88

minerals using two algorithms. The difference between these two approaches is in the utilization of these techniques in different hierarchies. Applying clustering or spectral comparison approaches for all data spectral points in these two algorithms is considered as the bottle neck for both algorithms due to the categorization task. Each of these algorithms, for all the data points can lead the entire algorithm to a high or low computational complexity. The algorithms have reasonable performance in the identification of the minerals. Some minerals such as goethite and smithsonite have no specific exterma in their LWIR spectra and their identification failed, regardless of which algorithm is applied (it is shown in Figure 6.6 and also table 6.2). In contrast, biotite, diopside, epidote, tourmaline, scheelite, quartz and kyanite have been identified more clearly due to their distinctive spectral signature in the LWIR.

6.6.2 Computational complexity of the algorithms

We analyzed two different algorithms using spectral comparison and clustering techniques applied in different hierarchies. The FCC-K-means algorithm calculates the spectral techniques for all the pixels of hyperspectral image spectra and gave false colors to these features and ultimately segmented these false color regions by applying clustering. On the contrary, the K-means-rank[1] NMF algorithm directly applies the clustering to all the pixels in the hyperspectral image. Then the first rank of NMF is selected as the spectral representative for each cluster (the statistical relationship among the clusters are shown by box-plots in figure 6.7). These spectra were compared with the reference spectra (ASTER spectral library) and this led to finale the segmentation process. The FCC-K-means algorithm shows to be more computational costly as compared to the K-means-rank[1] NMF algorithm because of the application of the spectral comparison approaches to the entire pixel's spectra of the hyperspectral images. Nevertheless, the results presented in Table 6.3 indicate that the K-means-rank[1] NMF algorithm is also computational costly due to direct clustering for the whole spectral pixel points. The computational complexity of the K-means algorithm for the fixed k and d (dimension) is $O(n^{(dk+1)} \log n)$ where n is the number of entities to be clustered (Aksenova et al.). Some heuristic algorithms such as Lloyds algorithm have the complexity of $O(nkdi)$, where k is the number of clusters, i is the number of iteration and n is the number of d-dimensional vectors (Ghasemzadeh-Barvarz et al., 2013). On the other hand, some algorithms such as SAM have a cosine function and have approximately the computational complexity of cosine which is $O(M(n)logn)$(for the algorithm of Arithmetic-geometric mean iteration) where $M(n)$ stands for the chosen multiplication algorithm complexity (Franc et al., 2005). Due to the division into the cosine function in the SAM, the complexity of $O(n^2)$ corresponds to the division itself which increases the whole complexity of the SAM function. The different computational complexity between clustering and spectral comparison techniques is the reason why calculation of the spectra for the K-means-rank[1] NMF algorithm shows considerably lower complexity as compared to the FCC-K-means algorithm.

The sensitivity of each algorithm depends on the spectral difference calculations. For example the FCC-K-means algorithm is sensitive to spectral techniques used for extraction of the RGB-FCC to finally clustering them. In the K-means-rank[1] NMF algorithm, the sensitivity of the system lies in the clustering approach and in particular, the number of initialization in K-

means clustering. Besides this, there are other factors nominally involved in the sensitivity of the proposed approaches such as the initialization of the clustering for the FCC-K-means approach and the spectral analysis in the K-means-rank[1] NMF method. In the K-means-rank[1] NMF algorithm, a spectrum from each selected cluster should be compared to reference spectra from the ASTER JPL-NASA spectral library. Several methods can be applied to select the best representative spectrum from each cluster such as randomly selecting one spectrum, spectral averaging or using factor analysis. Random or averaging selection of the spectrum might not be an efficient way to select the spectral representative in each cluster because of averaging and random calculation sensitivity against bad spectra (wrongly grouped spectra or noisy spectra) which may occur in the process. Some noisy spectra might be clustered into the mineral's category and random (or averaging) selection may not be able to exclude them from the spectral grouping and this ultimately influences the mineral identification. This matter can be a further research issue for correct identification of the spectra.

6.7 Conclusions

The proposed approach presented a geological hyperspectral infrared imagery (in the 7.7-11.8 μm-LWIR range) in laboratory conditions. This paper addressed a quantitative and qualitative assessments of two algorithms for the identification of several minerals. The FCC-K-means algorithm applied the spectral comparison techniques on the entire pixel-spectra of the input data cube and spectral library of JPL/NASA. It generated the spectral differ-ence which was presented in RGB-FCC form and a K-means clustering grouped the different composites. The K-means-rank[1] NMF algorithm clustered all the pixel-spectra in different categories. Then rank[1] extracted from NMF as representative for each cluster were compared to the spectral library of JPL/NASA through spectral comparison techniques which gener-ated RGB-FCC results. The results of the K-means-rank[1] NMF algorithm indicated more significant computational efficiency (more than 20 times faster) than the FCC-K-means al-gorithm. The K-means-rank[1] NMF algorithm showed more dependency to clustering rather then the FCC-K-means algorithm that was more sensitive to spectral comparison techniques. Both algorithms had promising performance for mineral identification having approximately 55% average accuracy using SAM. Several comparative popular spectral techniques were used such as AMSD, OSP, PLMF, SAM, and NCC but most of them showed similar accuracy

range (although PLMF exhibited a lower accuracy). Eleven different mineral grains (biotite, diopside, epidote, goethite, kyanite, scheelite, smithsonite, tourmaline, pyrope, olivine, and quartz) were studied. Future work can be more focused on clustering approaches and the noise effect in mineral identification to increase the performance of the system. Study of minerals with poorly shaped spectra is another important future research avenue.

Acknowledgement

Chapter 7

Automated LWIR Hyperspectral Infrared mineral identification reliability

(Submitted in Applied Optics Journal, 2018).

7.1 Résumé

L' élimination du continuum est une étape essentielle dans le processus d'analyse des images hyperspectrales qui permet d'utiliser les données pour toutes les applications et nécessite généralement certaines approximations ou hypothèses à effectuer. Une de ces approximations est liée au calcul des spectres de la température de corps noir de l'arrière plan. Nous présentons ici une nouvelle méthode pour calculer le processus d'élimination du continuum qui élimine ce calcul pour l'imagerie infrarouge hyperspectrale au sol en appliquant deux ensembles d'acquisition avant et après l'utilisation de la source de chauffage. L' approche décrit une expérience en laboratoire avec les ondes infrarouges longues (de $7.7\mu m$ à 11.8 μm), avec une lentille LWIR-macro, une plaque Infragold et une source de chauffage. Pour calculer l' élimination du continuum, l' approche applique la factorisation matricielle non négative (NMF) pour extraire le NMF de rang 1 et estimer le rayonnement de downwelling, puis le comparer avec d' autres méthodes conventionnelles. Pour obtenir le NMF de rang 1, NMF utilise des algorithmes d' optimisation basés sur la descente de gradient (GD) et des moindres carrés non négatifs (NNLS). L' analyse comparative est réalisée avec un bruit additionnel de $1 - 10\%$ pour tous les algorithmes utilisant Spectral Angle Mapper (SAM) et Normal Correliation Corrélation (NCC). Les résultats indiquent une performance relativement prometteuse en utilisant NMF-GD (moyenne de 72.5% pourcentage de similarité en utilisant NCC) et NMF-NNLS (moyenne de 77.6% de similitude en utilisant la NCC).

General Explanation

An automated system for mineral identification in long-wave infrared (LWIR) using data-mining approaches represented a reasonably good performance to identify the mineral grains. In general, an automated system to identify the mineral grains consists of spectral comparison methods, spectral libraries as reference spectra, and decision making unit which use the supervised or unsupervised method for mineral identification. Here, an automated system for mineral identification has been challenged in terms of reliability and correctness to identify eleven different mineral grains (biotite, epidote, goethite, diopside, smithsonite, tourmaline, kyanite, scheelite, pyrope, olivine, and quartz). The samples were tested by Micro X-ray Fluorescence (μXRF) and Scanning Electron Microscope (SEM) in order to retrieve information of the mineral aggregates and the grain's surface. The results of μXRF imagery compared with automatic mineral identification techniques, using ArcGIS, and showed a promising performance for automatic identification.

The results of this study were partially presented the 14th International Workshop on Advanced Infrared Technology and Applications, AITA 2017, Quebec city, Canada.

Contributing authors:

Bardia Yousefi (Ph.D. candidate): a part of the experiment planning, data collection, data analysis, designing and implementing the algorithm. Moreover, testing their accuracy and robustness throughout the process and writing the manuscript.

Clemente Ibarra Castanedo: the experiment planning, data collection, mineral preparation, revision and correction of the manuscript.

Xavier P.V. Maldague and **Georges Beaudoin**: (The main research director and co-director, respectively): supervision, revision and correction of the manuscript.

Other contributors:
Annette Schwerdtfeger (research officer): manuscript preparation.

Kévin Liaigre: Conducting μXRF and SEM experiments, ArcGIS stimulation, Assisting to generating the observed ground truth.

Saeed Sojasi: Generating the observed ground truth, assisting in μXRF and SEM experiments.

Martin Chamberland : LWIR hyperspectral camera preparation, experiment planning, data collection.

Automated LWIR Hyperspectral Infrared mineral identification reliability

Bardia Yousefi[1], Clemente Ibarra Castanedo[1], Xavier P.V. Maldague[1], Georges Beaudoin[2]

[1] *Computer Vision and System Laboratory, Department of Electrical and Computer Engineering, Laval University, 1065, av. de la Médecine, Quebec, QC, Canada*

[2] *Department of Geology and Geological Engineering, Laval University, 1065, av. de la Médecine, Quebec, QC, Canada*

Corresponding author: bardia.yousefi.1@ulaval.ca

7.2 Abstract

Application of hyperspectral infrared imagery for mineral grain identification suffers from lack of prediction on the irregular grain's surface along with the mineral aggregates. Here, we present an investigation on automatic mineral identification in the Long Wave Infrared (LWIR, 7.7-11.8 µm) with a LWIR-macro lens having a spatial resolution of 100 µm. We attempt to identify eleven different mineral grains (biotite, epidote, goethite, diopside, smithsonite, tourmaline, kyanite, scheelite, pyrope, olivine, and quartz). An automatic system compares all of the pixel-spectra to the ASTER spectral library of JPL/NASA using Spectral Angle Mapper (SAM), and Normalized Cross Correlation (NCC) to create false color maps. Then a hue-saturation-value (HSV) âPrinciple Component Analysis (PCA) based K-means clustering approach groups the mineral regions in different categories. The results were compared to two different Ground Truth (GT) (i.e. rigid-GT and observed-GT) for quantitative calculation. Observed-GT increased the accuracy up to 1.5 times higher than rigid-GT, from 45.67 % to 69.39 %. The samples were also examined by Micro X-ray Fluorescence (µXRF) and Scanning Electron Microscope (SEM) in order to retrieve information of the mineral aggregates and the grain's surface. The results of µXRF imagery compared with automatic mineral identification techniques, using ArcGIS, and represents a promising performance for automatic identification.

Keywords: Infrared and thermal image analysis, Mineral identification, Long wave infrared spectroscopy, clustering.

7.3 Introduction

Hyperspectral imagery is an efficient tool that has been successfully employed in a variety of applications ranging from food quality (Gowen et al., 2007) to mineralogy and geology (Kruse,

1996a; Liu et al., 2016; Calvin and Pace, 2016; Su et al., 2012; Eismann and Hardie, 2004) and more recently it has been expanded to astronomical analysis (Wray et al., 2013; Meunier et al., 2012; Clark et al., 2005). Here, a ground truth-based automatic mineral identification using spectral analysis for hyperspectral infrared imagery in laboratory conditions is presented. In contrast to remote sensing and airborne applications, the laboratory conditions used herein are less affected by spatial resolution difficulties. However, the empirical and analytical outcomes look different from theory. The incertitude is more related to the accuracy in identifying the mineral and how much hyperspectral infrared imagery is useful for mineral grain identification. The proposed approach addressed an analysis on the surface of the mineral grains involved in the process of automatic mineral identification to clarify the level of its reliability. The approach includes a comparison between different microscopic techniques and uses an automatic system to the system reliability. Hyperspectral imagery has been widely used for remote sensing (satellite based hyperspectral imagery) and airborne applications particularly in the mineralogy and geological field, especially in the area of hyperspectral unmixing and endmember algorithms (e.g. (Bioucas-Dias et al., 2012; Kwon and Nasrabadi, 2005)). This is due to the low spatial resolution of the images given the great distance between the hyperspectral camera and the targeted regions. In addition, data of remote sensing are affected by several factors such as signal-to-noise ratio (SNR) (Kruse et al., 2003) and image acquisition properties (Shahriari et al., 2015).

a Sample of mixed Biotite & Quartz grains — Biotite grain

b Sample of mixed Diopside & Quartz grains — Diopside grain

c Sample of Pyrope grains — Pyrope grain

d Sample of mixed Tourmaline & Quartz grains — Tourmaline grain

e Sample of mixed Goethite & Quartz grains — Goethite grain

f Sample of mixed Kyanite & Quartz grains — Kyanite grain
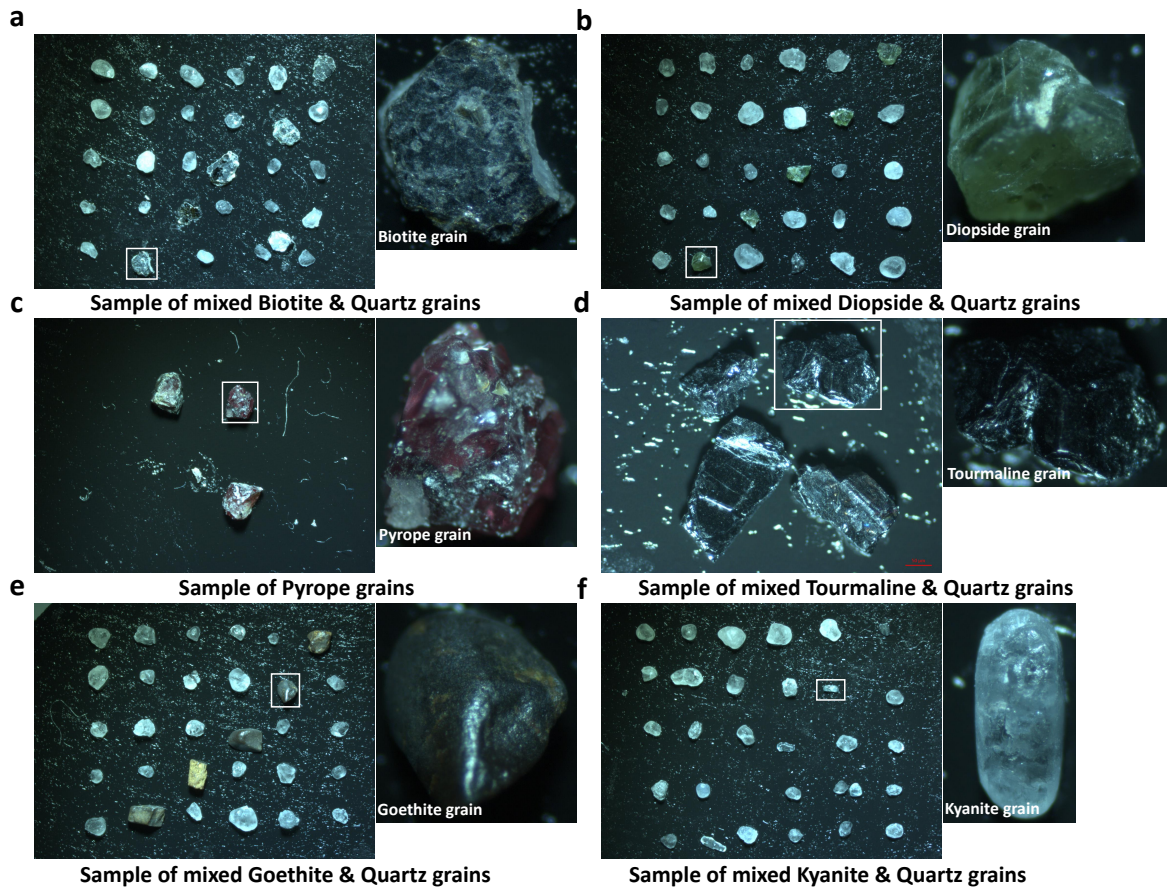
Figure 7.1: **Images of the grain's surface using a binocular microscope.** The surface structure of mineral grains are shown using binocular imagery. In each case, the targeted mineral grains which are visualized on a larger scale, are randomly selected in the mixed samples (except for pyrope grains **c** that is selected from pure set). The grains are attached to a carbon layer as substrate to allow them to be more easily discriminated from the background. The scale of the larger images from mixed samples are 50 μm and each zoom on the grain separately has more than 7.5 times higher magnification. As shown in the images, the grain's surface is irregular leading to caused by the reflection of the spectral radiation. For example in biotite, pyrope, and tourmaline cases, the surface is rough with several sharp edges. In contrast, diopside, kyanite, and goethite have a smoother surface. Hence, it is not possible to generalize the property of the grain's surface of these samples to all grains.

Mineral	Chemical formula	Short Description
Biotite	$K(Mg,Fe)_{2-3}Al_{1-2}Si_{2-3}O_{10}(OH,F)_2$	substantial group of dark mica minerals
Diopside	$MgCaSi_2O_6$	strong arrangements with hedenbergite ($FeCaSi2O_6$)
Epidote	$Ca_2(Al_2,Fe)(SiO_4)(Si_2O_7)O(OH)$	silicate mineral
Goethite	$(FeO(OH))$	
Kyanite	Al_2SiO_5	high-weight polymorph, sillimanite, shaped at high temperature, and andalusite is the low weight polymorph
Scheelite	$CaWO_4$	calcium tungstate mineral
Smithsonite	$(ZnCO_3)$	calcite group of minerals
Tourmaline	$((Na, Ca)(Mg,Li,Al,Fe^{2+})_3Al_6(BO_3)_3Si_6O_{18}(OH)_4)$	
Olivine	$(Mg^{+2}, Fe^{+2})_2 SiO_4$	
Pyrope	$Mg_3 Al_2 (SiO_4)_3$	garnet group minerals
Quartz	SiO_2	the most abundant mineral in the Earth's crust

Table 7.1. Characteristics of the minerals studied by LWIR.

The hyperspectral imagery in indoor conditions is usually limited to core logging applications (e.g. Kruse (1996a), Calvin and Pace (2016)). The spatial resolution of the hyperspectral camera is relatively better than in the remote sensing and airborne category given the shorter distances between the imagery device and the samples. Hence, the algorithms in such applications are more focused on mineral identification rather than unmixing and identifying the endmember. The experimental conditions are similar to the specimens studied herein with the difference that, in our case, the mineral grains are of a smaller size and thus an increased spatial resolution is required. In aqddition, similar to other hyperspectral infrared analysis, the reflection of heating source spectral radiation , i.e. the continuum, that affects the entire spectra needs to be removed. The process of removing this spectra is called the continuum removal (CR) (Clark and Roush, 1984; Clark and King, 1987). Performing CR is vital to allow spectral techniques to compare the targeted spectra to the reference spectra from a reference spectral library such as ASTER (Baldridge et al., 2009). CR corrects the radiometric parameters by eliminating the spectral radiation from the thermal source, and the spectral radiance from the environment (Yousefi et al., 2016b; Ruff et al., 1997). The method used herein involves two acquisitions, one before and one after heating the samples. An InfraGold reference panel (Labsphere, North Sutton, NH, USA) was used (Yousefi et al., 2016b, 2017; r19. The proposed approach investigates the automatic mineral identification reliability. First, minerals are automatically identified from their hyperspectral signatures and then results are compared to microscopic techniques and X-ray analysis to determine the mineral existing on the grains for better comparative assessments.
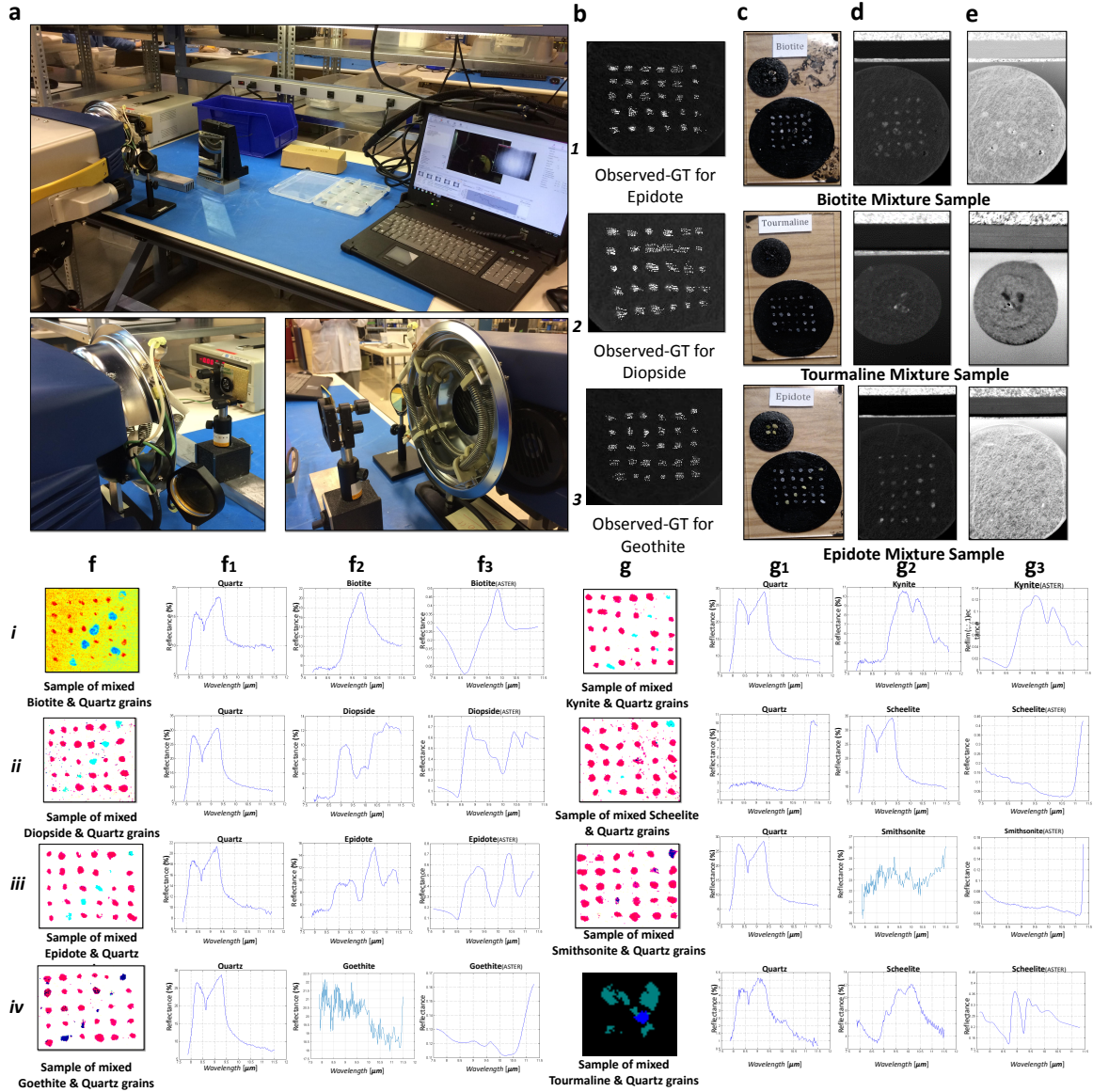
Figure 7.2: **Long-wave infrared hyperspectral imaging system and automated mineral identification results.** The figure represents the automatic mineral identification from the experimental setup using false colors. **a** shows the experimental setup and test conducted using a hyperspectral infrared camera in LWIR. Column **b** depicts the observed ground truth for epidote (**b.1**), Diopside (**b.2**), and goethite (**b.3**). Columns **c**,**d**,**e** present the pure and mixed samples, and the hyperspectral images after and before heating, respectively. Columns **f** and **g** show the false color results where minerals are shown in different colors in the images. Columns **f1**, **f2**,**g1**, and **g2** show the spectra corresponding to every color in the false color images. However, for every mineral case, spectra from the ASTER spectral library have been presented in columns **f3**, **g3**. As shown in **a**, each sample was tested using an InfraGold (Labsphere: Technical guide: Integrating sphere theory and applications) reference panel on the background image to estimate the down-welling radiation spectra (shown in **d.1**,**d.2**,**d.3**,**e.1**,**e.2**, and **e.3**).

7.4 Methods

Sample preparation. The mineral grains were first washed and categorized by sizes. Selected grains were than glued to carbon substrates (sheets) in two different categories; pure sets and mixed sample sets. The pure set was used for training or spectral referencing. ASTER spectral library was not used at this stage techniques. The mixed sample sets consisted of targeted mineral grains with in an array of quartz grains included for reference. The mineral grains are diagonally (form bottom-left to top right, Figure 7.1) arranged in the samples and used in testing stages or verification of the automatic mineral identification process.

Experimental setup and Image acquisition. A lightweight Hyper-Camera imaging spectroradiometer (HYPER-CAM LW from Telops) (Ding, 2005) operating in the LWIR band (from 7.7 to 11.8 μm) was used for our experiment conducted in a laboratory environment. It has a spectral resolution of $0.22\mu m$ and a spatial resolution of 320×256 pixels with a LWIR PV-MCT focal plane array detector. The Hyper-camera uses a Fourier-Transform Spectrometer (FTS or FT-IR) and has an instantaneous field-of-view (FOV) of 0.35 mrad (Ding, 2005). The image acquisitions were performed while the minerals were attached to a carbon substrate with an infragold plate in the background which was used for CR. The experiments were conducted before and after using the heating source. there are 88 channels of spectral resolution. The studied mineral grains were selected as they possess a distinctive a signature in the range of the hyperspectral-camera.

Classification models. A Hue-Saturation-Value (HSV) - Principal Component Analysis (PCA) based K-means clustering segmented the false color images are provided by spectral comparison techniques. As the clustering is performed based on applying the eigenvalues extracted from the data to make dimensional reduction before grouping, the clustering is considered as a spectral clustering method (Ng et al., 2002). This clustering has been used to categorize the false colors map created by spectral comparison techniques. The major reason for using HSV for clustering is due to the separation of the luma, which contains the intensity information of the image, from the chroma comprising the color information. Unlike the RGB color system, the HSV provides robustness to removing shadows or lighting variations. In HSV the actual color components are in the target whereas in the RGB color system, the implementation details concern the color display. This means that RGB represents more of

a computer-treated means of representing the color whereas HSV provides the components captured in the way in which humans perceive color. Response (or resonation) of the human eye is surprisingly limited to three main light frequencies red, green and blue. It is not linear and provides a pure color unique response of the retina combining three color component responses. It works regardless of lighting changes in the value channel and therefore practical clustering gives reasonable efficiency. K-means clustering efficiently provides categorization of ROI in the hyperspectral image. The entire computational process was carried out with a PC (Intel Core 2Quad CPU, Q6600, 2.40GHz, RAM 8.00GB, 64 bit Operating System) and data analysis was conducted using the MATLAB programming language.

7.5 Results

Mineral grains and their spectra. The surface structure of the studied mineral grains are illustrated in Fig. 7.1. The structure of the surface in mineral grains is irregular so our study considered only the general mineralogical composite assessment through hyperspectral infrared imaging for automatic grains identification, independent from the shape or geometry of their surface. The eleven minerals analyzed here are listed in Table 7.1 together with their chemical composition and a short description. The grain's sizes are varied between $0.6mm$ to $2.0mm$. A special lens was used for better spatial resolution (which is described in the next section). The grain groups were divided into two main sets containing pure and mixed minerals. The pure mineral grains were selected to be used for training and spectral reference along with the ASTER spectral library (Baldridge et al., 2009).

Hyperspectral Data Analysis. The first step of the identification process includes the CR process to remove the heating source spectral radiation from the data. This process is achieved by performing two image acquisitions, one before heating the sample and one after heating the sample. The heating source radiation was obtained from the InfraGold reference panel (Labsphere, North Sutton, NH, USA) which has a reflectivity of $92-96\%$ for $1-16\mu m$ wavelength radiation (r19). This CR process makes the spectral comparison between the targeted and reference spectra possible. Mineral identification using supervised/unsupervised approaches is a computational method to classify and segment the pixel-spectra. This is highly dependent on the spectral comparison techniques that are used to extract the spectral features from data. Using Spectral Angle Mapper (SAM) and Normalized Crossed Correlation

(NCC) showed considerable performance since these methods are dependent on the topology of spectra. These algorithms calculate the difference between the reference and targeted spectra in the form of an error (in the case of SAM) and correlation similarity parameter (in the case of NCC). The reference spectra for comparison is associated with the spectra corresponding to the pure minerals (Fig. 7.2.c.1., Fig. 7.2.c.2., Fig. 7.2.c.3.) and the spectra from the ASTER spectral library (Fig. 7.2.f3.i.,Fig. 7.2.f3.ii.,Fig. 7.2.f3.iii., Fig. 7.2.f3.iv., Fig. 7.2.g3.i., Fig. 7.2.g3.ii., Fig. 7.2.g3.iii., Fig. 7.2.g3.iv.)(Baldridge et al., 2009). The targeted mineral grains in LWIR have spectral profile similar to the ones found on the ASTER library (Fig. 7.2.f2.i.,Fig. 7.2.f2.ii.,Fig. 7.2.f2.iii., Fig. 7.2.f2.iv., Fig. 7.2.g2.i., Fig. 7.2.g1.ii., Fig. 7.2.g2.iii., Fig. 7.2.g2.iv.). The comparison was performed for each pixel spectrum and it provided the spectral coefficient amount for the targeted pixel-spectrum and continued by looping over all the spectral pixels in the hyperspectral cube. Ultimately, the spectral variation provided a map which represents the spectra similarity to targeted spectra, a false colors map that was segmented afterwards. Figure 7.2 depicts the experimental setup and automatic mineral identification using hyperspectral infrared imagery. It is clear that the spectra obtained for the targeted mineral grains in LWIR (Fig.7.2) compare very well with the spectra of the pure minerals as well as with the spectra from the ASTER spectral library.
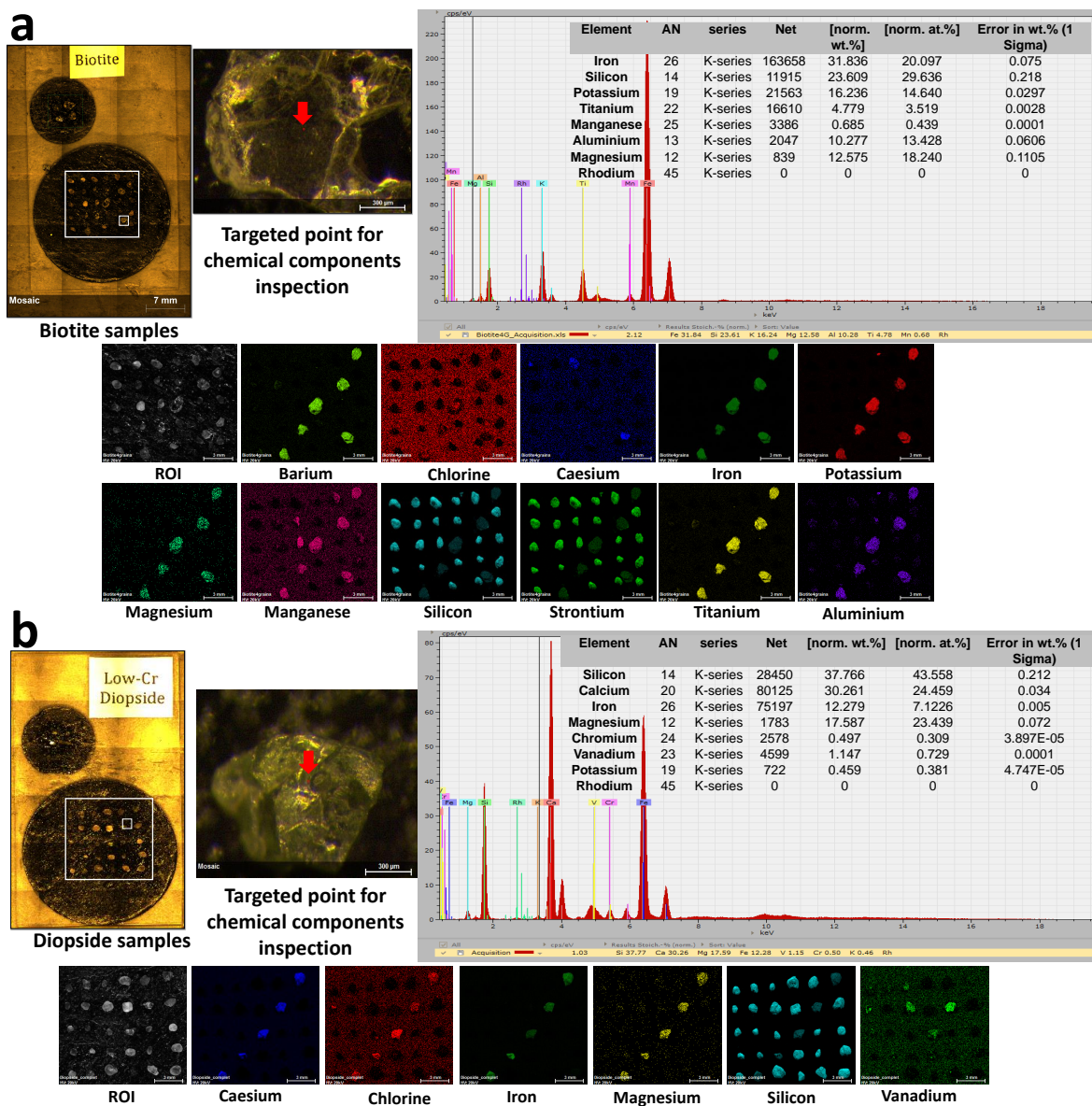
Figure 7.3: **Two examples of μXRF imagery for biotite and diopside.** the picture represents two examples of μXRF microscopy for biotite and diopside along with the representation of the mineral aggregates in the form of quantitative plots and tables. For each mineral there is an image that illustrates the ROI and images of mineral aggregates corresponding to the ROI's image. The mineral aggregates map indicates the presence of some minerals in the grains and shows the location of the grains in each sample.

Mineral	Spatial resolution of RoI	Rigid-GT		Observed-GT		Accuracy by Rigid-GT	Accuracy by Observed-GT
		Mineral	Quartz	Mineral	Quartz		
Biotite	123*138	434	483	78	434	52.45	89.16
Diopside	126*143	253	705	46	637	40.21	56.40
Epidote	123*148	216	706	38	516	48.64	80.95
Geothite	118*141	199	552	34	443	33.76	53.15
Kyanite	123*144	68	510	11	657	37.44	32.39
Scheelite	123*158	134	810	22	591	48.69	74.98
Smithsonite	119*160	343	913	9	507	28.39	69.11
Tourmaline	58*80	122	9	60	17	75.81	>99

Table 7.2. Accuracy of automatic mineral identification is presented for Rigid-GT and Observed-GT.

Automatic grain identification. Unsupervised mineral identification was performed using the HSV-PCA based K-means clustering approach. The clustering process was performed knowing the number of interested clusters. The entire automated classification system is shown in Figure 7.2 along with the processing results. The system accuracy was directly calculated by discriminating false color images through color based clustering in each mineral sample. The HSV-PCA clustering was constructed by using the first two eigenvectors (PCs) corresponding to the image variables in the HSV color system. The clustering output variables associated with index numbers for each segment were labeled to the targeted mineral which led to their identification. Applying the clustering method for eigenvectors of the input data converted the clustering process into the spectral clustering approach. As in each mineral mixture case, the targeted grains were mixed with quartz grains, therefore for each mixed sample the accuracy is estimated through the average accuracy for both two types of grains. Two types of error are shown as a false positive that represents wrong mineral identification and a false negative that reveals misidentified minerals and both are calculated in separate cases. Total accuracy for each mineral calculated by subtraction of the correct identification and the two errors for each sample. The overall accuracy of automatic mineral identification was 45.67 % (averaging of all the accuracy using NCC) which is shown in Table 7.2.

a

Live Time: 60,00 Count Rate: 1867 Dead Time: 18,89 %
Beam Voltage: 15,00 Beam Current: 1,00 Takeoff Angle: 30,00
EDS-Biotite-phase-foncee-intermediaire-grain-bas-gauche.pgt
FS: 900

Element	Wt%	At%	ChiSquared
O	40,83	58,05	19,11
Al	13,57	11,44	5,27
Si	20,14	16,31	15,98
Fe	14,11	5,75	1,32
K	4,19	2,44	1,29
Mg	5,67	5,31	6,25
Ti	1,50	0,71	0,28
Total	100,00	100,00	4,14

Element	Gross (cps)	BKG (cps)	Net (cps)	P:B Ratio	Z Corr	A Corr	F Corr
O	172,9	7,1	165,8	23,4	0,931	2,410	0,999
Al	157,0	17,2	139,8	8,1	1,007	1,533	0,993
Si	234,7	16,2	218,5	13,5	1,020	1,494	0,999
Fe	26,1	4,3	21,9	5,1	1,154	1,004	1,000
K	33,9	13,2	20,7	1,6	1,083	1,101	0,996
Mg	80,4	18,0	62,4	3,5	0,993	1,743	0,993
Ti	11,2	6,8	4,4	0,6	1,116	1,036	0,986

SEM image from a Biotite grain

b

Live Time: 60,00 Count Rate: 1783 Dead Time: 17,95 %
Beam Voltage: 15,00 Beam Current: 1,00 Takeoff Angle: 30,00
EDS-Biotite-phase-noire-grain-bas-gauche.pgt
FS: 1600

Element	Wt%	At%	ChiSquared
O	53,59	67,17	27,92
Al	35,58	26,45	37,95
Si	7,03	5,02	3,95
Fe	3,80	1,36	1,20
Total	100,00	100,00	5,28

Element	Gross (cps)	BKG (cps)	Net (cps)	P:B Ratio	Z Corr	A Corr	F Corr
O	213,7	6,8	206,9	30,5	0,959	1,864	0,999
Al	385,1	19,3	365,8	18,9	1,037	1,331	0,998
Si	78,0	18,8	59,2	3,2	1,051	1,665	1,000
Fe	6,8	3,0	3,8	1,3	1,187	0,998	1,000

c

Live Time: 60,00 Count Rate: 1647 Dead Time: 17,77 %
Beam Voltage: 15,00 Beam Current: 1,00 Takeoff Angle: 30,00
EDS-Biotite-phase claire-grain-bas-gauche.pgt
FS: 800

Element	Wt%	At%	ChiSquared
O	28,59	46,14	11,35
Al	7,67	7,34	7,46
Si	18,47	16,98	17,29
Fe	19,48	9,01	0,83
K	11,01	7,27	2,37
Mg	10,13	10,76	6,46
Ti	4,66	2,51	0,42
Total	100,00	100,00	3,31

Element	Gross (cps)	BKG (cps)	Net (cps)	P:B Ratio	Z Corr	A Corr	F Corr
O	99,1	6,1	93,0	15,3	0,908	3,170	0,999
Al	96,0	14,7	81,3	5,5	0,982	1,662	0,993
Si	194,8	13,9	180,9	13,0	0,996	1,499	0,998
Fe	32,6	4,6	28,0	6,1	1,128	1,012	1,000
K	72,0	17,5	54,5	3,1	1,057	1,097	0,993
Mg	98,5	15,8	82,8	5,2	0,969	1,823	0,995
Ti	20,3	6,8	13,5	2,0	1,090	1,051	0,985

Figure 7.4: **An example of SEM imagery for inspection of biotite's surface.** As shown in the SEM image, the grain's surface is irregular and has an unpredictable shape. This causes the non-uniform scattering of the spectral reflection in the hyperspectral image and consequently inaccurate signature for the mineral in the region. There are three randomly selected points in the grain's surface that have been analyzed for mineral component inspection.

Ground truth. The quantitative assessment and percentage of the accuracy depends on the ground truth and was carried out by comparing the identified mineral pixels with the grain's actual location. This called the Ground Truth (GT) and referred to a set of labeled images constructed by an expert space (geologist or knowledgeable data-analyzer) observation of the mineral positions, rigid-GT, or their spectra, observed-GT. GT has the size similarity to spatial-resolution of the hyperspectral images. Rigid-GT and manual labeling might not be a correct indicator for actual mineral presence for two reasons. First, the grains might not be absolutely pure and might have other mineral aggregates. Second, grains have irregular surfaces and might scatter the reflectance of the mineral and consequently the hyperspectral camera might not correctly see the mineral. So generating another GT by manual observation of the entire hyperspectral data cube is seemingly needed. To address this need, a Matlab user interface was developed for the pixel observation and labeling. This provided an opportunity to visually compare more than 200,000 pixel-spectra to those of the ASTER spectral library. Fig. 7.2.d provides a sample of the observed-GT which shows the selected regions in the mixed mineral sample. The number of the mineral samples in the observed-GT is lower than in the rigid-GT due to a slight scattering of radiation and non-homogeneous reflection received by the hyperspectral camera caused by the irregular surface of the grains. Table 7.2 presents the accuracy of the system using rigid-GT and observed-GT. The average identification accuracy using observed-GT is 1.5 time more accurate than when using rigid-GT, increasing from 45.67% to 69.39%.
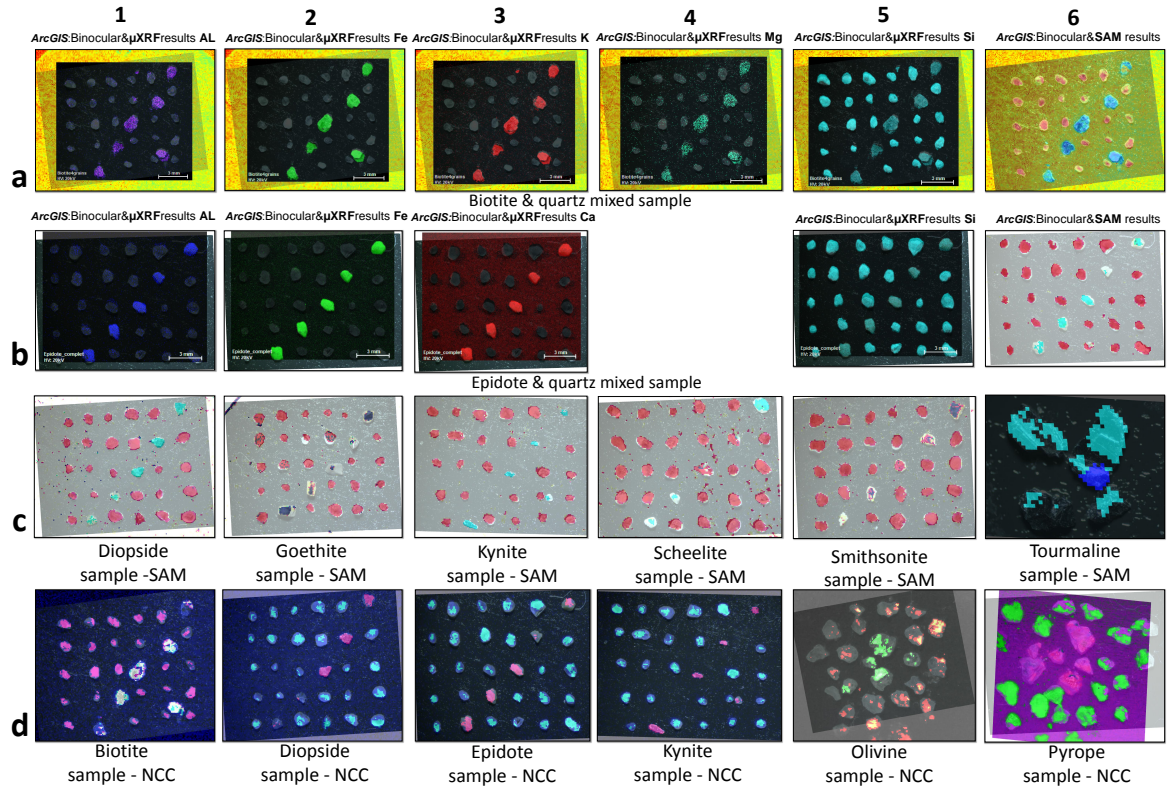
Figure 7.5: **The results of automatic identification fused by the** μXRF **and binocular images to determine the reliability.** The figure generated by ArcGIS v10.2 based on combining mineral aggregates images using μXRF microscopic imagery and binocular images from the samples. **a,b** show the results of μXRF along with the results of image fusion for biotite (**a**) and epidote (**b**), respectively. Rows **c,d** are the results of SAM and NCC for targeted mineral grains in the mixed samples.

Micro X-ray Fluorescence (μXRF). To provide a detailed investigation of the mineral grain's surface and mineral composition the Region Of Interest (ROI), an experiment was conducted using a μXRF (M4 TORNADO, 60 mm^2 XFlash SD detector); μXRF is a spectroscopy machine which enable an elemental analysis on very small samples.

μXRF uses direct X-ray excitation to induce the X-ray fluorescence emission and bombards to the samples using X-ray optics to limit the excitation beam size to focus on a small spot (TORNADO, 2015). The combined results of the automatic mineral identification and μXRF can represent the misclassification. This also indicated the presence of additional mineral aggregates within the ROI. The challenge in combining the information contained by these images is related to the different resolution of the images. To address this issue, ArcGIS software was used which fused the images of the automatic identification with the images obtained from μXRF (and even binocular images) and ultimately provided an image map that indicated different mineral content corresponding to the identification among the mineral grains. Fig. 7.3 depicts biotite and diopside examples (pure and mixed grains), the targeted point for the mineral decomposition at the grain and its corresponding result.

Scanning electron microscope (SEM). The difference in the rigid-GT and observed-GT indicated that there are some non-smooth surfaces on the mineral grains. To better analyze the grain's surface, some microscopic imagery was used such as binocular imagery (some results of binocular images from the grains are shown in Fig.7.1). However, a superior observation was provided by scanning electron microscope (SEM) technique. In addition, SEM gives the external morphological information and its chemical composition. Fig. 7.4 presents the SEM image from the biotite grain's surface and the chemical decomposition of three points on the surface of biotite which mineral assemblage. This sample was smoother than some other mineral grain samples, indicating that the scattering and non-homogeneous reflection process were minimal during the hyperspectral image acquisition.

Mineral	Accuracy			
	Pixel Based		Grains detected/ Total Number of grains (NCC)	Grains detected/ Total Number of grains (SAM)
	Accuracy -NCC	Accuracy -SAM		
Biotite	51.25	71.32	6/6	6/6
Diopside	50.81	74.3	5/5	5/5
Epidote	82.4	72.14	5/5	5/5
Geothite	■■■■■■	53.53	■■■■■■	5/5
Kyanite	76.22	61.49	5/5	5/5
Scheelite	75.29	65.73	5/5	5/5
Smithsonite	■■■■■■	45.47	■■■■■■	4/5
Tourmaline	■■■■■■	17.11	■■■■■■	1/1

Table 7.3. Accuracy of automatic mineral identification using ArcGIS mapped our results on binocular image.

7.6   Discussion

Following the objective of this research, which was to verify the reliability of this process, we automatically identified the mineral grains using hyperspectral comparison analysis such as SAM and NCC to create false color images and segmentation was then performed by HSV-spectral clustering. The accuracy was based on counting the correctly detected pixels in the hyperspectral images. There are two possible types of errors: a false positive signifies a wrong mineral identification and a false negative indicates mineral grain misidentification. Both of these errors were considered in each case. The overall accuracy was calculated by subtraction of the correct identification and two errors for each samples. Moreover, the accuracy of the system using ArcGIS is shown in Table 7.3.

The quantitative results were first performed using rigid-GT for mineral identification. Then, the quantitative comparison was performed by Observed-GT which increased the accuracy percentage with the exception of kynite, where accuracy decreased from 37.44% to 32.39% (Table 7.2) because of the presence of other minerals or irregular surface in its grain. The lower number of selected pixels of the observed-GT as compared to rigid-GT is a result of the non-smooth surface of the grains that led to non-homogeneous spectral reflectance and eventually to weaker spectral signatures. The irregular surface of the mineral grains was observed through SEM imagery along the points mineral composition of some randomly selected points. The SEM image indicated the irregular surface for the mineral grains that resulted in the scattering in the spectral radiation.

μXRF spectroscopy was used to test the mineral composition and the aggregates with other minerals. This method revealed the mineral content of each mineral along with some random exploration (Fig.7.3 presents the results of mineral identification). μXRF mineral composition indicated the different mineral contents, which ultimately led us to identify the grain. The resulting image provides, the location of grains fitted to the mineral grains as an automatic identification, thereby representing a good verification for the identification process. Fig.7.5 presents the results of ArcGIS image fusion.

For each mineral there are several key existing elements which were tracked by μXRF to verify the identification. μXRF decomposes the mineral mapping based on the mineral compositions. For example, biotite ($K(Mg, Fe)_3AlSi_3O_{10}(OH, F)_2$, Table 7.1) and μXRF provided aggregates maps for all of these elements (Fig.7.5 a1-5). Finally, a good match between binoc-

ular and automated results (Fig.7.5 a6) indicated a good system performance. For diopside ($CaMgSi_2o_6$, Table 7.1) the key elements are Si, Ca, and Mg and consequently μXRF gave a map for these minerals and ArcGIS mapped automatic detection into a binocular image. The system's results (Fig.7.5 c.1) show very good matching and correct identification. On the other hand, for smithsonite ($ZnCO_3$) and goethite ($FeO(OH)$) no Si aggregates exists for these minerals but the automated system found a small amount of Si which can be considered as a fault of the system.

7.7 Conclusions

The proposed approach investigated the automatic mineral grains identification using hyperspectral imagery in laboratory conditions. An experiment was conducted using a hyperspectral camera in the Long Wave Infrared (LWIR, 7.7-11.8 μm) with a LWIR-macro lens providing a spatial resolution of 100 μm per pixel (from a distance of 30 cm between the camera and the specimen), an infragold plate, and a heating source to generate the data. For mineral identification, first the system applied the spectral comparison techniques, SAM and NCC, on the pixel-spectra of the input data cube and the ASTER spectral library of JPL/NASA. This generated the spectral difference in the form of false colors so a HSV based spectral K-means clustering then grouped them into different mineral categories. Eleven different minerals (biotite, epidote, goethite, diopside, smithsonite, tourmaline, kyanite, scheelite, pyrope, olivine, and quartz) were tested in the targeted band and most of them had a signature in this band. The results were compared with GT to calculate the quantitative assessment of the system. Two types of GT were created and used; rigid-GT and observed-GT which led to an increase in the overall accuracy of the system by 23.7% from 45.67 % to 69.39 %. Moreover, the mixed samples have been examined by μXRF and SEM imagery systems to analysis the mineral aggregates and surface of the grains. The results of μXRF compared well with automatic mineral identification techniques using ArcGIS software and represented a promising performance of automatic identification. The comparison indicated a very reasonable accuracy and thus can be used to investigate additional minerals and wavelength bands of hyperspectral infrared image acquisition as future work.

Acknowledgements

Chapter 8

General conclusions and perspectives

8.1 Conclusions

The objective of the present thesis was to create an automated mineral identification system approach technique which provides suitable accuracy and involves relatively low computational complexity. The tool proposed herein uses hyperspectral infrared imagery data and processes the data through image analysis and machine learning methods to identify small size mineral grains used as mineral indicators. Moreover, it allows the system to be an additional computer-aided geological tool for mineral identification and creates a platform for any other derivation of hyperspectral infrared imagery. The main hypothesis stated that hyperspectral infrared imagery can be a useful tool to identify the small mineral grains through spectral data assessment and that automated/semi-automated or supervised/unsupervised data analysis methods for spectral technology are effective tools that would allow the relatively precise assessment of the mineral's locations in the samples.

Overall, a modified continuum removal approach was proposed for ground based spectroscopy which alleviated the process of calculating the blackbody temperature in the panels surface by conducting the acquisition before and after heating the samples. The calculation was verified by using data generated through an experiment conducted in the $7.7 \mu m$ to $11.8 \mu m$ LWIR wavelength range. Moreover, the subsequent calculations of the continuum removal were also modified by an estimation of the downwelling spectral radiance using Non-Negative Matrix Factorization (NMF) optimized by Gradient Descent (GD) and Non-Negative Least Square (NNLS) methods. The similarity percentage of the continuum removed spectra from

each method was compared to the spectra of the minerals from the ASTER spectral library using Spectral Angle Mapper (SAM) and Normalized Cross Correlation (NCC) which showed promising performances in terms of spectral retrieval.

Then a supervised method (kernel Extreme Learning Machine-ELM) and unsupervised method (K-means clustering) was used to create an automated system for mineral identification in long-wave infrared (LWIR) ground-based spectroscopy. Based on the performance of each system, the supervised classification significantly showed the dependence on the number of training samples and is considerably less efficient as compared to clustering due to the nature of the supervised learning process.

More favorable and easier to use unsupervised approaches (clustering) were studied in the third part of the performed analysis which included testing two different algorithms involving clustering strategies to group the spectra and ultimately achieve mineral identification for eleven different mineral grains (biotite, diopside, epidote, goethite, kyanite, scheelite, smithsonite, tourmaline, pyrope, olivine, and quartz). This clustering algorithm boosted a performance about twenty times faster with also a noticeable accuracy.

The reliability of the proposed automated system was also verified applying Micro X-ray Fluorescence (μXRF) and Scanning Electron Microscope (SEM) in order to retrieve information of the mineral aggregates and the grain's surface. The results of μXRF imagery were compared with automatic mineral identification techniques, using ArcGIS, and showed a promising reliability for automatic identification.

The analysis and the automated system used in this study was able to identify the grains and differentiate the different types of the minerals in a sample using LWIR hyperspectral analysis. However, the proposed system was not able to identify the minerals which have a significant spectral signature in another wavelength band range. The results demonstrate how positive is the impact of an automated system for mineral identification at LWIR and also highlight the important effect of the mineral's surface on the generated spectra and ultimately their identification. Finally, the results of the hyperspectral infrared imagery showed a promising performance as a good solution to identify small grains in a specific wavelength band range.

8.2 Futures perspectives

8.2.1 Possible modification of mineral grains

The mineral grain samples of this thesis involved non-mixed and mixed samples. To the mixed samples some more quartz samples were usually added into the arrangement. The mixed samples can be expanded to several different grains (not only quartz). That would increase the complexity of the analysis and demand a more powerful analyzer to perform the task and correctly identify the minerals. Moreover, the background substrate of the samples consisted of a carbon panel which had a particular signature which is easily eliminated. Unfortunately in some experiments the used cardboard was not of the same quality as the previous experiments which may have influenced the process. This background substrate can also be modified to a more constant substrate.

8.2.2 Experimental conditions

The experimental setup for all of the presented tests in LWIR involved a hyperspectral infrared camera, heating source, macro lens, and infragold plate. The setup in each of the conducted experiments was changed and even the spectral resolution and bands were also varied which created further variation requiring adjustment. This changed the analysis and would be more problematic once the system would be used for real world applications. An important factor to be considered in future efforts is to create a setup with fixed experimental conditions. It would not only dramatically alleviate the changes in the process but also reduce (or even eliminate) unnecessary disparities caused by setup variations.

8.2.3 Possible programming advancement

The entire programming implementation of this research work was deployed in MATLAB coding language to create a convenient prototype programming tool to test and verify performances of the proposed algorithms. Moreover the MATLAB programming provided a good opportunity to test the hypothesis and quickly create or modify the algorithms, this software exhibits lower computational efficiency as compared to other programing tools such as C++ and C. To increase the computational speed and reduce its complexity, such programming tools could be a great alternative to fulfill the requirement and create a fast and robust system.

8.2.4 Application of more advanced machine learning

The application of machine learning to perform the mineral identification in this thesis was just a commencement for the tools that could be developed. Application of the clustering could be unequivocally generalized into many different mathematical and computational models that could provide great tools to perform the task. Moreover, there are many pattern recognition methods that could be used to determine and discriminate the mineral classes which could be a new challenge of this research. In addition, there are plenty of the signal and spectral transforms techniques such as wavelet analysis that could pre-process the spectra before performing any decision making stage. Application of these pre-processing steps could increase the dimension of input data and ultimately might expand the precision of the system in the identification task.

8.2.5 Modifying the infrared technology

The current approach used a hyperspectral infrared wavelength band in the long wave infrared ($7.7\mu m$ to $11.8\mu m$). As it has been mentioned previously, there were some minerals that did not have any signature in LWIR which caused no response for their identification. Addition of other hyperspectral infrared bands such as Short-Wave Infrared band (SWIR) or Visible and Near Infrared (VNIR) band could provide this opportunity to investigate more minerals that might have a signature in SWIR or VNIR.

Appendix A

List of publications

Here, the list of articles submitted or published in different journals and conferences are presented:

1. **Continuum removal for ground based LWIR hyperspectral infrared imagery applying non-negative matrix factorization**, was submitted for Applied Optics journal, on January 5th 2018, Authors: Bardia Yousefi, Saeed Sojasi, Clemente Ibarra Castanedo, Xavier P.V. Maldague, Georges Beaudoin, Martin Chamberland.

2. **Automatic Mineral Identification using Ground-based Hyperspectral LWIR Infrared Spectral Analysis and Extreme Learning Machine**, was submitted for Infrared Physics Technology journal, on February 5th 2018. Authors: Bardia Yousefi, Saeed Sojasi, Clemente Ibarra Castanedo, Xavier P.V. Maldague, Georges Beaudoin, Martin Chamberland.

3. **Comparative clustering analysis applying K-means rank[1]-NMF and FCC on mineral identification in long wave hyperspectral infrared imagery**, was submitted for GIScience & Remote Sensing journal, on March 5th 2018. Authors: Bardia Yousefi, Saeed Sojasi, Clemente Ibarra Castanedo, Xavier P.V. Maldague, Georges Beaudoin, Martin Chamberland.

4. **Automated LWIR Hyperspectral Infrared mineral identification reliability** and is

submitted for Applied Optics journal, on January 5th 2018, Authors: Bardia Yousefi, Clemente Ibarra Castanedo, Xavier P.V. Maldague, Georges Beaudoin.

5. **Mineral Identification in LWIR Hyperspectral Imagery Applying Sparse based Clustering** and is going to be submitted for QIRT journal (was pre-selected from QIRT-Asia 2017), and to be submitted in their deadline, Authors: Bardia Yousefi, Clemente Ibarra Castanedo, Xavier P.V. Maldague, Georges Beaudoin.

6. Bardia Yousefi, Saeed Sojasi, Clemente Ibarra Castanedo, Georges Beaudoin, François Huot, Xavier PV Maldague, Martin Chamberland, and Erik Lalonde. **Mineral identification in hyperspectral imaging using Sparse-PCA**. In Thermosense: Thermal Infrared Applications XXXVIII, vol. 9861, p. 986118. International Society for Optics and Photonics, 2016.

7. Bardia Yousefi, Saeed Sojasi, Clemente Ibarra Castanedo, Georges Beaudoin, François Huot, Xavier PV Maldague, Martin Chamberland, and Erik Lalonde. **Emissivity retrieval from indoor hyperspectral imaging of mineral grains.** In Thermosense: Thermal Infrared Applications XXXVIII, vol. 9861, p. 98611C. International Society for Optics and Photonics, 2016.

8. Bardia Yousefi, Saeed Sojasi, Kévin Liaigre, Clemente Ibarra Castanedo, Georges Beaudoin, François Huot, Xavier PV Maldague, and Martin Chamberland. **Modified algorithm for mineral identification in LWIR hyperspectral imagery**. In Thermosense: Thermal Infrared Applications XXXIX, vol. 10214, p. 102141H. International Society for Optics and Photonics, 2017.

9. Saeed Sojasi, Bardia Yousefi, Kévin Liaigre, Clemente Ibarra-Castanedo, Georges Beaudoin, Xavier PV Maldague, François Huot, and Martin Chamberland. **The role of the continuous wavelet transform in mineral identification using hyperspectral imaging in the long-wave infrared by using SVM classifier**. In Thermosense: Thermal Infrared Appli-

cations XXXIX, vol. 10214, p. 102141K. International Society for Optics and Photonics, 2017.

10. Bardia Yousefi, Clemente Ibarra Castanedo, Georges Beaudoin, Xavier PV Maldague, François Huot, and Martin Chamberland. **Mineral identification in LWIR hyperspectral imagery applying sparse spectral clustering**. QIRT Asia, 2017.

Appendix B

Programming codes and implementations

This appendix summarized the MATLAB codes which used for implementation of my proposed algorithms. The documentation of these codes are based on presented chapters and articles. For every chapter the relevant code mentioned a long with a link corresponds to the code that can be downloaded online.

Note: The entire codes mentioned in this research are corresponded to LWIR hyperspectral camera 7.7-11.8 μm wavelength band range at Telops Inc. (Telops 2016) and for reading the raw hyperspectral image the relevant MATLAB codes must be used and they are under copyright protection law. The presented codes are supposed the reading process is already done and hyperspectral data cube are extracted.

B.1   Continuum Removal (Chapter 4)

This code requires two times reading the hyperspectral image with and without heating source to obtain $L_{i_{ON}(\lambda)}$ and $L_{i_{OFF}}(\lambda)$ spectral radiation through equation **??** in the 4th chapter. For that, a spectral radiation representative of $L_{i_{ON}(\lambda)}$ and $L_{i_{OFF}}(\lambda)$ separately calculated and then applied to the equation **??**.

```matlab
% by Bardia Yousefi. 10 April 2015 (bardia.yousefi@ieee.org) from MIVIM and E4M team Université
Laval project under supervision of: Prof. Xavier P.V. Maldague and Prof. Georges Beaudoin
% TELOPS Inc. provides the source codes for reading the hyperspectral images and this code
respects the copy right and kept the integrity of this collaboration and does not release their
codes.
clear; clc; close all, warning off
%%%%%%%%%%%%%%%%%%%%%%%%%%%%%%%%%%%%%%%%%%%%%%%%%%%%%%%%%%%%%%%%%%%%%%%%%%%
%  Select your mineral
% 'ILM' = 1  % 'OL' = 2  % 'PYR' = 3   % 'CHR' = 4  % 'QTZ' = 5 % 'BKG' = 6
% Min_num = 1;
%%%%%%%%%%%%%%%%%%%%%%%%%%%%%%%%%%%%%%%%%%%%%%%%%%%%%%%%%%%%%%%%%%%%%%%%%%%
esm =  {'ILM' 'OL' 'PYR' 'CHR' 'QTZ' 'Li'}; ,esm_color =  {'ob' '+k' '*' '.m' '.g' '*k'};

ShapeFeaturesNo = [6,33,34,52,65,81,82,85,87,90,95,100,107,129];
%%%%%%%%%%%%%%%%%%%%%%%%%%%%%%%%%%%%%%%%%%%%%%%%%%%%%%%%%%%%%%%%%%%%%%%%%%%
cd 'E:\B\Dr-IR-sp\Dr-IR-MATLAB\MIVIM-HyperSpectral\' %General directory of this MATLAB code
CF0 = cd(pwd); % saving the directory for further uses
  addpath(CF0);
    % codes path
  CF1 = [CF0, '\Matlab_customer\p_files'];
  addpath(CF1);
  cd(CF1);
  pathaddress = [CF1,'\Subfunctions'];
  addpath(pathaddress);
```

This part of code performs the set path

```matlab
% -----------------------------------------------------------------
FilePath = [CF0,'\mesures_2avril2015\'];
FileName = '20150402_211927875_OL_ON.radiance.sc'; % raw data heating source ON
filename = [FilePath,FileName];
% reading the hyperspectral image
[Data_ON,DerivedFromHeader_ON,Header_ON] = readHyperCam(filename);
    %Grid generation
  sigma = buildSigmaGrid(DerivedFromHeader_ON);
    %Plot broad band image
  kk = (sigma>850 & sigma<1250);
  IRimage = formImage(Header_ON,mean(real(Data_ON(kk,:))));
  Clims1 = imageScalingLimits(IRimage(:));
  figure;imshow(IRimage,Clims1)
% -----------------------------------------------------------------
```

Here we read the hyperspectral image while there is a heating source.

```matlab
%%
FilePath = [CF0,'\mesures_2avril2015\'];
 FileName = '20150402_212156460_OL_OFF_after.radiance.sc'; % raw data heating source OFF
 filename = [FilePath,FileName];
% reading the hyperspectral image
 [Data_OFF,DerivedFromHeader_OFF,Header_OFF] = readHyperCam(filename);
% -----------------------------------------------------------------
```

Here we read the hyperspectral image while there is no heating source.

```matlab
 % Here we are selecting spatial region corresponding to InfraGold to obtain the continuum
spectra
J = imadjust(IRimage,Clims1);
BW = roipoly(J);
[row,col] = find(BW == 1);
infraGold = [row,col];
%finding the pixels indices of infragold region
    pixels = getAoiIndices(Header_ON, buildAoi(1, 1, infraGold(:,2)-1, infraGold(:,1)-1));
```

Calculating down-welling spectra using Non-Negative Matrix Factorization

```matlab
% Down-welling radiation while heating source is ON; "Li_ON"
% -----------------------------------------------------------------
 [Wo,Ho] = nnmf(Data_ON(:,pixels),2); %calculating Non-Negative Matrix Factorization
 Li_ON = Wo(:,1); % selecting the first spectral basis from basis matrix
%Li_ON = mean(Data_ON(:,pixels),2); If you do not want to calculate the down-welling spectra
applying Non-Negative Matrix Factorization

[Wf,Hf] = nnmf(Data_OFF(:,pixels),2);
Li_OFF = Wf(:,1); % selecting the first spectral basis from basis matrix
%Li_OFF = mean(Data_ON(:,pixels),2); If you do not want to calculate the down-welling spectra
applying Non-Negative Matrix Factorization
% -----------------------------------------------------------------
```

```matlab
% Applying our simplification formula

for i = 1 : size(Data_ON,2)
     Reflectance(:,i) = (Data_ON(:,i) - Data_OFF(:,i)) ./ (Li_ON - Li_OFF);
end
```

$$\rho(\lambda) = \frac{L^*_{ON}(\lambda) - L^*_{OFF}(\lambda)}{L_{i_{ON}(\lambda)} - L_{i_{OFF}(\lambda)}}$$

% file "Reflectance" is Continuum Removed spectra ready to be used.

B.2 Classification or clustering (Chapter 5)

This section shows the MATLAB codes correspond to applying Extreme Learning Machine (ELM) and K-means clustering. [1]. In order to apply these techniques, a MATLAB hyperspectral image index analysis toolbox (Isaac, 2015) and modified Kernel ELM (Huang, 2013) were used.

---

[1]We provide the programming code in this link: `http://vision.gel.ulaval.ca/~bardia/PublicCodes/WebJ1-19May2017.zip`

```matlab
% This code perform classification for mineral identification using Kernelled-ELM

% Bardia Yousefi 12.May 2017 (bardia.yousefi.1@ulaval.ca) from MIVIM and E4M team Université
Laval project under supervision of: Prof. Xavier P.V. Maldague and Prof. Georges Beaudoin
% Université Laval, Quebec city, Canada
% ************************************************
clear; clc; close all, warning off, imtool close all
```
This part of code performs the set path
```matlab
cd('\\gel.ulaval.ca\Vision\Usagers\bayou2\MATLAB\J1_finalization\WebJ1\files'), CF0 = pwd;
addpath('\\gel.ulaval.ca\Vision\Usagers\bayou2\MATLAB\J1_finalization\WebJ1')
addpath('\\gel.ulaval.ca\Vision\Usagers\bayou2\MATLAB\J1_finalization\WebJ1')
```

```matlab
Mineral = 'Olivine'; % Name of mineral grains tested the alternatives are: Pyrope Olivine
load([Mineral,'_r.mat']);
load(['BY_',Mineral,'_r.mat']);
```
Recalling the mineral
```matlab
BW_J = imread([Mineral,'.png']); % Loading the first image from hyperspectral data cube.
nclstr = 6; % Number of cluster for when we are using clustering
th = 0.8;
ii = 2; %ssn = {'NCC','SAM','OSP','AMSD','HUD','MF','PLMF','RMFs','RMFml','RMFgml'};
```

```matlab
%% ASTER
cd([CF0,'\ASTER\'])
```
Recalling the spectra corresponding the tested minerals from ASTER/JPL NASA spectral library
```matlab
%%%%%
ASTER_Pyrope = importdata('PYROPE-
jhu.nicolet.mineral.silicate.nesosilicate.solid.pyrope1.spectrum.txt');
bandes_IR = find(10000./ASTER_Pyrope.data(:,1) > min(BY.sigma) & 10000./ASTER_Pyrope.data(:,1) <
max(BY.sigma));
ASTERO = [ASTER_Pyrope.data(bandes_IR,1),ASTER_Pyrope.data(bandes_IR,2)/100];
Pyrope = resample(ASTERO,size(BY.Reflectance,1),size(ASTERO,1));

%%%%%
ASTER_Olivine = importdata('Olivine (Fo92) (Fe+2,Mg)2SiO4 (2) -
jhu.nicolet.mineral.silicate.nesosilicate.solid.olivi12.spectrum.txt');
bandes_IR = find(10000./ASTER_Olivine.data(:,1) > min(BY.sigma) & 10000./ASTER_Olivine.data(:,1)
< max(BY.sigma));
ASTERO = [ASTER_Olivine.data(bandes_IR,1),ASTER_Olivine.data(bandes_IR,2)/100];
Olivine = resample(ASTERO,size(BY.Reflectance,1),size(ASTERO,1));

%%%%%
ASTER_Quartz = importdata('QUARTZ-
jhu.nicolet.mineral.silicate.tectosilicate.solid.quartz1.spectrum.txt');
bandes_IR = find(10000./ASTER_Quartz.data(:,1) > min(BY.sigma) & 10000./ASTER_Quartz.data(:,1) <
max(BY.sigma));
ASTERO = [ASTER_Quartz.data(bandes_IR,1),ASTER_Quartz.data(bandes_IR,2)/100];
Quartz = resample(ASTERO,size(BY.Reflectance,1),size(ASTERO,1));
%%%%%
load('bckgnd.mat');

ASTER = struct('ASTER_Pyrope',ASTER_Pyrope,'ASTER_Olivine',ASTER_Olivine ,
'ASTER_Quartz',ASTER_Quartz,...
    'Pyrope',Pyrope, 'Olivine',Olivine, 'Quartz',Quartz, 'bckgnd', bckgnd);
clear ASTER_Pyrope ASTER_Olivine ASTER_Quartz Pyrope Olivine Quartz ASTERO bckgnd ...
    BW row col infraGold pixels bckgnd0
%% Identification of the minerals (samples of the clusters)
tic
ss = {'Pyrope','Olivine','Quartz','bckgnd'}; % defining different classes for classification
%  cd([BY.CF0,'\HyperSpectralToolbox-master\functions\'])
```
Using Hyperspectral toolbox for using spectral comparison techniques
```matlab
for i0 = 1 : size(ss,2),
    a = eval(['ASTER.',num2str(ss{1,i0})]);
    for i = 1 : size(signals,2), disp(sprintf([num2str(i),'-',num2str(i0)]))
        [results_SCT(i)] = NCC(Norm2(signals(:,i)), Norm2(a(:,2))); %SAM NCC
    end
    MINERL_res{i0} = results_SCT;
end, time_SCT = toc;
```

```matlab
% figure; imshow(reshape(MINERL_res{1,3},[159 159])), colormap(parula)
for i = 1 : size(ss,2)
    IM = max(max(MINERL_res{1,i})) - MINERL_res{1,i};%reshape(MINERL_res{1,i},[159 159]);
    IMc{i} = IM - (max(max(IM)) - 1);
end
% IMc = MINERL_res;
%  extracting the labels using GT
cd([CF0,'\Labeled']);
L_m = rgb2gray(imread([Mineral,'.png']));, L_m = imresize(L_m(1:end-1,1:end-2),[size(BW_J,1)-1,size(BW_J,2)-2]);
L_q = rgb2gray(imread([Mineral,' - Q.png']));, L_q = imresize(L_q(1:end-1,1:end-2),[size(BW_J,1)-1,size(BW_J,2)-2]);
BKG = (L_m + L_q)<200;

L_m = (reshape(L_m,1,[])>200)*2; %===============================================
L_q = (reshape(L_q,1,[])>200) * 3;
BKG = (reshape(BKG,1,[])) * 4;

% merging the labels and the attributes 50% training 50%testing
% % here we just get the mineral location to be more precise
% km = find(L_m == 1);
% % for i = 1 : size(km,2)/2
%    M = IMc{1}(km);
for i = 1 : size(L_m,2),i
    if (L_m(:,i) ~= 0 & L_q(:,i) ~= 0)
        Label(:,i) = L_m(:,i);%+ L_q(:,i) + BKG(:,i)
    elseif (L_m(:,i) ~= 0)
        Label(:,i) = L_m(:,i);
    elseif (L_q(:,i) ~= 0 & BKG(:,i) ~= 0)
        Label(:,i) = L_q(:,i);
    else
        Label(:,i) = L_m(:,i) + L_q(:,i) + BKG(:,i);
    end
end
Label = Label';
```

```matlab
% Overal label matrix
Label_tt = [Label,IMc{1}',IMc{2}',IMc{3}',IMc{4}'];


% Training set
L_training = abs(Label_tt(1:((size(L_m,2)*2)/3),:));

% Testing set
L_testing = abs(Label_tt(((size(L_m,2)*2)/3) + 1:end,:));

% Overlapping for minerals existance
[km] = find( Label_tt(:,1)== 1 );
KM = abs(Label_tt(km,:));
```

```matlab
L_testing = [L_testing;KM];
clear idx a ans bandes_IR c i I i0 j Li_ON sample resultsNormXCorr
%% correction in training and testing

% L_training0 = L_training;
L_training2 = L_training(1,:);
for i = 1 : size(L_training,1)
    [m,ind]=max(L_training(i,2:end));
    if L_training(i,1) == ind;
        L_training2 = [L_training2;L_training(i,:)];
    end
end
```

Loading Ground Truth images for this case

Making our training set

157

```matlab
% testing
L_testing2 = L_testing(1,:);
for i = 1 : size(L_testing,1)
    [m,ind]=max(L_testing(i,2:end));
    if L_testing(i,1) == ind;
        L_testing2 = [L_testing2;L_testing(i,:)];
    end
end
%%
```

Making our testing set

```matlab
tic
% TXT training for ML; 5 classes only = no BKG class
cd([CF0,'\elm_kernel']);
    nameTXT = ['training.txt'];
    fid = fopen( nameTXT , 'wt' );
    for i = 1 : size(L_training2,1)
        fprintf( fid, '%f %f %f %f %f \n',L_training2(i,1),L_training2(i,2),...
            L_training2(i,3),L_training2(i,4),L_training2(i,5));
    end
    fclose(fid);


%%
cd([CF0,'\elm_kernel']);
    nameTXT = ['testing.txt'];
    fid = fopen( nameTXT , 'wt' );
    for i = 1 : size(L_testing2,1)
        fprintf( fid, '%f %f %f %f %f \n',L_testing2(i,1),L_testing2(i,2),...
            L_testing2(i,3),L_testing2(i,4),L_testing2(i,5));
    end
    fclose(fid);


%% Applying ELM for classification
tic
%%%%%%%%%%%%%%%%%%%%%%%%%%%%%%%%%%%%%%%%%%%%%%%%%%%%%%%%%%%%%%%%%%%%%%%%%
            KERNEL = 'lin_kernel';% lin poly RBF sig
%%%%%%%%%%%%%%%%%%%%%%%%%%%%%%%%%%%%%%%%%%%%%%%%%%%%%%%%%%%%%%%%%%%%%%%%%
    addpath([CF0,'\elm_kernel\elm_kernel']);
    addpath([CF0,'\elm_kernel\elm_kernel\results']);
    cd([CF0,'\elm_kernel']);
    v = [0.000001 0.1 0.1];    %wave %v=[-0.47 0.1]; RBF %v = 1; Sig v=[-0.47 0.1];
    %lin v = [0.000001 0.1 0.1]; poly v = [0.1 10];
    Nameac = ['accuracy',num2str(KERNEL),'.txt'];
    fid = fopen(num2str(Nameac), 'wt' );

    nametraining = ['training.txt'];
    nametesting = ['testing.txt'];
%    ['Classification accuracy for mineral ' num2str(Min_num) ' which represents'
esm{1,Min_num}]
    [TrainingTime, TestingTime, TrainingAccuracy, TestingAccuracy,TY,AC] = ...
        elm_kernel2(nametraining, nametesting, 1, 1,KERNEL,v);%testing
    fprintf( fid, 'TrainingTime= %f \n TestingTime= %f \n TrainingAccuracy= %f \n
TestingAccuracy= %f \n',...
        TrainingTime, TestingTime, TrainingAccuracy, TestingAccuracy);
time_elm = toc
    fclose(fid);
    Namety = ['AC',num2str(KERNEL)];
cd([CF0,'\elm_kernel\results']);
    save(Namety,'AC');
```

Applying kernel-ELM for classification

```matlab
% %%%%%%%%%%%%%%%%%%%% Target %%%%%%%%%%%%%%%%%%%%%%%%%%%%
%  making the manual target for creation of the confusion matrix
%    AC2 = [AC(:,1),AC(:,4),AC(:,2),AC(:,3)]; % enhanced pyrope
     AC2 = [AC(:,4),AC(:,1),AC(:,2),AC(:,3)]; % enhanced olivine
%    AC2 = [AC(:,2),AC(:,4),AC(:,1),AC(:,3)]; % enhanced
% AC2 = [AC(:,3),AC(:,1),AC(:,4),AC(:,2)]; % non-enhanced
% AC2 = AC;
 ACC = zeros(size(AC2));
     for i = 1 : size(L_testing2,1)
         ff = L_testing2(i,1);
            if ff ~= 0
                ACC(i,ff) = 1;
            end
     end
%  ACC(1,1:1000) = 1;ACC(2,1001:2000) = 1; ACC(3,2001:3000) = 1; ACC(4,3001:4000) = 1;
ACC(5,4001:5000) = 1; ACC(6,5001:6000) = 1;
% ACC = [ACC(:,1),ACC(:,3),ACC(:,4)];
 plotconfusion(ACC',AC2') %  plotting confusion matrix


 Namex = ['ConfusionMatrix_NCC_', Mineral,'_',num2str(KERNEL)];
saveas(gcf,[Namex,'.jpg'])
saveas(gcf,[Namex,'.fig'])
```

B.3   Two algorithms for clustering (Chapter 6)

B.3.1   K-means rank[1]-NMF algorithm

The algorithm clusters all the pixel-spectra to directly group the spectra. Then the rank-one of Non-negative Matrix Factorization (NMF) extracts the representative of each cluster and compares results with the spectral library of JPL/NASA through spectral comparison techniques. These techniques give the comparison values as features which convert into RGB-FCC as the results. The algorithm will be called K-means rank[1]-NMF. This section shows the MATLAB codes correspond to applying K-means clustering (K-means-rank[1] NMF algorithm). [2]. In order to apply these techniques, a MATLAB hyperspectral image index analysis toolbox (Isaac, 2015) was been used.

_____

[2]We provide the programming code in this link: `http://vision.gel.ulaval.ca/~bardia/PublicCodes/J2-10May2017.zip`

```matlab
% This code represents two strategies regarding the clustering of the
% hyperspectral
% Here, we have images ready to use as the preprocessing codes are under copy right of
% TELOPS company and we can not provide them.
%
% Author:        Bardia YOUSEFI (bardia.yousefi.1@ulaval.ca)
%
% ©2017. MIVIM research group. All rights reserved
%
% Created:           May 12, 2016.
% Last modification: May 15, 2017.
%
%**************************************************************************
clear; clc; close all, warning off, imtool close all
% your folder address
cd('H:\B\Dr-IR-sp\Dr-IR-MATLAB\MIVIM_Hyperspectral_s2\web_J2'), CF00 = pwd;
cd('H:\B\Dr-IR-sp\Dr-IR-MATLAB\MIVIM_Hyperspectral_s2\web_J2\files')
% Choose your mineral name
Mineral = 'Biotite'; % Biotite Diopside Epidote Geothite Kyanite Scheelite Smithsonite Tourmaline
Pyrope Olivine
load([Mineral,'_r.mat']);
load(['BY_',Mineral,'_r.mat']);
BW_J = imread([Mineral,'.png']);
nclstr = 6; % initial number of clustering
th = 0.8;
ii = 2; %ssn = {'NCC','SAM','OSP','AMSD','HUD','MF','PLMF','RMFs','RMFml','RMFgml'};
%% Second strategy using direct clustering first and then MAMs
```

This part of code performs the set path and recalling the targeted mineral

```matlab
%  Clustering
   [idx] = kmeans(signals',nclstr);  % Clustering the spectra
    ta = tabulate(idx);


% --------------------- Correcting the clusters for better identification ----------------------
---
acul = idx;
for i = 1 : size(idx,1)-10
    if i > 5
     if (idx(i) ~= idx(i+3)) && (idx(i) == idx(i+2)) && (idx(i) == idx(i+1)) && ...
           (idx(i) == idx(i-1)) && (idx(i) == idx(i-2)) && (idx(i) == idx(i-3))
        acul(i+3) = idx(i);
     elseif (idx(i) == idx(i+3)) && (idx(i) ~= idx(i+2)) && (idx(i) == idx(i+1)) && ...
           (idx(i) == idx(i-1)) && (idx(i) == idx(i-2)) && (idx(i) == idx(i-3))
        acul(i+2) = idx(i);
     elseif (idx(i) == idx(i+3)) && (idx(i) == idx(i+2)) && (idx(i) ~= idx(i+1)) && ...
           (idx(i) == idx(i-1)) && (idx(i) == idx(i-2)) && (idx(i) == idx(i-3))
        acul(i+1) = idx(i);
     elseif (idx(i) == idx(i+3)) && (idx(i) == idx(i+2)) && (idx(i) == idx(i+1)) && ...
           (idx(i) ~= idx(i-1)) && (idx(i) == idx(i-2)) && (idx(i) == idx(i-3))
        acul(i-1) = idx(i);
     elseif (idx(i) == idx(i+3)) && (idx(i) == idx(i+2)) && (idx(i) == idx(i+1)) && ...
           (idx(i) == idx(i-1)) && (idx(i) ~= idx(i-2)) && (idx(i) == idx(i-3))
        acul(i-2) = idx(i);
     elseif (idx(i) == idx(i+3)) && (idx(i) == idx(i+2)) && (idx(i) == idx(i+1)) && ...
           (idx(i) == idx(i-1)) && (idx(i) == idx(i-2)) && (idx(i) ~= idx(i-3))
        acul(i-3) = idx(i);
%      elseif (idx(i) ~= idx(i+3)) && (idx(i) == idx(i+2)) && (idx(i) == idx(i+1)) && ...
%            (idx(i) == idx(i-1)) && (idx(i) == idx(i-2)) && (idx(i) == idx(i-3))
%         acul(i+1) = idx(i);
%      elseif (idx(i) ~= idx(i+3)) && (idx(i) == idx(i+2)) && (idx(i) == idx(i+1)) && ...
%            (idx(i) == idx(i-1)) && (idx(i) == idx(i-2)) && (idx(i) == idx(i-3))
%         acul(i+1) = idx(i);
     end
    end
end
```

Finding the clusters

```matlab
% -------------------- Correcting the clusters for better identification ----------------------
---

CLSTR = struct('idx',idx, 'ta',ta, 'signals', signals,'J',BW_J, 'BW',BW_J, 'nclstr',nclstr);
%  clear J BW row col crd RoI_pixels idx ta signals J2 i j pix_x pix_y rect
%% ASTER
cd('H:\B\Dr-IR-sp\Dr-IR-MATLAB\MIVIM_Hyperspectral_s2\
```

Recalling the spectra corresponding the tested minerals from ASTER/JPL NASA spectral library

```matlab
ASTER_Biotite =
importdata('Biotite.jpl.nicolet.mineral.phyllo
bandes_IR = find(10000./ASTER_Biotite.data(:,1) > min(BY.sigma) & 10000./ASTER_Biotite.data(:,1)
< max(BY.sigma));
% Biotite = resample(ASTER_Biotite,size(BY.Reflectance,1),size(bandes_IR,1));
ASTERO = [ASTER_Biotite.data(bandes_IR,1),ASTER_Biotite.data(bandes_IR,2)/100];
Biotite = resample(ASTERO,size(BY.Reflectance,1),size(ASTERO,1));


%%%%%
ASTER_Diopside =
importdata('Diopside.jhu.nicolet.mineral.silicate.inosilicate.solid.diopsi1.spectrum.txt');
bandes_IR = find(10000./ASTER_Diopside.data(:,1) > min(BY.sigma) &
10000./ASTER_Diopside.data(:,1) < max(BY.sigma));
ASTERO = [ASTER_Diopside.data(bandes_IR,1),ASTER_Diopside.data(bandes_IR,2)/100];
Diopside = resample(ASTERO,size(BY.Reflectance,1),size(ASTERO,1));


%%%%%
ASTER_Epidote =
importdata('Epidote.jhu.nicolet.mineral.silicate.sorosilicate.solid.epidot1.spectrum.txt');
bandes_IR = find(10000./ASTER_Epidote.data(:,1) > min(BY.sigma) & 10000./ASTER_Epidote.data(:,1)
< max(BY.sigma));
ASTERO = [ASTER_Epidote.data(bandes_IR,1),ASTER_Epidote.data(bandes_IR,2)/100];
Epidote = resample(ASTERO,size(BY.Reflectance,1),size(ASTERO,1));


%%%%%
ASTER_Goethite =
importdata('Goethite.jhu.nicolet.mineral.hydroxide.none.solid.goethi2.spectrum.txt');
bandes_IR = find(10000./ASTER_Goethite.data(:,1) > min(BY.sigma) &
10000./ASTER_Goethite.data(:,1) < max(BY.sigma));
ASTERO = [ASTER_Goethite.data(bandes_IR,1),ASTER_Goethite.data(bandes_IR,2)/100];
Goethite = resample(ASTERO,size(BY.Reflectance,1),size(ASTERO,1));


%%%%%
ASTER_Kyanite =
importdata('Kyanite.jhu.nicolet.mineral.silicate.phyllosilicate.coarse.kyanit1.spectrum.txt');
bandes_IR = find(10000./ASTER_Goethite.data(:,1) > min(BY.sigma) &
10000./ASTER_Goethite.data(:,1) < max(BY.sigma));
ASTERO = [ASTER_Kyanite.data(bandes_IR,1),ASTER_Kyanite.data(bandes_IR,2)/100];
Kyanite = resample(ASTERO,size(BY.Reflectance,1),size(ASTERO,1));


%%%%%
ASTER_Scheelite =
importdata('Scheelite.jpl.nicolet.mineral.tungstate.none.coarse.t01a.spectrum.txt');
bandes_IR = find(10000./ASTER_Scheelite.data(:,1) > min(BY.sigma) &
10000./ASTER_Scheelite.data(:,1) < max(BY.sigma));
ASTERO = [ASTER_Scheelite.data(bandes_IR,1),ASTER_Scheelite.data(bandes_IR,2)/100];
Scheelite = resample(ASTERO,size(BY.Reflectance,1),size(ASTERO,1));


%%%%%
ASTER_Smithsonite =
importdata('Smithsonite.jpl.nicolet.mineral.carbonate.none.coarse.c11a.spectrum.txt');
bandes_IR = find(10000./ASTER_Smithsonite.data(:,1) > min(BY.sigma) &
10000./ASTER_Smithsonite.data(:,1) < max(BY.sigma));
ASTERO = [ASTER_Smithsonite.data(bandes_IR,1),ASTER_Smithsonite.data(bandes_IR,2)/100];
Smithsonite = resample(ASTERO,size(BY.Reflectance,1),size(ASTERO,1));
```

```
%%%%%
ASTER_Tourmaline =
importdata('Tourmaline.jhu.nicolet.mineral.silicate.cyclosilicate.solid.tourma1.spectrum.txt');
bandes_IR = find(10000./ASTER_Tourmaline.data(:,1) > min(BY.sigma) &
10000./ASTER_Tourmaline.data(:,1) < max(BY.sigma));
ASTERO = [ASTER_Tourmaline.data(bandes_IR,1),ASTER_Tourmaline.data(bandes_IR,2)/100];
Tourmaline = resample(ASTERO,size(BY.Reflectance,1),size(ASTERO,1));


%%%%%
ASTER_Pyrope = importdata('PYROPE-
jhu.nicolet.mineral.silicate.nesosilicate.solid.pyrope1.spectrum.txt');
bandes_IR = find(10000./ASTER_Pyrope.data(:,1) > min(BY.sigma) & 10000./ASTER_Pyrope.data(:,1) <
max(BY.sigma));
ASTERO = [ASTER_Pyrope.data(bandes_IR,1),ASTER_Pyrope.data(bandes_IR,2)/100];
Pyrope = resample(ASTERO,size(BY.Reflectance,1),size(ASTERO,1));


%%%%%
ASTER_Olivine = importdata('Olivine (Fo92) (Fe+2,Mg)2SiO4 (2) -
jhu.nicolet.mineral.silicate.nesosilicate.solid.olivi12.spectrum.txt');
bandes_IR = find(10000./ASTER_Olivine.data(:,1) > min(BY.sigma) & 10000./ASTER_Olivine.data(:,1)
< max(BY.sigma));
ASTERO = [ASTER_Olivine.data(bandes_IR,1),ASTER_Olivine.data(bandes_IR,2)/100];
Olivine = resample(ASTERO,size(BY.Reflectance,1),size(ASTERO,1));


%%%%%
ASTER_Quartz = importdata('QUARTZ-
jhu.nicolet.mineral.silicate.tectosilicate.solid.quartz1.spectrum.txt');
bandes_IR = find(10000./ASTER_Quartz.data(:,1) > min(BY.sigma) & 10000./ASTER_Quartz.data(:,1) <
max(BY.sigma));
ASTERO = [ASTER_Quartz.data(bandes_IR,1),ASTER_Quartz.data(bandes_IR,2)/100];
Quartz = resample(ASTERO,size(BY.Reflectance,1),size(ASTERO,1));
%%%%%
```
Recalling the spectra corresponding the tested minerals from ASTER/JPL NASA spectral library

Finding the spectra of background substrate (Carbon)

```
%  Background spectrum selection

% % tv3 = toc;
% BW = roipoly(BY.J); , tic, title(['Select Background region']);
%     [row,col] = find(BW == 1);
%     infraGold = [row,col];
% addpath('H:\B\Dr-IR-sp\Dr-IR-MATLAB\New Exp. Dec2014 TELOPS\TELOPS')
% addpath('H:\B\Dr-IR-sp\Dr-IR-MATLAB\New Exp. Dec2014 TELOPS\TELOPS\Matlab_customer\p_files')
%    pixels = getAoiIndices(BY.Header_ON, buildAoi(1, 1, col-1, row-1));
%
%     bckgnd = mean(BY.Reflectance(:,pixels));
%   bckgnd = resample(double(bckgnd0'), size(bckgnd0,2), size(ASTERO,1));

ASTER = struct('ASTER_Biotite',ASTER_Biotite, 'ASTER_Diopside',ASTER_Diopside
,'ASTER_Epidote',ASTER_Epidote,...
    'ASTER_Goethite',ASTER_Goethite, 'ASTER_Kyanite',ASTER_Kyanite ,
'ASTER_Scheelite',ASTER_Scheelite ,...
    'ASTER_Smithsonite',ASTER_Smithsonite , 'ASTER_Tourmaline',ASTER_Tourmaline ,
'ASTER_Pyrope',ASTER_Pyrope ,...
    'ASTER_Olivine',ASTER_Olivine , 'ASTER_Quartz',ASTER_Quartz,...
    'Biotite',Biotite , 'Diopside',Diopside, 'Epidote',Epidote , 'Goethite',Goethite ,
'Kyanite',Kyanite ,...
    'Scheelite',Scheelite , 'Smithsonite',Smithsonite , 'Tourmaline',Tourmaline ,
'Pyrope',Pyrope,...
    'Olivine',Olivine , 'Quartz',Quartz);
clear ASTER_Biotite ASTER_Diopside ASTER_Epidote ASTER_Goethite ASTER_Kyanite ASTER_Scheelite ...
    ASTER_Smithsonite ASTER_Tourmaline ASTER_Pyrope ASTER_Olivine ASTER_Quartz Biotite
Diopside...  Epidote Goethite Kyanite Scheelite Smithsonite Tourmaline Pyrope Olivine Quartz
ASTERO bckgnd ... BW row col infraGold pixels bckgnd0
```

```matlab
%% Finding a sample from each cluster!


%  here I am getting the number of each cluster. for exampale, I want to
%  know all the points clustered as first cluster of second or....

idx = 1;
while idx <= nclstr
    c = 1;
    for i = 1 : size(CLSTR.signals,2)
        if CLSTR.idx(i)== idx
            groups{c,idx} = i;
            c = c + 1;
        end
    end
    idx = idx + 1;
end
% Groups = cell2mat(groups);
% I got the location of each cluster, now I am going to find thier spectra
    c = 1;
for i = 1 : size(groups,2)

    for j = 1 : size(groups,1)
        if isempty(groups{j,i})~= true
            Groups(c,:) =([i,groups{j,i}, (CLSTR.signals(:,groups{j,i}))'])';
            c = c + 1;
        end
    end
end
% I sort the spectra label them(first column) and (2nd column) their
% location also and their spectra also, Now we are going to play with the
% spectra to find a method to precisely select them
```

Using Rank 1 Non-Negative Matrix Factorization for best representative spectra corresponds to each clusters

```matlab
for i = 1 : nclstr
    k{i} = find(Groups(:,1) == i); %K{i} = Groups(k{i},3:end);
    coeffnmf(:,i) = nnmf(Groups(k{i},3:end)',1);, figure; h =
plot(10000./BY.sigma,coeffnmf(:,i));, grid on, title(['Cluster Number ',num2str(i)])
%    cd(CFres);   imwrite(h,['K',num2str(i),'.jpg']);  %hgsave(['K',num2str(i),'.jpg'])A =
getimage(h);
end
```
```matlab
clear k1 k2 k3 k4 k5 i c idx j A

cd(CF00)
coeffnmF = Norm2(coeffnmf);

%% Identification of the minerals (samples of the clusters)

ss = {'Biotite','Diopside','Epidote','Goethite','Kyanite','Scheelite','Smithsonite',...
    'Tourmaline','Pyrope','Olivine','Quartz', 'bckgnd'};

tv4 = toc;tic
```

Applying Spectral Angle Mapper(SAM) to find out the error from ASTER library

```matlab
for i = 1 : nclstr
    idx = 1;
%   while idx <= size(ss,2)
    for i0 = 1 : size(ss,2)-1, disp(sprintf([num2str(i),'-',num2str(i0)]))
        a = eval(['ASTER.',num2str(ss{1,i0})]);
            % MAMS techniques
            % MAMs
    [resultsNormXCorr(i0)] = SAM(coeffnmF(:,i), Norm2(a(:,2))); %NCC   SAM

    end
    MAM_1{i} = resultsNormXCorr;
end
tvNMXC = toc; tic
```

```matlab
clear idx a ans bandes_IR c i I i0 j Li_ON sample resultsNormXCorr
%% What is what! :)
% close all
ssn = {'NCC','SAM','OSP','AMSD','HUD','MF','PLMF','RMFs','RMFml','RMFgml'};
name2 = [Mineral,'.png'];
    MAM = eval(['MAM_1']);%,num2str(ii)]);

% mam = MAM{:,1}; for i = 2 : nclstr, mam = cat(1,mam,MAM{:,i});,end
for i = 1 : size(MAM,2)
    mam = MAM{:,i};
    [c,I] = max(mam);
    if c > th
        rs{i,1} = ss{I}; rs{i,2} = I;
    elseif c < th
        rs{i,1} = ['NONE'];, rs{i,2} = 0;
%       elseif numel(I) > 1
    end
end

% rs
% dlmwrite('Results.txt',rs);
iix = BW_J; %imcrop(CLSTR.J, CLSTR.rect-1);
```

```matlab
% now we are painting the pixels with false colors to visually determine
% the minerals in the spatial domain
mxc = CLSTR.idx;
for i = 1 : nclstr, idx = find(CLSTR.idx==i); mxc(idx) = rs{i,2};end

mx = reshape(mxc,[size(CLSTR.BW,1)-1, size(CLSTR.BW,2)-1]);
mx2 = mx;
dx = mx;

% False color
for i = 1 : size(mx,1)
    for j = 1 : size(mx,2)
        if mx(i,j) == 0      % background BLACK
            mx2(i,j,1) = 0;, mx2(i,j,2) = 0;, mx2(i,j,3) = 0;
        elseif mx(i,j) == 1 % 'Biotite'
            mx2(i,j,1) = 0.5;, mx2(i,j,2) = 0.5;, mx2(i,j,3) = 0;
        elseif mx(i,j) == 2 %'Diopside'
            mx2(i,j,1) = 1;, mx2(i,j,2) = 1;, mx2(i,j,3) = 0;
        elseif mx(i,j) == 3  %'Epidote'
            mx2(i,j,1) = 0.5;, mx2(i,j,2) = 0;, mx2(i,j,3) = 0.5;
        elseif mx(i,j) == 4  %'Goethite'
            mx2(i,j,1) = 1;, mx2(i,j,2) = 0;, mx2(i,j,3) = 1;
        elseif mx(i,j) == 5  %'Kyanite'
            mx2(i,j,1) = 0;, mx2(i,j,2) = 0.5;, mx2(i,j,3) = 0.5;
        elseif mx(i,j) == 6 %'Scheelite'
            mx2(i,j,1) = 1;, mx2(i,j,2) = 1;, mx2(i,j,3) = 0.5;
        elseif mx(i,j) == 7  %'Smithsonite'
            mx2(i,j,1) = 1;, mx2(i,j,2) = 0.1;, mx2(i,j,3) = 0.1;
        elseif mx(i,j) == 8  %'Tourmaline'
            mx2(i,j,1) = 0;, mx2(i,j,2) = 0.5;, mx2(i,j,3) = 0;
        elseif mx(i,j) == 9  %'Pyrope'
            mx2(i,j,1) = 0;, mx2(i,j,2) = 1;, mx2(i,j,3) = 0;
        elseif mx(i,j) == 10 %'Olivine'
            mx2(i,j,1) = 0;, mx2(i,j,2) = 0;, mx2(i,j,3) = 0.5;
        elseif mx(i,j) == 11  %'Quartz'
            mx2(i,j,1) = 0;, mx2(i,j,2) = 0;, mx2(i,j,3) = 1;
        elseif mx(i,j) == 12  %'bckgnd'
            mx2(i,j,1) = 0;, mx2(i,j,2) = 0;, mx2(i,j,3) = 0;
        end
    end
end
tvF = toc;
```

Create False Color Composite (FCC) images

```matlab
figure; imshow(mx2), title([ssn{ii}])
clear A h

%% finding the quantitative assessment
% figure; imshow(mx2(:,:,1))   > 0.2
mxxx = mx2(:,:,1)<0.1;
figure; imshow(mxxx)
 k = find(mxxx == 1); size(k);


figure; imshow((mx2(:,:,3)))
mxxx = mx2(:,:,3)> 0.1;
figure; imshow(mxxx)
k = find(mxxx == 1); size(k);
```

B.3.2 FCC-K-means algorithm

The algorithm uses spectral comparison techniques for all the pixel-spectra and creates the RGB false color composites (FCC). Then a color based K-means clustering groups the regions. This algorithm will be called FCC-K-means.

```matlab
% This code represents two strategies regarding the clustering of the
% hyperspectral
% Here, we have images ready to use as the preprocessing codes are under copy right of
% TELOPS company and we can not provide them.
%
% Author:       Bardia YOUSEFI (bardia.yousefi.1@ulaval.ca)
%
% ©2017. MIVIM research group. All rights reserved
%
% Created:           May 12, 2016.
% Last modification: May 15, 2017.
%
%*********************************************************************  This part of code performs the set path
clear; clc; close all, warning off, imtool close all
% your folder address
cd('H:\B\Dr-IR-sp\Dr-IR-MATLAB\MIVIM_Hyperspectral_s2\web_J2'), CF00 = pwd;
cd('H:\B\Dr-IR-sp\Dr-IR-MATLAB\MIVIM_Hyperspectral_s2\web_J2\files')
% Choose your mineral name
Mineral = 'Biotite'; % Biotite Diopside Epidote Geothite Kyanite Scheelite Smithsonite Tourmaline
Pyrope Olivine
load([Mineral,'_r.mat']);
load(['BY_',Mineral,'_r.mat']);
BW_J = imread([Mineral,'.png']);
nclstr = 6; % initial number of clustering
th = 0.8;
ii = 2; %ssn = {'NCC','SAM','OSP','AMSD','HUD','MF','PLMF','RMFs','RMFml','RMFgml'};
%% The first strategy using direct clustering first and then MAMs
```

```matlab
%% ASTER
cd([BY.CF0,'\ASTER\'])                           Recalling the spectra corresponding the tested minerals
                                                 from ASTER/JPL NASA spectral library

ASTER_Biotite =
importdata('Biotite.jpl.nicolet.mineral.silicate.phyllosilicate.coarse.ps23a.spectrum.txt');
bandes_IR = find(10000./ASTER_Biotite.data(:,1) > min(BY.sigma) & 10000./ASTER_Biotite.data(:,1)
< max(BY.sigma));
% Biotite = resample(ASTER_Biotite,size(BY.Reflectance,1),size(bandes_IR,1));
ASTERO = [ASTER_Biotite.data(bandes_IR,1),ASTER_Biotite.data(bandes_IR,2)/100];
Biotite = resample(ASTERO,size(BY.Reflectance,1),size(ASTERO,1));


%%%%%
ASTER_Diopside =
importdata('Diopside.jhu.nicolet.mineral.silicate.inosilicate.solid.diopsi1.spectrum.txt');
bandes_IR = find(10000./ASTER_Diopside.data(:,1) > min(BY.sigma) &
10000./ASTER_Diopside.data(:,1) < max(BY.sigma));
ASTERO = [ASTER_Diopside.data(bandes_IR,1),ASTER_Diopside.data(bandes_IR,2)/100];
Diopside = resample(ASTERO,size(BY.Reflectance,1),size(ASTERO,1));


%%%%%
ASTER_Epidote =
importdata('Epidote.jhu.nicolet.mineral.silicate.sorosilicate.solid.epidot1.spectrum.txt');
bandes_IR = find(10000./ASTER_Epidote.data(:,1) > min(BY.sigma) & 10000./ASTER_Epidote.data(:,1)
< max(BY.sigma));
ASTERO = [ASTER_Epidote.data(bandes_IR,1),ASTER_Epidote.data(bandes_IR,2)/100];
Epidote = resample(ASTERO,size(BY.Reflectance,1),size(ASTERO,1));


%%%%%
ASTER_Goethite =
importdata('Goethite.jhu.nicolet.mineral.hydroxide.none.solid.goethi2.spectrum.txt');
bandes_IR = find(10000./ASTER_Goethite.data(:,1) > min(BY.sigma) &
10000./ASTER_Goethite.data(:,1) < max(BY.sigma));
ASTERO = [ASTER_Goethite.data(bandes_IR,1),ASTER_Goethite.data(bandes_IR,2)/100];
Goethite = resample(ASTERO,size(BY.Reflectance,1),size(ASTERO,1));
```

168

```matlab
%%%%%
ASTER_Kyanite =
importdata('Kyanite.jhu.nicolet.mineral.silicate.phyllosilicate.coarse.kyanit1.spectrum.txt');
bandes_IR = find(10000./ASTER_Goethite.data(:,1) > min(BY.sigma) &
10000./ASTER_Goethite.data(:,1) < max(BY.sigma));
ASTERO = [ASTER_Kyanite.data(bandes_IR,1),ASTER_Kyanite.data(bandes_IR,2)/100];
Kyanite = resample(ASTERO,size(BY.Reflectance,1),size(ASTERO,1));

%%%%%
ASTER_Scheelite =
importdata('Scheelite.jpl.nicolet.mineral.tungstate.none.coarse.t01a.spectrum.txt');
bandes_IR = find(10000./ASTER_Scheelite.data(:,1) > min(BY.sigma) &
10000./ASTER_Scheelite.data(:,1) < max(BY.sigma));
ASTERO = [ASTER_Scheelite.data(bandes_IR,1),ASTER_Scheelite.data(bandes_IR,2)/100];
Scheelite = resample(ASTERO,size(BY.Reflectance,1),size(ASTERO,1));

%%%%%
ASTER_Smithsonite =
importdata('Smithsonite.jpl.nicolet.mineral.carbonate.none.coarse.c11a.spectrum.txt');
bandes_IR = find(10000./ASTER_Smithsonite.data(:,1) > min(BY.sigma) &
10000./ASTER_Smithsonite.data(:,1) < max(BY.sigma));
ASTERO = [ASTER_Smithsonite.data(bandes_IR,1),ASTER_Smithsonite.data(bandes_IR,2)/100];
Smithsonite = resample(ASTERO,size(BY.Reflectance,1),size(ASTERO,1));

%%%%%
ASTER_Tourmaline =
importdata('Tourmaline.jhu.nicolet.mineral.silicate.cyclosilicate.solid.tourma1.spectrum.txt');
bandes_IR = find(10000./ASTER_Tourmaline.data(:,1) > min(BY.sigma) &
10000./ASTER_Tourmaline.data(:,1) < max(BY.sigma));
ASTERO = [ASTER_Tourmaline.data(bandes_IR,1),ASTER_Tourmaline.data(bandes_IR,2)/100];
Tourmaline = resample(ASTERO,size(BY.Reflectance,1),size(ASTERO,1));

%%%%%
ASTER_Pyrope = importdata('PYROPE-
jhu.nicolet.mineral.silicate.nesosilicate.solid.pyrope1.spectrum.txt');
bandes_IR = find(10000./ASTER_Pyrope.data(:,1) > min(BY.sigma) & 10000./ASTER_Pyrope.data(:,1) <
max(BY.sigma));
ASTERO = [ASTER_Pyrope.data(bandes_IR,1),ASTER_Pyrope.data(bandes_IR,2)/100];
Pyrope = resample(ASTERO,size(BY.Reflectance,1),size(ASTERO,1));

%%%%%
ASTER_Olivine = importdata('Olivine (Fo92) (Fe+2,Mg)2SiO4 (2) -
jhu.nicolet.mineral.silicate.nesosilicate.solid.olivi12.spectrum.txt');
bandes_IR = find(10000./ASTER_Olivine.data(:,1) > min(BY.sigma) & 10000./ASTER_Olivine.data(:,1)
< max(BY.sigma));
ASTERO = [ASTER_Olivine.data(bandes_IR,1),ASTER_Olivine.data(bandes_IR,2)/100];
Olivine = resample(ASTERO,size(BY.Reflectance,1),size(ASTERO,1));

%%%%%
ASTER_Quartz = importdata('QUARTZ-
jhu.nicolet.mineral.silicate.tectosilicate.solid.quartz1.spectrum.txt');
bandes_IR = find(10000./ASTER_Quartz.data(:,1) > min(BY.sigma) & 10000./ASTER_Quartz.data(:,1) <
max(BY.sigma));
ASTERO = [ASTER_Quartz.data(bandes_IR,1),ASTER_Quartz.data(bandes_IR,2)/100];
Quartz = resample(ASTERO,size(BY.Reflectance,1),size(ASTERO,1));
%%%%%
% Background spectrum selection
title(['Select Background region']);
tv3 = toc;
BW2 = roipoly(BY.J); , tic
    [row,col] = find(BW2 == 1);
    infraGold = [row,col];

  pixels = getAoiIndices(BY.Header_ON, buildAoi(1, 1, row-1, col-1));
```

Recalling the spectra corresponding the tested minerals from ASTER/JPL NASA spectral library

Finding the spectra of background substrate (Carbon)

```matlab
bckgnd = mean(BY.Reflectance(:,pixels));
%   bckgnd = resample(double(bckgnd0'), size(bckgnd0,2), size(ASTERO,1));


ASTER = struct('ASTER_Biotite',ASTER_Biotite, 'ASTER_Diopside',ASTER_Diopside
,'ASTER_Epidote',ASTER_Epidote,...
    'ASTER_Goethite',ASTER_Goethite, 'ASTER_Kyanite',ASTER_Kyanite ,
'ASTER_Scheelite',ASTER_Scheelite ,...
    'ASTER_Smithsonite',ASTER_Smithsonite , 'ASTER_Tourmaline',ASTER_Tourmaline ,
'ASTER_Pyrope',ASTER_Pyrope ,...
    'ASTER_Olivine',ASTER_Olivine , 'ASTER_Quartz',ASTER_Quartz,...
    'Biotite',Biotite , 'Diopside',Diopside, 'Epidote',Epidote , 'Goethite',Goethite ,
'Kyanite',Kyanite ,...
    'Scheelite',Scheelite , 'Smithsonite',Smithsonite , 'Tourmaline',Tourmaline ,
'Pyrope',Pyrope,...
    'Olivine',Olivine , 'Quartz',Quartz, 'bckgnd', bckgnd);
clear ASTER_Biotite ASTER_Diopside ASTER_Epidote ASTER_Goethite ASTER_Kyanite ASTER_Scheelite ...
    ASTER_Smithsonite ASTER_Tourmaline ASTER_Pyrope ASTER_Olivine ASTER_Quartz Biotite
Diopside...
    Epidote Goethite Kyanite Scheelite Smithsonite Tourmaline Pyrope Olivine Quartz ASTERO bckgnd
...
    BW2 row col infraGold pixels bckgnd0
tv4 = toc;



%% Identification of the minerals (samples of the clusters)
ss = {'Biotite','Diopside','Epidote','Goethite','Kyanite','Scheelite','Smithsonite',...
    'Tourmaline','Pyrope','Olivine','Quartz', 'bckgnd'};



tic
for i = 1 : size(signals,2)
%       idx = 1;
%      while idx <= size(signals,2)
    for i0 = 1 : size(ss,2)-1, disp(sprintf(['NCC',num2str(i),'-',num2str(i0)]))
        a = eval(['ASTER.',num2str(ss{1,i0})]);
         % MAMS techniques
        cd([BY.CF0,'\HyperSpectralToolbox-master\functions\'])
%   bckgnd = resample(double(ASTER.bckgnd'), size(a(:,2),1), size(ASTER.bckgnd,2));
%   if size(coeffnmF(:,i)) == size(Norm2(a(:,2)))
        [resultsNormXCorr(i0)] = hyperNormXCorr(signals(:,i), Norm2(a(:,2))); %hyperNormXCorr
hyperSam  hyperHud  hyperCem hyperGlrt
    end
    MAM_1{i} = resultsNormXCorr;
end
mx1 = FalseColor(MAM_1,ss,BW,5);, title(['NCC']);
tvNmXC = toc;
```

```matlab
tic
for i = 1 : size(signals,2)
%       idx = 1;
%      while idx <= size(signals,2)
    for i0 = 1 : size(ss,2)-1, disp(sprintf(['SAM',num2str(i),'-',num2str(i0)]))
        a = eval(['ASTER.',num2str(ss{1,i0})]);
         % MAMS techniques
        cd([BY.CF0,'\HyperSpectralToolbox-master\functions\'])
%   bckgnd = resample(double(ASTER.bckgnd'), size(a(:,2),1), size(ASTER.bckgnd,2));
%   if size(coeffnmF(:,i)) == size(Norm2(a(:,2)))
    [resultsNormXCorr(i0)] = hyperSam(Norm2(signals(:,i)), Norm2(a(:,2))); %hyperNormXCorr
hyperSam  hyperHud
    end
    MAM_2{i} = resultsNormXCorr;
end
mx2 = FalseColor(MAM_2,ss,BW,5);, title(['SAM']);
tvSAM = toc;
```

```matlab
tic
for i = 1 : size(signals,2)
%    idx = 1;
%    while idx <= size(signals,2)
     for i0 = 1 : size(ss,2)-1, disp(sprintf(['HUD',num2str(i),'-',num2str(i0)]))
        a = eval(['ASTER.',num2str(ss{1,i0})]);
          % MAMS techniques
        cd([BY.CF0,'\HyperSpectralToolbox-master\functions\'])
%    bckgnd = resample(double(ASTER.bckgnd'), size(a(:,2),1), size(ASTER.bckgnd,2));
%    if size(coeffnmF(:,i)) == size(Norm2(a(:,2)))
        bckgnd = resample(double(ASTER.bckgnd'), size(a(:,2),1), size(ASTER.bckgnd,2));
%    if size(coeffnmF(:,i)) == size(Norm2(a(:,2)))
     [resultsNormXCorr(i0)] = hyperHud(signals(:,i), bckgnd, Norm2(a(:,2))); %hyperNormXCorr
hyperSam  hyperHud  hyperMatchedFilter
%
     end
     MAM_3{i} = resultsNormXCorr;
end
tvHUD = toc;
time = tv0 + tv2 + tv3 + tv4 + tvHUD
mx3 = FalseColor(MAM_3,ss,BW,5);, title(['HUD']);
```

This part performs the hybrid unstructured detector (HUD) algorithm for the hyperspectral data cube

```matlab
tic
for i = 1 : size(signals,2)
%    idx = 1;
%    while idx <= size(signals,2)
     for i0 = 1 : size(ss,2)-1, disp(sprintf(['OSP',num2str(i),'-',num2str(i0)]))
        a = eval(['ASTER.',num2str(ss{1,i0})]);
          % MAMS techniques
        cd([BY.CF0,'\HyperSpectralToolbox-master\functions\'])
%    bckgnd = resample(double(ASTER.bckgnd'), size(a(:,2),1), size(ASTER.bckgnd,2));
%    if size(coeffnmF(:,i)) == size(Norm2(a(:,2)))
        bckgnd = resample(double(ASTER.bckgnd'), size(a(:,2),1), size(ASTER.bckgnd,2));
%    if size(coeffnmF(:,i)) == size(Norm2(a(:,2)))
     [resultsNormXCorr(i0)] = hyperOsp(signals(:,i), bckgnd, Norm2(a(:,2))); %hyperNormXCorr
hyperSam  hyperHud  hyperMatchedFilter
% hyperHud
     end
     MAM_3{i} = resultsNormXCorr;
end
mx3 = FalseColor(MAM_3,ss,BW,5);, title(['OSP']);

tvOSP = toc;
% cdd = pwd;
% cd(CFres)
% save(mx3,'osp.png')
% cd(cdd)
```

This part performs the othogonal subspace projection (OSP) algorithm for the hyperspectral data cube

```matlab
tic
for i = 1 : size(signals,2)
%    idx = 1;
%    while idx <= size(signals,2)
     for i0 = 1 : size(ss,2)-1, disp(sprintf(['AMSD',num2str(i),'-',num2str(i0)]))
        a = eval(['ASTER.',num2str(ss{1,i0})]);
          % MAMS techniques
        cd([BY.CF0,'\HyperSpectralToolbox-master\functions\'])
%    bckgnd = resample(double(ASTER.bckgnd'), size(a(:,2),1), size(ASTER.bckgnd,2));
%    if size(coeffnmF(:,i)) == size(Norm2(a(:,2)))
        bckgnd = resample(double(ASTER.bckgnd'), size(a(:,2),1), size(ASTER.bckgnd,2));
%    if size(coeffnmF(:,i)) == size(Norm2(a(:,2)))
     [resultsNormXCorr(i0)] = hyperAmsd(signals(:,i), bckgnd, Norm2(a(:,2))); %hyperNormXCorr
hyperSam  hyperHud  hyperMatchedFilter
% hyperHud
     end
     MAM_9{i} = resultsNormXCorr;
```

This part performs Adaptive matched subspace detector (AMSD) algorithm for the hyperspectral data cube

```
    end
mx3 = FalseColor(MAM_9,ss,BW,5);, title(['AMSD']);
tvAMSD = toc;


tic                                                    This part performs the Matching Filter (MF)
for i = 1 : size(signals,2)                                algorithm for the hyperspectral data cube
%       idx = 1;
%     while idx <= size(signals,2)
    for i0 = 1 : size(ss,2)-1, disp(sprintf(['MF',num2str(i),'-',num2str(i0)]))
        a = eval(['ASTER.',num2str(ss{1,i0})]);
          % MAMS techniques
        cd([BY.CF0,'\HyperSpectralToolbox-master\functions\'])
%     bckgnd = resample(double(ASTER.bckgnd), size(a(:,2),1), size(ASTER.bckgnd,2));
%     if size(coeffnmF(:,i)) == size(Norm2(a(:,2)))
    [resultsNormXCorr(i0)] = hyperMatchedFilter(signals(:,i), Norm2(a(:,2))); %hyperNormXCorr
hyperSam   hyperHud   hyperMatchedFilter

    end
    MAM_4{i} = resultsNormXCorr;
end
% mx4 = FalseColor(MAM_4,ss,BW,6);, title(['MF']);
tvMF = toc;

% Reconstructing the hyper-cube!
    Qi = signals';
for i = 1 : size(Qi,2)
    Q(:,:,i) = reshape(Qi(:,i),[size(BW,1)-1,size(BW,2)-1]);
end

tic                                                    This part performs the PCA local matched filter
% for i = 1 : nclstr                                    (PLMF) target detection algorithm for the
%   idx = 1;                                                hyperspectral data cube
%   while idx <= size(ss,2)
 for i0 = 1 : size(ss,2)-1, disp(sprintf(['PLMF',num2str(i),'-',num2str(i0)]))
          a = eval(['ASTER.',num2str(ss{1,i0})]);
            % MAMS techniques
            % MAMs
    cd([BY.CF0,'\HyperSpectralToolbox-master\functions\'])
    b = Norm2(a(:,2));
%   bckgnd = resample(double(ASTER.bckgnd'), size(a(:,2),1), size(ASTER.bckgnd,2));
%   if size(coeffnmF(:,i)) == size(Norm2(a(:,2)))
    MAM_5{i0} = hyperPlmf(Q, b,7); %hyperNormXCorr hyperSam  hyperHud  hyperMatchedFilter
 end
%     MAM_5 = resultsNormXCorr;
% end
mx5 = FalseColor2(MAM_5,ss,BW,5);, title(['PlMF']);
tvPLMF = toc; tic


    for i0 = 1 : size(ss,2)-1, disp(sprintf(['RMF_S',num2str(i),'-',num2str(i0)]))
          a = eval(['ASTER.',num2str(ss{1,i0})]);
            % MAMS techniques
            % MAMs
    cd([BY.CF0,'\HyperSpectralToolbox-master\functions\'])
    b = Norm2(a(:,2));
%   bckgnd = resample(double(ASTER.bckgnd'), size(a(:,2),1), size(ASTER.bckgnd,2));
%   if size(coeffnmF(:,i)) == size(Norm2(a(:,2)))
    MAM_6{i0} = hyperRmf(Q, b,7,'sum'); %hyperNormXCorr hyperSam  hyperHud  hyperMatchedFilter
end
mx6 = FalseColor2(MAM_6,ss,BW,5);, title(['MFs']);
tvRMFs = toc; tic

    for i0 = 1 : size(ss,2)-1, disp(sprintf(['RMF_ML',num2str(i),'-',num2str(i0)]))
```

```matlab
            a = eval(['ASTER.',num2str(ss{1,i0})]);
            % MAMS techniques
            % MAMs
    cd([BY.CF0,'\HyperSpectralToolbox-master\functions\'])
    b = Norm2(a(:,2));
%    bckgnd = resample(double(ASTER.bckgnd'), size(a(:,2),1), size(ASTER.bckgnd,2));
%    if size(coeffnmF(:,i)) == size(Norm2(a(:,2)))
    MAM_7{i0} = hyperRmf(Q, b,7,'meanLocal'); %hyperNormXCorr hyperSam  hyperHud
hyperMatchedFilter
end
mx7 = FalseColor2(MAM_7,ss,BW,5);, title(['MFml']);
tvRMFml = toc; tic

for i0 = 1 : size(ss,2)-1, disp(sprintf(['RMF_MGL',num2str(i),'-',num2str(i0)]))
            a = eval(['ASTER.',num2str(ss{1,i0})]);
            % MAMS techniques
            % MAMs
    cd([BY.CF0,'\HyperSpectralToolbox-master\functions\'])
    b = Norm2(a(:,2));
%    bckgnd = resample(double(ASTER.bckgnd'), size(a(:,2),1), size(ASTER.bckgnd,2));
%    if size(coeffnmF(:,i)) == size(Norm2(a(:,2)))
    MAM_8{i0} = hyperRmf(Q, b,7,'meanGlobalLocal'); %hyperNormXCorr hyperSam  hyperHud
hyperMatchedFilter
end
 mx8 = FalseColor2(MAM_8,ss,BW,5);, title(['MFmgl']);
 tvRMFmgl = toc; tic
```

This part performs the regularized matched filter (RMF) target detection algorithm for the hyperspectral data cube

```matlab
clear idx a ans bandes_IR c i I i0 j Li_ON sample resultsNormXCorr
%%

%   computational time!
['NormXCorr']
Time = tv0 + tv2 + tv3 + tv4 + tvNmXC

['SAM']
Time = tv0 + tv2 + tv3 + tv4 + tvSAM

 ['OSP']
 Time = tv0 + tv2 + tv3 + tv4 + tvHUD

['MF']
Time = tv0 + tv2 + tv3 + tv4 + tvMF

['PLMF']
Time = tv0 + tv2 + tv3 + tv4 + tvPLMF

['RMFs']
Time = tv0 + tv2 + tv3 + tv4 + tvRMFs

['RMFml']
Time = tv0 + tv2 + tv3 + tv4 + tvRMFml

['RMFmgl']
Time = tv0 + tv2 + tv3 + tv4 + tvRMFmgl
%%
['OSP']
Time = tv0 + tv2 + tv3 + tvOSP

['AMSD']
Time = tv0 + tv2 + tv3 + tvAMSD

%cd 'H:\B\Dr-IR-sp\Dr-IR-MATLAB\New Exp. Dec2014 TELOPS\Result 1ST algorithm_20July\'
```

B.3.3 Color-based clustering

Considering FCC image is already made, by determining the initial number of clustering, the color-based clustering can be performed using this function.

```matlab
function segmented_images = CLUSTER(Im, ncluster)
```

```matlab
 [Row Col Dim]=size(Im); % Taking information of the number of row, column and dimension of image
N=Row*Col;               % calculate the number of nodes
%% Change color space
%changing to HSV color space for getting more difference in value of pixels
%in image to get bigger covariance

hsIm=rgb2hsv(Im);
hsImx=reshape(hsIm,N,Dim);
%RhsImx=hsImx(:,1);
%GhsImx=hsImx(:,2);
%BhsImx=hsImx(:,3);

%% PCA process
%"standardization data" subtracting the sample mean from each observation,
%then dividing by the sample standard deviation. This centers and scales the data.

%constactimg = bsxfun(@minus, hsImx, mean(hsImx))*coeff(:,1:3) ;
hsImxMean=mean(hsImx);
hsImxstd=std(hsImx);
conststandimg = (hsImx - repmat(hsImxMean,[N 1])) ./ repmat(hsImxstd,[N 1]);
[coeff2 s2 eignval2]=pca(conststandimg);  %gettin eigenvector(coeff2),eigenvalue(eignval2),actual
principal component(s2)
%% Choosing eigenvectors
%We have chosen two first bigger eigenvectors corresponding to bigger
%eigenvalues, just make note it doesn`t matter which coeff2 we choose in
%this level we can make original image easily, because they are enough to
%make image again
%we can choose just one regarding to is biggest but for k-means won`t
%getting good result

constactimg = bsxfun(@minus, hsImx, mean(hsImx))*coeff2(:,1:2)*(coeff2(:,1:2))' ;
Imnewh=constactimg(:,1);  %observing every part of constarcting eigen vectors,Hue
Imnews=constactimg(:,2);  %observing every part of constarcting eigen vectors,Saturation
Imnewv=constactimg(:,3);  %observing every part of constarcting eigen vectors,value
imnewH=reshape(Imnewh,Row,Col);
imnewS=reshape(Imnews,Row,Col);
imnewV=reshape(Imnewv,Row,Col);
% figure,imshow(imnewH);
% figure,imshow(imnewS);
% figure,imshow(imnewV);
%% Improvement of water extraction
%This section doing filter of dame area, because in result it still remains
%with water then it seems better to extract it here and the constant the
% reconstruct eigenvectors

imgseg=zeros(Row,Col);
for i=1:Row
    for j=1:Col
     valuepca=imnewH(i,j);
     if valuepca<=0 || valuepca>0.4
         imgseg(i,j)=0;
     else
         imgseg(i,j)=imnewH(i,j);
     end
    end
end
% figure,imshow(imgseg);
Imnewh=reshape(imgseg,N,1); % replacement of new modify image to previous image
constactimg2=zeros(N,3);
for jcol=1:3
    for insert=1:N
      if jcol==1
```

```matlab
constractimg2(insert,jcol)=Imnewh(insert,1);  %put every matrix in constraction matrix again
        elseif jcol==2
                constractimg2(insert,jcol)=Imnews(insert,1);
        else
                constractimg2(insert,jcol)=Imnewv(insert,1);
        end
    end
end
%% Find relative segments
%K-means algorithm

% ncluster=15; % choose 4 cluster to separate dam area with another color of green, but we will
have problem on other images clustering
[idx center]= kmeans(constractimg2,ncluster);
labels = reshape(idx,Row,Col);
segmented_images = cell(3);
% Creating tiles for three different colors
hsv_label = repmat(labels,[1 1 3]);
% Assigning clustered objects to array(segmented_image)
for k = 1:ncluster
color = Im;
color(hsv_label ~= k) = 0;
segmented_images{k} = color;
end
% displaying different cluster objects
% figure,imshow(segmented_images{1}), title('objects in cluster 1');
```

Bibliography

Labsphere: Technical guide: Integrating sphere theory and applications. https://www.labsphere.com/site/assets/files/2553/a-guide-to-reflectance-materials-and-coatings.pdf. Accessed 08 September 2017.

N. Acito, M. Diani, and G. Corsini. Signal-dependent noise modeling and model parameter estimation in hyperspectral images. *IEEE Transactions on Geoscience and Remote Sensing*, 49(8):2957–2971, 2011a.

N. Acito, M. Diani, and G. Corsini. Residual striping reduction in hyperspectral images. In *Digital Signal Processing (DSP), 2011 17th International Conference on*, pages 1–7. IEEE, 2011b.

J. B. Adams. Interpretation of visible and near-infrared diffuse reflectance spectra of pyroxenes and other rock-forming minerals. *Infrared and Raman spectroscopy of lunar and terrestrial minerals*, pages 91–116, 1975.

M. V. Afonso, J. M. Bioucas-Dias, and M. A. Figueiredo. An augmented lagrangian approach to the constrained optimization formulation of imaging inverse problems. *Image Processing, IEEE Transactions on*, 20(3):681–695, 2011.

I. Ahonen, H. Riipinen, and A. Roos. Portable fourier transform infrared spectrometer for use as a gas analyser in industrial hygiene. *Analyst*, 121(9):1253–1255, 1996.

D. Aksenova, B. Yousefi, F. Larachi, X. P. Maldague, and G. Beaudoin. Monitoring thermal phenomena in co2 capture by brucite.

C. C. Alexay, W. L. Truett, C. D. Prozzo, and B. O'dwyer. Portable filter infrared spectrometer, May 21 1996. US Patent 5,519,219.

J. Amos. Clays in pacific lavas challenge wet early mars idea, 10 2012.

M. T. Applegarth and W. L. Stefanov. Use of thermal infrared multispectral scanner (tims) imagery to investigate upslope particle size controls on arid piedmont morphology. *Geomorphology*, 82(3):388–397, 2006.

ASD. Fieldspec-spectroradiometers, 2017. URL https://www.asdi.com/products-and-services/fieldspec-spectroradiometers.

A. O. Awiti, M. G. Walsh, K. D. Shepherd, and J. Kinyamario. Soil condition classification using infrared spectroscopy: A proposition for assessment of soil condition along a tropical forest-cropland chronosequence. *Geoderma*, 143(1):73–84, 2008.

B. Ayerdi and M. Graña. Hyperspectral image nonlinear unmixing and reconstruction by elm regression ensemble. *Neurocomputing*, 174:299–309, 2016.

Y. Bailin. Airborne shortwave infrared spectral remote sensing as a direct prospecting method for oil and gas resources. *Chinese Journal of Geochemistry*, 13(2):156–164, 1994.

P. Bajorski. Practical evaluation of max-type detectors for hyperspectral images. *IEEE Journal of Selected Topics in Applied Earth Observations and Remote Sensing*, 5(2):462–469, 2012.

A. Baldridge, S. Hook, C. Grove, and G. Rivera. The aster spectral library version 2.0. *Remote Sensing of Environment*, 113(4):711–715, 2009.

L. Balick, A. Gillespie, A. French, I. Danilina, J.-P. Allard, and A. Mushkin. Longwave thermal infrared spectral variability in individual rocks. *IEEE Geoscience and Remote Sensing Letters*, 6(1):52–56, 2009a.

L. Balick, A. Gillespie, A. French, I. Danilina, J.-P. Allard, and A. Mushkin. Longwave thermal infrared spectral variability in individual rocks. *IEEE Geoscience and Remote Sensing Letters*, 6(1):52–56, 2009b.

E. Bedini. Mineral mapping in the kap simpson complex, central east greenland, using hymap and aster remote sensing data. *Advances in Space Research*, 47(1):60–73, 2011.

S. Bernabᴄé, S. Sanchez, A. Plaza, S. López, J. A. Benediktsson, and R. Sarmiento. Hyperspectral unmixing on gpus and multi-core processors: A comparison. *IEEE Journal of Selected Topics in Applied Earth Observations and Remote Sensing*, 6(3):1386–1398, 2013.

G. Bilgin, S. Erturk, and T. Yildirim. Unsupervised classification of hyperspectral-image data using fuzzy approaches that spatially exploit membership relations. *IEEE Geoscience and Remote Sensing Letters*, 5(4):673–677, 2008.

J. M. Bioucas-Dias and J. M. Nascimento. Hyperspectral subspace identification. *IEEE Transactions on Geoscience and Remote Sensing*, 46(8):2435–2445, 2008.

J. M. Bioucas-Dias, A. Plaza, N. Dobigeon, M. Parente, Q. Du, P. Gader, and J. Chanussot. Hyperspectral unmixing overview: Geometrical, statistical, and sparse regression-based approaches. *IEEE Journal of Selected Topics in Applied Earth Observations and Remote Sensing*, 5(2):354–379, 2012.

C. Bishop, B. Rivard, C. De Souza Filho, and F. van der Meer. Geological remote sensing. *International Journal of Applied Earth Observation and Geoinformation*, 64:267–274, 2018.

M. Black, T. R. Riley, G. Ferrier, A. H. Fleming, and P. T. Fretwell. Automated lithological mapping using airborne hyperspectral thermal infrared data: A case study from anchorage island, antarctica. *Remote Sensing of Environment*, 176:225–241, 2016.

T. A. Blake, C. Chackerian, and J. R. Podolske. Prognosis for a mid-infrared magnetic rotation spectrometer for the in situ detection of atmospheric free radicals. *Applied optics*, 35(6): 973–985, 1996.

A. Blakeney, G. Batten, and L. Welsh. Leaf nitrogen determination using a portable near-infrared spectrometer. In *Near-infrared Spectrosc.: Future Waves, Proc. Int. Conf. Near-infrared Spectrosc., 7th*, pages 149–152, 1996.

J. W. Boardman. Inversion of imaging spectrometry data using singular value decomposition. 1989.

J. W. Boardman. Sedimentary facies analysis using imaging spectrometry. In *8th Thematic Conference on Geologic Remote Sensing*, volume 2, pages 1189–1199, 1991.

J. W. Boardman, F. A. Kruse, and R. O. Green. Mapping target signatures via partial unmixing of aviris data. 1995.

J. Bobin, Y. Moudden, J. Starck, and M. Elad. Multichannel morphological component analysis. *Proceedings of Spars05*, pages 103–106, 2005.

J. Bobin, J.-L. Starck, J. M. Fadili, and Y. Moudden. Sparsity and morphological diversity in blind source separation. *IEEE Transactions on Image Processing*, 16(11):2662–2674, 2007.

B. Borie. X-ray diffraction in crystals, imperfect crystals, and amorphous bodies. *Journal of the American Chemical Society*, 87(1):140–141, 1965.

K. C. Bradley, K. C. Gross, and G. P. Perram. Imaging fourier transform spectrometry of combustion events. *IEEE Sensors Journal*, 10(3):779–785, 2010.

M. Brandmeier, S. Erasmi, C. Hansen, A. Höweling, K. Nitzsche, T. Ohlendorf, M. Mamani, and G. Wörner. Mapping patterns of mineral alteration in volcanic terrains using aster data and field spectrometry in southern peru. *Journal of South American Earth Sciences*, 48: 296–314, 2013.

G. H. Brimhall, C. N. Alpers, G. A. Swayze, et al. Characterization of waste rock associated with acid drainage at the penn mine, california, by ground-based visible to short-wave infrared reflectance spectroscopy assisted by digital mapping. *Chemical Geology*, 215(1): 453–472, 2005.

H. Brindley and J. Russell. Improving gerb scene identification using seviri: Infrared dust detection strategy. *Remote Sensing of Environment*, 104(4):426–446, 2006.

L. M. Bruce and J. Li. Wavelets for computationally efficient hyperspectral derivative analysis. *IEEE Transactions on Geoscience and Remote Sensing*, 39(7):1540–1546, 2001.

C. E. Caefer, J. Silverman, O. Orthal, D. Antonelli, Y. Sharoni, and S. R. Rotman. Improved covariance matrices for point target detection in hyperspectral data. *Optical Engineering*, 47(7):076402–076402, 2008.

CALCMET. Calcmet, 2017. URL https://www.gasmet.com/products/software/calcmet-standard-version.

W. M. Calvin and E. L. Pace. Mapping alteration in geothermal drill core using a field portable spectroradiometer. *Geothermics*, 61:12–23, 2016.

C. Camy-Peyret, P. Jeseck, T. Hawat, et al. The lpma balloon-borne ftir spectrometer for remote sensing of atmospheric constituents. In *European rocket and balloon programmes and related research*, volume 370, page 323, 1995.

K. Canham, A. Schlamm, A. Ziemann, B. Basener, and D. Messinger. Spatially adaptive hyperspectral unmixing. *IEEE Transactions on Geoscience and Remote Sensing*, 49(11): 4248–4262, 2011.

F. Capaccioni, G. Bellucci, R. Orosei, S. Amici, R. Bianchi, M. Blecka, M. Capria, A. Coradini, S. Erard, S. Fonti, et al. Mars-irma: in-situ infrared microscope analysis of martian soil and rock samples. *Advances in Space Research*, 28(8):1219–1224, 2001.

M. H. Carr and J. W. Head. Geologic history of mars. *Earth and Planetary Science Letters*, 294(3):185–203, 2010.

J. Carter, F. Poulet, J.-P. Bibring, and S. Murchie. Detection of hydrated silicates in crustal outcrops in the northern plains of mars. *Science*, 328(5986):1682–1686, 2010.

A. N. Chabane, N. Islam, and B. Zerr. Incremental clustering of sonar images using self-organizing maps combined with fuzzy adaptive resonance theory. *Ocean Engineering*, 142: 133–144, 2017.

C. T. Chaffin, T. Marshall, W. Fateley, and R. Hammaker. Infrared analysis of volcanic plumes: a case study in the application of open-path ft–ir monitoring techniques. *Spectrosc. Europe*, 7:18–24, 1995.

C.-I. Chang. Spectral information divergence for hyperspectral image analysis. In *Geoscience and Remote Sensing Symposium, 1999. IGARSS'99 Proceedings. IEEE 1999 International*, volume 1, pages 509–511. IEEE, 1999.

C.-I. Chang and S.-S. Chiang. Anomaly detection and classification for hyperspectral imagery. *IEEE Transactions on Geoscience and Remote Sensing*, 40(6):1314–1325, 2002.

C.-I. Chang, J.-M. Liu, B.-C. Chieu, H. Ren, C.-M. Wang, C.-S. Lo, P.-C. Chung, C.-W. Yang, D.-J. Ma, et al. Generalized constrained energy minimization approach to subpixel target detection for multispectral imagery. *Optical Engineering*, 39(5):1275–1281, 2000.

L. Chang, Y.-L. Chang, Z. Tang, and B. Huang. Group and region based parallel compression method using signal subspace projection and band clustering for hyperspectral imagery. *IEEE Journal of Selected Topics in Applied Earth Observations and Remote Sensing*, 4(3): 565–578, 2011.

D. Chen and R. J. Plemmons. Nonnegativity constraints in numerical analysis. In *The birth of numerical analysis*, pages 109–139. World Scientific, 2010.

Y. Chen, N. M. Nasrabadi, and T. D. Tran. Hyperspectral image classification via kernel sparse representation. *IEEE Transactions on Geoscience and Remote Sensing*, 51(1):217–231, 2013.

Y.-C. Cho and S. Choi. Nonnegative features of spectro-temporal sounds for classification. *Pattern Recognition Letters*, 26(9):1327–1336, 2005.

A. Chudnovsky, A. Kostinski, L. Herrmann, I. Koren, G. Nutesku, and E. Ben-Dor. Hyperspectral spaceborne imaging of dust-laden flows: Anatomy of saharan dust storm from the bodélé depression. *Remote Sensing of Environment*, 115(4):1013–1024, 2011.

R. N. Clark and T. V. King. Automatic continuum analysis of reflectance spectra. 1987.

R. N. Clark and T. L. Roush. Reflectance spectroscopy: Quantitative analysis techniques for remote sensing applications. *Journal of Geophysical Research: Solid Earth*, 89(B7): 6329–6340, 1984.

R. N. Clark and G. A. Swayze. Mapping minerals, amorphous materials, environmental materials, vegetation, water, ice and snow, and other materials: the usgs tricorder algorithm. 1995.

R. N. Clark, T. V. King, M. Klejwa, G. A. Swayze, and N. Vergo. High spectral resolution reflectance spectroscopy of minerals. *Journal of Geophysical Research: Solid Earth*, 95(B8): 12653–12680, 1990.

R. N. Clark, G. A. Swayze, K. E. Livo, R. F. Kokaly, S. J. Sutley, J. B. Dalton, R. R. McDougal, and C. A. Gent. Imaging spectroscopy: Earth and planetary remote sensing with the usgs tetracorder and expert systems. *Journal of Geophysical Research: Planets*, 108(E12), 2003.

R. N. Clark, R. H. Brown, R. Jaumann, D. P. Cruikshank, R. M. Nelson, B. J. Buratti, T. B. McCord, J. Lunine, K. Baines, G. Bellucci, et al. Compositional maps of saturn's moon phoebe from imaging spectroscopy. *Nature*, 435(7038):66, 2005.

R. N. Clark, G. A. Swayze, R. Wise, K. E. Livo, T. Hoefen, R. F. Kokaly, and S. J. Sutley. Usgs digital spectral library splib06a. *US geological survey, digital data series*, 231:2007, 2007.

R. Clarke. Chapter 1: Spectroscopy of rocks and minerals, and principles of spectroscopy, manual of remote sensing, remote sensing for the earth sciences (pp. 3–58), 1999.

E. Cloutis. Review article hyperspectral geological remote sensing: evaluation of analytical techniques. *International Journal of Remote Sensing*, 17(12):2215–2242, 1996.

D. Cozzolino. Near infrared spectroscopy as a tool to monitor contaminants in soil, sediments and waterâstate of the art, advantages and pitfalls. *Trends in Environmental Analytical Chemistry*, 9:1–7, 2016.

A. P. Crósta and C. R. de Souza Filho. Hyperspectral remote sensing for mineral mapping: a case-study at alto paraíso de goías, central brazil. *Revista Brasileira de Geociências*, 30(3): 551–554, 2017.

J. Crowley, D. Williams, J. Hammarstrom, N. Piatak, I.-M. Chou, and J. Mars. Spectral reflectance properties (0.4–2.5 μm) of secondary fe-oxide, fe-hydroxide, and fe-sulphate-hydrate minerals associated with sulphide-bearing mine wastes. *Geochemistry: Exploration, Environment, Analysis*, 3(3):219–228, 2003.

CSES. Center for the study of earth from space (cses). In *SIPS Userâs Guide, Spectral Image Processing System*, volume Version 1.2, page 88p. Center for the Study of Earth from Space, Boulder, CO, 4.

M. Cubero-Castan, J. Chanussot, V. Achard, X. Briottet, and M. Shimoni. A physics-based unmixing method to estimate subpixel temperatures on mixed pixels. *IEEE Transactions on Geoscience and Remote Sensing*, 53(4):1894–1906, 2015.

T. Cudahy and P. Barry. Earth magmatic-seawater hydrothermal alteration revealed through satellite-borne hyperion imagery at panorama, western australia. In *Geoscience and Remote Sensing Symposium, 2002. IGARSS'02. 2002 IEEE International*, volume 1, pages 590–592. IEEE, 2002.

J. Cui, B. Yan, X. Dong, S. Zhang, J. Zhang, F. Tian, and R. Wang. Temperature and emissivity separation and mineral mapping based on airborne tasi hyperspectral thermal

infrared data. *International Journal of Applied Earth Observation and Geoinformation*, 40: 19–28, 2015.

P. J. Curran and J. L. Dungan. Estimation of signal-to-noise: a new procedure applied to aviris data. *IEEE Transactions on Geoscience and Remote sensing*, 27(5):620–628, 1989.

C. O. Davis. Airborne hyperspectral remote sensing. Technical report, NAVAL RESEARCH LAB WASHINGTON DC, 2001.

F. De Boissieu, B. Sevin, T. Cudahy, M. Mangeas, S. Chevrel, C. Ong, A. Rodger, P. Maurizot, C. Laukamp, I. Lau, et al. Regolith-geology mapping with support vector machine: A case study over weathered ni-bearing peridotites, new caledonia. *International Journal of Applied Earth Observation and Geoinformation*, 2017.

C. Deng, S. Zhang, S. Wang, W. Tian, and Z. Wu. Sparse hyperspectral unmixing based on smoothed â0 regularization. *Infrared Physics & Technology*, 67:306–314, 2014.

C. Ding. Spectral clustering, principal component analysis and matrix factorizations for learning. In *Intâl Conf. on Machine Learning (Tutorial)*, 2005.

C. Ding, X. He, and H. D. Simon. On the equivalence of nonnegative matrix factorization and spectral clustering. In *Proceedings of the 2005 SIAM International Conference on Data Mining*, pages 606–610. SIAM, 2005.

N. Dobigeon and N. Brun. Spectral mixture analysis of eels spectrum-images. *Ultramicroscopy*, 120:25–34, 2012.

I. Dópido, M. Zortea, A. Villa, A. Plaza, and P. Gamba. Unmixing prior to supervised classification of remotely sensed hyperspectral images. *IEEE Geoscience and Remote Sensing Letters*, 8(4):760–764, 2011.

I. Dópido, A. Villa, A. Plaza, and P. Gamba. A quantitative and comparative assessment of unmixing-based feature extraction techniques for hyperspectral image classification. *IEEE Journal of selected topics in applied earth observations and remote sensing*, 5(2):421–435, 2012.

I. Dópido, J. Li, P. R. Marpu, A. Plaza, J. M. B. Dias, and J. A. Benediktsson. Semisupervised self-learning for hyperspectral image classification. *IEEE transactions on geoscience and remote sensing*, 51(7):4032–4044, 2013.

R. Douglas, S. Nawar, M. Alamar, A. Mouazen, and F. Coulon. Rapid prediction of total petroleum hydrocarbons concentration in contaminated soil using vis-nir spectroscopy and regression techniques. *Science of The Total Environment*, 616:147–155, 2018.

Q. Du and J. E. Fowler. Low-complexity principal component analysis for hyperspectral image compression. *The International Journal of High Performance Computing Applications*, 22 (4):438–448, 2008.

T. B. Egevskaya. Portable âdouble catâs eyeâ ft-ir spectrometer. In *Progress in Fourier Transform Spectroscopy*, pages 767–768. Springer, 1997.

B. L. Ehlmann, J. F. Mustard, S. L. Murchie, J.-P. Bibring, A. Meunier, A. A. Fraeman, and Y. Langevin. Subsurface water and clay mineral formation during the early history of mars. *Nature*, 479(7371):53–60, 2011.

A. Eisele, S. Chabrillat, C. Hecker, R. Hewson, I. C. Lau, C. Rogass, K. Segl, T. J. Cudahy, T. Udelhoven, P. Hostert, et al. Advantages using the thermal infrared (tir) to detect and quantify semi-arid soil properties. *Remote Sensing of Environment*, 163:296–311, 2015.

M. T. Eismann and R. C. Hardie. Stochastic spectral unmixing with enhanced endmember class separation. *Applied optics*, 43(36):6596–6608, 2004.

G. N. Elliott, H. Worgan, D. Broadhurst, J. Draper, and J. Scullion. Soil differentiation using fingerprint fourier transform infrared spectroscopy, chemometrics and genetic algorithm-based feature selection. *Soil Biology and Biochemistry*, 39(11):2888–2896, 2007.

I. Entezari, B. Rivard, M. Geramian, and M. G. Lipsett. Predicting the abundance of clays and quartz in oil sands using hyperspectral measurements. *International Journal of Applied Earth Observation and Geoinformation*, 59:1–8, 2017.

C. Fan, H. Xie, J. Q. Wu, and S. Birnbaum. Implication from the examination of spectral library of hydroxylated and/or hydrated silicate minerals at 1.0–2.5 um wavelengths. In *Hyperspectral Image and Signal Processing: Evolution in Remote Sensing (WHISPERS), 2011 3rd Workshop on*, pages 1–4. IEEE, 2011.

V. Farmer. The infra-red spectra of minerals. *Mineralogical Society, London*, page 539, 1974.

J. Feng, B. Rivard, D. Rogge, and A. Sánchez-Azofeifa. The longwave infrared (3–14μm) spectral properties of rock encrusting lichens based on laboratory spectra and airborne sebass imagery. *Remote sensing of environment*, 131:173–181, 2013a.

J. Feng, B. Rivard, D. Rogge, and A. Sanchez-Azofeifa. The longwave infrared (3–14μm) spectral properties of rock encrusting lichens based on laboratory spectra and airborne sebass imagery. *Remote Sensing of Environment*, 131:173–181, 2013b.

J. Feng, D. Rogge, and B. Rivard. Comparison of lithological mapping results from airborne hyperspectral vnir-swir, lwir and combined data. *International Journal of Applied Earth Observation and Geoinformation*, 2017.

A. M. Filippi and J. R. Jensen. Effect of continuum removal on hyperspectral coastal vegetation classification using a fuzzy learning vector quantizer. *IEEE transactions on geoscience and remote sensing*, 45(6):1857–1869, 2007.

E. M. Fischer and C. M. Pieters. Remote determination of exposure degree and iron concentration of lunar soils using vis-nir spectroscopic methods. *Icarus*, 111(2):475–488, 1994.

V. Franc, V. Hlaváč, and M. Navara. Sequential coordinate-wise algorithm for the non-negative least squares problem. In *CAIP*, volume 3691, pages 407–414. Springer, 2005.

J. N. Franklin. *Matrix theory*. Courier Corporation, 2012.

M. Frezzotti, J. Selverstone, Z. Sharp, and R. Compagnoni. Carbonate dissolution during subduction revealed by diamond-bearing rocks from the alps. *Nature Geoscience*, 4(10): 703–706, 2011.

C. C. Funk, J. Theiler, D. A. Roberts, and C. C. Borel. Clustering to improve matched filter detection of weak gas plumes in hyperspectral thermal imagery. *IEEE Transactions on Geoscience and Remote Sensing*, 39(7):1410–1420, 2001.

S. Gaffey, L. McFadden, D. Nash, and C. Pieters. Ultraviolet, visible, and near-infrared reflectance spectroscopy: Laboratory spectra of geologic materials. *Remote geochemical analysis: Elemental and mineralogical composition*, pages 43–77, 1993.

F. R. Gamble. X-ray diffraction grating crystals, Aug. 29 1972. US Patent 3,688,109.

L.-R. Gao, B. Zhang, X. Zhang, W.-J. Zhang, and Q.-X. Tong. A new operational method for estimating noise in hyperspectral images. *IEEE Geoscience and remote sensing letters*, 5(1):83–87, 2008.

X. Gao, K. Zhang, D. Tao, and X. Li. Image super-resolution with sparse neighbor embedding. *IEEE Transactions on Image Processing*, 21(7):3194–3205, 2012.

Y. Gao, J. Li, and B. Zhang. The infrared microscope and rapid identification of gemstones. *J. Gemmol*, 24(6):411–14, 1995.

P. B. Garcia-Allende, O. M. Conde, J. Mirapeix, A. M. Cubillas, and J. M. López-Higuera. Data processing method applying principal component analysis and spectral angle mapper for imaging spectroscopic sensors. *IEEE Sensors Journal*, 8(7):1310–1316, 2008.

geotechnos. http://www.geotechnos.co.jp, 2004.

S. Ghaffarian and S. Ghaffarian. Automatic histogram-based fuzzy c-means clustering for remote sensing imagery. *ISPRS Journal of Photogrammetry and Remote Sensing*, 97:46–57, 2014.

P. Ghamisi, A.-R. Ali, M. S. Couceiro, and J. A. Benediktsson. A novel evolutionary swarm fuzzy clustering approach for hyperspectral imagery. *IEEE Journal of Selected Topics in Applied Earth Observations and Remote Sensing*, 8(6):2447–2456, 2015.

M. Ghasemzadeh-Barvarz, A. Ramezani-Kakroodi, D. Rodrigue, and C. Duchesne. Multivariate image regression for quality control of natural fiber composites. *Industrial & Engineering Chemistry Research*, 52(35):12426–12436, 2013.

R. Gholami, A. Moradzadeh, and M. Yousefi. Assessing the performance of independent component analysis in remote sensing data processing. *Journal of the Indian Society of Remote Sensing*, 40(4):577–588, 2012.

A. R. Gillespie, A. B. Kahle, and R. E. Walker. Color enhancement of highly correlated images. i. decorrelation and hsi contrast stretches. *Remote Sensing of Environment*, 20(3): 209–235, 1986.

A. R. Gillespie, A. B. Kahle, and R. E. Walker. Color enhancement of highly correlated images. ii. channel ratio and âchromaticityâ transformation techniques. *Remote Sensing of Environment*, 22(3):343–365, 1987.

G. D. Gillespie, C. D. Everard, and K. P. McDonnell. Prediction of biomass pellet quality indices using near infrared spectroscopy. *Energy*, 80:582–588, 2015.

A. F. Goetz. Three decades of hyperspectral remote sensing of the earth: A personal view. *Remote Sensing of Environment*, 113:S5–S16, 2009.

A. F. Goetz, G. Vane, J. E. Solomon, and B. N. Rock. Imaging spectrometry for earth remote sensing. *science*, 228(4704):1147–1153, 1985.

G. H. Golub and C. F. Van Loan. *Matrix computations*, volume 3. JHU Press, 2012.

C. Gomez, P. Lagacherie, and G. Coulouma. Continuum removal versus plsr method for clay and calcium carbonate content estimation from laboratory and airborne hyperspectral measurements. *Geoderma*, 148(2):141–148, 2008.

C. Gonzalez, S. Lopez, D. Mozos, and R. Sarmiento. Fpga implementation of the hysime algorithm for the determination of the number of endmembers in hyperspectral data. *IEEE Journal of Selected Topics in Applied Earth Observations and Remote Sensing*, 8(6):2870–2883, 2015.

R. Goodacre, E. M. Timmins, P. J. Rooney, J. J. Rowland, and D. B. Kell. Rapid identification of streptococcus and enterococcus species using diffuse reflectance-absorbance fourier transform infrared spectroscopy and artificial neural networks. *FEMS Microbiology Letters*, 140(2-3):233–239, 1996.

S. Gou, Z. Yue, K. Di, and J. Wang. Mineral abundances and different levels of alteration around mawrth vallis, mars. *Geoscience Frontiers*, 6(5):741–758, 2015.

H. Govil. Prospecting for hydrothermal mineral deposits in the himalaya using short-wave infrared spectroscopy. In *Hyperspectral Image and Signal Processing: Evolution in Remote Sensing (WHISPERS), 2015 7th Workshop on*, pages 1–4. IEEE, 2016.

A. Gowen, C. O'Donnell, P. Cullen, G. Downey, and J. Frias. Hyperspectral imaging–an emerging process analytical tool for food quality and safety control. *Trends in Food Science & Technology*, 18(12):590–598, 2007.

P. Graves and D. Gardiner. Practical raman spectroscopy, 1989.

A. A. Green, M. Berman, P. Switzer, and M. D. Craig. A transformation for ordering multispectral data in terms of image quality with implications for noise removal. *IEEE Transactions on geoscience and remote sensing*, 26(1):65–74, 1988.

R. O. Green. Determination of the in-flight spectral and radiometric characteristics of the airborne visible/infrared imaging spectrometer (aviris). *Imaging Spectroscopy: Fundamentals and Prospective Applications*, pages 103–123, 1992.

U. Grenander. The nyquist frequency is that frequency whose period is two sampling intervals. *Probability and statistics: the Harald Cramér volume*, page 434, 1959.

R. Gribonval and S. Lesage. A survey of sparse component analysis for blind source separation: principles, perspectives, and new challenges. In *ESANN'06 proceedings-14th European Symposium on Artificial Neural Networks*, pages 323–330. d-side publi., 2006.

M. Griffin. Detectors for far-infrared spectroscopy of the earth's atmosphere and beyond. *SPECTRUM-PRETORIA-*, 34:22–37, 1996.

H. Guo. A simple algorithm for fitting a gaussian function [dsp tips and tricks]. *IEEE Signal Processing Magazine*, 28(5):134–137, 2011.

N. Gupta. Development of spectropolarimetric imagers for imaging of desert soils. In *Applied Imagery Pattern Recognition Workshop (AIPR), 2014 IEEE*, pages 1–7. IEEE, 2014.

N. Hagen, M. Kupinski, and E. L. Dereniak. Gaussian profile estimation in one dimension. *Applied optics*, 46(22):5374–5383, 2007.

P. J. M. T. T. M. W. M. F. W. Hammaker, R.M. Remote sensing of volatile organic compounds in the atmosphere using a fourier transform nearinfrared spectrometer. *Leaping Ahead Near-infrared Spectrosc*, pages 510–513, 1995.

C. Hecker, M. Van der Meijde, H. van der Werff, and F. D. van der Meer. Assessing the influence of reference spectra on synthetic sam classification results. *IEEE Transactions on geoscience and remote sensing*, 46(12):4162–4172, 2008.

C. Hecker, M. van der Meijde, and F. D. van der Meer. Thermal infrared spectroscopy on feldsparsâsuccesses, limitations and their implications for remote sensing. *Earth-Science Reviews*, 103(1):60–70, 2010.

D. C. Heinz, C. E. Davidson, and A. Ben-David. Temporal-spectral detection in long-wave ir hyperspectral imagery. *IEEE Sensors Journal*, 10(3):509–517, 2010.

R. Herrmann and C. Onkelinx. Quantities and units in clinical chemistry: nebulizer and flame properties in flame emission and absorption spectrometry (provisional). *Pure and Applied Chemistry*, 56(10):1499–1504, 1984.

W. Herrmann, M. Blake, M. Doyle, D. Huston, J. Kamprad, N. Merry, and S. Pontual. Short wavelength infrared (swir) spectral analysis of hydrothermal alteration zones associated with base metal sulfide deposits at rosebery and western tharsis, tasmania, and highway-reward, queensland. *Economic Geology*, 96(5):939–955, 2001.

E. Hirsch and E. Agassi. Detection of gaseous plumes in ir hyperspectral imagesâperformance analysis. *IEEE Sensors Journal*, 10(3):732–736, 2010.

S. J. Hook and A. B. Kahle. The micro fourier transform interferometer (μftir)âa new field spectrometer for acquisition of infrared data of natural surfaces. *Remote Sensing of Environment*, 56(3):172–181, 1996.

A. Horta, B. Malone, U. Stockmann, B. Minasny, T. Bishop, A. McBratney, R. Pallasser, and L. Pozza. Potential of integrated field spectroscopy and spatial analysis for enhanced assessment of soil contamination: a prospective review. *Geoderma*, 241:180–209, 2015.

E. S. Howell. Probing asteroid composition using visible and near-infrared spectroscopy. 1995.

G.-B. Huang. http://www.ntu.edu.sg/home/egbhuang/elm$_k$ernel.html, 2013.

G.-B. Huang, Q.-Y. Zhu, and C.-K. Siew. Extreme learning machine: a new learning scheme of feedforward neural networks. In *Neural Networks, 2004. Proceedings. 2004 IEEE International Joint Conference on*, volume 2, pages 985–990. IEEE, 2004a.

G.-B. Huang, L. Chen, and C.-K. Siew. Universal approximation using incremental constructive feedforward networks with random hidden nodes. *Neural Networks, IEEE Transactions on*, 17(4):879–892, 2006.

J. Huang, Y. Ma, X. Mei, and F. Fan. A hybrid spatial-spectral denoising method for infrared hyperspectral images using 2dpca. *Infrared Physics & Technology*, 79:68–73, 2016.

Z. Huang, B. J. Turner, S. J. Dury, I. R. Wallis, and W. J. Foley. Estimating foliage nitrogen concentration from hymap data using continuum removal analysis. *Remote Sensing of Environment*, 93(1-2):18–29, 2004b.

B. E. Hubbard, J. K. Crowley, and D. R. Zimbelman. Comparative alteration mineral mapping using visible to shortwave infrared (0.4-2.4/spl mu/m) hyperion, ali, and aster imagery. *IEEE Transactions on geoscience and remote sensing*, 41(6):1401–1410, 2003.

G. Hunt. Spectroscopic properties of rocks and minerals. *Handbook of physical properties of rocks*, 1:295–385, 1982.

G. R. Hunt. Spectral signatures of particulate minerals in the visible and near infrared. *Geophysics*, 42(3):501–513, 1977.

S. HUZIKAWA, K. OHKAWA, and S. TANAKA. Automatic identification of alteration mineral using a portable infrared spectralmeter. *Journal of The Remote Sensing Society of Japan*, 21 (2):206–209, 2001.

M.-D. Iordache, J. M. Bioucas-Dias, and A. Plaza. Sparse unmixing of hyperspectral data. *Geoscience and Remote Sensing, IEEE Transactions on*, 49(6):2014–2039, 2011.

M.-D. Iordache, J. M. Bioucas-Dias, and A. Plaza. Total variation spatial regularization for sparse hyperspectral unmixing. *Geoscience and Remote Sensing, IEEE Transactions on*, 50 (11):4484–4502, 2012.

M.-D. Iordache, J. M. Bioucas-Dias, and A. Plaza. Collaborative sparse regression for hyperspectral unmixing. *Geoscience and Remote Sensing, IEEE Transactions on*, 52(1):341–354, 2014.

Isaac. https://github.com/isaacgerg/matlabhyperspectraltoolbox, 2015.

E. Izquierdo-Verdiguier, L. Gomez-Chova, L. Bruzzone, and G. Camps-Valls. Semisupervised kernel feature extraction for remote sensing image analysis. *IEEE transactions on geoscience and remote sensing*, 52(9):5567–5578, 2014.

J. Jehlička, A. Culka, P. Vandenabeele, and H. G. Edwards. Critical evaluation of a handheld raman spectrometer with near infrared (785nm) excitation for field identification of minerals. *Spectrochimica Acta Part A: Molecular and Biomolecular Spectroscopy*, 80(1):36–40, 2011.

X. Jia and J. A. Richards. Cluster-space representation for hyperspectral data classification. *IEEE Transactions on Geoscience and Remote Sensing*, 40(3):593–598, 2002.

L.-I. Jiménez, G. Martin, and A. Plaza. Hypermix: A new tool for quantitative evaluation of end member identification and spectral unmixing techniques. In *Geoscience and Remote Sensing Symposium (IGARSS), 2012 IEEE International*, pages 1393–1396. IEEE, 2012.

X. Jin, S. Paswaters, and H. Cline. A comparative study of target detection algorithms for hyperspectral imagery. In *Proceedings of SPIE*, volume 7334, page 73341W, 2009.

C. Jing, Y. Bokun, W. Runsheng, T. Feng, Z. Yingjun, L. Dechang, Y. Suming, and S. Wei. Regional-scale mineral mapping using aster vnir/swir data and validation of reflectance and mineral map products using airborne hyperspectral casi/sasi data. *International Journal of Applied Earth Observation and Geoinformation*, 33:127–141, 2014.

D. H. Johnson. Signal-to-noise ratio. *Scholarpedia*, 1(12):2088, 2006.

I. M. Johnstone and A. Y. Lu. On consistency and sparsity for principal components analysis in high dimensions. *Journal of the American Statistical Association*, 104(486):682–693, 2009.

I. T. Jolliffe. Principal component analysis and factor analysis. In *Principal component analysis*, pages 115–128. Springer, 1986.

S. Kaewpijit, J. Le Moigne, and T. El-Ghazawi. A wavelet-based pca reduction for hyperspectral imagery. In *Geoscience and Remote Sensing Symposium, 2002. IGARSS'02. 2002 IEEE International*, volume 5, pages 2581–2583. IEEE, 2002.

J. P. Kerekes and J. E. Baum. Hyperspectral imaging system modeling. *Lincoln Laboratory Journal*, 14(1):117–130, 2003.

M. Khaleghi, H. Ranjbar, J. Shahabpour, and M. Honarmand. Spectral angle mapping, spectral information divergence, and principal component analysis of the aster swir data for exploration of porphyry copper mineralization in the sarduiyeh area, kerman province, iran. *Applied Geomatics*, 6(1):49–58, 2014.

M. Khanmohammadi, A. B. Garmarudi, and M. de la Guardia. Characterization of petroleum-based products by infrared spectroscopy and chemometrics. *TrAC Trends in Analytical Chemistry*, 35:135–149, 2012.

M. Khodadadzadeh, J. Li, A. Plaza, and J. M. Bioucas-Dias. A subspace-based multinomial logistic regression for hyperspectral image classification. *IEEE Geoscience and Remote Sensing Letters*, 11(12):2105–2109, 2014a.

M. Khodadadzadeh, J. Li, A. Plaza, H. Ghassemian, J. M. Bioucas-Dias, and X. Li. Spectral–spatial classification of hyperspectral data using local and global probabilities for mixed pixel characterization. *IEEE Transactions on Geoscience and Remote Sensing*, 52(10):6298–6314, 2014b.

T. Kim, T. Eltoft, and T.-W. Lee. Independent vector analysis: An extension of ica to multivariate components. In *International Conference on Independent Component Analysis and Signal Separation*, pages 165–172. Springer, 2006.

J. L. Kinsey. Laser-induced fluorescence. *Annual Review of Physical Chemistry*, 28(1):349–372, 1977.

G. Kirchhoff. I. on the relation between the radiating and absorbing powers of different bodies for light and heat. *The London, Edinburgh, and Dublin Philosophical Magazine and Journal of Science*, 20(130):1–21, 1860.

K. C. Kiwiel. Convergence and efficiency of subgradient methods for quasiconvex minimization. *Mathematical programming*, 90(1):1–25, 2001.

J. Koch, S. Chakraborty, B. Li, J. M. Kucera, P. Van Deventer, A. Daniell, C. Faul, T. Man, D. Pearson, B. Duda, et al. Proximal sensor analysis of mine tailings in south africa: An exploratory study. *Journal of Geochemical Exploration*, 181:45–57, 2017.

V. Kopačková. Using multiple spectral feature analysis for quantitative ph mapping in a mining environment. *International Journal of Applied Earth Observation and Geoinformation*, 28: 28–42, 2014.

A. R. Korb, P. Dybwad, W. Wadsworth, and J. W. Salisbury. Portable fourier transform infrared spectroradiometer for field measurements of radiance and emissivity. *Applied Optics*, 35(10): 1679–1692, 1996.

S. Kotthaus, T. E. Smith, M. J. Wooster, and C. Grimmond. Derivation of an urban materials spectral library through emittance and reflectance spectroscopy. *ISPRS Journal Of Photogrammetry And Remote Sensing*, 94:194–212, 2014.

F. Kowkabi, H. Ghassemian, and A. Keshavarz. Hybrid preprocessing algorithm for endmember extraction using clustering, over-segmentation, and local entropy criterion. *IEEE Journal of Selected Topics in Applied Earth Observations and Remote Sensing*, 2017.

D. Krupnik, S. Khan, U. Okyay, P. Hartzell, and H.-W. Zhou. Study of upper albian rudist buildups in the edwards formation using ground-based hyperspectral imaging and terrestrial laser scanning. *Sedimentary Geology*, 345:154–167, 2016.

F. Kruse. Identification and mapping of minerals in drill core using hyperspectral image analysis of infrared reflectance spectra. *International journal of remote sensing*, 17(9):1623–1632, 1996a.

F. Kruse. Identification and mapping of minerals in drill core using hyperspectral image analysis of infrared reflectance spectra. *International journal of remote sensing*, 17(9):1623–1632, 1996b.

F. Kruse. Visible-infrared sensors and case studies. *Manual of Remote Sensing*, 3, 1999.

F. Kruse, A. Lefkoff, J. Boardman, K. Heidebrecht, A. Shapiro, P. Barloon, and A. Goetz. Sips user's guide, the spectral image processing system. *Center for the Study of Earth from Space (CSES)*, 1(1):74, 1992.

F. Kruse, A. Lefkoff, J. Boardman, K. Heidebrecht, A. Shapiro, P. Barloon, and A. Goetz. The spectral image processing system (sips)âinteractive visualization and analysis of imaging spectrometer data. *Remote sensing of environment*, 44(2-3):145–163, 1993a.

F. Kruse, A. Lefkoff, and J. Dietz. Expert system-based mineral mapping in northern death valley, california/nevada, using the airborne visible/infrared imaging spectrometer (aviris). *Remote Sensing of Environment*, 44(2-3):309–336, 1993b.

F. Kruse, J. Boardman, and J. Huntington. Comparison of eo-1 hyperion and airborne hyperspectral remote sensing data for geologic applications. In *Aerospace Conference Proceedings, 2002. IEEE*, volume 3, pages 3–3. IEEE, 2002a.

F. Kruse, J. Boardman, J. Huntington, P. Mason, and M. Quigley. Evaluation and validation of eo-1 hyperion for geologic mapping. In *Geoscience and Remote Sensing Symposium, 2002. IGARSS'02. 2002 IEEE International*, volume 1, pages 593–595. IEEE, 2002b.

F. A. Kruse. Mapping surface mineralogy using imaging spectrometry. *Geomorphology*, 137(1): 41–56, 2012.

F. A. Kruse and S. L. Perry. Regional mineral mapping by extending hyperspectral signatures using multispectral data. In *Aerospace Conference, 2007 IEEE*, pages 1–14. IEEE, 2007.

F. A. Kruse, J. W. Boardman, and J. F. Huntington. Comparison of airborne hyperspectral data and eo-1 hyperion for mineral mapping. *IEEE Transactions on Geoscience and Remote Sensing*, 41(6):1388–1400, 2003.

C. Kumar, A. Shetty, S. Raval, R. Sharma, and P. C. Ray. Lithological discrimination and mapping using aster swir data in the udaipur area of rajasthan, india. *Procedia Earth and Planetary Science*, 11:180–188, 2015.

H. Kwon and N. M. Nasrabadi. Kernel orthogonal subspace projection for hyperspectral signal classification. *IEEE Transactions on Geoscience and Remote Sensing*, 43(12):2952–2962, 2005.

D. A. Landgrebe and E. Malaret. Noise in remote-sensing systems: The effect on classification error. *IEEE transactions on geoscience and remote sensing*, (2):294–300, 1986.

Landsat-8. Landsat-8, 2017. URL https://landsat.usgs.gov/landsat-8.

I. Lau, G. Heinson, P. James, and A. Mauger. Hyperspectral mapping of regolith materials and landforms for mineral exploration, olary domain, south australia. In *Geoscience and Remote Sensing Symposium, 2003. IGARSS'03. Proceedings. 2003 IEEE International*, volume 5, pages 3329–3331. IEEE, 2003.

C. M. Lee, M. L. Cable, S. J. Hook, R. O. Green, S. L. Ustin, D. J. Mandl, and E. M. Middleton. An introduction to the nasa hyperspectral infrared imager (hyspiri) mission and preparatory activities. *Remote Sensing of Environment*, 167:6–19, 2015.

D. D. Lee and H. S. Seung. Learning the parts of objects by non-negative matrix factorization. *Nature*, 401(6755):788–791, 1999.

J. B. Lee, A. S. Woodyatt, and M. Berman. Enhancement of high spectral resolution remote-sensing data by a noise-adjusted principal components transform. *IEEE Transactions on Geoscience and Remote Sensing*, 28(3):295–304, 1990.

H. Li and L. Zhang. A hybrid automatic endmember extraction algorithm based on a local window. *IEEE Transactions on Geoscience and Remote Sensing*, 49(11):4223–4238, 2011.

Q. Li, B. Zhang, L. Gao, L. Lu, and Q. Jiao. The identification of altered rock in vegetation-covered area using hyperspectral remote sensing. In *Geoscience and Remote Sensing Symposium (IGARSS), 2014 IEEE International*, pages 2910–2913. IEEE, 2014.

S. Li, B. Zhang, A. Li, X. Jia, L. Gao, and M. Peng. Hyperspectral imagery clustering with neighborhood constraints. *IEEE Geoscience and Remote Sensing Letters*, 10(3):588–592, 2013a.

W. Li, S. Prasad, and J. E. Fowler. Classification and reconstruction from random projections for hyperspectral imagery. *IEEE Transactions on Geoscience and Remote Sensing*, 51(2): 833–843, 2013b.

L. Liu, J. Zhou, D. Jiang, D. Zhuang, L. R. Mansaray, Z. Hu, and Z. Ji. Mineral resources prospecting by synthetic application of tm/etm+, quickbird and hyperion data in the hatu area, west junggar, xinjiang, china. *Scientific reports*, 6, 2016.

G. Lulu, Z. Xicun, H. Zhaoying, W. Ling, Z. Gengxing, and Y. JIANG. Spectroscopy based estimation of soil organic matter in brown-forest areas of the shandong peninsula, china. *Pedosphere*, 2017.

X. Ma, H. Wang, and J. Wang. Semisupervised classification for hyperspectral image based on multi-decision labeling and deep feature learning. *ISPRS Journal of Photogrammetry and Remote Sensing*, 120:99–107, 2016.

X. Maldague. Theory and practice of infrared technology for nondestructive testing. 2001.

Z. Malenovskỳ, L. Homolová, R. Zurita-Milla, P. Lukeš, V. Kaplan, J. Hanuš, J.-P. Gastellu-Etchegorry, and M. E. Schaepman. Retrieval of spruce leaf chlorophyll content from airborne image data using continuum removal and radiative transfer. *Remote Sensing of Environment*, 131:85–102, 2013.

D. F. Malley, P. C. Williams, and M. P. Stainton. Rapid measurement of suspended c, n, and p from precambrian shield lakes using near-infrared reflectance spectroscopy. *Water Research*, 30(6):1325–1332, 1996.

D. Manolakis, C. Siracusa, and G. Shaw. Hyperspectral subpixel target detection using the linear mixing model. *IEEE Transactions on Geoscience and Remote Sensing*, 39(7):1392–1409, 2001.

G. Martin and A. Plaza. Region-based spatial preprocessing for endmember extraction and spectral unmixing. *IEEE Geoscience and Remote Sensing Letters*, 8(4):745–749, 2011.

G. Martin and A. Plaza. Spatial-spectral preprocessing prior to endmember identification and unmixing of remotely sensed hyperspectral data. *IEEE journal of selected topics in applied earth observations and remote sensing*, 5(2):380–395, 2012.

G. Martin, J. Plaza, and A. Plaza. On the incorporation of spatial information to endmember identification algorithms without the pure pixel assumption. In *Hyperspectral Image and Signal Processing: Evolution in Remote Sensing (WHISPERS), 2011 3rd Workshop on*, pages 1–4. IEEE, 2011.

P. Martin and M. Fehér. Diode lasers. application of near infrared diode lasers in atmospheric and on-line process emission monitoring. *NIR news*, 7(3):10–12, 1996.

R. Mayer, F. Bucholtz, and D. Scribner. Object detection by using" whitening/dewhitening" to transform target signatures in multitemporal hyperspectral and multispectral imagery. *IEEE transactions on geoscience and remote sensing*, 41(5):1136–1142, 2003.

S. Mei, Q. Du, and M. He. Equivalent-sparse unmixing through spatial and spectral constrained endmember selection from an image-derived spectral library. *Selected Topics in Applied Earth Observations and Remote Sensing, IEEE Journal of*, 8(6):2665–2675, 2015.

M. Mercurio, M. Rossi, F. Izzo, P. Cappelletti, C. Germinario, C. Grifa, M. Petrelli, A. Vergara, and A. Langella. The characterization of natural gemstones using non-invasive ft-ir spectroscopy: New data on tourmalines. *Talanta*, 178:147–159, 2018.

M. Meroni and R. Colombo. 3s: A novel program for field spectroscopy. *Computers & Geosciences*, 35(7):1491–1496, 2009.

Meteosat-8. Meteosat-8, 9 July 2007. URL http://sat-nd.com/failures/msg1.html.

A. Meunier, S. Petit, B. L. Ehlmann, P. Dudoignon, F. Westall, A. Mas, A. El Albani, and E. Ferrage. Magmatic precipitation as a possible origin of noachian clays on mars. *Nature Geoscience*, 5(10):739–743, 2012.

J. D. Miller, M. Yalamanchili, A. Atia, and J. Drelich. Characterization of interfacial water at hydrophilic and hydrophobic surfaces by in situ ftir/internal reflection spectroscopy. 1995.

E. J. Milton, M. E. Schaepman, K. Anderson, M. Kneubühler, and N. Fox. Progress in field spectroscopy. *Remote Sensing of Environment*, 113:S92–S109, 2009.

Mindat. http://mindat.org, 2012.

A. Mir-Marqués, M. Martínez-García, S. Garrigues, M. L. Cervera, and M. de la Guardia. Green direct determination of mineral elements in artichokes by infrared spectroscopy and x-ray fluorescence. *Food chemistry*, 196:1023–1030, 2016.

M. Mishali and Y. C. Eldar. From theory to practice: Sub-nyquist sampling of sparse wideband analog signals. *IEEE Journal of Selected Topics in Signal Processing*, 4(2):375–391, 2010.

D. Model and M. Zibulevsky. Signal reconstruction in sensor arrays using sparse representations. *Signal Processing*, 86(3):624–638, 2006.

MODIS. Modis-2017, 2017. URL https://modis.gsfc.nasa.gov/data/.

Y. E. Molan, D. Refahi, and A. H. Tarashti. Mineral mapping in the maherabad area, eastern iran, using the hymap remote sensing data. *International Journal of Applied Earth Observation and Geoinformation*, 27:117–127, 2014.

R. V. Morris, H. V. Lauer, C. A. Lawson, E. K. Gibson, G. A. Nace, and C. Stewart. Spectral and other physicochemical properties of submicron powders of hematite (α-fe2o3), maghemite (γ-fe2o3), magnetite (fe3o4), goethite (α-feooh), and lepidocrocite (γ-feooh). *Journal of Geophysical Research: Solid Earth*, 90(B4):3126–3144, 1985.

Y. Moudden and J. Bobin. Hyperspectral bss using gmca with spatio-spectral sparsity constraints. *IEEE Transactions on Image processing*, 20(3):872–879, 2011.

V. Mulder, S. de Bruin, J. Weyermann, R. F. Kokaly, and M. Schaepman. Characterizing regional soil mineral composition using spectroscopy and geostatistics. *Remote sensing of environment*, 139:415–429, 2013.

R. Murphy. The effects of surficial vegetation cover on mineral absorption feature parameters. *International Journal of Remote Sensing*, 16(12):2153–2164, 1995.

R. J. Murphy, S. Schneider, and S. T. Monteiro. Consistency of measurements of wavelength position from hyperspectral imagery: Use of the ferric iron crystal field absorption at

$$\backslash$$

$sim\,900nmasanindicatorofmineralogy.IEEE\,Transactions\,on\,Geoscience\,and\,Remote\,Sensing, 52$ $(5) : 2843 − −2857, 2014.$

R. J. Murphy, A. Chlingaryan, and A. Melkumyan. Gaussian processes for estimating wavelength position of the ferric iron crystal field feature at 900 nm from hyperspectral imagery acquired in the short-wave infrared (1002–1355 nm). *IEEE Transactions on Geoscience and Remote Sensing*, 53(4):1907–1920, 2015.

J. F. Mustard and J. M. Sunshine. Spectral analysis for earth science: investigations using remote sensing data. *Remote sensing for the earth sciences: Manual of remote sensing*, 3: 251–307, 1999.

J. F. Mustard, S. L. Murchie, S. Pelkey, B. Ehlmann, R. Milliken, J. A. Grant, J.-P. Bibring, F. Poulet, J. Bishop, E. N. Dobrea, et al. Hydrated silicate minerals on mars observed by the mars reconnaissance orbiter crism instrument. *Nature*, 454(7202):305, 2008.

O. Mutanga, A. K. Skidmore, and H. Prins. Predicting in situ pasture quality in the kruger national park, south africa, using continuum-removed absorption features. *Remote sensing of Environment*, 89(3):393–408, 2004.

D. Nash and J. Conel. Spectral reflectance systematics for mixtures of powdered hypersthene, labradorite, and ilmenite. *Journal of Geophysical Research*, 79(11):1615–1621, 1974.

N. M. Nasrabadi. Hyperspectral target detection: An overview of current and future challenges. *IEEE Signal Processing Magazine*, 31(1):34–44, 2014.

A. Y. Ng, M. I. Jordan, and Y. Weiss. On spectral clustering: Analysis and an algorithm. In *Advances in neural information processing systems*, pages 849–856, 2002.

M. Nowak and H. Behrens. The speciation of water in haplogranitic glasses and melts determined by in situ near-infrared spectroscopy. *Geochimica et Cosmochimica Acta*, 59(16):3445–3450, 1995.

R. N. Okparanma, F. Coulon, and A. M. Mouazen. Analysis of petroleum-contaminated soils by diffuse reflectance spectroscopy and sequential ultrasonic solvent extraction–gas chromatography. *Environmental Pollution*, 184:298–305, 2014.

S. O'Rourke, U. Stockmann, N. Holden, A. McBratney, and B. Minasny. An assessment of model averaging to improve predictive power of portable vis-nir and xrf for the determination of agronomic soil properties. *Geoderma*, 279:31–44, 2016.

S. Padma and S. Sanjeevi. Jeffries matusita based mixed-measure for improved spectral matching in hyperspectral image analysis. *International journal of applied earth observation and geoinformation*, 32:138–151, 2014.

Y. Panagakis, C. Kotropoulos, and G. R. Arce. Non-negative multilinear principal component analysis of auditory temporal modulations for music genre classification. *IEEE Transactions on Audio, Speech, and Language Processing*, 18(3):576–588, 2010.

A. Paoli, F. Melgani, and E. Pasolli. Clustering of hyperspectral images based on multiobjective particle swarm optimization. *IEEE transactions on geoscience and remote sensing*, 47(12): 4175–4188, 2009.

K. Pearson. Liii. on lines and planes of closest fit to systems of points in space. *The London, Edinburgh, and Dublin Philosophical Magazine and Journal of Science*, 2(11):559–572, 1901.

N. Pendock, P. Harris, P. Linton, and M. Sears. Going straight: Preprocessing hyperspectral core log images. In *Hyperspectral Image and Signal Processing (WHISPERS), 2012 4th Workshop on*, pages 1–4. IEEE, 2012.

J. Peng, F. Liu, F. Zhou, K. Song, C. Zhang, L. Ye, and Y. He. Challenging applications for multi-element analysis by laser-induced breakdown spectroscopy in agriculture: A review. *TrAC Trends in Analytical Chemistry*, 85:260–272, 2016.

C. Persello and L. Bruzzone. Active and semisupervised learning for the classification of remote sensing images. *IEEE Transactions on Geoscience and Remote Sensing*, 52(11):6937–6956, 2014.

A. Plaza, J. A. Benediktsson, J. W. Boardman, J. Brazile, L. Bruzzone, G. Camps-Valls, J. Chanussot, M. Fauvel, P. Gamba, A. Gualtieri, et al. Recent advances in techniques for hyperspectral image processing. *Remote sensing of environment*, 113:S110–S122, 2009.

L. Pompilio, M. Pepe, G. Pedrazzi, and L. Marinangeli. Informational clustering of hyperspectral data. *IEEE Journal of Selected Topics in Applied Earth Observations and Remote Sensing*, 7 (6):2209–2223, 2014.

A. B. Pour and M. Hashim. The application of aster remote sensing data to porphyry copper and epithermal gold deposits. *Ore Geology Reviews*, 44:1–9, 2012a.

A. B. Pour and M. Hashim. Identifying areas of high economic-potential copper mineralization using aster data in the urumieh–dokhtar volcanic belt, iran. *Advances in Space Research*, 49 (4):753–769, 2012b.

A. B. Pour and M. Hashim. Evaluation of earth observing-1 (eo1) data for lithological and hydrothermal alteration mapping: A case study from urumieh-dokhtar volcanic belt, se iran. *Journal of the Indian Society of Remote Sensing*, 43(3):583–597, 2015a.

A. B. Pour and M. Hashim. Hydrothermal alteration mapping from landsat-8 data, sar cheshmeh copper mining district, south-eastern islamic republic of iran. *Journal of Taibah University for Science*, 9(2):155–166, 2015b.

A. B. Pour, M. Hashim, and J. van Genderen. Detection of hydrothermal alteration zones in a tropical region using satellite remote sensing data: Bau goldfield, sarawak, malaysia. *Ore Geology Reviews*, 54:181–196, 2013.

H. Preissler and G. Loercher. Extraction of soil properties from laboratory and imaging spectrometry data. In *Geoscience and Remote Sensing Symposium, 1995. IGARSS'95.'Quantitative Re-*

mote Sensing for Science and Applications', *International*, volume 3, pages 1968–1970. IEEE, 1995.

Y. Qian and M. Ye. Hyperspectral imagery restoration using nonlocal spectral-spatial structured sparse representation with noise estimation. *IEEE Journal of Selected Topics in Applied Earth Observations and Remote Sensing*, 6(2):499–515, 2013.

S. Rajendran, S. Nasir, T. M. Kusky, A. Ghulam, S. Gabr, and M. A. El-Ghali. Detection of hydrothermal mineralized zones associated with listwaenites in central oman using aster data. *Ore geology reviews*, 53:470–488, 2013.

R. Rajesh and J. S. Prakash. Extreme learning machinesâa review and state-of-the-art. *International journal of wisdom based computing*, 1(1):35–49, 2011.

J. O. Ramsay. *Functional data analysis*. Wiley Online Library, 2006.

K. A. Reath and M. S. Ramsey. Exploration of geothermal systems using hyperspectral thermal infrared remote sensing. *Journal of Volcanology and Geothermal Research*, 265:27–38, 2013.

A. Remon, S. Sanchez, A. Paz, E. S. Quintana-Orti, and A. Plaza. Real-time endmember extraction on multicore processors. *IEEE Geoscience and Remote Sensing Letters*, 8(5):924–928, 2011.

A. Resnick, C. Persons, and G. Lindquist. Polarized emissivity and kirchhoffâs law. *Applied optics*, 38(8):1384–1387, 1999.

A. Riaza, P. Strobl, U. Beisl, A. Hausold, and A. Müller. Spectral mapping of rock weathering degrees on granite using hyperspectral dais 7915 spectrometer data. *International Journal of Applied Earth Observation and Geoinformation*, 3(4):345–354, 2001.

J. Ricardo, A. De França, J.-M. Brustet, and J. Fontan. Multispectral remote sensing of biomass burning in west africa. *Journal of Atmospheric Chemistry*, 22(1-2):81–110, 1995.

B. Rivard, P. J. Thomas, D. Pollex, A. Hollinger, J. R. Miller, and R. Dick. A field-portable thermal infrared grating spectrometer (thirspec). *IEEE transactions on geoscience and remote sensing*, 32(2):307–314, 1994.

B. Rivard, J. Feng, A. Gallie, and A. Sanchez-Azofeifa. Continuous wavelets for the improved use of spectral libraries and hyperspectral data. *Remote Sensing of Environment*, 112(6): 2850–2862, 2008.

B. Rivard, D. Lyder, J. Feng, A. Gallie, E. Cloutis, P. Dougan, S. Gonzalez, D. Cox, and M. Lipsett. Bitumen content estimation of athabasca oil sand from broad band infrared reflectance spectra. *The Canadian Journal of Chemical Engineering*, 88(5):830–838, 2010.

D. Rogge, B. Rivard, K. Segl, B. Grant, and J. Feng. Mapping of nicu–pge ore hosting ultramafic rocks using airborne and simulated enmap hyperspectral imagery, nunavik, canada. *Remote sensing of environment*, 152:302–317, 2014.

P.-S. Ross, A. Bourke, and B. Fresia. A multi-sensor logger for rock cores: Methodology and preliminary results from the matagami mining camp, canada. *Ore Geology Reviews*, 53:93–111, 2013.

S. W. Ruff, P. R. Christensen, P. W. Barbera, and D. L. Anderson. Quantitative thermal emission spectroscopy of minerals: A laboratory technique for measurement and calibration. *Journal of Geophysical Research: Solid Earth*, 102(B7):14899–14913, 1997.

S. Salehi, D. Rogge, B. Rivard, B. H. Heincke, and R. Fensholt. Modeling and assessment of wavelength displacements of characteristic absorption features of common rock forming minerals encrusted by lichens. *Remote Sensing of Environment*, 199:78–92, 2017.

J. Salisbury. Mid-infrared spectroscopy: Laboratory data. *Remote geochemical analysis: Elemental and mineralogical composition*, pages 79–98, 1993.

J. W. Salisbury and N. Vergo. *Infrared (2.1-25 um) spectra of minerals*. Johns Hopkins University Press, 1991.

J. W. Salisbury, A. Wald, and D. M. D'Aria. Thermal-infrared remote sensing and kirchhoff's law: 1. laboratory measurements. *Journal of Geophysical Research: Solid Earth*, 99(B6): 11897–11911, 1994.

I. D. Sanches, C. R. Souza Filho, and R. F. Kokaly. Spectroscopic remote sensing of plant stress at leaf and canopy levels using the chlorophyll 680nm absorption feature with continuum removal. *ISPRS Journal of Photogrammetry and Remote Sensing*, 97:111–122, 2014.

S. H. Savage, T. E. Levy, and I. W. Jones. Prospects and problems in the use of hyperspectral imagery for archaeological remote sensing: A case study from the faynan copper mining district, jordan. *Journal of Archaeological Science*, 39(2):407–420, 2012.

R. D. M. Scafutto, C. R. de Souza Filho, and B. Rivard. Characterization of mineral substrates impregnated with crude oils using proximal infrared hyperspectral imaging. *Remote Sensing of Environment*, 179:116–130, 2016.

A. C. Scheinost, D. G. Schulze, and U. Schwertmann. Diffuse reflectance spectra of a1 substituted goethite: A ligand field approach. *Clays and Clay Minerals*, 47(2):156–164, 1999.

E. Sefton-Nash, D. Catling, S. Wood, P. M. Grindrod, and N. Teanby. Topographic, spectral and thermal inertia analysis of interior layered deposits in iani chaos, mars. *Icarus*, 221(1): 20–42, 2012.

G. S. Senesi. Laser-induced breakdown spectroscopy (libs) applied to terrestrial and extraterrestrial analogue geomaterials with emphasis to minerals and rocks. *Earth-Science Reviews*, 139:231–267, 2014.

M. Sgavetti, L. Pompilio, C. Carli, M. C. de Sanctis, F. Capaccioni, G. Cremonese, and E. Flamini. Bepicolombo simbio-sys data: Preliminary evaluation for rock discrimination and recognition in both low and high resolution spectroscopic data in the visible and near infrared spectral intervals. *Planetary and Space Science*, 55(11):1596–1613, 2007.

H. Shahriari, M. Honarmand, and H. Ranjbar. Comparison of multi-temporal aster images for hydrothermal alteration mapping using a fractal-aided sam method. *International Journal of Remote Sensing*, 36(5):1271–1289, 2015.

Z. Shao, L. Zhang, X. Zhou, and L. Ding. A novel hierarchical semisupervised svm for classification of hyperspectral images. *IEEE Geoscience and Remote Sensing Letters*, 11(9):1609–1613, 2014.

H. Shin, J. Yu, Y. Jeong, L. Wang, and D.-Y. Yang. Case-based regression models defining the relationships between moisture content and shortwave infrared reflectance of beach sands. *IEEE Journal of Selected Topics in Applied Earth Observations and Remote Sensing*, 10(10): 4512–4521, 2017.

T. Shuai, X. Zhang, L. Zhang, and J. Wang. Mapping global lunar abundance of plagioclase, clinopyroxene and olivine with interference imaging spectrometer hyperspectral data considering space weathering effect. *Icarus*, 222(1):401–410, 2013.

K. Siegbahn and P. Axel. Alpha-, beta-, and gamma-ray spectroscopy. *American Journal of Physics*, 34(3):275–276, 1966.

B. W. Silverman et al. Smoothed functional principal components analysis by choice of norm. *The Annals of Statistics*, 24(1):1–24, 1996.

K. D. Singh, D. Ramakrishnan, and L. Mansinha. Relevance of transformation techniques in rapid endmember identification and spectral unmixing: A hypespectral remote sensing perspective. In *Geoscience and Remote Sensing Symposium (IGARSS), 2012 IEEE International*, pages 4066–4069. IEEE, 2012a.

K. D. Singh, D. Ramakrishnan, and L. Mansinha. A novel method for automatic minerals identification and their abundance estimation for material type discrimination using hyperspectral data. In *Hyperspectral Image and Signal Processing (WHISPERS), 2012 4th Workshop on*, pages 1–4. IEEE, 2012b.

K. Sjöstrand, L. H. Clemmensen, R. Larsen, and B. Ersbøll. Spasm: A matlab toolbox for sparse statistical modeling. *Journal of Statistical Software*, 2012.

M. R. Smith, J. L. Bandfield, E. A. Cloutis, and M. S. Rice. Hydrated silica on mars: Combined analysis with near-infrared and thermal-infrared spectroscopy. *Icarus*, 223(2):633–648, 2013.

J. A. Sobrino, C. Mattar, P. Pardo, J. C. Jiménez-Muñoz, S. J. Hook, A. Baldridge, and R. Ibañez. Soil emissivity and reflectance spectra measurements. *Applied optics*, 48(19): 3664–3670, 2009.

J. Soriano-Disla, L. Janik, M. McLaughlin, S. Forrester, J. Kirby, C. Reimann, and T. E. G. P. Team. The use of diffuse reflectance mid-infrared spectroscopy for the prediction of the concentration of chemical elements estimated by x-ray fluorescence in agricultural and grazing european soils. *Applied geochemistry*, 29:135–143, 2013.

M. Soto-Cámara, A. Gaitán-Jurado, and J. Domínguez. Application of near infrared spectroscopy technology for the detection of fungicide treatment on durum wheat samples. *Talanta*, 97:298–302, 2012.

L. Spampinato, S. Calvari, C. Oppenheimer, and E. Boschi. Volcano surveillance using infrared cameras. *Earth-Science Reviews*, 106(1):63–91, 2011.

M. Speta, B. Rivard, J. Feng, M. Lipsett, and M. Gingras. Hyperspectral imaging for the characterization of athabasca oil sands drill core. In *Geoscience and Remote Sensing Symposium (IGARSS), 2013 IEEE International*, pages 2184–2187. IEEE, 2013.

S. Sra and I. S. Dhillon. Generalized nonnegative matrix approximations with bregman divergences. In *Advances in neural information processing systems*, pages 283–290, 2006.

J.-L. Starck, M. Elad, and D. L. Donoho. Image decomposition via the combination of sparse representations and a variational approach. *IEEE transactions on image processing*, 14(10): 1570–1582, 2005.

B. Stenberg, R. A. V. Rossel, A. M. Mouazen, and J. Wetterlind. Chapter five-visible and near infrared spectroscopy in soil science. *Advances in agronomy*, 107:163–215, 2010.

H. Su, H. Yang, Q. Du, and Y. Sheng. Semisupervised band clustering for dimensionality reduction of hyperspectral imagery. *IEEE Geoscience and Remote Sensing Letters*, 8(6):1135–1139, 2011.

H. Su, Y. Sheng, P. Du, and K. Liu. Adaptive affinity propagation with spectral angle mapper for semi-supervised hyperspectral band selection. *Applied optics*, 51(14):2656–2663, 2012.

L. Sun and S. Khan. Ground-based hyperspectral remote sensing of hydrocarbon-induced rock alterations at cement, oklahoma. *Marine and Petroleum Geology*, 77:1243–1253, 2016.

Y. Sun, P. K. Seccombe, and K. Yang. Application of short-wave infrared spectroscopy to define alteration zones associated with the elura zinc–lead–silver deposit, nsw, australia. *Journal of Geochemical Exploration*, 73(1):11–26, 2001.

J. M. Sunshine and C. M. Pieters. Estimating modal abundances from the spectra of natural and laboratory pyroxene mixtures using the modified gaussian model. *Journal of Geophysical Research: Planets*, 98(E5):9075–9087, 1993.

M. R. Swain, P. Deroo, C. A. Griffith, G. Tinetti, A. Thatte, G. Vasisht, P. Chen, J. Bouwman, I. J. Crossfield, D. Angerhausen, et al. A ground-based near-infrared emission spectrum of the exoplanet hd 189733b. *Nature*, 463(7281):637–639, 2010.

G. A. Swayze. *The hydrothermal and structural history of the Cuprite Mining District, south-western Nevada: An integrated geological and geophysical approach.* 1997.

G. Takacs, T. Pokorny, and I. Banyasz. Application of a portable near-infrared analyzer for wheat measurement. In *Near-infrared Spectrosc.: Future Waves, Proc. Int. Conf. Near-infrared Spectrosc., 7th*, pages 92–97, 1996.

K. L. Tanaka. The stratigraphy of mars. *Journal of Geophysical Research: Solid Earth*, 91(B13), 1986.

M. C. Tappert, B. Rivard, D. Giles, R. Tappert, and A. Mauger. The mineral chemistry, near-infrared, and mid-infrared reflectance spectroscopy of phengite from the olympic dam iocg deposit, south australia. *Ore Geology Reviews*, 53:26–38, 2013.

Y. Tarabalka, J. C. Tilton, J. A. Benediktsson, and J. Chanussot. A marker-based approach for the automated selection of a single segmentation from a hierarchical set of image segmentations. *IEEE Journal of Selected Topics in Applied Earth Observations and Remote Sensing*, 5 (1):262–272, 2012.

Telops. Telops, 2016. URL http://telops.com/products/hyperspectral-cameras/item/download/76_856bf981c221d53f5c8f73bffe75d6cb.

K. E. Themelis, A. A. Rontogiannis, and K. D. Koutroumbas. A novel hierarchical bayesian approach for sparse semisupervised hyperspectral unmixing. *Signal Processing, IEEE Transactions on*, 60(2):585–599, 2012a.

K. E. Themelis, F. Schmidt, O. Sykioti, A. A. Rontogiannis, K. D. Koutroumbas, and I. A. Daglis. On the unmixing of mex/omega hyperspectral data. *Planetary and Space Science*, 68 (1):34–41, 2012b.

K. Thompson and R. J. Reynolds. *Atomic absorption, fluorescence, and flame emission spectroscopy: a practical approach.* Halsted Press, 1978.

S. M. Thulin, M. J. Hill, and A. A. Held. Spectral sensitivity to carbon and nitrogen content in diverse temperate pastures of australia. In *Geoscience and Remote Sensing Symposium, 2004. IGARSS'04. Proceedings. 2004 IEEE International*, volume 2, pages 1459–1462. IEEE, 2004.

R. Tibshirani. Regression shrinkage and selection via the lasso. *Journal of the Royal Statistical Society. Series B (Methodological)*, pages 267–288, 1996.

TORNADO. small-spot micro x-ray fluorescence (micro-xrf): M4 tornado. `https://www.bruker.com/products/x-ray-diffraction-and-elemental-analysis/micro-xrf-and-txrf/m4-tornado/overview.html`, 2015. Online; accessed 31 May 2017.

J. A. Tropp and S. J. Wright. Computational methods for sparse solution of linear inverse problems. *Proceedings of the IEEE*, 98(6):948–958, 2010.

D. Tuia and G. Camps-Valls. Urban image classification with semisupervised multiscale cluster kernels. *IEEE Journal of Selected Topics in Applied Earth Observations and Remote Sensing*, 4(1):65–74, 2011.

G. L. Turin. An introduction to digitial matched filters. *Proceedings of the IEEE*, 64(7):1092–1112, 1976.

J. S. Tyo, A. Konsolakis, D. I. Diersen, and R. C. Olsen. Principal-components-based display strategy for spectral imagery. *IEEE Transactions on Geoscience and Remote Sensing*, 41(3):708–718, 2003.

P. C. Uden. *Element-specific chromatographic detection by atomic emission spectroscopy*. ACS Publications, 1992.

M. O. Ulfarsson and V. Solo. Smooth principal component analysis with application to functional magnetic resonance imaging. In *Acoustics, Speech and Signal Processing, 2006. ICASSP 2006 Proceedings. 2006 IEEE International Conference on*, volume 2, pages II–II. IEEE, 2006.

F. D. Van der Meer, H. M. Van der Werff, F. J. van Ruitenbeek, C. A. Hecker, W. H. Bakker, M. F. Noomen, M. van der Meijde, E. J. M. Carranza, J. B. de Smeth, and T. Woldai. Multi- and hyperspectral geologic remote sensing: A review. *International Journal of Applied Earth Observation and Geoinformation*, 14(1):112–128, 2012.

M. van der Meijde, N. M. Knox, S. L. Cundill, M. F. Noomen, H. Van der Werff, and C. Hecker. Detection of hydrocarbons in clay soils: A laboratory experiment using spectroscopy in the mid-and thermal infrared. *International Journal of Applied Earth Observation and Geoinformation*, 23:384–388, 2013.

F. J. van Ruitenbeek, W. H. Bakker, H. M. van der Werff, T. E. Zegers, J. H. Oosthoek, Z. A. Omer, S. H. Marsh, and F. D. van der Meer. Mapping the wavelength position of deepest absorption features to explore mineral diversity in hyperspectral images. *Planetary and Space Science*, 101:108–117, 2014.

G. Vane, J. Duval, and J. Wellman. Imaging spectroscopy of the earth and other solar system bodies. *Remote Geochemical Analysis: Elemental and Mineralogical Composition. Cambridge University Press, New York*, pages 121–166, 1993.

R. G. Vaughan and W. M. Calvin. Synthesis of high-spatial resolution hyperspectral vnir/swir and tir image data for mapping weathering and alteration minerals in virginia city, nevada. In *Geoscience and Remote Sensing Symposium, 2004. IGARSS'04. Proceedings. 2004 IEEE International*, volume 2, pages 1296–1299. IEEE, 2004.

L. E. Vicente and C. R. de Souza Filho. Identification of mineral components in tropical soils using reflectance spectroscopy and advanced spaceborne thermal emission and reflection radiometer (aster) data. *Remote Sensing of Environment*, 115(8):1824–1836, 2011.

P. Vítek, E. M. Ali, H. G. Edwards, J. Jehlička, R. Cox, and K. Page. Evaluation of portable raman spectrometer with 1064nm excitation for geological and forensic applications. *Spectrochimica Acta Part A: Molecular and Biomolecular Spectroscopy*, 86:320–327, 2012.

C. E. Viviano and J. E. Moersch. Using themis data to resolve the discrepancy between crism/omega and tes modeled phyllosilicate abundance in mawrth vallis. *Icarus*, 226(1):497–509, 2013.

X. Wan, C. Zhao, Y. Wang, and W. Liu. Stacked sparse autoencoder in hyperspectral data classification using spectral-spatial, higher order statistics and multifractal spectrum features. *Infrared Physics & Technology*, 86:77–89, 2017.

C. Wang, T. Zhang, and X. Pan. Potential of visible and near-infrared reflectance spectroscopy for the determination of rare earth elements in soil. *Geoderma*, 306:120–126, 2017.

Y. Wang, Q. Lin, Q. Wang, and Y. Chen. A method to improve mineral identification accuracy based on hyperspectral data. In *IOP Conference Series: Earth and Environmental Science*, volume 17, page 012206. IOP Publishing, 2014.

Y. Wang, T. Huang, J. Liu, Z. Lin, S. Li, R. Wang, and Y. Ge. Soil ph value, organic matter and macronutrients contents prediction using optical diffuse reflectance spectroscopy. *Computers and Electronics in Agriculture*, 111:69–77, 2015.

Y. Wang, F. Xie, and J. Wang. Short-wave infrared signature and detection of aicraft in flight based on space-borne hyperspectral imagery. *Chinese Optics Letters*, 14(12):122801, 2016.

S. M. Watson, R. T. Kroutil, C. A. Traynor, E. S. Edgerton, J. J. Bowser, R. B. Zweidinger, R. N. Olson, R. P. Dalley, W. J. Bone, and R. Price. Remote-sensing and in-situ atmospheric chemistry studies with the use of a manned hot air balloon platform. *Field Analytical Chemistry & Technology*, 1(1):13–22, 1996.

E. W. Weisstein. Gaussian function, 2017. URL http://mathworld.wolfram.com/GaussianFunction.html.

C. Wöhler, A. Grumpe, A. Berezhnoy, M. U. Bhatt, and U. Mall. Integrated topographic, photometric and spectral analysis of the lunar surface: Application to impact melt flows and ponds. *Icarus*, 235:86–122, 2014.

H. Worden, R. Beer, and C. P. Rinsland. Airborne infrared spectroscopy of 1994 western wildfires. *Journal of Geophysical Research: Atmospheres*, 102(D1):1287–1299, 1997.

J. J. Workman Jr. Review of process and non-invasive near-infrared and infrared spectroscopy: 1993–1999. *Applied spectroscopy reviews*, 34(1-2):1–89, 1999.

J. J. Wray, S. T. Hansen, J. Dufek, G. A. Swayze, S. L. Murchie, F. P. Seelos, J. R. Skok, R. P. Irwin III, and M. S. Ghiorso. Prolonged magmatic activity on mars inferred from the detection of felsic rocks. *Nature Geoscience*, 6(12):1013–1017, 2013.

B. Xiaojia, M. Fang, W. Bin, L. Jiaguang, and W. Dong. Hyperion hyperspectral remote sensing application in altered mineral mapping in east kunlun of the qinghai-tibet plateau. In *Challenges in Environmental Science and Computer Engineering (CESCE), 2010 International Conference on*, volume 1, pages 519–523. IEEE, 2010.

D. Xu, L. Sun, J. Luo, and Z. Liu. Analysis and denoising of hyperspectral remote sensing image in the curvelet domain. *Mathematical Problems in Engineering*, 2013, 2013.

Y. Xue and S. Jin. Martian minerals components at gale crater detected by mro crism hyperspectral images. In *Instrumentation and Measurement, Sensor Network and Automation (IMSNA), 2013 2nd International Symposium on*, pages 1067–1070. IEEE, 2013.

T. Yajima, K. Ohkawa, and S. Huzikawa. Hyperspectral alteration mineral mapping using the posam method. In *Geoscience and Remote Sensing Symposium, 2004. IGARSS'04. Proceedings. 2004 IEEE International*, volume 2, pages 1491–1493. IEEE, 2004.

J. Yang and Q. Cheng. A comparative study of independent component analysis with principal component analysis in geological objects identification, part i: Simulations. *Journal of Geochemical Exploration*, 149:127–135, 2015.

K. Yang, P. Browne, J. Huntington, and J. Walshe. Characterising the hydrothermal alteration of the broadlands–ohaaki geothermal system, new zealand, using short-wave infrared spectroscopy. *Journal of Volcanology and Geothermal Research*, 106(1):53–65, 2001a.

K. Yang, J. Huntington, T. Cudahy, P. Mason, and K. Scott. Spectrally mapping the compositional variation of white micas in hydrothermal systems and the application in mineral exploration. In *Geoscience and Remote Sensing Symposium, 2001. IGARSS'01. IEEE 2001 International*, volume 7, pages 3294–3296. IEEE, 2001b.

K. Yang, J. Huntington, J. Gemmell, and K. Scott. Variations in composition and abundance of white mica in the hydrothermal alteration system at hellyer, tasmania, as revealed by infrared reflectance spectroscopy. *Journal of Geochemical Exploration*, 108(2):143–156, 2011.

B. Yousefi. Continuum removal. `http://vision.gel.ulaval.ca/~bardia/PublicCodes/web_J0_29May2018.zip`, 2018.

B. Yousefi, S. Sojasi, C. I. Castanedo, G. Beaudoin, F. Huot, X. Maldague, M. Chamberland, and E. Lalonde. Mineral identification in hyperspectral imaging using sparse-pca. In *SPIE Commercial+ Scientific Sensing and Imaging*, pages 986118–986118. International Society for Optics and Photonics, 2016a.

B. Yousefi, S. Sojasi, C. I. Castanedo, G. Beaudoin, F. Huot, X. P. Maldague, M. Chamberland, and E. Lalonde. Emissivity retrieval from indoor hyperspectral imaging of mineral grains. In *Thermosense: Thermal Infrared Applications XXXVIII*, volume 9861, page 98611C. International Society for Optics and Photonics, 2016b.

B. Yousefi, S. Sojasi, K. Liaigre, C. I. Castanedo, G. Beaudoin, F. Huot, X. P. Maldague, and M. Chamberland. Modified algorithm for mineral identification in lwir hyperspectral imagery. In *Thermosense: Thermal Infrared Applications XXXIX*, volume 10214, page 102141H. International Society for Optics and Photonics, 2017.

N. Zabcic, B. Rivard, C. Ong, and A. Mueller. Using airborne hyperspectral data to characterize the surface ph and mineralogy of pyrite mine tailings. *International Journal of Applied Earth Observation and Geoinformation*, 32:152–162, 2014.

F. Zambon, M. C. De Sanctis, S. Schröder, F. Tosi, A. Longobardo, E. Ammannito, D. T. Blewett, D. W. Mittlefehldt, J.-Y. Li, E. Palomba, et al. Spectral analysis of the bright materials on the asteroid vesta. *Icarus*, 240:73–85, 2014.

F. Zhang, B. Du, L. Zhang, and L. Zhang. Hierarchical feature learning with dropout k-means for hyperspectral image classification. *Neurocomputing*, 187:75–82, 2016a.

H. Zhang, L. Yu, U. Hassler, H. Fernandes, M. Genest, F. Robitaille, S. Joncas, W. Holub, Y. Sheng, and X. Maldague. An experimental and analytical study of micro-laser line thermography on micro-sized flaws in stitched carbon fiber reinforced polymer composites. *Composites Science and Technology*, 126:17–26, 2016b.

L. Zhang, L. Zhang, D. Tao, X. Huang, and B. Du. Hyperspectral remote sensing image subpixel target detection based on supervised metric learning. *IEEE transactions on geoscience and remote sensing*, 52(8):4955–4965, 2014.

L. Zhang, L. Zhang, and B. Du. Deep learning for remote sensing data: A technical tutorial on the state of the art. *IEEE Geoscience and Remote Sensing Magazine*, 4(2):22–40, 2016c.

H. Zhao, L. Zhang, X. Zhang, J. Liu, T. Wu, and S. Wang. Hyperspectral feature extraction based on the reference spectral background removal method. *IEEE Journal of Selected Topics in Applied Earth Observations and Remote Sensing*, 8(6):2832–2844, 2015.

Y. Zhong, L. Zhang, B. Huang, and P. Li. An unsupervised artificial immune classifier for multi/hyperspectral remote sensing imagery. *IEEE Transactions on Geoscience and Remote Sensing*, 44(2):420–431, 2006.

Y. Zhong, X. Wang, L. Zhao, R. Feng, L. Zhang, and Y. Xu. Blind spectral unmixing based on sparse component analysis for hyperspectral remote sensing imagery. *ISPRS Journal of Photogrammetry and Remote Sensing*, 119:49–63, 2016.

T. Zhou and D. Tao. Double shrinking sparse dimension reduction. *IEEE Transactions on Image Processing*, 22(1):244–257, 2013.

H. Zou and T. Hastie. Regularization and variable selection via the elastic net. *Journal of the Royal Statistical Society: Series B (Statistical Methodology)*, 67(2):301–320, 2005.

H. Zou, T. Hastie, and R. Tibshirani. Sparse principal component analysis. *Journal of computational and graphical statistics*, 15(2):265–286, 2006.

J. O. Zwicker. Intercomparison of data from open-path fourier transform infrared spectrometers collected during the epa/api cooperative remote sensing/dispersion study at duke forest, north carolina january 9 to 27, 1995. In *Optical Remote Sensing for Environmental and Process Monitoring*, volume 2883, page 550, 1996.